

Supported photocatalysts for model pollutant degradation and bacterial inactivation: Preparation, evaluation and characterization

THÈSE N° 7836 (2017)

PRÉSENTÉE LE 25 AOÛT 2017
À LA FACULTÉ DES SCIENCES DE BASE
GROUPE PULGARIN

PROGRAMME DOCTORAL EN CHIMIE ET GÉNIE CHIMIQUE

ÉCOLE POLYTECHNIQUE FÉDÉRALE DE LAUSANNE

POUR L'OBTENTION DU GRADE DE DOCTEUR ÈS SCIENCES

PAR

Laura Victoria SUÁREZ MURILLO

acceptée sur proposition du jury:

Dr G. Wagnières, président du jury
Prof. C. Pulgarin, directeur de thèse
Dr R. Comparelli, rapporteur
Prof. R. Torres Palma, rapporteur
Dr Y. Leterrier, rapporteur



ÉCOLE POLYTECHNIQUE
FÉDÉRALE DE LAUSANNE

Suisse
2017

***To my nieces: Isabela and Luciana and in loving memory of
Consuelo, Tina, Resfa and Rosa***

A mis sobrinas: Isabela y Luciana y en memoria de mis queridas Consuelo, Tina, Resfa y Rosa

Acknowledgements

My highest acknowledgments to Prof. César Pulgarín and Dr. John Kiwi for their excellent roles as supervisors. Both have taught me and supported me and I will always treasure their academic and life lessons. Very special thanks to Professor Pulgarín whom excels knowledge transmission and has the ability to induce self-awareness in his students while managing to plant seeds of curiosity and daily self-improvement. It was an honor to have my life transformed by his influence. Moreover, I would like to acknowledge the LIMPID project and extend my gratitude to the great working team I had the honor to meet.

Very special thanks to Professors Georges wagnières, Roberto Comparelli, Yves Leterrier and Ricardo Torres Palma, whom were the juries of my thesis defense and enabled an interesting and fruitful discussion.

My acknowledgements for the Swiss Confederation and the EPFL for facilitating the formation of people like me by means of the “Bourse de l'excellence”. Especial thanks and a huge hug to Karin Jullierat, her patience and kindness kept me standing during difficult times.

My deep respect and felt acknowledgments to the people that with good will and patience elucidated essential concepts for my Thesis: Dr. Manuel Mendez, Dr. Rosendo Sanjines, Dr. Michäel Bensimone and Mr Pierre Mettraux. Also to the colleagues from other laboratories: Oliver Beswick, and Masoud Talebi; and very special thanks and admiration to Professor Kevin Sivula, who was always thoughtful and supportive.

I cannot thank enough my excellent colleagues Stefanos G and Sami, both helped me, guided me and taught me so much. My deep and felt gratefulness also goes to Cristina, Paola, Angelica, Jasmin, Pilar and Marco; you all provided not only excellent insight but also shared your daily-life wisdom with me. Special thanks also to: Dong, Wei and Oualid; working with you was effective and fruitful, thanks for the patience and for the things we shared. An honorable mention to Christian Pinilla, who has had my back for the last two years. Thanks and blessings to my incredible summer 2016 students team: Helena, Francesco and Leily. Your empathy towards others and outstanding potential for science made you unforgettable. Another special mention goes to sweet Sofia, thanks for being around during sicknesses, blues or frustrations. Thanks to my good friend Maurizio Pezzoli, always with a great attitude, good advices, fun comments and smiles.

My affection and gratefulness to my Professors from Universidad de Antioquia: César Botache and Felipe Bustamante. Thanks for believing in me, for supporting me and for ratifying that efforts and perseverance could be as valuable as a bright intellect. Thanks to the brilliant people I met at EPMA during my Master thesis: Ulrich Vogt, Michal Gorbar, Daniel Wiedenmann, Jelena Stojadinovic and Leyre Sagarna, your support and good examples adjusted my path in science. Very especial acknowledgements to the SDC Colombia team: Diana Rojas, Sergio Perez, Luz Angela Bernal, Catalina Sierra, Diana Cifuentes, Tania García, Walter Reithebuch, Martin Jaggi, Maly Puerto and Patricia Romero. I remember you all with affection, working with you gave me new perspectives and reaffirmed my will to direct my acquired knowledge towards the wellbeing of our society.

Thanks to my Colombian family in Turin- Italy: Jorge Tobón, Monica Grajales, John Jairo Betancur, and Andrés Perez; you guys are family and seeing you from time to time was revitalizing, thanks for

the online company as well, I love you guys! Thanks to the Colombian people in Lausanne: Juan David, thanks for your patience, your advices, your company in dark moments, thanks for the good laughs, for the books and for the joy we shared during metal concerts; in addition, thanks to your life companion Caro, who managed to leave important lessons regardless the brief period we shared. Very special thanks to Marcela, Angela, Johnny, Camilo, Nicolas, Mariluz and Monica, always willing to help and always creating the surreal sensation of being in our beautiful Colombia... I deeply thank you for all the good moments.

Acknowledgments to my enormous family: Suárez side and Murillo side. You trusted I had the capabilities to start a life away from home and supported me. Special thanks to my uncle Julián for whom I have always felt an especial affection due to his great sense of humor and inexhaustible kindness.

And my warmest feelings and infinite gratefulness to the following people:

To my father and mother: I can proudly say that anything good I have, I have inherited it from you two. You have been both responsible hard workers, you taught me to be honest, to persist, to care for others, you planted the love for nature and animals in me, you have believed in me and you have supported me no matter what. Thanks for accepting me with flaws and virtues, thanks for allowing me to develop my own ideas and for respecting them. Thanks for giving me wings and help me fly away. You two are my dearest treasure and every single small achievement in my life is fruit of all the efforts you two put together. Mom, to you especially, thanks for helping me believe I could do so many things against the odds, against the hard circumstances, against the lack of resources... you are my favorite warrior in the world and you shaped me into an independent strong person.

To my brothers: Juampa and Andrés, growing up while having you two as examples was a blessing. I don't get tired of showing off how especial my brothers are and how beautiful our relationship is. You are kind-hearted, caring, persistent, strong, smart, and thoughtful, you haven't stopped guiding me towards improvement, you have always remembered me I worth and the most beautiful memories I cherish involve you two. Thanks my brothers, you made me proud every single day.

To my life companion: Alexis, you have struggled with me these last two intense and difficult years. Your love is my light and your company gives me strength, I am happy and excited to keep making dreams come true while holding your hand. I love you deeply, mi amor.

And last but not least; to Darwin and Claudia: the best couple in the world; to Ana Cristina, Cindy, and Erika: my amazing empowered Murillo XX cousin team; to Ana Maria: my sweet cousin-sister-friend.

All your support, all your faith in me, all the experiences, all the things you shared with me have made me what I am, you are the most important people in my life and I love you all immensely!

Abstract

Water quality and bacterial infections are directly related to human health and wellbeing, thus waste water treatment is a necessary procedure for avoiding disturbances to ecosystems and for assuring human health. Furthermore, bacterial contamination in water bodies, the appearance of antibiotic resistant bacteria in hospitals and public places have to be addressed and not only by means of proper aseptic practices. Water quality improvement and antibacterial surfaces call for the need to design new supported catalysts/photocatalysts.

The above mentioned issues have given rise to a research field called advanced photochemical oxidation processes (APO's). This Thesis is based on APO's while designing, testing and characterizing supported photocatalysts. The used supports were: Polyethylene thin films, glass Raschig rings and Glass fiber mats. Photocatalysts as TiO₂, Fe-oxides, Cu-decorated TiO₂ and copper oxides were deposited by dip coating and sputtering on the mentioned supports.

The photocatalysts were tested mostly under solar simulated light irradiation for the degradation of methylene blue (MB) in solution, the inactivation of bacteria (*E. coli*) in solution and inactivation of bacteria on solid-air interface. Characterization techniques allowed describing/optimizing the surface of the catalyst/photocatalyst leading to pollutant degradation and bacterial disinfection.

Photocatalysts supported on polyethylene films (PE-TiO₂ and PE-FeOx) showed activity in the degradation of MB in solution over several use cycles, suggesting a potential practical use. The TiO₂ light absorbance in the visible region was improved by the addition of Cu/CuO and moreover, the contact between photocatalyst and targets (MB or *E. coli*) was increased by using glass Raschig rings or glass fiber mats (GF) as supports. Only very low amounts of Cu were enough to increase MB degradation kinetics. Self-cleaning of MB was evaluated on GF-TiO₂-Cu-mats under simulated solar irradiation as well. Bacterial inactivation in solution by means of GF-TiO₂-Cu 3%-mats showed to be much faster than via GF-TiO₂-mats. Regarding antibacterial films, copper oxides were deposited on polyethylene by direct current magnetron sputtering (DCMS) showing antibacterial activity not only under very low light intensity but also in the dark.

Keywords: Advanced photochemical oxidation processes, TiO₂, iron oxides, copper oxides, photo-Fenton, methylene blue, *E. coli*, polyethylene, Raschig rings, Glass fiber mats

Résumé

La qualité de l'eau et les infections bactériennes sont directement liées à la santé et au bien-être. Le traitement des eaux usées est donc une procédure nécessaire pour éviter les perturbations des écosystèmes et assurer la santé humaine. En outre, la contamination bactérienne dans les plans d'eau, l'apparition de bactéries résistantes aux antibiotiques dans les hôpitaux et les lieux publics doivent être abordées, pas seulement par des pratiques aseptiques appropriées. L'amélioration de la qualité de l'eau et les surfaces antibactériennes nécessitent la conception de nouveaux catalyseurs / photocatalyseurs supportés.

Les questions susmentionnées ont donné lieu à un domaine de recherche appelé processus d'oxydation photochimique avancée (APO). Cette thèse est basée sur APO's tout en concevant, testant et caractérisant les photocatalyseurs supportés. Les supports utilisés étaient les suivants: films minces en polyéthylène, anneaux Rashig en verre et nattes en fibre de verre. Des photocatalyseurs tels que le TiO_2 , des oxydes de fer, du TiO_2 décoré par du Cu et des oxydes de cuivre ont été déposés par trempage et par pulvérisation sur les supports mentionnés.

Les photocatalyseurs ont été testés principalement sous irradiation solaire simulée pour la dégradation du bleu de méthylène (MB) en solution, l'inactivation de bactéries (*E. coli*) en solution et l'inactivation de bactéries sur interface solide-air. Les techniques de caractérisation ont permis de décrire / optimiser la surface du catalyseur / photocatalyseur conduisant à la dégradation des polluants et à la désinfection bactérienne.

Les photocatalytiques supportés sur des films de polyéthylène (PE- TiO_2 et PE-FeOx) ont montré une activité dans la dégradation du MB en solution sur plusieurs cycles d'utilisation, suggérant une utilisation pratique potentielle. L'absorption de TiO_2 dans la région visible a été améliorée par addition de Cu / CuO et, en outre, le contact entre photocatalyseur et cibles (MB ou *E. coli*) a été augmenté en utilisant des anneaux Raschig en verre ou des tapis de fibres de verre (GF) comme supports. Seulement de très faibles quantités de Cu ont été suffisantes pour augmenter la cinétique de dégradation du MB. L'auto-nettoyage du MB a également été évalué sur des nattes de GF- TiO_2 -Cu sous irradiation solaire simulée. L'inactivation bactérienne en solution au moyen de matrices GF- TiO_2 -Cu 3% s'est avérée beaucoup plus rapide que par des nattes de GF- TiO_2 . En ce qui concerne les films antibactériens, les oxydes de cuivre ont été déposés sur du polyéthylène par pulvérisation cathodique par magnétron à courant continu (DCMS) montrant une activité antibactérienne non seulement sous une très faible intensité lumineuse mais également dans l'obscurité.

Mots-clés : Procédés d'oxydation photochimique avancés, TiO_2 , oxydes de fer, oxydes de cuivre, photo-Fenton, bleu de méthylène, *E. coli*, polyéthylène, anneaux de Raschig, tapis de fibres de verre

Table of Contents

Prologue.....	1
1. Chapter 1: Supported Photocatalysts: Principles, preparation techniques, performance evaluation, state of the art and Thesis objectives (structure)	3
1.1 Introduction	3
1.2 Advanced Photochemical Oxidation Processes.....	4
1.2.1 Heterogeneous photocatalysis	4
1.2.2 Homogeneous photocatalysis	6
1.3 Supported Photocatalysis.....	7
1.3.1 Supports pretreatment: RF-Plasma and UVC.....	8
1.4 Photocatalysts' deposition techniques	8
1.4.1 Physical deposition	9
1.5 Performance assessment for the developed photocatalysts	10
1.5.1 Evaluation of photocatalyst for pollutants degradation in solution: methylene blue (MB) as model molecule	11
1.5.2 Evaluation of photocatalyst in disinfection: E. coli as model microorganism	13
1.5.3 Assessment of efficiency as self-cleaning or antibacterial surface.....	14
1.6 State of the art.....	14
1.6.1 TiO ₂ supported on polymers.....	14
1.6.2 TiO ₂ -Cu and glass as photocatalyst support.....	15
1.6.3 Glass fiber mats as supports and TiO ₂ -Cu.....	16
1.6.4 Antibacterial films for tackling hospital acquired infections	16
1.6.5 Iron oxides supported on polymers for photo-Fenton approaches	17
1.7 Objectives of the Thesis and structure.....	17
2. Chapter 2: Materials and methods.....	23
2.1 Reagents.....	23
2.2 Bacteria.....	23
2.3 Analytical measurements	23
2.3.1 MB degradation by spectrophotometry	23
2.3.2 Assessment of Total Organic Carbon (TOC) reduction.....	23
2.3.3 Determination of •OH by Fluorescence	24
2.3.4 Determination of ions leached out during reaction by inductively coupled-plasma mass-spectrometry (ICP-MS).....	24
2.3.5 High Performance Liquid Chromatography (HPLC).....	24
2.4 Reactive Oxygen Species Scavenging during photocatalytic reactions in solution .	24

2.5	Determination of surface potential and pH evolution during photocatalytic reactions in solution	24
2.6	Photocatalyst characterization.....	25
2.6.1	X-ray Fluorescence for determination of material composition in weight percentage	25
2.6.2	Optical density and light absorbance of photocatalytic films	25
2.6.3	Dynamic contact angle determination for films	25
2.6.4	X-Ray photoelectron spectroscopy (XPS) for the photocatalyst.....	25
2.6.5	Atomic Force Microscopy (AFM)	25
2.6.6	X-ray Diffraction (XRD).....	25
2.6.7	Diffuse Reflectance Spectroscopy (DRS)	26
2.6.8	Scanning Electron Microscopy (SEM) and Energy Dispersive X-ray (EDX).....	26
3.	Chapter 3: Preparation, kinetics, mechanism and properties of semi-transparent photocatalytic stable films active in dye degradation	27
3.1	Introduction	29
3.2	Experimental section	30
3.2.1	Photocatalyst preparation.....	30
3.2.2	Reactor geometry, irradiation source and actinometry.....	30
3.3	Results and discussion.....	31
3.3.1	MB discoloration kinetics and effect of the TiO ₂ loadings on the PE-TiO ₂ films	31
3.3.2	Effect of light intensity on MB discoloration and ICP-MS evidence for the stable performance of PE-TiO ₂ during repetitive use.....	33
3.3.3	Scavenging of the oxidative species leading to MB degradation. Mechanism of reaction	35
3.3.4	Temporal evolution of radicals on PE-TiO ₂ , OH-radical detection by fluorescence and optical absorption by PE-TiO ₂ samples.....	37
3.3.5	Implications of the hydrophobic-hydrophilic transformation under TiO ₂ band-gap irradiation and dark reverse reaction of PE-TiO ₂ films	39
3.3.6	X-Ray photoelectron spectroscopy (XPS) peak changes during the MB-discoloration process.....	41
3.4	Conclusions.....	43
4.	Chapter 4: Cu-decorated Raschig-TiO ₂ rings inducing MB repetitive discoloration without release of Cu-ions under solar light.....	45
4.1	Introduction	47
4.2	Experimental section	47
4.2.1	Materials and photocatalyst preparation	47
4.2.2	Irradiation source and reactors.....	48
4.3	Results and discussion.....	49

4.3.1	MB discoloration kinetics	49
4.3.2	Repetitive MB-discoloration and evidence for the RR@TiO ₂ -Cu-0.004% stability 52	
4.3.3	Light intensity effects on the MB-discoloration kinetics and ROS detected during the MB-degradation	53
4.3.4	Suggested reaction mechanism, involvement of Cu intra-gap states.....	56
4.3.5	Surface properties of RR@TiO ₂ -Cu.....	57
4.4	Conclusions.....	61
5.	Chapter 5: New evidence for disinfection, self-cleaning and pollutant degradation mediated by GF-TiO ₂ -Cu mats under solar/visible light in mild oxidative conditions.....	63
5.1	Introduction	65
5.2	Experimental section	65
5.2.1	Photocatalyst preparation and materials.....	65
5.2.2	Reactors and irradiation source.....	66
5.2.3	Monitoring water disinfection (<i>E. coli</i> inactivation)	67
5.2.4	Monitoring GF-TiO ₂ -Cu self-cleaning	68
5.3	Results and Discussion	68
5.3.1	Composition of the GF-TiO ₂ -Cu photocatalysts	68
5.3.2	Water disinfection mediated by GF-TiO ₂ and GF-TiO ₂ -Cu mats under solar simulated light, visible light and in the dark.....	69
5.3.3	Self-cleaning of MB stains on GF-TiO ₂ and GF-TiO ₂ -Cu mats under solar irradiation	72
5.3.4	MB solution degradation by means of GF-TiO ₂ -Cu mats	73
5.3.5	Identification of photo-generated radical-species in solution.....	77
5.3.6	In situ monitoring of the surface potential and pH and suggested mechanism of degradation	79
5.3.7	Surface characteristics of GF-TiO ₂ -Cu mats detected by SEM, EDX and XPS analyses.....	81
5.4	Conclusions.....	83
6.	Chapter 6: Sputtered Cu-Polyethylene films inducing bacteria inactivation in the dark and under low intensity sunlight.....	85
6.1	Introduction	87
6.2	Experimental section	87
6.2.1	Photocatalyst preparation.....	87
6.2.2	Irradiation source and reactors.....	88
6.2.3	Monitoring bacterial inactivation	89
6.2.4	Monitoring Cu-leaching by Inductively Coupled Plasma Mass Spectrometry (ICP-MS).....	89

6.2.5	Composition of the PE-CuOx photocatalysts	89
6.3	Results and discussion.....	90
6.3.1	Optical properties of PE-CuOx films	90
6.3.2	Bacterial inactivation kinetics, Cu-release during repetitive recycling and effect of the applied light intensity	91
6.3.3	X-ray photoelectron spectroscopy (XPS) species found during bacterial inactivation	94
6.4	Conclusions.....	96
7.	Chapter 7: Innovative Photo-Fenton catalysis by PE-FeOx films leading to methylene blue (MB) degradation: kinetics, surface properties and mechanism	97
7.1	Introduction	99
7.2	Experimental section	99
7.2.1	Photocatalyst preparation.....	99
7.2.2	Irradiation source and reactors.....	99
7.3	Results and discussion.....	100
7.3.1	MB discoloration kinetics as a function of solution parameters, MB and H ₂ O ₂ concentration and identification of the radical intermediates leading to MB-degradation 100	
7.3.2	Lifetime and diffusion distance of the OH-radical away from the PE-FeOx intervening in MB-degradation.....	104
7.3.3	Fe-leached out during MB-degradation and repetitive dye degradation.....	105
7.3.4	Properties of PE-FeOx films: optical absorption, X-ray diffraction (XRD) particle size, film roughness and X-ray photoelectron spectroscopy (XPS).....	106
7.4	Conclusions.....	112
8.	Chapter 8: Conclusions and perspectives.....	113
	References.....	117
	Annex A: Supplementary material for Chapter 4.....	129
	Annex B: Supplementary material for Chapter 5.....	133
	Annex C: Supplementary material for Chapter 7.....	139
	Curriculum Vitae of the candidate.....	145

List of figures

Figure 1.1. Scheme showing some of the photochemical and photophysical events that might take place on an irradiated semiconductor particle	5
Figure 1.2. Solar radiation in earth and classification of Photocatalytic Oxidation Processes according to their active wavelength and spectral domain of excitation	5
Figure 1.3. Scheme for regular direct current sputtering principle	10
Figure 1.4. Representation of the trajectory of electrons and Argon atoms in the sputtering process for a non-magnetron sputtering system (I) and a magnetron sputtering system (II) .	10
Figure 1.5. Use of supported photocatalysts for: (I) water disinfection or degradation of molecule in solution and (II) antibacterial surfaces or self-cleaning materials	11
Figure 1.6. 3D structure of methylene blue (MB)	12
Figure 1.7. <i>E. coli</i> schematic representation, adapted image [54].	13
Figure 3.1. Pseudo-first order rates of MB discoloration on PE-TiO ₂ (0.90 TiO ₂ wt % / wt PE) for different initial MB concentrations: 1) 1x10 ⁻⁵ mol L ⁻¹ , 2) 3x10 ⁻⁵ mol L ⁻¹ , 3) 5x10 ⁻⁵ mol L ⁻¹ . Inserts: a) Mercury lamps emission, 4.3 mW cm ⁻² , b) Reactor	31
Figure 3.2. Dependence of the pseudo-first order rate constant k, on the PE-TiO ₂ loading, MB initial concentration: 1x10 ⁻⁵ mol L ⁻¹ . Insert. a) Total organic carbon reduction for an aqueous	32
Figure 3.3. MB 1x10 ⁻⁵ M discoloration as a function of time on (0.90 TiO ₂ wt % PE-TiO ₂) films at different mercury light intensities: 1) Dark run and runs under light on PE-TiO ₂ , (2) 1.1 mW cm ⁻² , (3) 1.9 mW cm ⁻² , (4) 2.8 mW cm ⁻² , (5) 3.5 mW cm ⁻² , (6) 4.3 mW cm ⁻²	34
Figure 3.4. Repetitive MB 1x10 ⁻⁵ mol L ⁻¹ discoloration as function of re-use on PE-TiO ₂ (0.90 TiO ₂ wt % / wt PE) films, Mercury irradiation 4.3 mWcm ⁻²	35
Figure 3.5. MB discoloration on PE-TiO ₂ of a solution MB 3x10 ⁻⁵ mol L ⁻¹ , PE-TiO ₂ : (0.90 TiO ₂ wt%/ wt PE) under mercury light 4.3 mW cm ⁻² . Scavengers used: Methanol 20 mmol L ⁻¹ (HO•), NaN ₃ 20 mmol L ⁻¹ (¹ O ₂), EDTA-2Na 20 mmol L ⁻¹ (h ⁺) and Benzoquinone(BQ) mmol L ⁻¹ (O ₂ ^{•-} /HO ₂ [•]): (1) No scavenger, (2) Methanol, (3) NaN ₃ , (4) BQ, (5) EDTA - 2Na	36
Figure 3.6. MB 1x10 ⁻⁵ mol L ⁻¹ , discoloration on PE-TiO ₂ , PE-TiO ₂ (0.9 TiO ₂ wt % / wt PE); mercury lamps: 4.33 mW cm ⁻² : a) No scavenger at pH = 3, b) No scavenger at pH 6; c) BQ (2 mmol L ⁻¹) at pH = 3, d) BQ (2 mmol L ⁻¹) at pH = 6, e) NaN ₃ (20 mmol L ⁻¹) pH = 3; f) BQ (2 mmol L ⁻¹) + NaN ₃ (2 mmol L ⁻¹) pH =3; g) BQ (2 mmol L ⁻¹) + NaN ₃ (2 mmol L ⁻¹) pH = 6	37
Figure 3.7. Relative fluorescence increase in a solution 2-hydroxyterephthalic acid irradiated up to 4h (mercury light 4.3 mW cm ⁻²) on a PE-TiO ₂ (0.90 TiO ₂ wt %/ wt PE) sample	38
Figure 3.8. a) Optical density (OD) of the PE-TiO ₂ films: (1) 0.46 TiO ₂ wt % / wt PE, (2) 0.57 TiO ₂ wt % / wt PE, (3) 0.63 TiO ₂ wt%/ wt PE, (4) 0.88 TiO ₂ wt%/wt PE, (5) 0.90 TiO ₂ wt%/wt PE. b) absorbance of the PE films	39
Figure 3.9. Hydrophobic/hydrophilic transformations for a sample PE-TiO ₂ . a) Change in contact angle, b) change in surface free energy (0.90 TiO ₂ wt %/wt PE), under mercury light 4.3 mW cm ⁻² (1) hydrophobic to hydrophilic conversion under light, (2) hydrophilic to hydrophobic dark reverse reaction	40
Figure 3.10. XPS signals of Ti, C and O at: 1) time zero 2) after discoloration of a MB 3x10 ⁻⁵ mol L ⁻¹ solution, under mercury light irradiation 4.3 mW cm ⁻² on PE-TiO ₂ films (0.90 TiO ₂ wt % /wt PE)	42
Figure 4.1. Schemes of the reactor and irradiation source. A Teflon support was placed concentrically inside the reactor for holding the RR@TiO ₂ -Cu bed. The reactors contained 70	

ml of MB. Before photocatalytic reaction, the MB solution was equilibrated with the RR@TiO ₂ -Cu for 30 min.....	48
Figure 4.2 MB 4x10 ⁻⁵ mol L ⁻¹ solution discoloration under Suntest irradiation (90 mW cm ⁻²), Traces: (1) MB in contact with RR@TiO ₂ -Cu 0.004% in the dark, (2) MB in contact with Raschig rings in the dark, (3) MB in contact with Raschig rings under Suntest irradiation (90 mW cm ⁻²), (4) MB in contact with RR@TiO ₂ -Cu-0.053% under Suntest irradiation (90 W cm ⁻²), (5) MB in contact with RR@TiO ₂ under Suntest irradiation (90 W cm ⁻²), (6) MB in contact with RR@TiO ₂ -Cu-0.004% under Suntest irradiation (90 W cm ⁻²). The initial pH of the solution was 5.7-6.0	50
Figure 4.3 Dependence of the pseudo-first order rate constant <i>k</i> on the Cu-content of the RR@TiO ₂ -Cu photocatalyst during the discoloration of a solution MB 4x10 ⁻⁵ mol L ⁻¹ under Suntest light set at 90m W cm ⁻² . The initial pH of the solution was 5.7-6.0.....	50
Figure 4.4 Absorption spectra of MB 4x10 ⁻⁵ mol L ⁻¹ in contact with diverse RR@TiO ₂ -Cu photocatalysts under Suntest light set at 90 mW cm ⁻² : a) RR@TiO ₂ -Cu-0.004%, b) RR@TiO ₂ -Cu-0.018%, c) RR@TiO ₂ -Cu-0.053%, d) RR@TiO ₂ -Cu-0.081%. The initial pH of the solution was 5.7-6.0.....	51
Figure 4.5 Total organic carbon (TOC) decrease during the photocatalytic degradation of MB 4x10 ⁻⁵ mol L ⁻¹ mediated by RR@TiO ₂ -Cu-0.004% under Suntest light (90 mW cm ⁻²). Initial pH of the MB solution: (1) pH 5.7 and (2) pH 10	52
Figure 4.6 a) Rate constants (<i>k</i>) for the repetitive MB 4x10 ⁻⁵ mol L ⁻¹ discoloration by RR@TiO ₂ -Cu 0.004% b) Ti-ions released during MB-discoloration up to the 5 th use cycle and c) Cu-ions released during MB-discoloration up to the 5 th use cycle. Suntest light set at 90 mW cm ⁻²	53
Figure 4.7 Discoloration of MB 4 × 10 ⁻⁵ mol L ⁻¹ on RR@TiO ₂ -Cu-0.004% as a function of the Suntest simulated sunlight intensity: (1) 120 mW cm ⁻² , (2) 90 mW cm ⁻² , (3) 60 mW cm ⁻² , (4) 90 mW cm ⁻² with UV filter at 400 nm and (5) 30 mW/cm ⁻²	54
Figure 4.8 Discoloration of a solution MB (4x10 ⁻⁵ M) on RR@TiO ₂ -Cu 0.005% showing the intermediates radical-species being identified by appropriate scavengers: (1) run without scavengers, (2) run in the presence of 0.2 mM methanol, (3) run in the presence of 0.2 mM NaN ₃ , (4) run in the presence of 0.2 mM p-benzoquinone, (5) run in the presence of 0.2 mM EDTA-2Na.....	55
Figure 4.9 DRS spectra for different Cu weight percentages in RR@TiO ₂ . (1) RR@TiO ₂ , (2) RR@TiO ₂ -Cu 0.004%, (3) RR@TiO ₂ -Cu 0.018%, (4) RR@TiO ₂ -Cu 0.053% and (5) RR@TiO ₂ -Cu 0.081%.....	57
Figure 4.10 XRD for different Cu weight percentages in RR@TiO ₂ and references of TiO ₂ , Cu and Cu oxides. (1) RR@TiO ₂ - Cu 0.018%, (2) RR@TiO ₂ - Cu 0.053 %. Reference XRD: (3) Anatase (R100013), (4) Rutile (R040049), (5) Copper (R061078), (6) Cu ₂ O (R050384), (7) CuO (R120076) [155]	58
Figure 4.11 (a) AFM- topography of RR@TiO ₂ -Cu 0.018% taken at a resolution of (2 × 2 μM), (b) AFM-topography of RR@TiO ₂ -Cu 0.081% taken at a resolution of (2 × 2 μM)	59
Figure 4.12 XPS signals of Ti a), Cu b), O c) and C d) at time zero (1) and after discoloration of a MB 4 × 10 ⁻⁵ (mol L ⁻¹) solution on RR@TiO ₂ – Cu 0.004 % (2). Suntest irradiation set at 90 mW cm ⁻²	60
Figure 5.1. a) Reactor used for water disinfection (bacterial inactivation) experiments containing 20 ml of bacterial solution ~10 ⁶ CFU/ml showing the GF-TiO ₂ -Cu mats supported on the stainless steel-mesh, b) same reactor as in a) filled with a solution of MB 4x10 ⁻⁵ M for pollutant degradation in solution, c) GF-TiO ₂ -Cu mat placed in a Petri-dish (approach for self-	

cleaning experiments), d) GF-TiO ₂ -Cu mat impregnated with 1 ml MB 4x10 ⁻⁵ M for self-cleaning runs (time zero: 30 minutes in contact with the MB in the dark).....	67
Figure 5.2. Set-up used for water disinfection and pollutant (MB) degradation in solution by means of GF-TiO ₂ -Cu mats. The suntest provided simulated solar and visible light irradiation	67
Figure 5.3. <i>E.coli</i> inactivation (water disinfection) for an initial bacterial solution (~10 ⁶ CFU/ml) by means of GF-TiO ₂ -Cu mats under: (a) solar light irradiation (90 mW cm ⁻²), (b) visible light irradiation (filter cut-off at 400 nm / 70 mW cm ⁻²) and (c) in the dark. (1) GF-TiO ₂ , (2) GF-TiO ₂ -Cu 0.05%, (3) GF-TiO ₂ -Cu 0.2%, (4) GF-TiO ₂ -Cu 1%, (5) GF-TiO ₂ -Cu 3%.....	69
Figure 5.4. Set-up used for the evaluating MB self-cleaning of GF-TiO ₂ and GF-TiO ₂ -Cu-mats	73
Figure 5.5. MB self-cleaning on GF-TiO ₂ and GF-TiO ₂ -Cu mats irradiated up to 240 min under solar light (90 mW cm ⁻²). Samples: GF-TiO ₂ , GF-TiO ₂ -Cu 0.05% and GF-TiO ₂ -Cu 3% mats	73
Figure 5.6. Decrease of concentration for a MB 4x10 ⁻⁵ M solution (model organic pollutant) under Suntest irradiation (90 mW cm ⁻²) or dark mediated by GF, GF-TiO ₂ , or GF-TiO ₂ -Cu mats. Traces: (1) Degradation mediated by GF-TiO ₂ -Cu 0.05% under suntest irradiation; (2) Degradation mediated by GF-TiO ₂ under suntest irradiation; (3) Degradation mediated by GF-TiO ₂ -Cu 3% under suntest irradiation; (4) MB discoloration under Suntest irradiation (5) MB discoloration in the presence of GF-mat under Suntest irradiation, (6) MB intake of GF-TiO ₂ -Cu 0.05% in the dark, (7) MB intake of GF-mat in the dark. Initial solution pH=5.7.....	74
Figure 5.7. Pseudo-first order rate constant (<i>k</i>) for the degradation of MB (4x10 ⁻⁵ M) in solution as a function of the Cu-content on GF-TiO ₂ -Cu mats. Reactions taking place under Suntest irradiation (90 mW cm ⁻²). Initial MB solution pH=5.7.	75
Figure 5.8. Total organic carbon (TOC) decrease for MB 4x10 ⁻⁵ M by the action of GF-TiO ₂ -Cu mats under Suntest light (90 mW cm ⁻²). Equilibration period in the dark: 30 minutes. Traces: (1) GF-TiO ₂ -Cu 0.05%, (2) GF-TiO ₂ , (3) GF-TiO ₂ -Cu 0.2%, (4) GF-TiO ₂ -Cu 1%, (5) GF-TiO ₂ -Cu 3%	76
Figure 5.9. Degradation of a MB 4x10 ⁻⁵ M solution by means of GF-TiO ₂ -Cu mats under Suntest light irradiation (90 mW cm ⁻²) followed by high performance liquid chromatography (HPLC). The characteristic peaks of MB at 245, 292, 615 and 668 nm were monitored as a function of reaction time for: (1) GF-TiO ₂ , (2) GF-TiO ₂ -Cu 0.05%, (3) GF-TiO ₂ -Cu 0.2%, (4) GF-TiO ₂ -Cu 1%, (5) GF-TiO ₂ -Cu 3% mats	76
Figure 5.10. Degradation of MB 4x10 ⁻⁵ M solution under Suntest irradiation (90 mW cm ⁻²) in the absence of a radical scavenger and in the presence of radical scavengers (0.2mM): NaN ₃ , p-benzoquinone, methanol and EDTA-2Na. Mats used: a) GF-TiO ₂ , b) GF-TiO ₂ -Cu 0.05%	77
Figure 5.11. Degradation cycles of MB solution (4 x10 ⁻⁵ M) under Suntest irradiation (90 mW cm ⁻²). (1) GF-TiO ₂ mats, (2) GF-TiO ₂ -Cu mats.....	79
Figure 5.12. Evolution of surface potential (trace (1)) and solution's pH (trace (2)) in the solid-liquid interface during the degradation of MB 4x10 ⁻⁵ M solution by means of GF-TiO ₂ -Cu mats under Suntest irradiation (90 mW cm ⁻²): a) GF-TiO ₂ , b) GF-TiO ₂ -Cu 0.05%, c) GF-TiO ₂ -Cu 3%.....	80
Figure 5.13. Scanning electron microscopy (SEM) of mats' fibers. a) Fibers from GF, 1.5K magnification; b) Fibers from GF, 50.00K magnification; c) Fibers from GF-TiO ₂ -Cu 0.05%, 1.5K magnification; d) Fibers from GF-TiO ₂ -Cu 0.05%, 50.00K magnification; e) Fibers from GF-TiO ₂ -Cu 3%, 1.5K magnification; f) Fibers from GF-TiO ₂ -Cu 3%, 50.00K magnification.....	81

Figure 5.14. XPS signals for GF-TiO₂-Cu 0.05% samples (left hand side column) and for GF-TiO₂-Cu 3.0% samples (right hand side column). Time zero (30 minutes MB in contact with the GF-TiO₂-Cu mat) corresponds to Trace (1) and Trace (2) corresponds to 60 minutes reaction under irradiation by sunlight of a 2x2 cm sample stained with 1ml MB 4x10⁻⁵ M82

Figure 6.1 Nominal thickness of Cu-layers detected by profilometry on Si-wafers sputtered at: (1) 200 mA, (2) 100 mA and (3) 50 mA.....88

Figure 6.2 Absorption of PE-CuOx films in Kubelka-Munk units detected by Diffuse reflectance spectroscopy (DRS). Cu-layers sputtered during 40s at: (1) 100 mA and (2) 200 mA.....90

Figure 6.3 *E. coli* inactivation on PE-CuOx sputtered at different energies: (1) Cu sputtered for 40 s on PE at 200 mA (Sample (I)), (2) Cu sputtered for 60 s on PE at 200 mA, (3) Cu sputtered for 20 s on PE at 200 mA, (4) Cu sputtered for 40 s on PE at 100 mA, (5) Cu sputtered for 10 s on PE at 200 mA, (6) Cu sputtered for 5 s on PE at 200 mA, (7) Cu sputtered for 40 s on PE at 200 mA in the dark, (8) the irradiation of the PE sample was carried out in the cavity of a Suntest simulator (20 mW/cm²). Error bars: standard deviation (P<0.05)91

Figure 6.4 Recycling of *E. coli* inactivation on PE-CuOx (Sample (I)) up to five cycles under sunlight irradiation (20 mW/cm²). Error bars: standard deviation (P<0.05).....93

Figure 6.5 *E. coli* inactivation on PE-CuOx films sputtered for 40 s at 200 mA as a function of the applied solar simulated light intensity: (1) 20 mW/cm², (2) 10 mW/cm² and (3) 5 mW/cm². Error bars: standard deviation (P<0.05).....93

Figure 6.6 XPS peak signal deconvolution of the Cu2p peaks for a PE-CuOx film sputtered for 40 s at 200 mA a) before and b) after bacterial inactivation. For other details see text95

Figure 7.1. Discoloration of MB (4x10⁻⁵ M) under different conditions at an initial pH 6 in solution: (1) MB alone under solar simulated irradiation (50 mW/cm²), (2) PE-FeOx (Fe 0.30%) in the presence of H₂O₂ (10mM) in the dark, (3) H₂O₂ (10mM) under solar simulated irradiation (50 mW/cm²), (4) Fe-ions in solution added to the MB-solution containing H₂O₂ (10mM) under solar simulated irradiation (50 mW/cm²), (5) MB discoloration on PE-FeOx (Fe 0.30%) in the presence of H₂O₂ (10mM) under solar simulated irradiation (50 mW/cm²) in the presence of a cut- off filter at 400 nm, (6) MB discoloration on PE-FeOx (Fe 0.30%) in the presence of H₂O₂ (10mM) under solar simulated irradiation (50 mW/cm²). Insert: TOC decrease of MB (4x10⁻⁵ M) in the presence of PE-FeOx (Fe 0.30%) film and H₂O₂ (10mM). Suntest light intensity: 50 mW/cm²101

Figure 7.2. (a) Discoloration of MB by on a PE-FeOx (Fe 0.30%) film irradiated under solar simulated irradiation (50 mW/cm²) as a function of the initial MB concentration initial in a solution H₂O₂ (10mM). MB: 1) 4x10⁻⁵ M, (2) 2x10⁻⁵ M, (3) 1x10⁻⁵ M. (b) Discoloration of MB by on a PE-FeOx (Fe 0.30%) film irradiated under solar simulated irradiation (50 mW/cm²) as a function of the initial H₂O₂ concentration, MB 4x10⁻⁵ M, and the H₂O₂ concentration in traces: (1) 1 mM, (2) 2 mM, (3) 5 mM, (4) 10 mM, (5) 20 mM.....102

Figure 7.3. Discoloration of MB (4x10⁻⁵ M) by means of PE-FeOx (Fe 0.30%) film, H₂O₂ (10mM) and ROS scavengers under sunlight irradiation: (1) 0.2 mM methanol, (2) 0.2 mM NaN₃, (3) 0.2 mM p-benzoquinone, (4) 0.2 mM EDTA-2Na, (5) run without scavengers102

Figure 7.4 Fe-ions released by the PE-FeOx (0.30%) film into the MB (4x10⁻⁵ M) solution containing H₂O₂ (10mM), Suntest light intensity 50 mW/cm².....105

Figure 7.5 Repetitive MB (4x10⁻⁵ M) discoloration on PE-FeOx (Fe 0.30%), H₂O₂ (10mM), Suntest light intensity 50 mW/cm²106

Figure 7.6 Optical density (O.D) of PE-FeOx films: (1) 0.37 Fe wt % / wt PE, (2) 0.30 Fe wt % / wt PE, (3) 0.18 Fe wt % / wt PE, (4) 0.17 Fe wt % / wt PE, (5) 0.10 Fe wt % / wt PE.....107

Figure 7.7 XRD results for FeOx deposited on glass under the similar conditions as used to load Fe on PE. Peak in Figure 7b for the two Fe and Cl-loading % used: (1) ClFeO, (2) FeCl₂·2H₂O, (3) FeCl₂·4H₂O, (4) FeCl₃, (5) FeCl₃108

Figure 7.8 (a) Roughness of PE-FeOx (Fe 0.37%) film taken at a roughness resolution of 20x20 μm, (b) Roughness of PE-FeOx (Fe 0.37%) film taken at a roughness resolution of 4x4μm, (c) Roughness of PE-FeOx (Fe 0.17%) film taken at a roughness resolution of 20x20μm, (d) Roughness of PE-FeOx (Fe 0.17%) film taken at a roughness resolution of 4x4μm.109

Figure 7.9 XPS signals of Fe, O and C at time zero and after discoloration of a MB 4x10⁻⁵ (mol L⁻¹ solution), under Suntest irradiation 50 mW/cm⁻² on PE-FeOx films (0.30 Fe wt % / wt PE)111

List of tables

Table 3.1. TiO ₂ wt % /wt PE determined by X-ray fluorescence as a function of the TiO ₂ content during the preparation of PE-TiO ₂ . Additionally, assessed cm ³ TiO ₂ / cm ² PE based on XRF data and material properties.	34
Table 3.2. Surface percentage atomic concentration of PE-TiO ₂ during MB discoloration as determined by XPS. The first row refers to a samples of PE-TiO ₂ contacted with MB for a short period in the dark.....	41
Table 4.1 Weight percentage of TiO ₂ and Cu in the RR samples of RR@TiO ₂ -Cu as determined by X-ray fluorescence (XRF). Additionally, assessed cm ³ TiO ₂ -CuOx / cm ² RR based on XRF data and material properties.	49
Table 4.2. Atomic percentage concentration of the elements of the sample RR@TiO ₂ -Cu-0.004%, during the degradation of MB: 4x10 ⁻⁵ mol L ⁻¹	61
Table 5.1. Physical properties of the non-woven glass fiber mat (GF) used as support for TiO ₂ -Cu	66
Table 5.2. Composition of the prepared GF-TiO ₂ -Cu mats in weight percentage as determined by X-ray fluorescence (XRF). Additionally, assessed cm ³ TiO ₂ -CuOx / cm ² GF based on XRF data and material properties.	68
Table 5.3. Ti and Cu ions concentration detected by ICP-MS in the bulk of the reactor after water disinfection under Suntest irradiation (90 mW/cm ²), visible light irradiation (cut-off at 400nm / 70 mW/cm ²) and in the dark.....	70
Table 5.4. Ti and Cu ions concentration detected by ICP-MS in the bulk of the reactor after MB 4x10 ⁻⁵ M degradation by means of GF-TiO ₂ -Cu under Suntest irradiation (90 mW/cm ²) after several use cycles	78
Table 6.1 X-ray Fluorescence (XRF) determination of the Cu weight % / weight PE-film. Additionally, assessed cm ³ Cu ₂ O / cm ² PE based on XRF data and material properties.....	90
Table 6.2 Cu-release in ppb from CuOx-PE films as found by ICP-MS after different washing cycles for Cu-PE films contacted and not contacted with bacteria.	94
Table 6.3. Surface atomic concentration percentages found by XPS on the PE-CuOx (Sample (I)) before and after bacterial inactivation	96
Table 7.1 Fe and Cl wt % /wt PE determined by X-ray fluorescence as a function of the FeCl ₃ content during the preparation of PE-FeOx. Additionally, assessed cm ³ FeCl ₃ / cm ² PE based on XRF data and material properties.	108
Table 7.2 PE-roughness as a function of Fe loadings in the PE-FeOx film	109
Table 7.3. Surface percentage atomic concentration of PE-FeOx during MB discoloration determined by XPS. The PE-FeOx samples used were put in contact with MB for a short period in the dark (30s).....	110

Abbreviations

- PE: Polyethylene
- LDPE: Low density polyethylene
- RR: Raschig Rings
- GF: Glass Fiber
- MB: Methylene Blue
- TiO₂: Titanium Dioxide
- FeOx: Iron Oxides
- H₂O₂: Hydrogen Peroxyde
- CuOx: Copper Oxides
- Cu: Copper
- ROS: Reactive Oxygen Species
- *E. Coli*: *Escherichia coli*
- DCMS: Direct Current Magnetron Sputtering
- HAIs: Hospital Acquired Infections
- XPS: X-ray Photoelectron Spectroscopy
- XRF: X-ray Fluorescence
- XRD: X-ray Diffraction
- CA: Contact Angle
- UV: Ultraviolet
- Vis: Visible light
- TiO₂-Cu: Copper decorated TiO₂
- Ar: Argon
- N₂: Nitrogen
- cb: Conduction band
- vb: Valence band
- CFU: Colony Forming Unit
- DRS: Diffuse Reflectance Spectroscopy
- ICP-MS: Ion Coupled Plasma Mass Spectrometry
- HPLC: Hight performance liquid chromatography
- TOC: Total Organic Carbon
- Wt: Weight
- RF-plasma: Radio-Frequency generated Plasma
- Rg: Roughness
- mW: miliwatts
- mA: miliamperes
- eV: Electron Volts

Prologue

Fresh water is one of our most valuable resources and it is tightly linked to economic growth and population wellbeing. Only 2.5 % of all the water in earth is freshwater and 98% of it is either groundwater or glaciers [1]. Part of this fresh water is intended for domestic and industrial use leading to contamination, for this reason waste water treatment is necessary, allowing a safe water cycle avoiding disturbances to ecosystems. Waste water treatment is divided in three main steps: primary, secondary and tertiary treatment. Primary and secondary treatments are focused on suspended solids removal and biological removal of organic matter respectively, tertiary treatment goes beyond the first two treatment steps using sophisticated technology to further remove specific pollutants.

Another important water related issue is the water access and water quality in developing countries; approximately 660 million people have no access to safe drinking water [2] and 2.4 billion have no proper sanitation [3]. Waste water tertiary treatments and drinking water quality improvement can be handled by Advanced Photochemical Oxidation Processes (APO's) which use light to induce the generation of oxidative species that degrade organic molecules or attack microorganisms inactivating them. Photochemical oxidation comprising suspensions are available and to simplify this treatment, supported photoactive catalysts have been developed avoiding the catalyst recovery necessary for its reuse.

Continuing with the issue of wellbeing and human health, hospital acquired infections (HAI's) have been an increasing issue becoming an area of concern. These infections are caused by antibiotic resistant microorganisms such as methicillin-resistant *Staphylococcus aureus* (MRSA) and *P. aeruginosa* which account for 70% of the bacteria that infect people in hospitals [4-6]. New antibacterial/bactericide materials are therefore needed not only to neutralize the infections in hospitals, health facilities but also in the food processing industry. Advanced Photochemical Oxidation Processes can also be implemented to tackle this challenging situation, this by the deposition of photoactive material in suitable supports as fabrics or plastics, which mimic the surfaces commonly found in a hospital environment. The light irradiation would activate the supported material generating species that attack and inactivate the bacteria, blocking its spreading.

In brief, supported photocatalysts offer the advantages of optimizing parameters for water treatment as well as the possibility of developing antibacterial films on materials commonly used by humans.

1. Chapter 1: Supported Photocatalysts: Principles, preparation techniques, performance evaluation, state of the art and Thesis objectives (structure)

1.1 Introduction

Domestic waste water can be treated in municipal stations biologically, chemically (thermal oxidation, chlorination, ozonation, etc.) or by adsorption. In the case of recalcitrant pollutants from industrial waste “Advanced Oxidation Processes” are used. These processes involve the production of powerful oxidative species such as hydroxyl radical ($\cdot\text{OH}$). If the energy source for producing such radical comes from light, the treatment process is named “Advanced Photochemical Oxidation Process”. Among these processes there are two main methodologies:

- Photocatalytic degradation processes using semiconductors as photocatalysts (heterogeneous photocatalysis). The photocatalytic process in semiconductors needs a band-gap photo-excitation for the generation of electron-hole pairs which induces the production of highly oxidative hydroxyl radicals in water [7]. (This particular process is the most suitable for the development of antibacterial surfaces)
- Photo-Fenton, which is based on the production of ($\cdot\text{OH}$) by means of the iron dependent decomposition of hydrogen peroxide (H_2O_2). ($\text{Fe}^{(II)}$) is oxidized to ferric iron ($\text{Fe}^{(III)}$) in presence of H_2O_2 leading to the formation of ($\cdot\text{OH}$) and OH^- . The regeneration of $\text{Fe}^{(II)}$ through the reduction of $\text{Fe}^{(III)}$ can occur either in the presence of a chemical reducing agent as H_2O_2 or via photoreduction of ferric iron complexes [8].

The advanced photochemical oxidation processes usually comprise the suspension of the photoactive material in aqueous solutions [9]. Catalyst slurries would face difficulties when applied in large-scale since light penetration is limited and the catalyst would have to be recovered after the degradation, implying higher costs. These complications could be avoided by depositing photocatalysts as TiO_2 or Fenton-based onto suitable supports. Photoactive antibacterial films, on the other hand, require the deposition of a photocatalyst onto a specific support, particularly surfaces found in hospitals.

Degradation of organic pollutants and bacteria inactivation by means of supported photocatalysts are broad subjects that allow the design of innovative materials. Plenty of studies have been addressed regarding the design of materials suitable for application in water treatment and bacterial inactivation. The tests of photoactive materials depend on the kind of interfaces involved in the photoreaction, solid-air interface (self-cleaning and antibacterial materials) or solid-liquid interface (water treatment or water disinfection). Solid-liquid interface approaches usually comprise the degradation of a model molecule (pollutant) in solution or the inactivation of a microorganism in solution. Solid-air interface approaches comprise the degradation of stains or microorganisms adsorbed on surfaces. Among pollutants model

molecules, dyes are widespread due to their simple degradation assessment; however there is the drawback of the dye's sensitivity to light. This drawback can be corrected by the proper run of control experiments and complementary instrumental analysis. Regarding photocatalytic inactivation of bacteria, the most common probe is *E. coli* due to its availability, fast growth rates and low toxicity.

In the following sections, the mechanisms of Advanced Photochemical Oxidation Processes will be presented, as well as deposition techniques for the preparation of supported photocatalysts and their evaluation in water treatment/antibacterial surfaces. The state of the art will also be presented to subsequently define the general and specific objectives of the Thesis.

1.2 Advanced Photochemical Oxidation Processes

The Advanced Oxidation Processes (AOP) were developed as an alternative for waste water treatment and water disinfection [7, 10-13]. These processes occur following different types of oxidation reactions that involve hydroxyl radical:



The Advanced Photochemical Oxidation Processes (APO) are a particular kind of Advanced Oxidation Processes. These are based on a free radical mechanism initiated by the interaction of photons with either molecules in a solution or catalysts. Such photons must have a proper energy level in order to modify the nature of the catalyst or the chemical species in solution. The APO technologies can be classified according to the catalyst's form in the reactive system.

1.2.1 Heterogeneous photocatalysis

This concept began being studied when Fujishima and Honda reported the photocatalytic decomposition of water on TiO_2 electrodes [14]. From this moment on, photo-catalysis has been applied for the degradation of several pollutants such as alkanes, alkenes, alcohols, carboxylic acids, phenols, dyes, aromatic hydrocarbons and pesticides [15, 16].

TiO_2 has shown to be the most suitable when it comes to environmental applications since it is not susceptible to photocorrosion or chemical corrosion and it is economic [17]. The valence band VB and the conduction band CV energies of the TiO_2 are estimated to be +3.1 and -0.1 eV respectively, which means that TiO_2 's band gap energy is 3.2 eV and absorbs in the near UV light ($\lambda < 0.387 \mu\text{m}$).

Mechanism of the TiO_2 -Photo-catalysed degradation under solar light

When TiO_2 semiconductor, is in contact with water and irradiated with ultraviolet (UV) light below 387 nm, free hydroxyl $\bullet\text{OH}$ radicals are generated. What happens first, as a consequence of the radiation's absorption is the generation of electron-hole pairs. An electron moves from the valence band to the conduction band leaving a hole. The reactions of an organic substance (RH) with TiO_2 under UV light are shown in Figure 1.1.

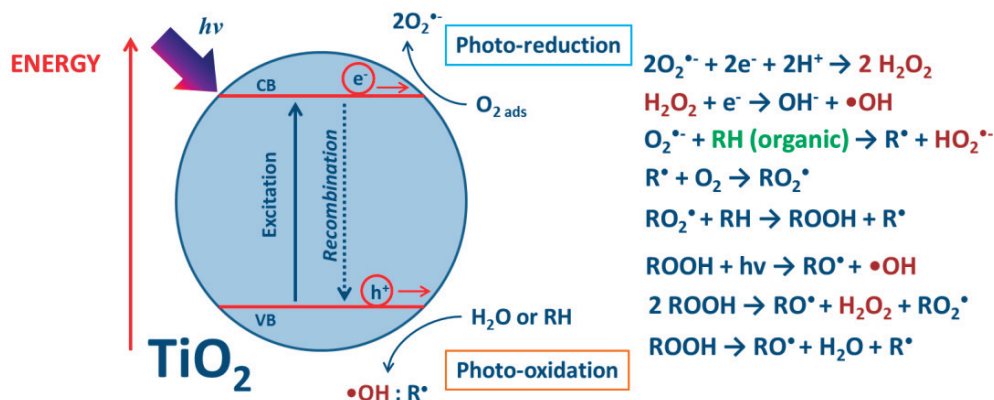
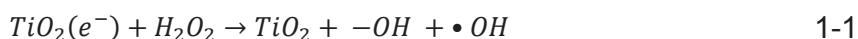


Figure 1.1. Scheme showing some of the photochemical and photophysical events that might take place on an irradiated semiconductor particle

It has been shown that hydrogen peroxide addition increases the photo-degradation rate. This could be due to reaction 1-1 taking place; where H_2O_2 is reduced by CB electrons [18, 19].



It is known that photoinduced catalytic processes are efficient within a characteristic wavelength range of excitation. The natural solar spectrum shown in Figure 1.2 is mainly composed of near UV and visible light of intermediate length. 6.8% of total solar radiation is between 295 to 400 nm, 55.4% is reaching the earth between 400 to 800 nm and the remaining 37.8% of it is between 800 to 2450 nm [20].

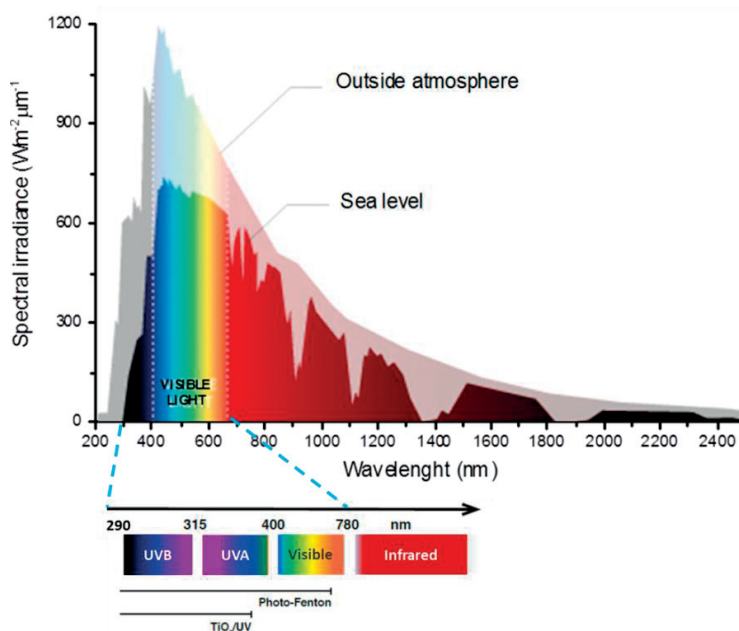


Figure 1.2. Solar radiation in earth and classification of Photocatalytic Oxidation Processes according to their active wavelength and spectral domain of excitation

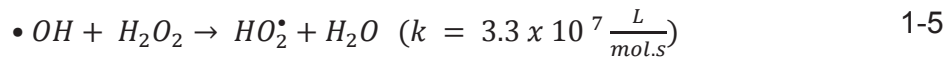
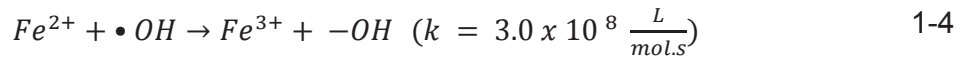
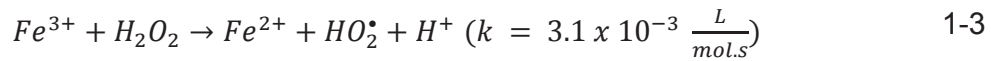
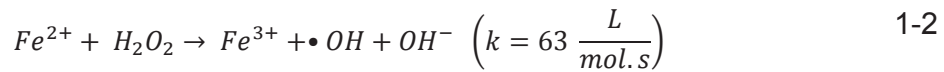
As mentioned previously, TiO₂ absorbs light below 387 nm (3.2 eV) to form electron-hole pairs. Photodegradation reactions are affected by factors such as: catalyst concentration, initial pollutant's concentration, temperature, pH, inorganic ions, light intensity, oxygen concentration, adsorption and reactor design. The combined effect of these factors on the photodegradation kinetics is the object of many studies involving TiO₂ photocatalysis.

1.2.2 Homogeneous photocatalysis

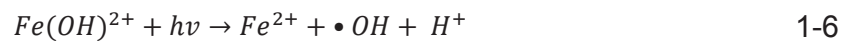
When the light is the factor enhancing the oxidative process by means of •OH radicals' generation, the reaction is classified as photo-oxidative. In order to generate •OH radical species, the presence of oxidant substances (oxygen, ozone, hydrogen peroxide) is necessary. According to this, three of the most used photo-induced processes are: Hydrogen peroxide (UV/H₂O₂), Ozone (UV/O₃) and the Photo-Fenton system (UV-vis/Fe³⁺/H₂O₂).

Mechanism of Photo-Fenton reaction

The Fenton reaction consists in the oxidation of Fe(II) to Fe(III) through the reaction between dissolved Fe(II) and H₂O₂ in aqueous acid solution (reaction 1-2). Under these conditions, almost all of the Fe(II) is rapidly converted to Fe(III) and the reduction of the later to Fe(II) takes places slowly. This is shown by reactions 1-2 and 1-3. Reaction 1-3 limits the kinetics of the Fenton reagents and reactions 1-4 and 1-5 show the possible scavenging of the the •OH species [21].



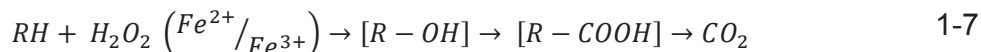
Fenton's reaction rate increases when irradiating with proper wavelengths (180-580 nm). This kind of photo-assisted reaction is known as Photo-Fenton (reaction 1-6) [22-25]. The positive effect of irradiation accelerating the degradation rate is the photochemical regeneration of the ferrous ion Fe²⁺ from the photo-reduction of aqueous complexes of ferric ion which simultaneously lead to the additional generation of •OH radicals.



The main advantage of the Photo-Fenton process is the light sensitivity to wavelengths up to 580 nm (35% of the solar radiation) in the presence of Fe-aqua complexes within a defined pH range Light penetration to the system is high and the contact probability between contaminant and oxidizing agent is thus high since everything happens in homogeneous solution [26].

Photo-Fenton induced mineralization is shown in reaction 1-7. First the organic pollutant RH is transformed into alcohols, then to acids (lowering the pH of the

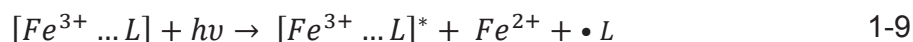
system). As a final phase, if total mineralization is reached the systems' pH value increases due to the formation of carbon dioxide.



One of the main disadvantages of the Photo-Fenton process in homogeneous solution is that it requires a low pH value (lower than 4.5) to avoid iron oxide precipitation. Reaction 1-8 illustrates how aqueous iron complex deprotonates at a pH value above 2.8



Some authors have tried to cope with pH value limitation by grafting iron ions on supports like polymers [27], glass and carbon wools [28], cation exchange resins [29], zeolites [30], saponites [31] or montmorillonites [32]. The use of the supports has shown effective results at pH values > 4.7 up to 8 for several pollutants at low concentrations releasing low amounts of Fe into the solution. The mechanism of reaction at near to neutral pH values is show in reaction 1-9 involving Fe-organo-complexes. These iron-complexes form organo-ligands (L) that result from bacterial lysis or from pollutant degradation.



Fenton and Photo-Fenton processes have been used for degradation pollutants in aqueous media. In general, the degradation path is similar but photo-Fenton processes might need shorter exposure times depending on the resistance to degradation of each substance [33-36].

1.3 Supported Photocatalysis

Polymers are widely used, they are inexpensive, they have good physical and chemical properties and they are easy to process. However, it can happen that the polymeric material does not have the necessary surface properties for a specific application. Surface modification techniques would allow transforming inexpensive material into products with added value due to new attributed properties. Among the most common surface modification techniques there are treatments by flame, plasmas, photons, electron beams, ion beams, X-rays and Y-rays. These treatments could aim for instance to increase hydrophilicity consequently improving dyeability [37].

Polymers plasma treatment is probably the most versatile surface treatment. Oxygen plasma for example, increases the oxygen negative binding sites e.g. $-COO^-$ of polymer films and textiles. These negatively charged groups bind/attach to oxides like TiO_2 and FeO/Fe_2O_3 . The main disadvantage of this technique is that it requires vacuum, increasing operational costs.

In 2005 some authors reported natural and synthetic fibers' pre-treatment by RF-plasma, MW-plasma and vacuum-UV radiation (V-UV). Apparently, these pretreatments lead to the formation of chelating groups' species on the fibres surface which allowed the binding of the slightly positive TiO_2 on the textile surface [38-42].

1.3.1 Supports pretreatment: RF-Plasma and UVC

Oxygen and oxygen-containing plasmas are most commonly employed to modify polymer surfaces. A frequency of 50-100 Hz would be enough to provide a continuous RF-discharge and it can be initiated and sustained by external electrodes in a reactor vessel [43, 44]. This surface pretreatment is uniform and the chemical modification is a function of the used gas, avoids the swelling related to wet chemical techniques for polymers. RF-Plasma modification takes place on the surface without affecting the bulk properties of the support; the depth of the modification does not overpass the order of a hundred angstroms.

Regarding UV pretreatment, their extent of reactions depends on the reactants, the light intensity and the absorption coefficient. Light intensity of low-pressure mercury lamps is generally low, a few mW/cm^2 , while medium pressure and high pressure mercury lamps have much higher light intensity with their output ranging from the deep UV to the visible red light region [45]. UV modifications involving molecular oxygen are popular as O_2 absorbs at UV wavelengths < 250 nm producing O_3 [46]. Ozone itself absorbs at wavelengths < 310 nm and is further decomposed to molecular and atomic oxygen. If the photolysis of ozone proceeds in the presence of water, H_2O_2 is formed which is further photolyzed to $\bullet\text{OH}$ radicals.

1.4 Photocatalysts' deposition techniques

The deposition of a photocatalyst onto a substrate or support is defined as the settling of the photoactive particles from solution, suspension or vapor on the substrate surface. The thickness of the deposited layers can be controlled depending on the technique and depositions can follow a chemical process or a physical process.

Chemical deposition

This approach relies on the fluidity of the precursor which suffers chemical changes when gets in contact with a solid surface (substrate or support). This kind of approach leads to a uniform thickness of the supported material along the interface.

Plating

Plating consists on covering a conductive surface with metals. Usually the precursors are aqueous solutions containing salts of said metals.

Sol-gel

Sol-gel uses as precursors organometallic particles in a solvent aiming to produce solid material starting from small molecules. The deposition of photoactive material onto supports by this technique usually involves dipping and subsequent calcination.

Spin coating

This technique uses a liquid precursor which is placed on the center of the substrate and then submitted to rotation at high speed making the coating of the support possible due to centrifugal force. The thickness of the desired layer varies as a function of the rotation time.

Chemical vapor deposition

Chemical vapor deposition uses a gas-phase precursor which is a halide or hydride of the element to be deposited; it produces highly pure solid materials.

Atomic layer deposition

This deposition aims to a conformal deposition using a gas precursor and depositing layer by layer by repeating cycles of sequential operations. These operations consist on injection of the precursors in the chamber (usually two chemicals), pulse perturbation of the chamber for inducing chemical reactions and chamber's purging. The thickness of the layers produced by this technique is a function of the number of cycles.

1.4.1 Physical deposition

This approach bases the deposition process on the use of mechanics, electrochemistry or thermodynamics. Films or coatings produced by this approach are directional.

1.4.1.1 Thermal evaporation

An electric resistance heater is used to melt the material to be deposited and raise its vapor pressure. This melting happens inside a vacuum chamber for allowing the material to reach the substrate without reacting with residual gases. It has to be taken into account that the elements to be deposited have to have a higher vapor pressure than the one of the electric resistance heater for avoiding contamination.

1.4.1.2 Sputtering

With this technique the material to be deposited is taken from a source named "target" and it is removed one atom at the time by means of Argon plasma. A DC voltage placed between the target and the substrate ionizes Argon atoms and forms plasma. The Argon ions are accelerated towards the target and this collision ejects atoms from the target, these atoms move towards the substrate (anode) and deposit. The electrons generated during Argon ionization move towards the anode substrate colliding with Argon atoms, which creates more ions and electrons giving place to a continuous cycle. The coverage by this technique is mostly conformal.

- ***Direct Current Magnetron Sputtering***

A direct current sputtering deposition rate can be enhanced by the addition of a strong magnetic field close to the target area that holds the electrons near by forcing them to follow a spiral trajectory instead of being attracted towards the substrate. These electrons also travel longer distances which increases the chances of ionizing Argon atoms, in this way stable plasma is generated. The more ions produced, the more collisions generated which finally leads to a more efficient deposition. This process is faster and as a consequence, there are less chances of forming impurities the film.

In a non-magnetron sputtering (Figure 1.4(I)) the plasma moves freely inside the chamber and sometimes could collide with the substrate, in a magnetron sputtering the plasma is restricted to move in the magnetic field area (Figure 1.4 (II)). The fact that the plasma and the target are closer implies faster deposition rates.

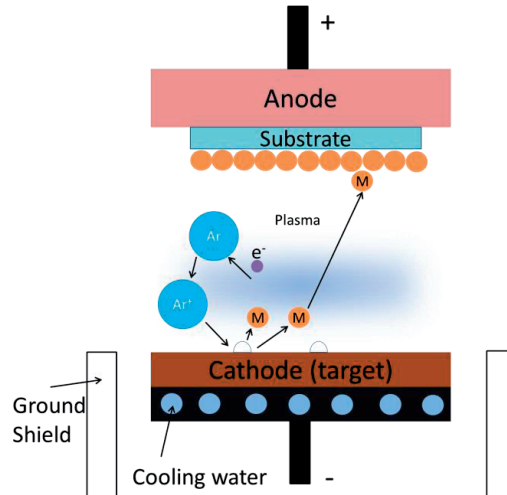


Figure 1.3. Scheme for regular direct current sputtering principle

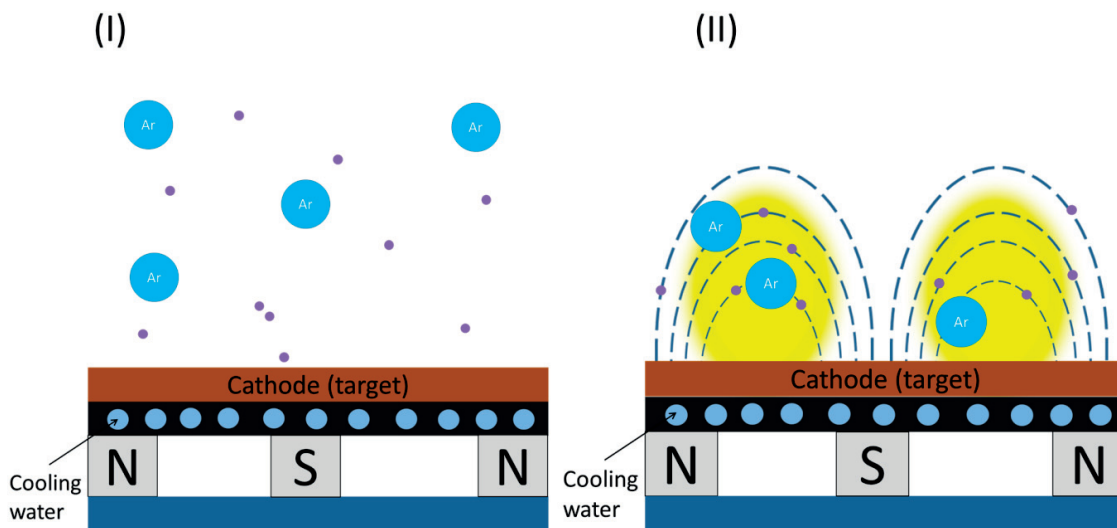


Figure 1.4. Representation of the trajectory of electrons and Argon atoms in the sputtering process for a non-magnetron sputtering system (I) and a magnetron sputtering system (II)

1.5 Performance assessment for the developed photocatalysts

Depending on the projected purpose of a developed photocatalyst, the conditions and the targets of the produced oxidant species have to be sorted. When it comes to water disinfection or degradation of contaminants in solution, the conditions involve a solid-liquid interface and a bulk of solution where either the pollutant molecules or the bacteria are dispersed. If the purpose of the photocatalyst is to act as a self-cleaning

or antibacterial surface, the interface involved is mostly solid-air, there is no bulk of solution, the molecules or the bacteria are adsorbed on the surface of the photocatalyst. A schematization of the two mentioned uses for supported photocatalysts is highlighted in Figure 1.5.

It is worth noting that results obtained in approaches involving bulk of solutions can be extrapolated to solid-air interface approaches. In the latter cases, the conditions are more favorable, diffusion limitations for example are significantly removed. Concluding, if a material leads to a degradation of a target in solution, most probably will lead to degradation of the same target in the solid-air interface.

Usually the evaluation of the performance of a designed supported photocatalyst for degrading a pollutant in solution consists on monitoring the degradation of a model molecule by means of techniques as light spectrophotometry, TOC, liquid chromatography and/or mass spectrometry. When the target of the photocatalysts is bacteria, a very common and well known model microorganism is *E. coli*, its inactivation usually is monitored by bacterial counting which is a standardized method.

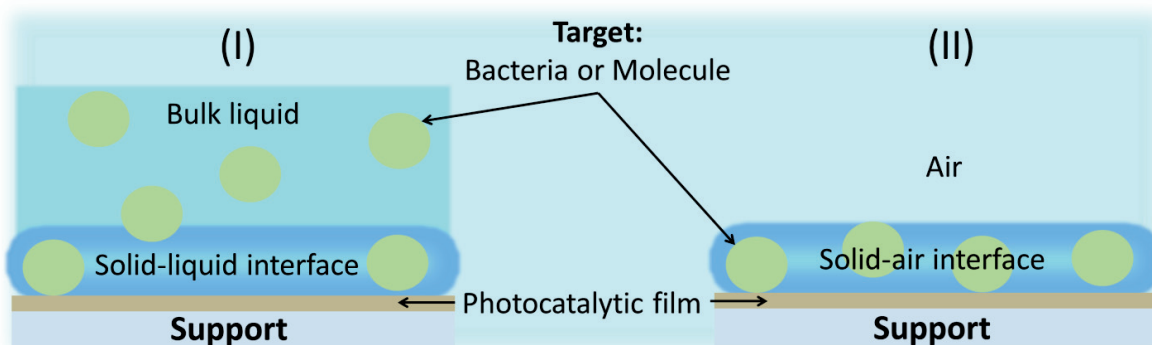


Figure 1.5. Use of supported photocatalysts for: (I) water disinfection or degradation of molecule in solution and (II) antibacterial surfaces or self-cleaning materials

1.5.1 Evaluation of photocatalyst for pollutants degradation in solution: methylene blue (MB) as model molecule

Assessing how efficient a designed photocatalyst is degrading pollutants in solution has to be tested first with a single model molecule in solution for the sake of a simple standard process that can be followed and reproduced. Molecules as organic dyes have been widely used as model pollutants due to the simplicity of the degradation monitoring, yet this approach is controversial due to the dyes' light sensitivity, usually in the visible range [47].

The ISO standard 10678:2010 gives guidelines for determining the photocatalytic activity of surfaces in an aqueous medium by degradation of methylene blue (MB); it highlights factors to be accounted for such as: dye purity, adsorption and pH, light source, stirring and diffusion [48]. In 2012 Mills provided some suggestions to the ISO 10678:2010 including the use of a highly pure MB, pH values ranging from 5.5 to

6, UVA light source, low solution height and stirring overnight to discard photo-bleaching [49].

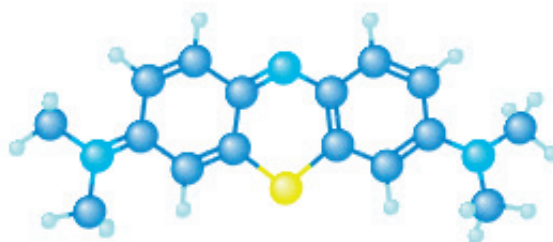


Figure 1.6. 3D structure of methylene blue (MB)

Methylene blue (3,7-bis(dimethylamino)phenothiazin-5-ium) consists of dark green crystalline powder. It results in a strong blue color solution when dissolved in water or alcohols. It is used as a bacteriologic stain and as an indicator. It has been used also to treat cyanide poisoning [50].

The use of methylene blue as model molecule for photocatalysis has been the object of several observations due to the following factors:

- It can be reduced to colorless *leuco*-methylene blue (LMB) in oxygen depleted conditions and low pH.
- Mineralization of the methylene blue solution proceeds slowly within long irradiation periods.
- The degradation of methylene blue starts as a light sensitization by visible light, thus the generalization of degradation path induced by the photocatalyst would be limited.
- The photocatalyst activity takes place fully only when the MB has lost the color due to degradation of the intermediates in solution [51].

For overcoming these factors and achieve a successful photocatalyst evaluation in pollutant degradation in solution, the following has to be accounted:

- Make sure the initial pH of the MB solution is between 5.5 and 6 besides providing aeration and stirring. In this way, the favourable conditions for reduction of MB to LMB are removed.
- UVA light sources activating only TiO_2 (366nm) can be used for avoiding MB sensitization.
- If solar light or visible light is used, carry out optimization experiments in order to identify a MB concentration balancing the ratio MB/photocatalyst and the light sensitization of MB. This concentration should be fixed for further experiments. The run of proper control experiments involving light and the fixed MB concentration solution would facilitate the allocation of the contribution of light sensitization during photocatalytic experiments.

- Besides light spectrophotometry for the assessment of the MB concentration abatement additional techniques as Total Organic Carbon measurements or liquid chromatography would give more accurate information about the extent of mineralization throughout the photocatalytic reaction. The liquid chromatography technique allows the assessment of the decay of MB in a more precise way as the moieties that appear during reaction are separated in the column, the assessment of the disappearance of one specific molecule can be individuated from the absorbance of other molecules (MB dimers in this case for example).

1.5.2 Evaluation of photocatalyst in disinfection: *E. coli* as model microorganism

Regarding the assessment of a photocatalyst for water disinfection or antibacterial surfaces, the target is the same: bacteria. *E. coli* has been widely used as model target when studying the performance of a disinfection system since this bacteria is easy to cultivate and is commonly present in water matrices [52, 53].

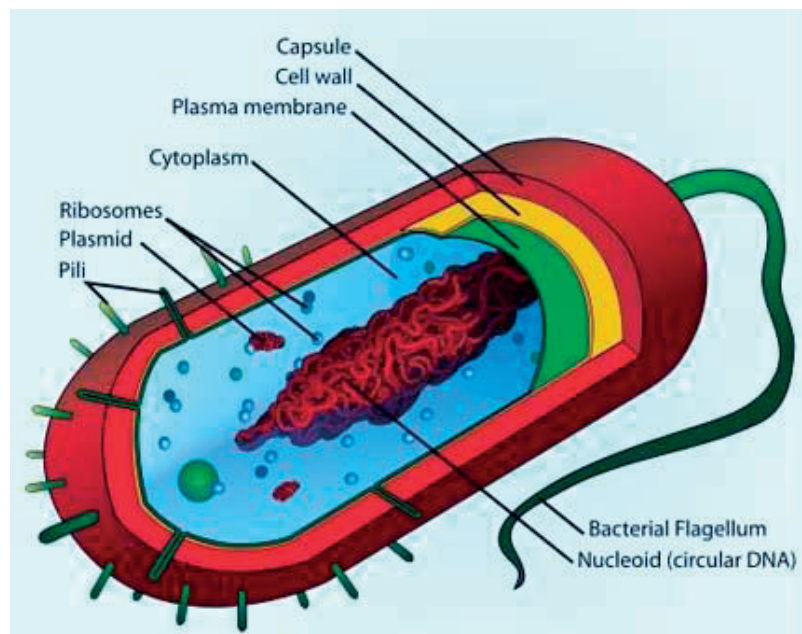


Figure 1.7. *E. coli* schematic representation, adapted image [54].

Bacterial inactivation is understood as the inability of the microorganism to replicate and it can occur due to the mere action of light or by the action of foreign substances. Light with wavelengths < 340 nm can be absorbed by the proteins in the bacteria cell wall and kill the microorganism. Also, light can induce Fenton-like processes inside the cell leading to accumulation of ROS that attack the cell from inside. Furthermore, the UVB fraction of the solar light leads to the formation of same-strand photo-adducts or double stranded DNA, these effects cause the bacteria not to be able to replicate [55-58].

Bacterial inactivation due to ROS generated outside the cell happens when •OH-radicals (produced either by Fenton-like reactions or semiconductor photochemistry) damage the external cell membrane leading to eventual death or inability to reproduce.

1.5.3 Assessment of efficiency as self-cleaning or antibacterial surface

As stated at the beginning of this section, self-cleaning or antibacterial surfaces do not involve a bulk of solution posing a diffusion limitation. Self-cleaning properties can be followed visually; first the supported photocatalyst has to be impregnated with a colored stain (organic pollutant), then equilibration in the dark has to be allowed and finally the disappearance of the stain throughout irradiation can be monitored. Surface methods such as X-ray Photoelectron Spectroscopy (XPS) provide more clear information about the degradation process. This technique permits the detection of species/elements on a surface as well as their binding energies to identify redox reactions.

The antibacterial characteristics of a supported photocatalyst or photocatalytic film can be assessed in the same way as in water disinfection, meaning bacterial counting by the standard plate method. For antibacterial surfaces, instead of immersing the supported photocatalyst in bacterial solution, a droplet of bacterial solution is placed on the surface of the photocatalyst. After pre-selected irradiation times, the photocatalytic film is removed from irradiation, washed out with saline solution (same matrix as bacterial solution) to remove the remaining bacteria present on the surface and aliquots of this washing step are subsequently plated.

1.6 State of the art

The synthesis of eco-friendly supported catalysts produced under ambient temperatures, with low consumption of chemical substances and using simple equipment is a primary focus of environmental catalysis/photocatalysis [59-64]. Photocatalysis allows the use of a resource with relative high availability and easy access: sunlight. TiO₂ has been the main photocatalyst utilized over decades due to its power of generating oxidative radicals under band-gap irradiation, these radicals are able to destroy pollutants and bacteria in the presence of air (O₂), (H₂O) and band gap photons [60, 61]. Many studies have reported the photocatalyzed destruction of pollutants on TiO₂ coated surfaces like glass, iron plates and Raschig rings [63]. These are substrates with a high thermal resistance and good surface but they could get structurally damaged during the TiO₂ annealing. Flexible but chemical resistant polymer films, such as polyethylene (PE) seemed to be a good option due to its high availability, low cost, stability, flexibility and corrosion resistance. Furthermore, PE films are UV-resistant, do not undergo oxidation in air, they are also durable and chemical inert.

1.6.1 TiO₂ supported on polymers

The degradation of pollutants on TiO₂-polymer films has been popular during the last years, some polymer films have shown to be useful as catalyst supports leading to

catalysis/photocatalysis with acceptable kinetics at the solid-air interface besides presenting a very low absorption of organic compounds (pollutants) in the dark [64-67]. The techniques for attaching TiO₂ nanoparticles onto polymers from colloidal suspensions include mostly: dip coating, phosphonate coupling, chemical reduction, emulsion polymerization and spreading [68-74]. Generally, polymers are coated with TiO₂ by corroding the polymer surface with solvents or by using the TiO₂ itself under irradiation which induces binding sites for the TiO₂ to attach better [75-79]. PE-TiO₂ films have been prepared as well by sputtering techniques showing to be successful in bacteria inactivation and self-cleaning processes [80, 81].

1.6.2 TiO₂-Cu and glass as photocatalyst support

The support of either TiO₂ or iron oxides onto polymeric films allows the use of a flexible reusable photocatalyst. TiO₂ has the drawback of absorbing mainly the UV portion of the solar light. Studies aiming to shift TiO₂ light absorbance to the visible range by the incorporation of another anionic or cationic dopants in the TiO₂ lattice have been followed. The incorporation of Cu is of particular interest because besides increasing the TiO₂ activity under solar light it has a cytotoxic effect that can be exploited for bacterial inactivation. Ni et al. have reported a method for synthesizing Cu/TiO₂ for hydrogen generation by a grinding method; their studies provided evidence of improvement of TiO₂ performance by an optimal Cu addition [82]. A different application for Cu-modified TiO₂-SiO₂ was reported recently by Čížmar et al. A colloidal solution of Cu-modified TiO₂-SiO₂ nanoparticles was prepared by low temperature sol-gel synthesis. The catalytic activity of TiO₂-SiO₂ for oxidizing terephthalic acid to 2-hydroxyterephthalic acid was reported to be enhanced for a factor of 10 when 0.1 mol% of Cu was added to the TiO₂-SiO₂ matrix [83]. Bensouici et al. reported the synthesis of Cu-TiO₂ films onto flat glass substrate via a simple wet chemical route (sol-gel dip-coating) for its use in MB degradation. They reported that photocatalytic activity of Cu-TiO₂ films is not enhanced compared to pure TiO₂ [84]; however the experiments included the use of UVC light during the degradation reaction, the use of flat glass as support and no exploration of lower Cu amounts added to TiO₂. Pham et al. reported the photocatalytic activity of Cu-doped TiO₂/reduced graphene oxide thin films supported on quartz flat substrates in MB discoloration under UVA light irradiation; they reported that the Cu presence narrowed TiO₂ bandgap, improved the degradation of MB and increased the film's hydrophilicity [85]. Garlisi et al. reported methylene blue discoloration (self-cleaning) by means of TiO₂ and Cu-TiO₂ supported on glass by e-beam evaporation under visible light (450-950 nm), the discoloration by means of Cu-TiO₂ was faster than the one observed for TiO₂ [86].

Based on the reports of photocatalysts supported on polymeric films and the reports of Cu modification increasing the activity of TiO₂ itself, the possibility of exploring the performance of Cu-modified TiO₂ (active under UV and visible irradiation) onto a support that provides higher surface area than polymeric films gains interest.

The study of supported photocatalysts on glass and metal plates offers good

performance [60-62, 64, 87, 88]. TiO₂ coated Raschig rings have been used for the degradation of pollutants in diluted solutions under band-gap irradiation to abate the dye direct-red 16 [89]. This approach has also been used to degrade several aromatic compounds in aqueous solution [59, 90, 91]. Our laboratory has reported Raschig rings coated by TiO₂ as a catalyst to degrade phenol [92], phenol-compounds [93] and chlorophenols [94].

1.6.3 Glass fiber mats as supports and TiO₂-Cu

Besides pollutants degradation in solution, water disinfection is a field of increasing interest for research. Developing a material that not only could degrade pollutants in solution but also could inactivate bacteria in solution becomes appealing. Based on what discussed so far, a factor that could still be explored is the increase of contact between the targets (bacteria or chemical pollutant) and the photocatalyst. Materials for photocatalyst support such as glass fiber mats could offer higher specific area than raschig rings. High specific area and increased activity of TiO₂ by Cu could be an interest combination for addressing water treatment issues. Robert et. al. and Sun et. al. have reported the degradation of Benzamide and Crystal Violet respectively by means of TiO₂ supported on glass fibers under UV irradiation, the influence of factors such as thermal treatment and glass fiber morphology were sorted out [95, 96]. Regarding bacteria inactivation some authors have presented the positive effect that TiO₂-Cu has in *E. coli* inactivation the Cu and TiO₂/Cu photocatalysts were prepared by sol-gel method [97, 98]. Lin et. al. and Bodson et. al. reported the activity of iron doped TiO₂ for the degradation of phenol and silver doped TiO₂ for the degradation of p-nitrophenol respectively, both doped materials were supported on glass fiber [99, 100]. Pham T. D and collaborators reported Cu doped TiO₂/GF and Ag doped TiO₂/GF for bacterial inactivation at the air-solid interface and compared its performance to TiO₂/GF, doped photocatalysts showed to improve bacterial inactivation activity. The experiments consisted on an *E.coli* bioaerosol passing through a chamber illuminated with visible light which contained the Cu or Ag doped TiO₂/GF [101, 102].

1.6.4 Antibacterial films for tackling hospital acquired infections

Hospital acquired infections (HAIs) has become a subject of rising interest in the last decade, which has led to research in the preparation of films able to avoid the formation of infecting biofilms. Some studies present the antibacterial power of Cu films on textiles, polymer and glass as it has been reported to be an active agent to preclude biofilm formation and bacterial growth [103-110]. Several research groups have reported antibacterial Ag, Cu and TiO₂ coatings on glass and polymer films by chemical vapor deposition (CVD) and by other sputtering related techniques [111]. Direct current (DC) magnetron sputtering has been shown to allow the deposition of metal/metal oxides at relatively low temperatures not exceeding 120-140°C [37]. Bacterial inactivation on textiles by Ag has been reviewed [112] but textiles sputtered by Cu have been recently gaining attention. Studies on Cu-polyester [113-116] and

Cu/CuO-TiO₂ mediated bacterial inactivation [117-119] have also been reported during the last 5 years.

1.6.5 Iron oxides supported on polymers for photo-Fenton approaches

Another interesting photocatalytic approach for supported material is photo-Fenton. The deposition of iron sources onto suitable supports together with the possibility of undergo Fenton reactions at near neutral pH make this tactic attractive to practical application. Photo-Fenton processes by means of thin polymer films have been a field of study as well. In 1990 a Nafion thin polymer film was reported to bind Fe³⁺(Fe₂O₃) by electrostatic attraction avoiding the use Fe-chelators/complexes to bind Fe-ions to polymer substrates [28]. A different study was reported on Fe-chelated on negative maleic anhydride fused on PE films [27, 120]. Later on, colloidal preparations of Mn/Al/Fe-oxides on polymer/PE films were reported, these photocatalysts were used for phenol degradation under solar light [121]. Supported rutile and iron-oxides extruded and casted on 10 micron thick PE films has also been used as photocatalyst for the degradation of phenol as well [122]. Photo-Fenton catalysts were prepared by immobilizing iron species onto functionalized polyethylene and polypropylene films for the degradation of resorcinol, the conversion and mineralization were correlated to iron dissolution [123]. The immobilization of iron on polyvinyl fluoride films for its use in the degradation of phenol, nalidixic acid, mixture of pesticides, and another emerging contaminants in water was reported to be efficient for most of the contaminants, some of them not reaching complete mineralization [124]. Moreover, immobilized Fe-Oxide on functionalized PET has been reported to be efficient in photoassisted bacterial inactivation in the presence of H₂O₂ [125]. According to what stated before, these results could be extrapolated to solid-air interface approaches, meaning the application as antibacterial surfaces for HAI's.

1.7 Objectives of the Thesis and structure

The general objective of this work is the *preparation, evaluation and characterization of supported photocatalysts for the degradation of a model pollutant in solution and the inactivation of bacteria (water disinfection or antibacterial films)*. The strategy for the design of the photocatalysts was the combination of factors influencing its performance, for instance: type of support, type of photocatalyst (along with its synthesis and its amount) and the source of irradiation.

The Thesis is organized into chapters and some of them correspond to specific objectives addressing the degradation of a model pollutant and the inactivation of *E. coli* by heterogeneous photocatalysis in solution or at the solid-air interface.

Chapter 1: Supported Photocatalysts: Principles, preparation techniques, performance evaluation, state of the art and Thesis objectives (structure)

The present chapter is intended to recollect the basic principles of photocatalysis and the different techniques for preparing supported photocatalysts as well as their

performance tests; it also comprises the state of the art and the specification of the Thesis objectives.

Chapter 2: Materials and methods

This chapter collects the common analytical and characterization techniques for all the photocatalysts prepared and tested throughout the work of the Thesis.

Chapter 3: Preparation, kinetics, mechanism and properties of semi-transparent photocatalytic stable films active in dye degradation.

Objective 1: To test the performance of commercial TiO₂ supported on polyethylene films degrading a model pollutant in solution under low intensity UV-light

The purpose of this part of the Thesis was to use highly available material (commercial TiO₂ and polyethylene films) keeping a very simple preparation method that would lead to a photocatalyst that allows light penetration by preserving some of the transparency of the polyethylene film. This material would be not only a suitable option for water treatment but also for self-disinfecting applications involving depositions in one side of the polymeric film, the side which would be exposed hand contact, avoiding bacterial spreading.

This chapter presents the preparation of PE-TiO₂ films and its potential for degrading methylene blue (MB), the model pollutant. The cyclic performance and surface properties are fully described. The PE-TiO₂ was prepared under mild conditions, at low temperatures and did not require expensive instrumentation. Scavenging experiments identifying the oxidative species leading to MB degradation are reported and the TiO₂vbh⁺ was shown to be the most influencing species. The diffusion length for the HO₂[•] and •OH radicals was estimated reaching short distances away from the PE-TiO₂ films. Evidence is presented for the PE-TiO₂ contact angle (CA) conversion from the initial hydrophobic (92°) to super-hydrophilic values (<5°). The time of the conversion was concomitant with the MB-discoloration time (5 h). The PE-TiO₂ films show a potential for practical applications to degrade dyes in water-treatment as shown by their stable repetitive photocatalytic performance.

Chapter 4: Cu-decorated Raschig-TiO₂ rings inducing MB repetitive discoloration without release of Cu-ions under solar light.

Objective 2: To improve performance of model pollutant degradation in solution under solar-simulated light by means of Cu-decoration of TiO₂ and its deposition on higher specific surface area support (Raschig rings)

This part of the Thesis work aimed to increase the efficiency of the TiO₂ by integration of CuOx particles that would facilitate electronic circulation, lowering the electron-hole recombination. CuOx particles would also slightly shift the TiO₂ absorption to the visible-light range. In addition, the nature of the

support would allow high temperature treatments during preparation and its 3D geometry would optimize the ratio: *amount of TiO₂-Cu/specific surface of support*, if compared to 2D supports (polymeric films). Moreover, the diffusion limitations due to the solution's bulk would be reduced.

This chapter describes the preparation of Cu-decorated TiO₂ Raschig rings (RR@TiO₂-Cu) and the details related to MB-degradation under solar irradiation. Cu-decoration induces intra-gap-electronic states in the TiO₂ facilitating the indirect electron transition in the TiO₂ band-gap. The results obtained during MB discoloration showed that a Cu- addition of 0.004% on RR@TiO₂ led to the highest photocatalytic activity. The addition of Cu on RR@TiO₂ shifted the photocatalyst absorbance into the visible region. The Cu intra-gap states in the optimal RR@TiO₂-Cu could not be characterized due to the low amounts of Cu present in the photocatalyst. Higher Cu-levels on the TiO₂ surface seem to act as recombination centers for the photogenerated charges decreasing the rate of MB-discoloration. By the use of appropriate scavengers (TiO₂vb (h⁺)) was found to be the most important intermediate species leading to MB-degradation. The XPS-shifts during the photocatalytic degradation of MB provided the evidence for redox events between CuOx/TiO₂ and the MB. The AFM results indicate that a low Cu-loading on the RR@TiO₂ rings showed a close packed *contour* compared to the wide-spaced *contour* obtained with higher Cu-loadings. A close packed *contour* in the low Cu-loading provides more contact points with MB leading to faster degradation.

Chapter 5: New evidence for disinfection, self-cleaning and pollutant degradation mediated by GF-TiO₂-Cu mats under solar/visible light in mild oxidative conditions.

Objective 3: To use solar simulated light and improve the performance of model pollutant degradation in solution as well as to explore water disinfection and self-cleaning purposes by means of Cu-decoration of TiO₂ and its deposition on glass fiber mats

As the results from Chapter 4 suggested a good performance of Cu- decorated TiO₂, it was decided to explore: a) the impact of this photocatalyst (TiO₂-Cu) in water disinfection (bacterial inactivation) and b) the use of a light, flexible, mechanically resistant and high specific surface area support such as glass fiber mats (GF). The water disinfection performance of this photocatalyst could be extrapolated to the solid-air interface for application in self-disinfecting filters to be used in airplanes, for instance.

This chapter addressed the photocatalytic performance of Cu-decorated TiO₂ particles supported on glass fiber mats (GF-mats) to disinfect solutions, promote MB stains self-cleaning and mediate the degradation of MB in solution. The GF-TiO₂-Cu mats are low cost, stable, thermally and mechanically resistant thanks to the nature of the support (Techmat® A 04008 E Glass mats). These mats induced a slow kinetics bacterial inactivation in the dark but led to complete water disinfection within 3h under indoor light irradiation (visible light). Self-cleaning and pollutant (MB)

degradation in solution by means of GF-TiO₂-Cu 0.05% were faster when compared to GF-TiO₂. The MB degradation process was observed to remain independent of Cu-content when irradiated with visible light (> 400 nm). A wider variety of oxidative radical species were generated by the GF-TiO₂-Cu 0.05% mats due to the Cu-presence compared to radicals generated on the GF-TiO₂ mats. Evidence is presented for the stable photocatalytic recycling of the mats under sunlight irradiation. This suggests the practical potential of this photocatalyst for environmental cleaning applications.

Chapter 6: Sputtered Cu-polyethylene films inducing bacteria inactivation in the dark and under low intensity sunlight.

Objective 4: To explore the field of solid-air interfaces related to antibacterial CuOx photoactive films deposited on a highly used material such as polyethylene

The studies carried out in Chapter 5 pointed out the cytotoxic characteristics of CuOx; it can inactivate bacteria in contact with fixed CuOx interstices not reached by light and it can also trigger Fenton-like reactions. Moreover, CuOx can also act as a semiconductor under visible light irradiation. Given these CuOx characteristics, it was decided to explore CuOx deposition on Polyethylene (PE) in the field of antibacterial surfaces for healthcare acquired infections (HAI's) prevention. Polyethylene was used as support for the CuOx films, as it is a material commonly found in hospital environments and daily life. The CuOx deposition was made by Direct Current Magnetron Sputtering, which is a more sophisticated technique that would allow better attachment and more uniform coverage of the films. The prepared antibacterial films would be active in low intensity light and in the dark.

This chapter presents the optimization of the experimental conditions during sputtering to graft the Cu on PE in order to attain rapid inactivation kinetics. Very low levels of sunlight were necessary to induce an acceptable bacterial inactivation. Inactivation in the minute range was observed on sputtered Cu-films in the dark. This property of the Cu-films is more important in practical applications compared to the photo-induced bacterial inactivation processes since the bacterial inactivation in this case proceeds in absence of an external energy source. The effect of the PE-CuOx films is due predominantly to the Cu-oxides behaving as a semiconductor since the inactivation kinetics was observed to be a function of the intensity of the applied light and not due to the intrinsic Cu-cytotoxicity.

Chapter 7: Innovative Photo-Fenton catalysis by PE-FeOx films leading to methylene blue (MB) degradation: kinetics, surface properties and mechanism.

Objective 5: To test the performance of commercial iron oxides supported on polyethylene films degrading a model pollutant in solution under low intensity solar-simulated light

Taking into account that results of a photocatalyst performance for degradation of molecules or bacterial inactivation in solution can be extrapolated to solid-air interface and aiming to replace the use of CuOx, for a more ecofriendly semiconductor, the use of FeOx supported on PE is explored. The purpose is to develop a simple photocatalyst, prepared with highly accessible materials. Iron oxides are economic and have semiconductor properties absorbing not only UV-light but also visible-light, allowing the use of a wider range of the solar spectra.

This chapter comprises the preparation of PE-FeOx and its performance for discoloring/degrading the MB in solution under simulated low intensity sunlight/visible light. The MB-degradation on PE-FeOx films followed mass transfer controlled reactions. Evidence is presented for the specific nature of the oxidative radical intermediates intervening in the MB- degradation. The limited contribution of vb holes (h^+) and the quasi-absence of light intensity effects suggested that the FeOx intervening as a semiconductor played a modest role during MB-degradation. A mechanism leading to MB-degradation was suggested based on the experimental work. The PE-FeOx films induce Fenton/photo-Fenton by a progressive co-participation of homogeneous and heterogeneous catalysis. The PE-FeOx film surface composition was characterized by several surface techniques.

Chapter 8 describes the Thesis conclusions and the perspectives as well as brief comments on the potential practical applications of the materials developed during the Thesis work.

2. Chapter 2: Materials and methods

The work of this Thesis involved the preparation of different photocatalysts deposited on different supports, these materials were evaluated under different irradiation sources and disposed in different reactors; therefore particular details as photocatalyst preparation, reactors and irradiation sources will be clearly presented in each chapter corresponding to each different objective. This chapter will describe the recurrent materials used throughout the work, the most common methods of performance assessment and photocatalyst characterization methods made to almost all the photocatalysts.

2.1 Reagents

The methylene blue (3, 7-bis (Dimethylamino) phenazathionium chloride) was a Sigma-Aldrich reagent (MB). NaN_3 , 1, 4-benzoquinone, methanol, ethylene-diamine tetra-acetic acid disodium salt (EDTA-2Na), NaOH and $\text{FeCl}_3 \cdot 7\text{H}_2\text{O}$ were Sigma-Aldrich. The Titanium dioxide used was commercial Degussa P25 and $\text{CuNO}_3 \cdot 3\text{H}_2\text{O}$ was Acros Organics. Terephthalic acid 98% was Across Chemical.

2.2 Bacteria

The strain of *Escherichia coli* (*E. coli* K12) used to monitor bacterial inactivation was obtained from Deutsche Sammlung von Mikro-organismen und Zellkulturen GmbH (DSMZ), Braunschweig, Germany. The agar for plating was purchased from Merck GmbH, Microbiology division KGaA, (catalogue No.1.05463.0500).

2.3 Analytical measurements

For the experiments related to the photocatalyst's performance, a period of 30 minutes in the dark was allowed so the photocatalyst and the targets could reach stabilization after adsorption (equilibrium).

2.3.1 MB degradation by spectrophotometry

The MB degradation was followed by measuring its light absorbance at 668 nm in a single beam spectrophotometer UV-1800 (Shimadzu, Japan) and relating it with its concentration by means of the Beer-Lambert law. Calibration was necessary and MB concentrations within a linear relationship with absorbance were always used for this work.

2.3.2 Assessment of Total Organic Carbon (TOC) reduction

The total organic carbon (TOC) measurements were performed in a Shimadzu TOC 500 provided with an ASI auto-sampler. This equipment assesses both the inorganic carbon and the total carbon mineralizing the samples, subsequently it assesses the difference. MB initial concentrations between 4×10^{-5} and 8×10^{-5} M were used for TOC reduction measurements.

2.3.3 Determination of •OH by Fluorescence

The quantification of the ROS (mainly •OH) was carried out based on the method proposed by Ishibashi et al. [126]. This method involves addition reaction of •OH radicals with terephthalic acid (non-fluorescent) to form 2-hydroxyterephthalic acid (fluorescent at ~425 nm after excitation at 315nm).

2.3.4 Determination of ions leached out during reaction by inductively coupled-plasma mass-spectrometry (ICP-MS)

The determination by inductively coupled plasma mass-spectrometry (ICP-MS) of the ions eluted during photocatalytic reactions was carried out by an ICP-MS Finnigan™ unit equipped with a double focusing reverse geometry mass spectrometer. It has an extremely low background signal and a high ion-transmission coefficient. The treated solutions were digested with nitric acid 69% (1:1 HNO₃ + H₂O) to remove the organics and to insure that there were no adhered ions remaining on the reactor's walls. The samples droplets were introduced into the ICP-MS through a peristaltic pump to the nebulizer chamber at ~7700°C. This allows the complete sample evaporation.

2.3.5 High Performance Liquid Chromatography (HPLC)

The degradation of MB in solution was also monitored by following the intensity of the MB's characteristic peaks in a HP-1100 Agilent series. The mobile phase consisted of two solutions: 0.01% formic acid and acetonitrile 60/40. The temperature in the HPLC was kept at 40 °C and the samples injected were 10µl in volume. The column used was a RP-C18 (4.6 mm × 250 mm). The detection peaks were fixed at 245, 292, 615 and 668 nm.

2.4 Reactive Oxygen Species Scavenging during photocatalytic reactions in solution

In order to identify the contribution of the different ROS to the photocatalytic reactions, the experiments of MB degradation in solution were carried out in the presence of low concentrations of ROS scavengers. If MB degradation takes place in a slower fashion when a specific ROS scavenger is in the system, the extent of this modification is related to the activity obstruction of said ROS. NaN₃ Fluka was used as oxygen singlet scavenger (¹O₂). 1,4-benzoquinone (BQ) and methanol were used respectively as O₂^{•-} radical scavenger and •OH scavengers [127]. Ethylenediamine tetra-acetic acid disodium salt (*EDTA-2Na*) was used as TiO₂vb hole scavenger [51].

2.5 Determination of surface potential and pH evolution during photocatalytic reactions in solution

The interfacial potential and pH during MB degradation were followed on a Jenco microelectrode 6230N, San Diego, USA provided with a microprocessor and a RS-232-C IBM interface. The pH-meter recorded pH-changes with a sensitivity of 0.01 pH- units. The microelectrode was immersed in the solution and in contact with the photocatalyst's surface, measurements under irradiation started after the 30 min equilibration period.

2.6 Photocatalyst characterization

2.6.1 X-ray Fluorescence for determination of material composition in weight percentage

The content of the photocatalysts on the different supports was evaluated by X-ray fluorescence in a PANalytical PW 2400 unit. According to this technique, each element emits a defined X-ray wavelength that is associated with its particular atomic number.

2.6.2 Optical density and light absorbance of photocatalytic films

The optical density (OD) of photocatalysts that were semitransparent was measured in a Cary 16 spectrophotometer. The absorbance, on the other hand was measured in an aRTie F2-RT device because the samples presented some light scattering.

2.6.3 Dinamic contact angle determination for films

The hydrophilicity of the PE-TiO₂ films, for instance, was determined on a Data Physics OCA 35 unit assessing the contact angle (CA) of a water droplet deposited by the sessile drop method.

2.6.4 X-Ray photoelectron spectroscopy (XPS) for the photocatalyst

The X-ray photoelectron spectroscopy (XPS) of the photocatalysts was determined using an AXIS NOVA photoelectron spectrometer (Kratos Analytical, Manchester, UK) provided with monochromatic AlK_a ($h\nu=1486.6$ eV) operated at 15 kV and 10 mA. The XPS spectra were obtained with a multi-detection electron-energy analyzer (VSW FAT mode CL 150). The XPS resolution was between 0.9 and 1.0 eV and the pressure in the spectrometer analyzer chamber was $\sim 10^{-6}$ mbar. The carbon C1s line with position at 284.6 eV was used as a reference to correct the charging effects. The surface atomic concentration was determined by XPS from the peak areas. The surface percentages composition was determined within 10 atomic layers with a thickness of 2nm [128, 129]. Spectrum background was subtracted according to Shirley [130].

2.6.5 Atomic Force Microscopy (AFM)

The atomic force microscopy (AFM) image signals were acquired in contact mode using a PSIA Xe-100 AFM. Silicon nitride cantilevers were used with feedback set points around 1.0 nN. The AFM scanner and position sensors were calibrated using standard samples from Mikromash. The experimental error in the roughness was below 10%. The mean surface roughness (RMS) was calculated for scanned areas of 2x2 μm , 4x4 μm and 20x20 μm depending on the type of sample evaluated.

2.6.6 X-ray Diffraction (XRD)

X-ray diffraction (XRD) patterns were evaluated for the PE-FeOx films and RR@TiO₂-Cu. They were recorded on a Philips X'Pert PRO diffractometer equipped with an X'Celerator detector and a Ni-filtered Cu K radiation operating at 40 kV and 40 mA.

2.6.7 Diffuse Reflectance Spectroscopy (DRS)

Diffuse reflectance spectroscopy was carried out in a Perkin Elmer Lambda 900 UV-VIS-NIR spectrometer provided for with a PELA-1000 accessory within the wavelength range of 200–800 nm and a resolution of 1 nm.

2.6.8 Scanning Electron Microscopy (SEM) and Energy Dispersive X-ray (EDX)

Scanning electron microscopy (SEM) was carried out for the GF mats fibers and was performed in a Philips FEI XL30-FEG unit provided with an Everhart-Thornley secondary-electron (SE) detector tuned at voltages between 5-15 kV. Some fibers of the GF-TiO₂-Cu were taken from the outer surface of the mat to decrease its insulating character. This step was necessary to carry out SEM-work. These fibers were then immobilized on a conductive carbon tape sputtered with Au/Pd in an Ar atmosphere to build the conductive metallic coating required for the SEM analysis. By Energy Dispersive X-ray (EDX), the chemical composition analysis of the GF-mats was determined at 15.0 kV. The data reported was the results of 4-scans.

3. Chapter 3: Preparation, kinetics, mechanism and properties of semi-transparent photocatalytic stable films active in dye degradation

Published work:

L. Suárez, C. Pulgarin, C. Roussel, J. Kiwi. "Preparation, kinetics, mechanism and properties of semi-transparent photocatalytic stable films active in dye degradation" *Applied Catalysis A: General* 516 (2016): 70-80.

Web link:

<http://www.sciencedirect.com/science/article/pii/S0926860X16300412>

Reproduced with permission of Elsevier, Copyright 2017 (license number 4077030523326)

Doctoral candidate's contribution:

Investigator and co-author

3.1 Introduction

The synthesis of environmentally friendly supported catalyst not needing high temperatures, organic solvents and expensive/sophisticated equipment is a primary focus of environmental catalysis/photocatalysis [59-64]. TiO₂ has been utilized for over four decades as the “golden standard” since it generates oxidative radicals under band-gap irradiation able to destroy pollutants and bacteria in the presence of air (O₂), (H₂Ov) [60, 61]. Many studies have reported the photocatalyzed destruction of pollutants on TiO₂ coated surfaces like glass, iron plates and Raschig rings [63]. These are substrates with a high thermal resistance needing the annealing of TiO₂ up to few hundred degrees.

In the last decade laboratories have focused on the discoloration degradation of pollutants/dyes on TiO₂ polymer films due to the polymers low-cost, high availability, stability, flexibility and corrosion resistance. Furthermore, PE films have UV-resistance, lack of oxidation in air, durability and chemical inertness. Polymer films have shown to be useful as catalyst supports leading to catalysis/photocatalysis with acceptable kinetics at the solid-air interfaces [64-67].

TiO₂ nanoparticles have been attached on polymers from colloidal suspensions, dip coating, phosphonate coupling, chemical reduction and emulsion polymerization [68-74]. TiO₂ is also attached to the polymer surface via organic solvents or TiO₂ corroding the substrate surface under light. This induces on the substrate a sufficient number of TiO₂ binding sites [75-79]. More recently, PE-TiO₂ films have been prepared by sputtering techniques and shown to be successful in bacteria inactivation as well as in self-cleaning processes (MB) [80, 81].

Methylene blue (MB) has been taken as the probe to test discoloration/degradation on PE-TiO₂. TiO₂ supported films avoid the undesirable problem of TiO₂ recovery after the pollutant degradation in aqueous solutions. The latter process is expensive consuming time, labor and reagent costs.

The UV- and sunlight photo-activated MB degradation mediated by TiO₂ suspensions has been reported [59-64]. Under sunlight, both the MB and TiO₂ are photosensitized, MB injects electrons into the TiO₂cb and in parallel converts MB to the MB^{+•} cation radical [61, 63]. Under visible light, the electron injected into the TiO₂ reacts with O₂ and generates highly oxidative radicals discoloring/degrading MB, as shown below (reactions 3-1 to 3-5)



This part of the Thesis presents a warranted study on PE-TiO₂ due to: the PE low-cost, corrosion resistance and high adhesion of TiO₂ on PE during repetitive MB-degradation. Only the UVA excitation of the PE-TiO₂ has been addressed by applying UV 366 nm light to photoactivate specifically the TiO₂ avoiding the MB's photosensitization [131, 132].

3.2 Experimental section

3.2.1 Photocatalyst preparation

The low-density polyethylene (LDPE) is a highly branched low crystalline film with formula H(CH₂-CH₂)_nH. The (LDPE) 0.1 mm thick was obtained from Goodfellow, UK (ET311201). The film presented mechanical stability, had a density of 0.92 g cm⁻³ and was thermally stable up to 96°C.

TiO₂ sols were prepared adding drop-wise a 1:1 volume mixture of Ti-isopropoxide and isopropanol to a 0.2 mol L⁻¹ nitric acid solution and refluxing for 6 hours. Then PE polymer films 6 cm diameter were cleaned with acetone and then coated with the TiO₂ sol. A second series of TiO₂ suspensions used preformed TiO₂ Degussa P25 powders. The TiO₂ film deposition on PE was carried out by immersing the PE film in a TiO₂ 30 g L⁻¹ ethanol-suspension for 2h under agitation. The films were then left to dry overnight, washed gently with de-ionized water and dried at 90°C. The TiO₂ films prepared by using the synthesized TiO₂ sol showed a less reproducible MB discoloration kinetics compared to dispersions of TiO₂ Degussa P 25. For this reason, we focused on the last preparation throughout this study.

3.2.2 Reactor geometry, irradiation source and actinometry

The photochemical reactors used shown in the insert of Figure 3.1 were cylindrical with a diameter of 8 cm and contained an MB volume set at 60 ml. Experiments were performed according to the ISO standards 10678: 2010 and 10676: 2010 [131] taking into consideration: a) initial pH of the MB-solution ~6, b) the use of BLB UVA light, c) stirring of the MB-solution during the reaction, d) the height of the solution in the reactor kept around 2 cm, e) equilibration of the MB-solution in contact with PE-TiO₂ before the degradation runs.

A Philips low-pressure mercury vapor lamp model TL-D-15W/08 SLV was used for the photochemical experiments. The mercury lamp used provides an output of 1.2x10¹⁷ photons s⁻¹ (4.3 mW cm⁻²) at 366 nm.

The actinometry addressed the photolytic reduction of Fe³⁺ to Fe²⁺ [68] with a quantum of 1.26 reported for light at 366 nm. Ferrioxalate (K₃Fe(C₂O₄)₃·3H₂O) solutions were irradiated with a mercury light (366 nm) during different periods to obtain different concentrations of Fe²⁺. The irradiated solutions were mixed with 1,10 phenanthroline 0.1% and buffered with CH₃COONa·3H₂O. This allowed the complexing reaction between Fe²⁺ and 1,10 phenanthroline. Subsequently, the Fe²⁺ was quantified by measuring the absorbance of the colored complex at 510 nm. The

procedure described renders the amount of ferrous iron produced per unit of time (moles $\text{Fe}^{2+} \text{ s}^{-1}$).

3.3 Results and discussion

3.3.1 MB discoloration kinetics and effect of the TiO_2 loadings on the PE- TiO_2 films

Figure 3.1 presents the initial discoloration rates (r_0) for MB on PE- TiO_2 (0.9 TiO_2 wt %/wt PE) films at different initial MB concentrations. These experimental runs were carried out following the ISO-standard for MB degradation described by A. Mills [63, 131]. The MB-discoloration takes place due to the mercury light (366 nm) reaching the PE- TiO_2 surface, as MB presents an almost negligible optical absorption between 350 and 460nm [61, 64, 81]. The evaluated concentrations are in the range of 10^{-5} mol L^{-1} . MB absorbance at 664 nm (strongest peak) was used to quantify the MB discoloration. For the runs under evaluation shown in Figure 3.1, the calculated initial discoloration rates were: $r_{0(1)}$ 7×10^{-6} mol $\text{L}^{-1} \text{ h}^{-1}$, $r_{0(2)}$ 1.3×10^{-5} mol $\text{L}^{-1} \text{ h}^{-1}$ and $r_{0(3)}$ 1.1×10^{-5} mol $\text{L}^{-1} \text{ h}^{-1}$ for initial concentrations of 1×10^{-5} mol L^{-1} , 3×10^{-5} mol L^{-1} and 5×10^{-5} mol L^{-1} respectively. It is observed that as the initial concentration increases the initial discoloration rate increases as well.

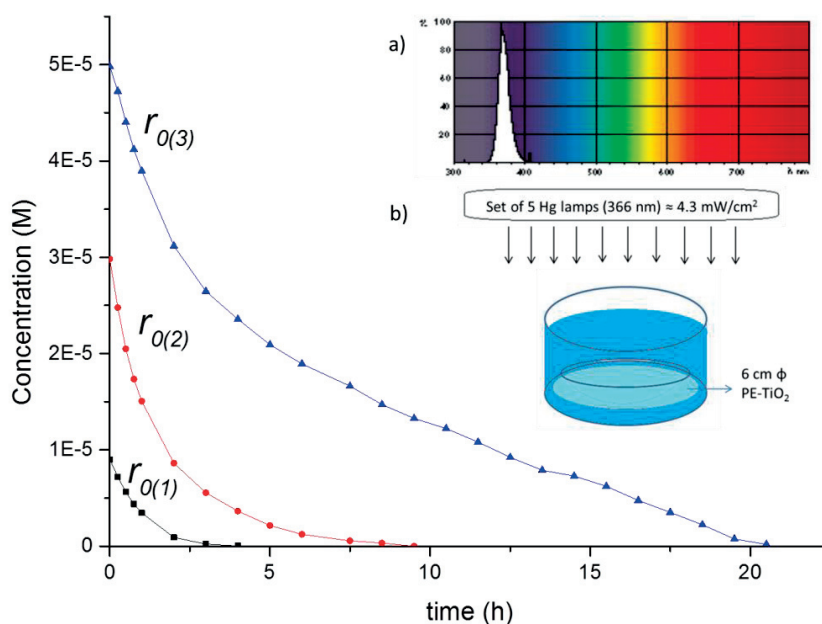


Figure 3.1. Pseudo-first order rates of MB discoloration on PE- TiO_2 (0.90 TiO_2 wt % / wt PE) for different initial MB concentrations: 1) 1×10^{-5} mol L^{-1} , 2) 3×10^{-5} mol L^{-1} , 3) 5×10^{-5} mol L^{-1} . Inserts: a) Mercury lamps emission, 4.3 mW cm^{-2} , b) Reactor

The proximity of the r_0 values corresponding to the two highest concentrations suggests that a nearly constant value of initial discoloration rate can be achieved for concentrations between 3×10^{-5} mol L^{-1} and 5×10^{-5} mol L^{-1} . The initial pH of the MB solution was pH 5.9 - 6.3 depending on the MB concentration in solution. Figure 3.1

shows that MB discoloration proceeded from time zero. The electrostatic interaction between the cationic dye and the slightly positive TiO_2 (IEP ~ 6.6) seems to be low and not to hinder the contact of MB with the PE- TiO_2 film. Since the MB discoloration was determined by spectrophotometry, the rate constants reported in Figure 3.1 not only refer to MB disappearance but might involve colored intermediates in solution. The overall quantum yield for MB degradation was found to be $\sim 0.25\%$ calculated based on what described in section 3.2.2.

Figure 3.2 shows the dependence of the rate constant k for the discoloration of MB on the TiO_2 loading of the PE films. A MB solution $1 \times 10^{-5} \text{ mol L}^{-1}$ was used for these experiments. Results show that the MB discoloration kinetics was proportional to the amount of TiO_2 on the PE film, up to a TiO_2 content of 0.90 wt %/ wt PE. A second order polynomial was used to fit the data presented and the correlation (R^2) found was 0.9963.

The insert in Figure 3.2 shows a Total Organic Carbon decrease (TOC) from 8.7 mg organic C L^{-1} to 3.5 mg organic C L^{-1} for a MB $5 \times 10^{-5} \text{ mol L}^{-1}$ solution. This concentration of MB was used for the TOC experiments because the reproducibility of the TOC data for a solution $5 \times 10^{-5} \text{ mol L}^{-1}$ was higher compared to a MB $1 \times 10^{-5} \text{ mol L}^{-1}$ solution. Total mineralization was not achieved. This agrees with the results reported by J-M Herrmann et al. [133] reporting that long-lived C-containing intermediates were produced during the photocatalyzed degradation of MB on TiO_2 suspensions.

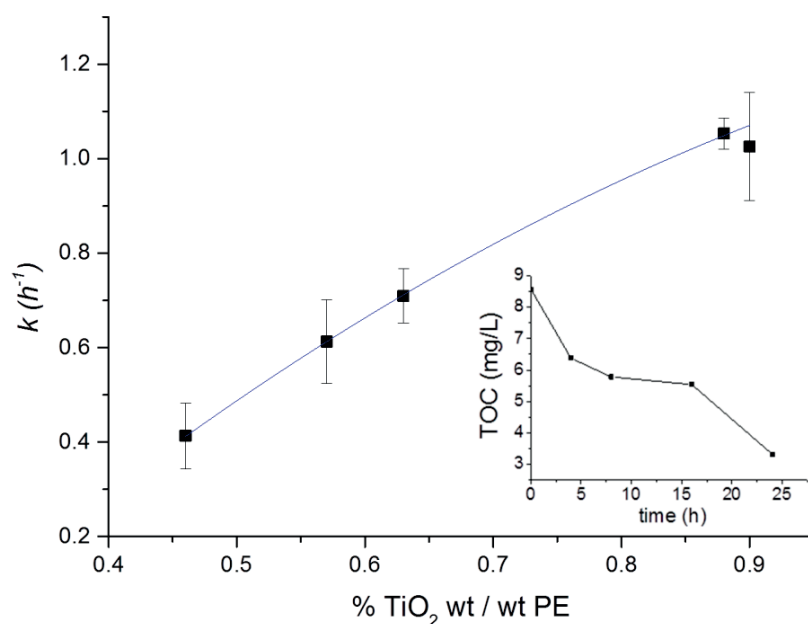


Figure 3.2. Dependence of the pseudo-first order rate constant k , on the PE- TiO_2 loading, MB initial concentration: $1 \times 10^{-5} \text{ mol L}^{-1}$. Insert. a) Total organic carbon reduction for an aqueous

3.3.2 Effect of light intensity on MB discoloration and ICP-MS evidence for the stable performance of PE-TiO₂ during repetitive use

Figure 3.3 shows the significant effect of the light intensity (photon flux) in the MB-discoloration kinetics. A small decrease of 5 % was observed by MB adsorption on PE-TiO₂ (Figure 3.3, trace 1). MB adsorbs on the PE-TiO₂ film, which by itself does not degrade MB.

The trend in the MB-discoloration times shown in Figure 3.3 suggests that radical species and holes (vbh^+) generated at the PE-TiO₂ surface lead to MB-discoloration and the reactive oxygen species (ROS) diffuse within short distances. These distances can be estimated in the following way: a) a rate of production of HO₂[•] ($k_a[HO_2^{\bullet}] \approx 10^6 \text{ M}^{-1}\text{s}^{-1}$) has been reported for the reaction between the HO₂[•] and anthracene, a molecule with a 3 ring structure close to MB [60, 61]. For the reaction between HO₂[•] and MB ($1 \times 10^{-5} \text{ mol L}^{-1}$), it is possible to assess the lifetime of the reaction-pair HO₂[•] and MB as $\frac{1}{\tau} = k_a[OH_2^{\bullet}][MB]$ with $k_a[HO_2^{\bullet}] \approx 10^6 \text{ M}^{-1}\text{s}^{-1}$. Next, the Smoluchowski simplified relation $x^2 = D\tau$ is used taking $D = 5 \times 10^{-6} \text{ cm}^2\text{s}^{-1}$ as an average value for low molecular weight molecules, in this case MB diffusing in aqueous solution. This leads to a value of 7.1 microns for the diffusion length of HO₂[•], b) by a similar approach and taking for the •OH $k_b[•OH] \approx 10^9 \text{ M}^{-1}\text{s}^{-1}$ leads to a diffusion length of ~ 0.2 microns for the •OH away from the PE-TiO₂ films.

Table 3.1 presents mass ratio for the loading of TiO₂ on PE obtained by X-ray fluorescence (XRF) as a function of the TiO₂ Degussa P25 content of the suspension used during the preparation step. The quantum yield for the MB $1 \times 10^{-5} \text{ mol L}^{-1}$ discoloration under 5 lamps irradiation (4.3 mW cm^{-2}) was 0.25 %. This latter value was estimated in the following way: a value of 1.26 was taken for the Fe²⁺ yield. The moles of photons s⁻¹ were estimated ($1.95 \times 10^{-7} \text{ Einsteins s}^{-1}$). The transformed moles of MB per second were estimated as $4.93 \times 10^{-10} \text{ moles s}^{-1}$ from the degradation of a solution MB $1 \times 10^{-5} \text{ mol L}^{-1}$ on a sample PE-TiO₂: 0.9%TiO₂ wt/wt PE under a mercury light dose of 4.3 mW cm^{-2} . The amount of molecules of MB per second was then divided by the Einsteins s⁻¹ to report the quantum efficiency of 0.25 %.

In a separate set of experiments, degradation of MB at concentrations $< 10^{-5}$ were seen to require a lower number of photons to induce an acceptable MB-discoloration kinetics. Saturation effects were found in Figure 3.3 during the irradiation of MB $1 \times 10^{-5} \text{ mol L}^{-1}$ when the number of photons was increased by a factor >4 by increasing the applied light intensity as shown in Figure 3.3 traces 2 to 5. This shows that sufficient MB molecules were present to absorb higher levels of UVA photons $\text{cm}^{-2} \text{ s}^{-1}$. Higher applied light intensities (traces (5,6) led to a slower increase in the MB-discoloration kinetics. A slower increase in the dye degradation kinetics was observed when the applied light intensity was increased during the degradation of colored pigments in commercial paints as reported by T. Egerton et al. [134]. A change in the applied higher light doses in Figure 3.3 affects less the MB-degradation compared to a variation of the light dose applied at low intensities.

Table 3.1. TiO₂ wt % /wt PE determined by X-ray fluorescence as a function of the TiO₂ content during the preparation of PE-TiO₂. Additionally, assessed cm³ TiO₂ / cm² PE based on XRF data and material properties.

TiO ₂ Degussa P25 suspension concentration (g/L)	TiO ₂ wt % /wt PE	Experimental error (%)	(cm ³ TiO ₂ / cm ² PE)
2.5 g/L	0.46	0.02	1.09E-05
5.0 g/L	0.57	0.02	1.36E-05
10.0 g/L	0.63	0.02	1.50E-05
20.0 g/L	0.88	0.03	2.09E-05
30.0 g/L	0.9	0.03	2.14E-05

Figure 3.4 shows the recycling use of a PE-TiO₂ sample up to the 5th cycle. No loss of activity was observed during the repetitive degradation of MB 1x10⁻⁵ mol L⁻¹. The sample was thoroughly washed after each recycling run. By ICP-MS, values < 1 ppb Ti were detected to leach out of the PE-TiO₂ sample after each recycling. This means that practically no TiO₂ could be detected out of the samples during repetitive MB-degradation. But when a MB sample 5x10⁻⁵ mol L⁻¹ was discolored for 3 times, Ti concentrations between 14 and 28 ppb were detected. However, these latter concentrations of suspended TiO₂ were not sufficient for MB solution degradation.

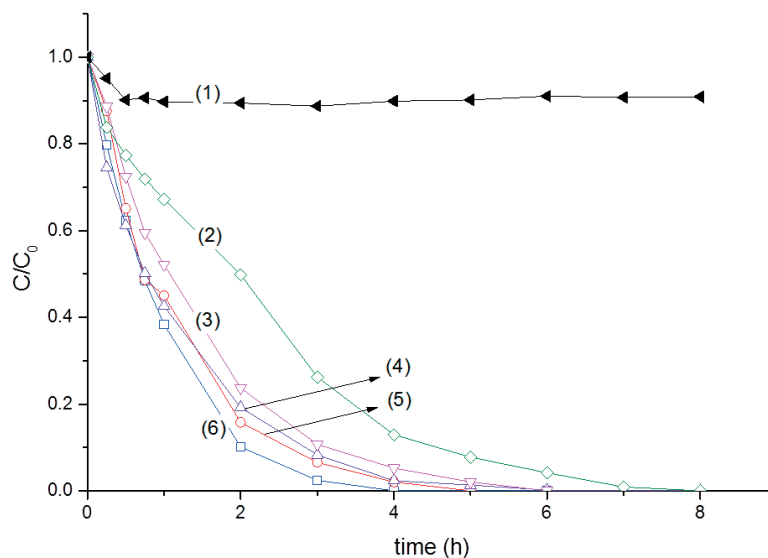


Figure 3.3. MB 1x10⁻⁵ M discoloration as a function of time on (0.90 TiO₂ wt % PE-TiO₂) films at different mercury light intensities: 1) Dark run and runs under light on PE-TiO₂, (2) 1.1 mW cm⁻², (3) 1.9 mW cm⁻², (4) 2.8 mW cm⁻², (5) 3.5 mW cm⁻², (6) 4.3 mW cm⁻²

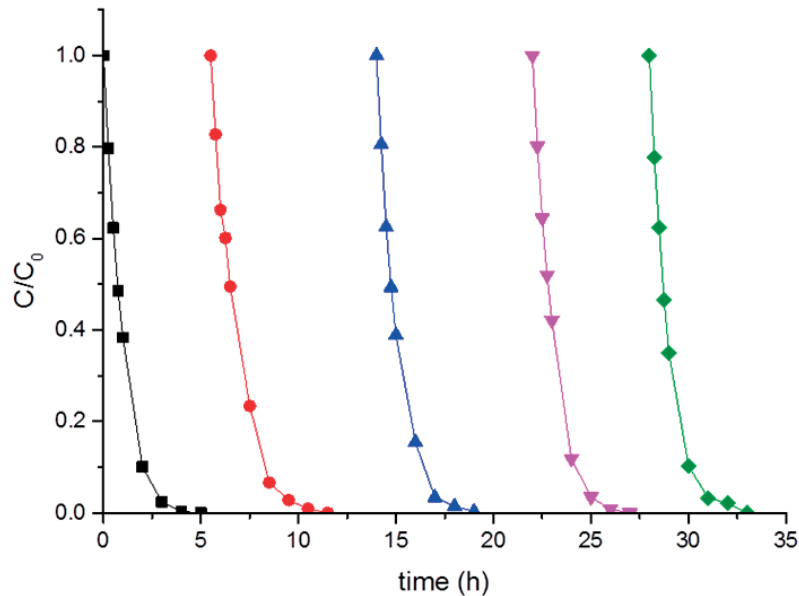
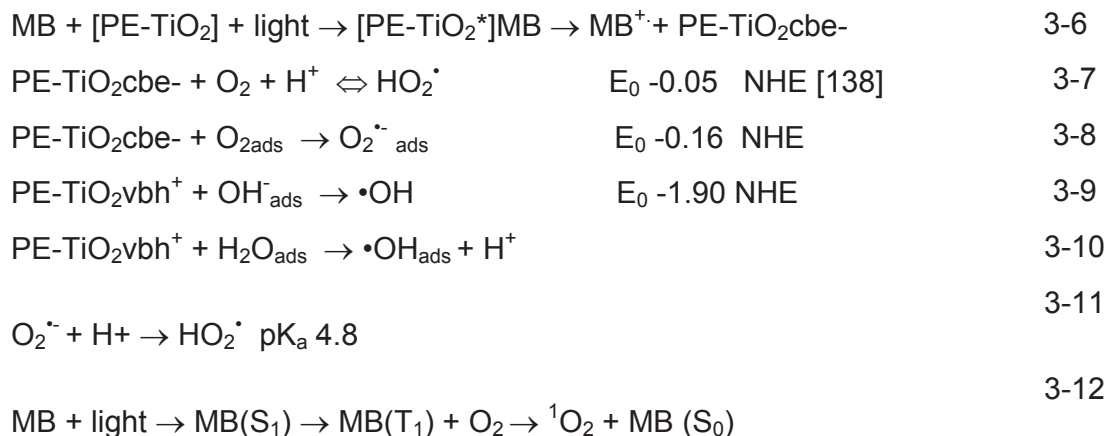


Figure 3.4. Repetitive MB 1×10^{-5} mol L⁻¹ discoloration as function of re-use on PE-TiO₂ (0.90 TiO₂ wt % / wt PE) films, Mercury irradiation 4.3 mWcm^{-2}

3.3.3 Scavenging of the oxidative species leading to MB degradation. Mechanism of reaction

Reactive oxygen species (ROS) are chemically reactive molecules containing oxygen, like superoxide, hydroxyl radical, and singlet oxygen. The different ROS radicals have been widely documented as being photo-induced by TiO₂ band-gap irradiation [62-64]. The contribution of these ROS in the study of MB degradation by PE-TiO₂ was monitored and is presented below in Figure 3.5.

Figure 3.5 presents the results of the scavenging of radicals during the photodegradation of a MB 3×10^{-5} solution under band-gap irradiation up to 6 hours. The relative contributions of the radicals generated at the PE-TiO₂ surface show: a) trace (1) MB discoloration mediated by PE-TiO₂, b) trace (2) MB discoloration in the presence of methanol 20 mmol L^{-1} a quencher of $\bullet\text{OH}$ -radicals, c) trace (3) MB discoloration in the presence of NaN₃ 20 mmol L^{-1} [60, 61, 135] a scavenger of oxygen singlet $^1\text{O}_2$, d) trace (4) MB discoloration in the presence of benzoquinone 20 mmol L^{-1} [136, 137] a quencher of $\text{O}_2^{\bullet-}/\text{HO}_2^{\bullet}$ e) trace (5) MB discoloration in the presence of 20 mmol L^{-1} ethylene-diamine tetra-acetic acid disodium salt (EDTA-2Na), a widely used TiO₂vb(h⁺) scavenger [59-61]. Based on the results shown in Figure 3.5, the scavengers (2-5) quench the radical intermediates leading to MB degradation. EDTA-Na 2 mmol L^{-1} is shown to be the most active species precluding almost completely MB degradation due the scavenging of the TiO₂vbh⁺ species. The relative importance of the species intervening in MB discoloration would be: vbh⁺ > $\text{O}_2^{\bullet-}/\text{HO}_2^{\bullet}$ > $^1\text{O}_2$ > OH[•]. A simplified MB-degradation mechanism including the radical species leading to the dye degradation is suggested below:



In reaction (3-11) the HO_2^\bullet radical is stable at $\text{pH} < 4.8$, above this pH more than 50% is present in the form of $\text{O}_2^{\bullet-}$. The MB initial pH for solutions in Figure 3.5 was 6.1 - 6.2 and the final pH was 4.6 - 4.7 after 6 hours irradiation. This is more than a tenfold increase in the solution H^+ -concentration which would favor the back reaction and therefore the build-up of the HO_2^\bullet radical in reaction (3-7). Reaction(3-10) is the most important reaction leading to MB degradation due to: a) the strong scavenging effect of the vbh+ previously shown in Figure 3.5 by EDTA-Na 2 mmol L^{-1} , b) the observed increase in acidity of the MB solution far above one pH unit and finally c) the OH^\bullet -radicals in reaction (3-10) undergo the one electron reduction reaction $\text{OH}^\bullet/\text{OH}^-$ with $E_0 1.90 \text{ NHE}$ vs HO_2^\bullet radicals undergoing the reduction $\text{O}_2^{\bullet-}/\text{HO}_2^\bullet$ at a somewhat lower level of $E_0 0.75 \text{ NHE}$.

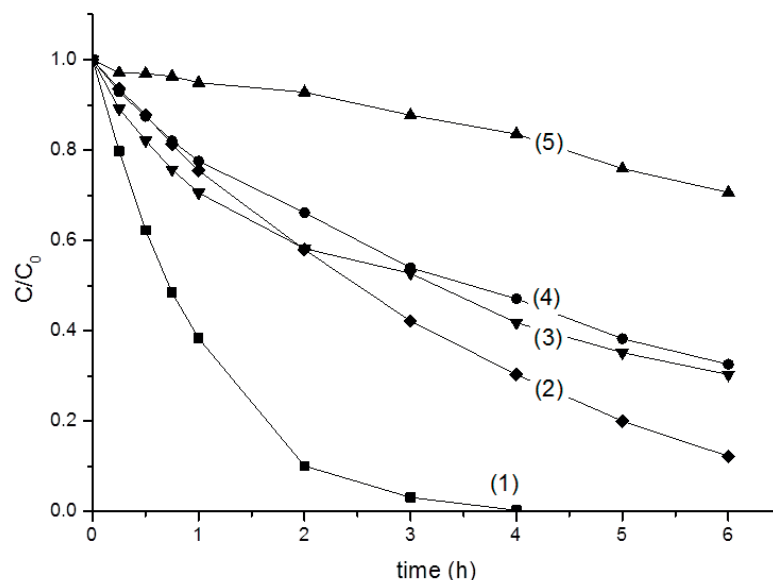


Figure 3.5. MB discoloration on PE-TiO₂ of a solution MB $3 \times 10^{-5} \text{ mol L}^{-1}$, PE-TiO₂: (0.90 TiO₂ wt%/ wt PE) under mercury light 4.3 mW cm^{-2} . Scavengers used: Methanol 20 mmol L^{-1} (HO^\bullet), NaN_3 20 mmol L^{-1} (${}^1\text{O}_2$), EDTA-2Na 20 mmol L^{-1} (h^+) and Benzoquinone(BQ) mmol L^{-1} ($\text{O}_2^{\bullet-}/\text{HO}_2^\bullet$): (1) No scavenger, (2) Methanol, (3) NaN_3 , (4) BQ, (5) EDTA - 2Na

3.3.4 Temporal evolution of radicals on PE-TiO₂, OH-radical detection by fluorescence and optical absorption by PE-TiO₂ samples

Figure 3.6a shows that the MB discoloration within 3 hours is almost complete at pH 3. Figure 3.6b shows the results for the same solution as used in Figure 3.6a but at pH 6. A faster MB discoloration rate was observed at pH 6. Next, we added benzoquinone (BQ) 2 mmol L⁻¹ to the MB-solution at pH 3. The MB discoloration shown in Figure 6c was slower compared to the discoloration without addition of BQ (Figure 3.6a). BQ is added next at pH 6. Figure 3.6d shows faster discoloration kinetics compared to the data reported in Figure 3.6c. This due to the effect of the non-protonated superoxide anion-radical (O₂^{•-}) being more effective than the HO₂[•] present at pH 3, based on what explained for reaction (3-11). The diffusion controlled electron transfer at pH 6 is shown in reaction (3-13)



Figure 3.6e shows the effect of the addition of the ¹O₂ quencher NaN₃ (20 mmol L⁻¹) at pH 3. A strong decrease is observed in the MB discoloration initial stages < 1 hour indicating that the oxygen singlet ¹O₂ intervenes from the beginning in MB discoloration. An almost similar effect was observed for the NaN₃ addition to a MB solution at pH 6. The NaN₃ effect decreases strongly after 1h (Figure 3.6e). This suggests that NaN₃ the ¹O₂ is produced in the initial reaction stages and subsequently reacts with long-lived intermediates produced during MB degradation further generating O₂^{•-} [133].

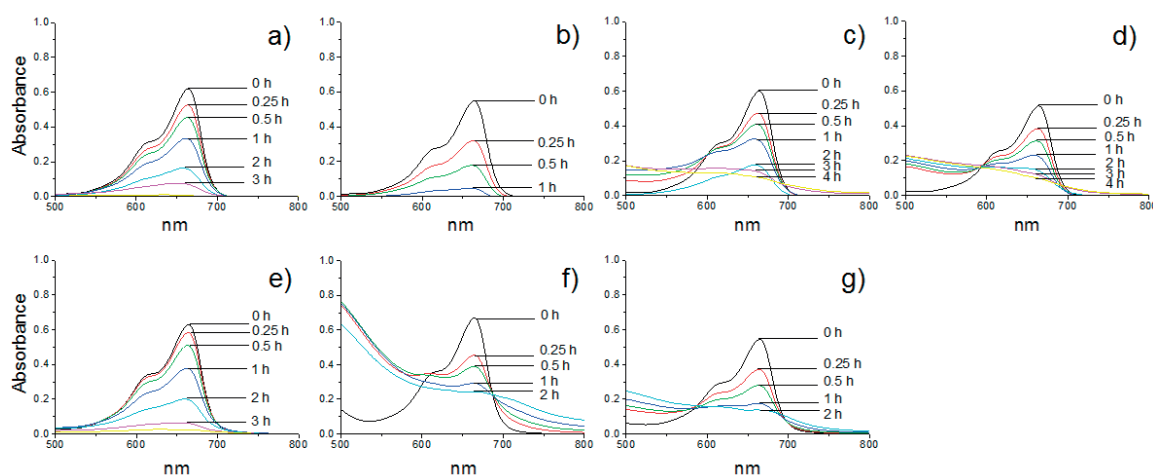


Figure 3.6. MB 1x10⁻⁵ mol L⁻¹, discoloration on PE-TiO₂, PE-TiO₂ (0.9 TiO₂ wt % / wt PE); mercury lamps: 4.33 mW cm⁻²: a) No scavenger at pH = 3, b) No scavenger at pH = 6; c) BQ (2 mmol L⁻¹) at pH = 3, d) BQ (2 mmol L⁻¹) at pH = 6, e) NaN₃ (20 mmol L⁻¹) pH = 3; f) BQ (2 mmol L⁻¹) + NaN₃ (2 mmol L⁻¹) pH =3; g) BQ (2 mmol L⁻¹) + NaN₃ (2 mmol L⁻¹) pH = 6

Next BQ + NaN₃ were added at pH3 and pH6 to sort out the effects of the combined quenchers on MB-discoloration as a function of the solution pH. Figure 3.6f) shows that at pH 3, the added scavengers were more effective than at pH 6 (Figure 3.6g)). MB-discoloration seems to be controlled mainly by the HO₂⁻ /O₂⁻ as suggested by the equilibrium in reaction (3-11).

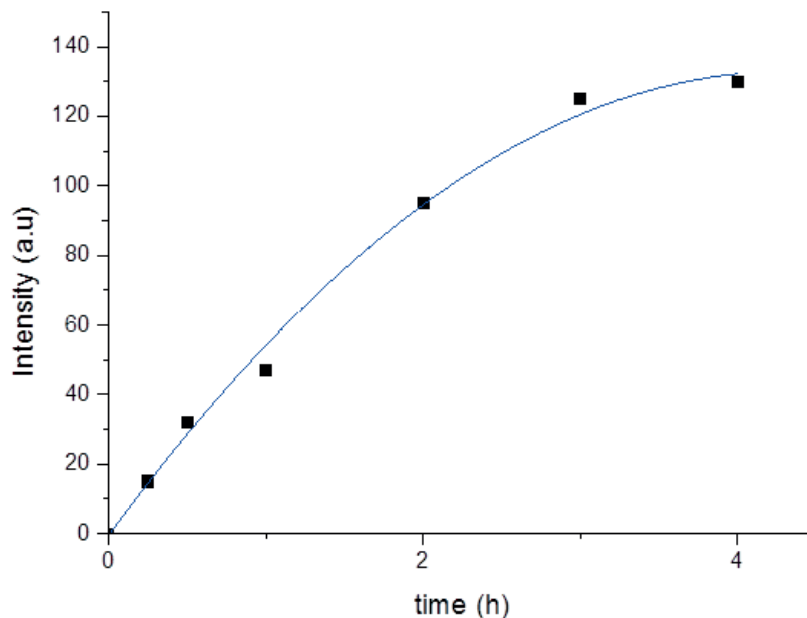


Figure 3.7. Relative fluorescence increase in a solution 2-hydroxyterephthalic acid irradiated up to 4h (mercury light 4.3 mW cm⁻²) on a PE-TiO₂ (0.90 TiO₂ wt %/ wt PE) sample

Figure 3.7 shows the increase in •OH species as a function of the PE-TiO₂ irradiation time. The increase in the fluorescence intensity is proportional to the concentration of •OH in solution. Details of the analysis have been already described in the experimental section [126]. This data further confirms the presence of •OH radicals during MB-discoloration as previously shown in a qualitatively way in Figure 3.5.

The optical density (OD) of the different PE-TiO₂ films is shown in Figure 3.8. The TiO₂ absorption occurs below 400 nm and in Figure 3.8 a tail absorption is seen at longer wavelengths. For this reason a second set of measurements was carried out in an instrument designed to measure reflectance and transmittance of films (aRTie (F2-RT) Filmetrics) [80].

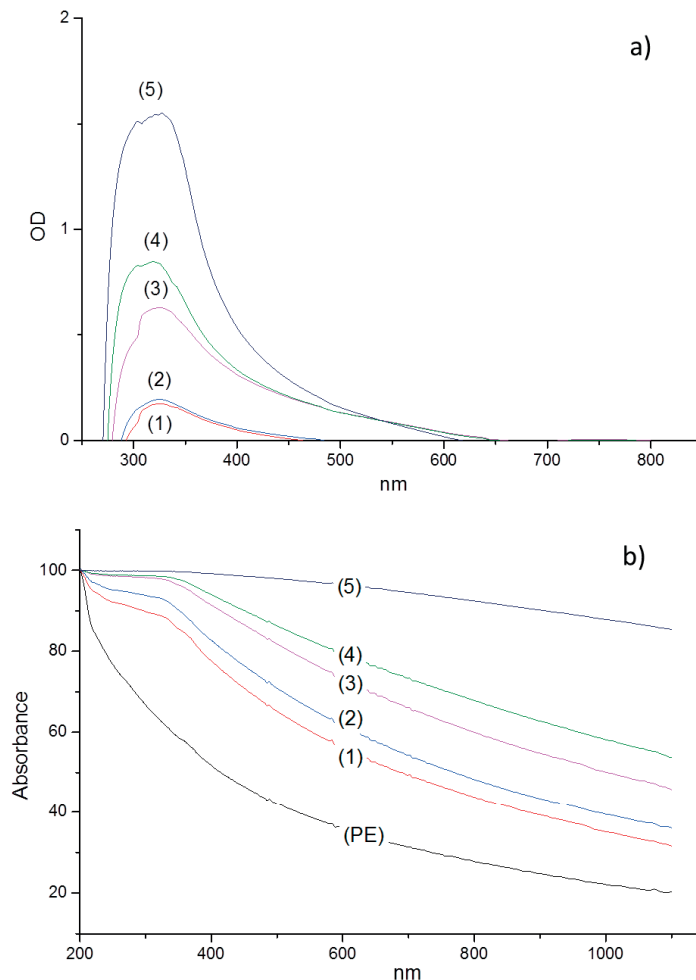


Figure 3.8. a) Optical density (OD) of the PE-TiO₂ films: (1) 0.46 TiO₂ wt % / wt PE, (2) 0.57 TiO₂ wt % / wt PE, (3) 0.63 TiO₂ wt%/ wt PE, (4) 0.88 TiO₂ wt%/wt PE, (5) 0.90 TiO₂ wt%/wt PE. b) absorbance of the PE films

3.3.5 Implications of the hydrophobic-hydrophilic transformation under TiO₂ band-gap irradiation and dark reverse reaction of PE-TiO₂ films

Figure 3.9a shows the reduction in the CA of the PE-TiO₂ film under mercury light irradiation from the hydrophobic CA of 92° at time zero to a value < 5° within ~5 hours. The hydrophobic-hydrophilic transformation is induced by the photo-generated holes of the TiO₂ involving trapped lattice oxygen sites [60, 61, 139]. The reverse transformation to the initially hydrophobic PE-TiO₂ was observed to be complete in about 100 hours. This implies that the repetitive discoloration of MB solutions 1x10⁻⁵ M by means of PE-TiO₂ film, requires a long photocatalyst recovery.

Figure 3.9b shows the hydrophobic to hydrophilic transformation expressed as Y_S under mercury light irradiation within ~5 hours and the back transformation to the hydrophobic initial state in the dark within 100 hours. This plot, expressing the

wettability was obtained by integrating “cos Θ ” from the contact angle (CA/ Θ) in the Young’s equation [60, 61].

$$Y_S = Y_{SL} + Y_L \cdot \cos \theta$$

3-15

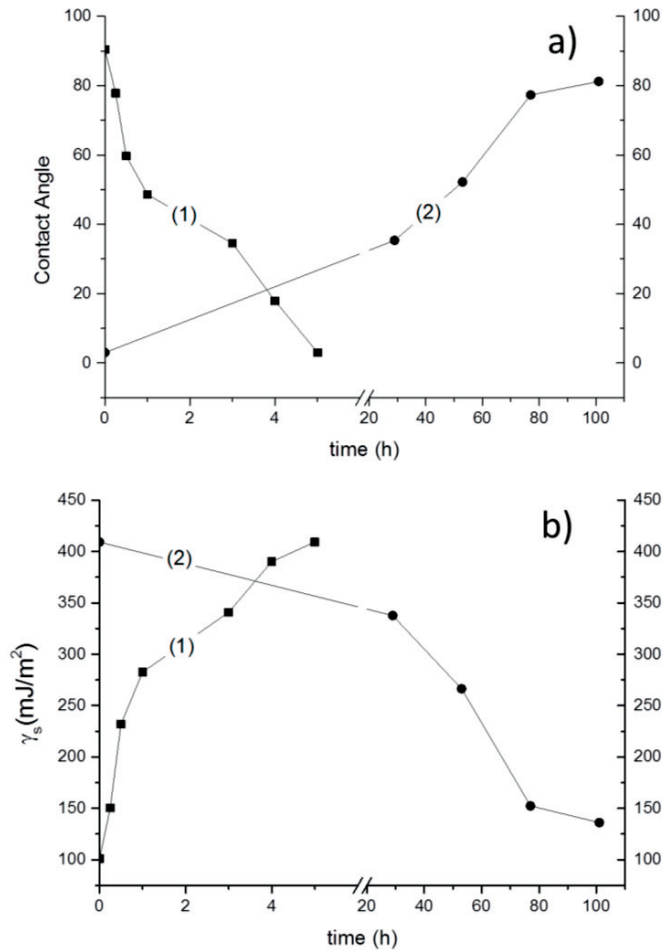


Figure 3.9. Hydrophobic/hydrophilic transformations for a sample PE-TiO₂. a) Change in contact angle, b) change in surface free energy (0.90 TiO₂ wt %/wt PE), under mercury light 4.3 mW cm⁻² (1) hydrophobic to hydrophilic conversion under light, (2) hydrophilic to hydrophobic dark reverse reaction

In equation (3-15) Y_S and Y_L are the surface free energies per unit area of the solid and liquid respectively, and Y_{SL} is the interfacial free energy per unit area. In addition, Y_{SL} can be approximated using the Girifalco-Good equation [126], with Y_S and Y_L , as

$$Y_{SL} = Y_S + Y_L - \Phi(Y_S Y_L)^{1/2}$$

3-16

Here, Φ is a constant parameter ranging from 0.6 to 1.1, depending on the solid. In addition, Y_L is the water surface free energy, with a constant value of 74 mJ m⁻². Therefore, by combining (3-15) and (3-16), the Y_S can be expressed as:

$$Y_S = C (1 + \cos \theta)^2 \quad (C: \text{constant})$$

3-17

3.3.6 X-Ray photoelectron spectroscopy (XPS) peak changes during the MB-discoloration process

Table 3.2 presents the atomic surface concentration percentage variation of several elements during the discoloration of MB on PE-TiO₂ photocatalyst. It is readily seen that the C, N and S content increase during the first 4h due to the residues (intermediates long-lived organic decomposition products, sulfate-ions, nitrate-ions) accumulating on the film surface. After 8h, their percentages decrease since the long-lived C-residues convert to CO₂ and the oxidation of N and S in the presence of air (O₂) takes place, being converted into volatile N- and S-species. The O-content and the Ti-content seem to decrease within the first 4h, as the MB-decomposition residues shield the O and Ti-signal of the PE-TiO₂ surface. Once the organic and N, S fragments from MB degradation are removed after 8 hours, the Ti initial surface content is re-established. This shows the catalytic removal of MB is possible by the PE-TiO₂ photocatalyst.

Table 3.2. Surface percentage atomic concentration of PE-TiO₂ during MB discoloration as determined by XPS. The first row refers to a samples of PE-TiO₂ contacted with MB for a short period in the dark

Reaction time (h)	C	N	O	S	Ti
0	57.0	0.43	30.7	0.20	11.65
0.5	57.6	2.10	29.1	0.30	10.80
1	59.6	1.92	27.3	0.84	10.25
2	68.3	2.57	20.8	0.62	7.58
4	68.0	2.74	21.6	0.77	6.86
8	55.0	1.48	31.4	0.52	11.50C

Figure 3.10 shows the peaks of Ti, C, and O before and after 4 hours irradiation of a solution MB 3×10^{-5} . The carbon C1s at 284.6 eV was used as the reference for the peak positions of Ti, C, and O the XPS spectrogram [128, 129]. The Shirley correction was used to correct the electrostatic charging effect during the XPS measurement [130]. The Ti2p doublet peak binding energy BE is seen to shift from 457.01eV to 457.26 eV. This suggests the MB-degradation proceeds concomitant with redox reactions in the PE-TiO₂ film. This is a further evidence for the photocatalysis proceeding through Ti³⁺/Ti⁴⁺ species on the surface of the films since the peak shift is > 0.2 eV [38]. The shift in the C1s BE originating from the PE is seen by the peak shift from 283.38 eV to 283.12 eV. This again confirms redox

reactions occurring in the C- within the time of MB discoloration. Redox behavior was again observed during the O1s peak shift in the last graph of Figure 3.10.

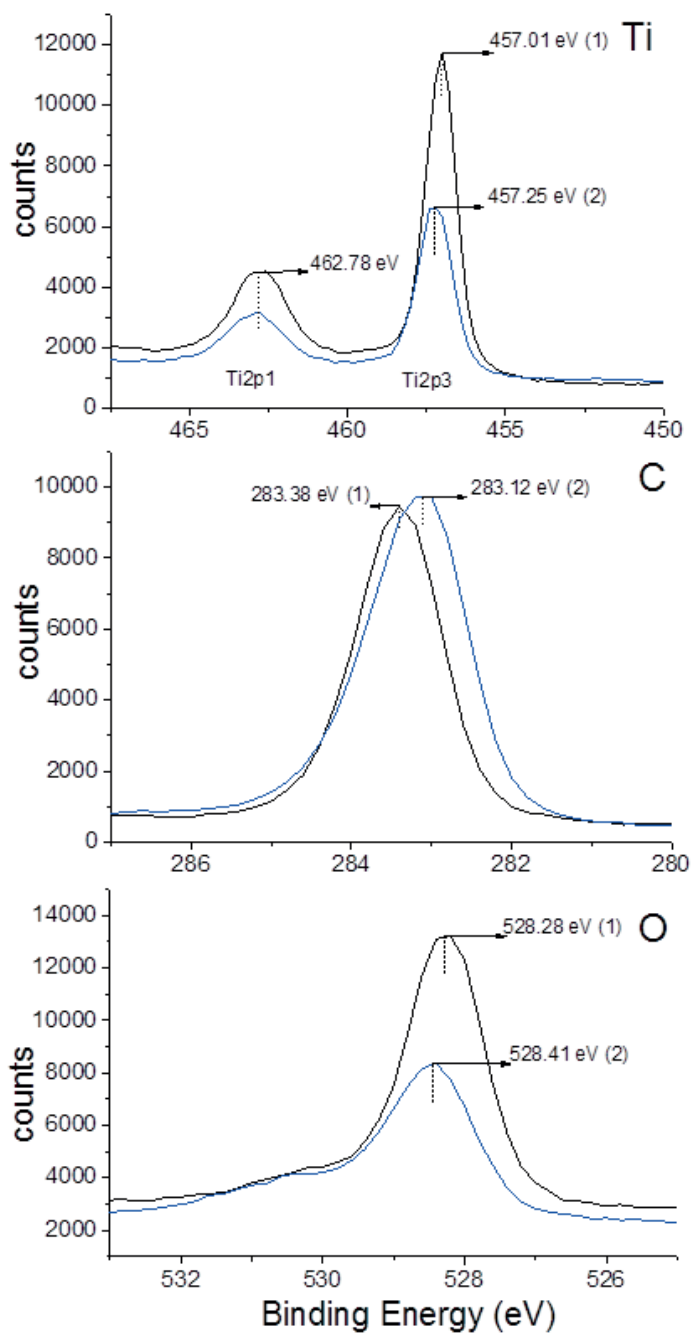


Figure 3.10. XPS signals of Ti, C and O at: 1) time zero 2) after discoloration of a MB $3 \times 10^{-5} \text{ mol L}^{-1}$ solution, under mercury light irradiation 4.3 mW cm^{-2} on PE-TiO₂ films (0.90 TiO₂ wt% /wt PE)

3.4 Conclusions

A comprehensive, detailed and systematic study is presented for a stable PE-TiO₂ film leading to the degradation of MB with acceptable kinetics under TiO₂ band-gap irradiation. An adhesive coating of TiO₂ on PE is presented; the photocatalyst kept some of the transparency of the polyethylene and it was prepared under mild, simple conditions, at low temperatures and did not require expensive instrumentation. Evidence is presented for the PE-TiO₂ films able to degrade MB under low UV-light irradiation in a repetitive way showing the same MB-degradation kinetics. Scavenging experiments identifying the ROS species leading to MB degradation are reported showing the TiO₂vbh⁺ to be the most effective species during degradation reaction. The diffusion length for the HO₂[•] and •OH radicals was estimated reaching short distances away from the PE-TiO₂ films this is why a constant stirring is key to surpass the diffusion limitations during reaction. Evidence is presented for the PE-TiO₂ contact angle (CA) conversion from the initial hydrophobic (92°) to super-hydrophilic values (<5°). The time of the conversion was concomitant with the MB-discoloration time (5 h) and this feature is expected to have a great impact if the degradation approach is taken to the solid-air interface (self-cleaning material). The PE-TiO₂ films show a potential for practical applications to degrade dyes in water treatment due to their stable repetitive photocatalytic performance, however the diffusion limitations have to be overcome either by: a) photocatalyst deposition inside the reactor or reactor design, b) reaction of solution's bulk, c) optimization of stirring.

4. Chapter 4: Cu-decorated Raschig-TiO₂ rings inducing MB repetitive discoloration without release of Cu-ions under solar light

Published work:

Laura Suárez, Zhang Wei, Helena Teixidó, Rosendo Sanjinés, Michaël Bensimon, César Pulgarín, John Kiwi. "Cu-decorated Raschig-TiO₂ rings inducing MB repetitive discoloration without release of Cu-ions under solar light". Journal of Environmental Chemical Engineering 5 (2017) 68-77.

Web link:

<http://www.sciencedirect.com/science/article/pii/S2213343716304468>

Reproduced with permission of Elsevier, Copyright 2017 (license number 4077120064490)

Supplementary material:

Annex A

Doctoral's Candidate contribution:

Investigator and co-author

4.1 Introduction

Supporting the photocatalysts on fixed-beds of Raschig rings could be an option that facilitates the optimization of solar light and resources. TiO₂ coated Raschig rings were recently reported to be used for the degradation of dye direct-red 16 [89]. This approach has also been used to degrade several aromatic compounds in aqueous solution [59, 90, 91]. Our laboratory has reported Raschig rings coated by TiO₂ as a catalyst to degrade phenol [92], phenol-compounds [93] and chlorophenols [94].

In this chapter, the dye methylene blue (MB) was kept as a model pollutant and Raschig rings were used as a low cost inert support for the Cu-decorated TiO₂. This TiO₂ decoration was achieved by adding small amounts of Cu/CuO to the TiO₂ in order to extend the light absorption into the visible region increasing the dye degradation kinetics under solar irradiation.

The preparation of a low-cost RR@TiO₂-Cu photocatalyst and its testing with the degradation of MB is addressed aiming to avoid the separation of the catalyst from the solution at the end of the dye degradation process. Also, the degradation kinetics of Cu-decorated TiO₂ Raschig rings, the reaction mechanism, the Cu-ions leaching from the catalyst surface and the characterization of the optimized photocatalyst surface is reported in this chapter.

4.2 Experimental section

4.2.1 Materials and photocatalyst preparation

The Raschig rings that served as support for the RR@TiO₂-Cu were 4 x 4 mm in size and 1 mm thick, were made out of soda lime glass composed by: 70% SiO₂, 10% (Na₂O, CaO, MgO K₂O) and 5% (Fe₂O₃, Al₂O₃). TiO₂ used in the suspensions was Degussa P25 and the CuNO₃·3H₂O was Acros Organics. The polyethylene-graft-maleic anhydride powder (PEGMA) was a Sigma–Aldrich No.456624, Mw 2300. The reagent 3, 7-bis (Dimethylamino) phenazathionium chloride or Methylene Blue (MB from now) was Sigma-Aldrich and used as received.

The supported catalyst was prepared according to the following sequence: the Raschig rings were washed with detergent and then treated with HNO₃ 30% for 10 min at 50 °C, then drained and rinsed with Milli-Q water. The clean Raschig rings were subsequently immersed in PEGMA dissolved in toluene 5% (wt/wt), then drained and dried overnight at room temperature. The dry Raschig rings with PEGMA on their surface were dipped in TiO₂ suspensions (5g/l) and CuNO₃·3H₂O was added according to the amount selected to decorate the RR@TiO₂. The rings were drained and dried at 110 °C for 1 h. The latter step was repeated 3 times and the RR@TiO₂-Cu was calcined at 500 °C during 10 h to eliminate the PEGMA, the interfacial binder. TiO₂ /Cu was deposited on the external and internal surfaces of the Raschig rings. The reproducibility of the amount of Cu deposited on the RR@TiO₂ was ± 20% and it was kept by following the preparation protocol.

4.2.2 Irradiation source and reactors

Photolysis experiments were performed in the cavity of a solar simulated Hanau Suntest Lamp with a tunable light intensity attachment equipped with an IR filter to remove IR radiation > 800 nm. The UV-radiation < 305 nm was removed by the Pyrex wall of the reaction vessels. The Raschig rings used to fix the $\text{TiO}_2\text{-Cu}$ were positioned between a central Teflon cylindrical tube and the reactor wall; in this way the photocatalytic bed was fixed inside the reactor. The Teflon support was fitted with small holes (2mm diameter) to allow diffusion of the solution in the reactor. In the bottom of the reactor, and concentrically to both the Teflon tube and the reactor, a magnetic stirrer was positioned to keep the diffusion of the reactive species. Pictures of the reactor are supplied in Supplementary material Ch4-S1 (Annex A).

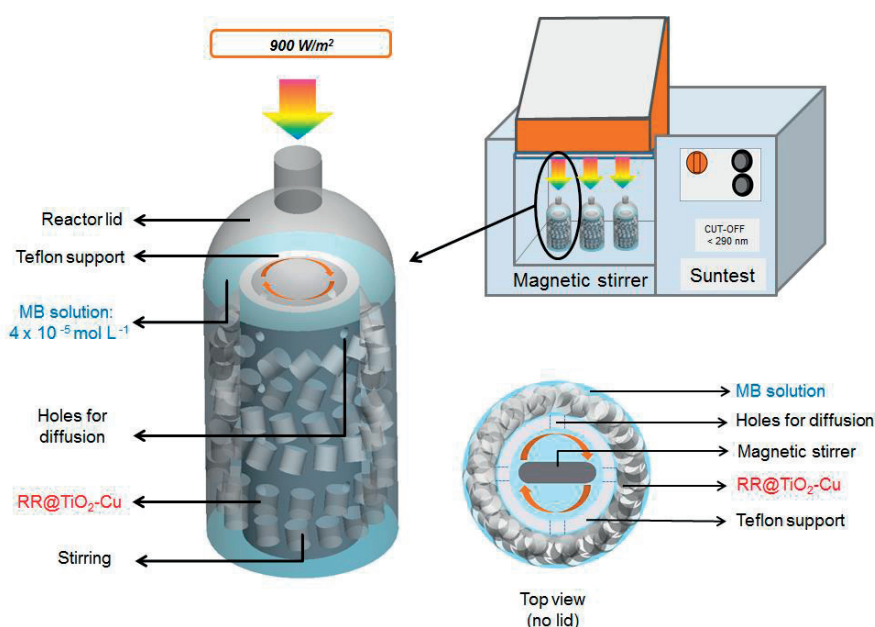


Figure 4.1. Schemes of the reactor and irradiation source. A Teflon support was placed concentrically inside the reactor for holding the $\text{RR@TiO}_2\text{-Cu}$ bed. The reactors contained 70 ml of MB. Before photocatalytic reaction, the MB solution was equilibrated with the $\text{RR@TiO}_2\text{-Cu}$ for 30 min.

The Suntest solar simulator (Heraeus, Hannau, Germany) is shown in Figure 4.1. The reactor's cavity was ~ 30 cm wide, 20 cm long and 20 cm high. The distance between the Xe-lamp and the photo-reactor lid was 10 cm. The photo-reactor was 7 cm high without the lid and 11 cm high with the lid. Before each photocatalytic run the MB-solution (70 ml) was equilibrated in the dark with the $\text{RR-TiO}_2\text{-Cu}$ (35 g) for 30 min.

4.3 Results and discussion

4.3.1 MB discoloration kinetics

Table 4.1 presents the percentage of Cu and TiO₂ on the Raschig-rings obtained by X-ray fluorescence (XRF).

Table 4.1 Weight percentage of TiO₂ and Cu in the RR samples of RR@TiO₂-Cu as determined by X-ray fluorescence (XRF). Additionally, assessed cm³ TiO₂-CuOx / cm² RR based on XRF data and material properties.

Sample	%wt / % wt glass		(cm ³ TiO ₂ -CuOx / cm ² RR)
	TiO ₂	Cu	
RR@TiO ₂	11.3	< 0.001	0.003
RR@TiO ₂ -Cu 0.004 %	11.98	0.004	0.003
RR@TiO ₂ -Cu 0.018 %	22.67	0.018	0.006
RR@TiO ₂ -Cu 0.053%	18.73	0.053	0.005
RR@TiO ₂ - Cu 0.081%	13.04	0.081	0.003

Figure 4.2, traces (1) and (2) show the MB adsorption in the dark on the RR@TiO₂-Cu 0.004% surface and on bare Raschig rings. There is no significant difference between runs (1) and (2) shown in Figure 4.2 due to the low percentages of TiO₂ and Cu on the support (~15% TiO₂ and 0.004% Cu). Figure 4.2, trace (3) shows the low light effect on MB-discoloration in presence of Raschig rings during 240 min. A RR@TiO₂-Cu-0.053% photocatalyst (trace (4)) shows no complete discoloration after 240 min. RR@TiO₂ is presented in trace (5), it displays a higher initial degradation rate compared to the RR@TiO₂-Cu-0.053% photocatalyst (trace (4)). RR@TiO₂-Cu-0.004% (trace (6)) is seen to lead to a faster discoloration compared to RR@TiO₂-Cu-0.053% (trace (4)) despite the lower Cu content (13.5 times less Cu). Also, RR@TiO₂-Cu-0.004% (trace (6)) performs better than RR@TiO₂ (trace (5)) with higher initial degradation rate and being able to reach complete discoloration.

These obtained results suggest that the Cu-sites deposited on the RR@TiO₂ surface may involve to intra-gap sites facilitating the TiO₂ charge transfer to MB under band-gap irradiation. However, at higher concentrations of Cu on the TiO₂ surface the Cu-sites may act as charge recombination centers decreasing the amount of photogenerated charges [60-62, 64, 87, 88]. The position of the potential energy level of the Cu-intra-gap states lies between the TiO₂ vb (3.1eV) and the TiO₂ cb (-0.1eV) and can be estimated to be close to 0.15 eV [140]. The Cu^{1+/2+} on the TiO₂ under

band-gap irradiation would work as an electron acceptor enhancing MB-degradation [141].

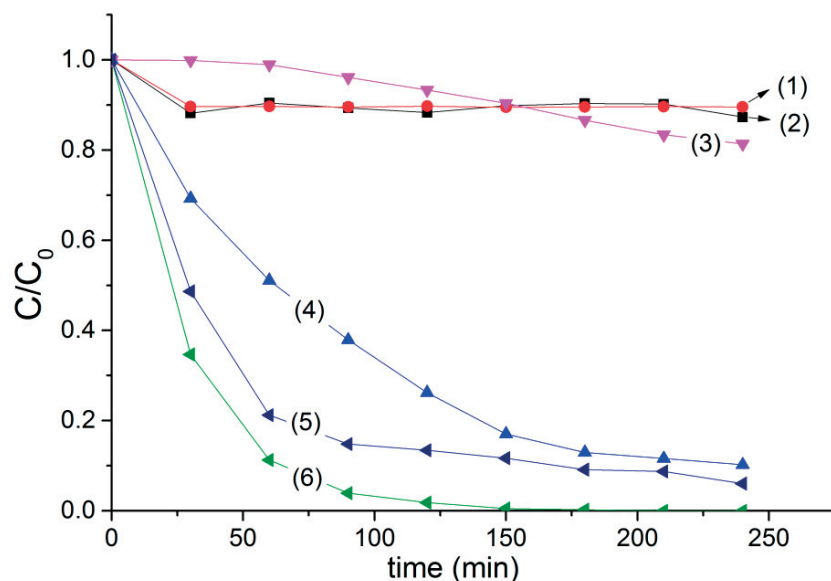


Figure 4.2 MB 4×10^{-5} mol L⁻¹ solution discoloration under Suntest irradiation (90 mW cm⁻²), Traces: (1) MB in contact with RR@TiO₂-Cu 0.004% in the dark, (2) MB in contact with Raschig rings in the dark, (3) MB in contact with Raschig rings under Suntest irradiation (90 mW cm⁻²), (4) MB in contact with RR@TiO₂-Cu-0.053% under Suntest irradiation (90 W cm⁻²), (5) MB in contact with RR@TiO₂ under Suntest irradiation (90 W cm⁻²), (6) MB in contact with RR@TiO₂-Cu-0.004% under Suntest irradiation (90 W cm⁻²). The initial pH of the solution was 5.7-6.0

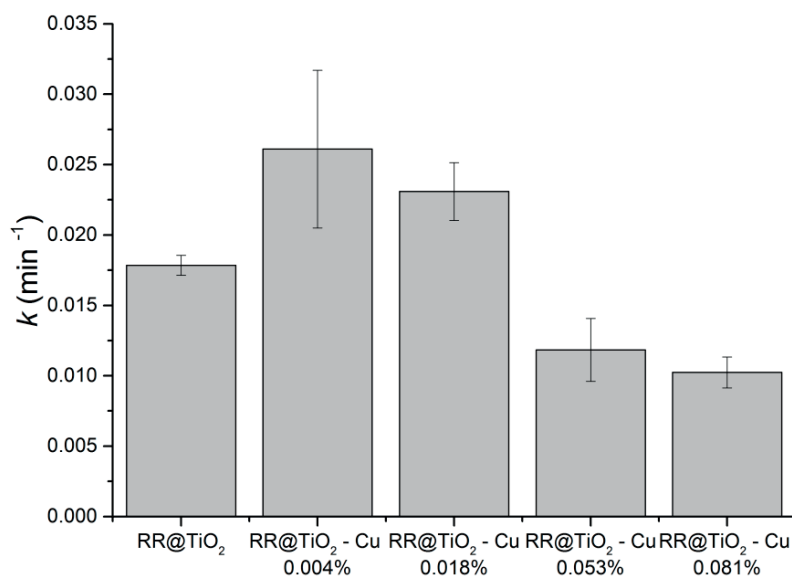


Figure 4.3 Dependence of the pseudo-first order rate constant k on the Cu-content of the RR@TiO₂-Cu photocatalyst during the discoloration of a solution MB 4×10^{-5} mol L⁻¹ under Suntest light set at 90m W cm⁻². The initial pH of the solution was 5.7-6.0

Figure 4.3 shows the pseudo-first order rate constant k of MB-discoloration as a function of the Cu-amount added to RR@TiO₂. Figure 4.3 shows that the k for the MB-discoloration by RR@TiO₂-Cu-0.004% is higher compared to the k by the RR@TiO₂-Cu-0.018% photocatalyst and the other photocatalysts used to discolor MB (see Figure 4.3 caption). This is the evidence for the RR@TiO₂-Cu-0.004% sample acting as a trap for the TiO₂vb (h⁺) increasing the charge separation and concomitantly decreasing the electron-hole recombination in TiO₂. Higher amounts of Cu decorating RR@TiO₂ above Cu 0.004% act as charge recombination sites/centers decreasing the k values during MB-discoloration (see Figure 4.3). The MB-discoloration kinetics as a function of the initial MB-concentration and the initial pH are reported in Supplementary material Ch4-S2 & Ch4-S3.

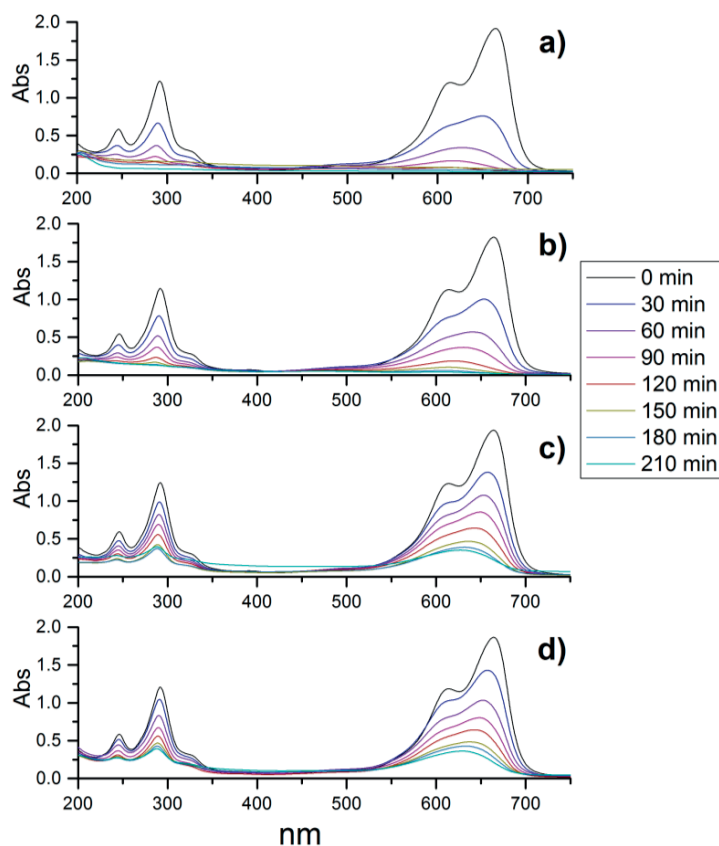


Figure 4.4 Absorption spectra of MB 4×10^{-5} mol L⁻¹ in contact with diverse RR@TiO₂-Cu photocatalysts under Suntest light set at 90 mW cm⁻²: a) RR@TiO₂-Cu-0.004%, b) RR@TiO₂-Cu-0.018%, c) RR@TiO₂-Cu-0.053%, d) RR@TiO₂-Cu-0.081%. The initial pH of the solution was 5.7-6.0

Figure 4.4 presents the changes in the MB-absorbance spectra between 200 and 800 nm for MB solutions 4×10^{-5} mol L⁻¹ in contact with RR@TiO₂ rings decorated with different amounts of Cu under Suntest light. The spectra in Figure 4.4(a-d) show that the MB-peak at 664 nm decreases more slowly as the Cu-content increases, which is consistent with results reported above in Figure 4.3. The MB-bands between 600-700 nm correspond to the conjugated π system comprising MB monomers/dimers [142].

The aromatic ring bands < 300 nm were observed also to disappear after around 120 min reflecting the progressive cleavage of the MB-aromatic ring. The small absorbance < 300 nm is assigned to long-lived organic intermediates left in solution [143]. The existence of long-lived intermediates in solution is further confirmed by the TOC results presented next for MB- degradation in Figure 4.5.

Total organic carbon (TOC) decrease during the photocatalytic degradation of MB $4 \times 10^{-5} \text{ mol L}^{-1}$ mediated by RR@TiO₂-Cu-0.004% under Suntest light (90 mW cm^{-2}) at initial pH values of (1) pH 5.7 and (2) pH 10 is presented in Figure 4.5. For the two pH-values investigated the initial TOC drops by 75%. The mineralization varied only in a narrow range on the Cu amounts added on the RR@TiO₂ rings. This information is available in Supplementary material Ch4-S4.

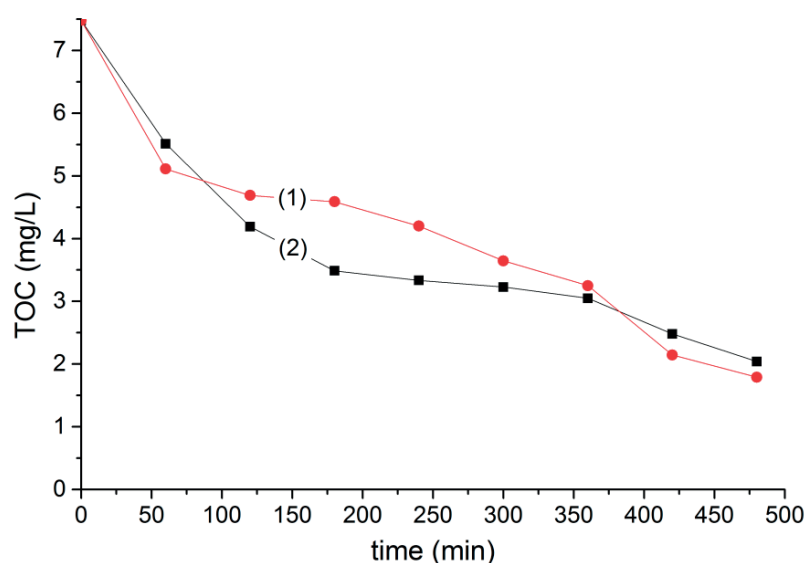


Figure 4.5 Total organic carbon (TOC) decrease during the photocatalytic degradation of MB $4 \times 10^{-5} \text{ mol L}^{-1}$ mediated by RR@TiO₂-Cu-0.004% under Suntest light (90 mW cm^{-2}). Initial pH of the MB solution: (1) pH 5.7 and (2) pH 10

4.3.2 Repetitive MB-discoloration and evidence for the RR@TiO₂-Cu-0.004% stability

Figure 4.6a shows the kinetic constants during the discoloration of MB by RR@TiO₂-Cu-0.004% up to the 5th use cycle. The k values vary only 10% up to the 3rd cycle and became lower in the 5th cycle. The photocatalyst rings were carefully washed and dried after each cycle. Figure 4.6b shows by ICP-MS the Ti-ions leached after each recycling, the values reported in Figure 4.6b were far below the allowed limit set by sanitary regulations for the toxicity on mammalian cells, up to one gram TiO₂/L [144]. Figure 4.6c shows the ICP-MS amounts of the Cu-ions leached during the MB-discoloration into the solution.

The values of 1 ppb of Cu detected after the 5th cycle were far below the limit of 25 ppb set by some sanitary regulations [145]. The low levels found for the release of Ti and Cu indicate that we are in the presence of an oligodynamic effect involving

catalysis by contact with metal and/or oxides and taking place with an almost negligible release of ions [146].

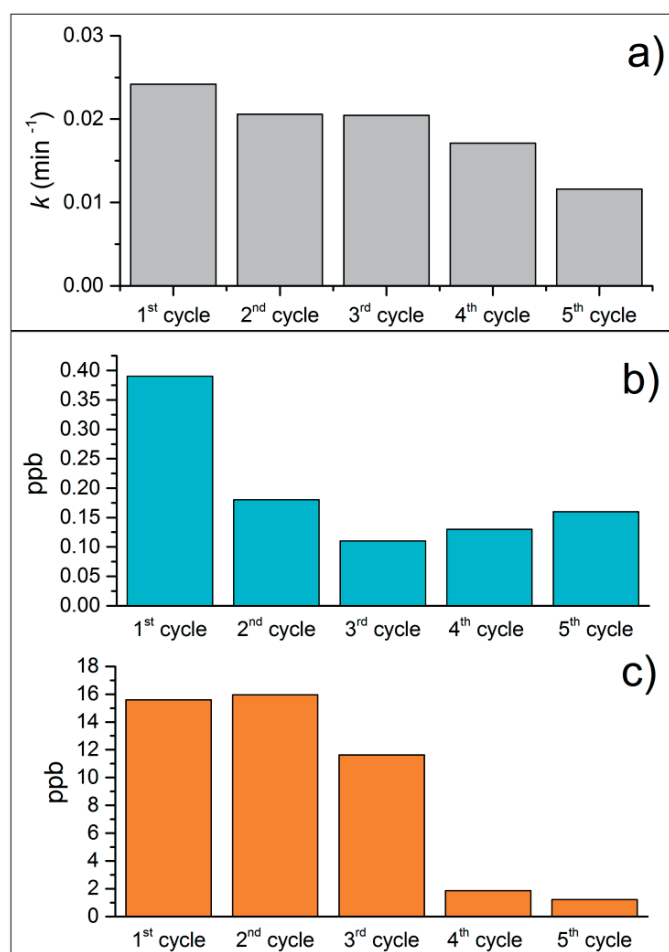


Figure 4.6 a) Rate constants (k) for the repetitive MB 4×10^{-5} mol L⁻¹ discoloration by RR@TiO₂-Cu 0.004% b) Ti-ions released during MB-discoloration up to the 5th use cycle and c) Cu-ions released during MB-discoloration up to the 5th use cycle. Suntest light set at 90 mW cm⁻²

4.3.3 Light intensity effects on the MB-discoloration kinetics and ROS detected during the MB-degradation

Figure 4.7 shows the effect of light intensity on MB discoloration in the presence of RR@TiO₂-Cu. The faster MB-discoloration kinetics was observed under a higher applied light intensity increasing the photogenerated charges in TiO₂ making up > 99.9% of the RR@TiO₂-Cu 0.004%. The run shown in Figure 4.7, trace 4) at 90mW/cm², was carried out in the presence of a cut-off filter 400 nm to block the UV light. Although the UV-light is present in a relation of about 1:20 compared to the photons in the Suntest simulated light cavity emitting light in the visible range (400-800 nm), their high energy is seen to contribute to the MB-discoloration up to ~50%. Only semiconductor materials show an increased amount of photogenerated charges due to a higher applied light intensity. Figure 4.7 shows that TiO₂ and not the Cu

intra-gap absorbers are responsible for the observed MB-discoloration. This suggests that the TiO₂cbe-reacting with the adsorbed O₂ is the main channel leading in later stages to MB-discoloration.

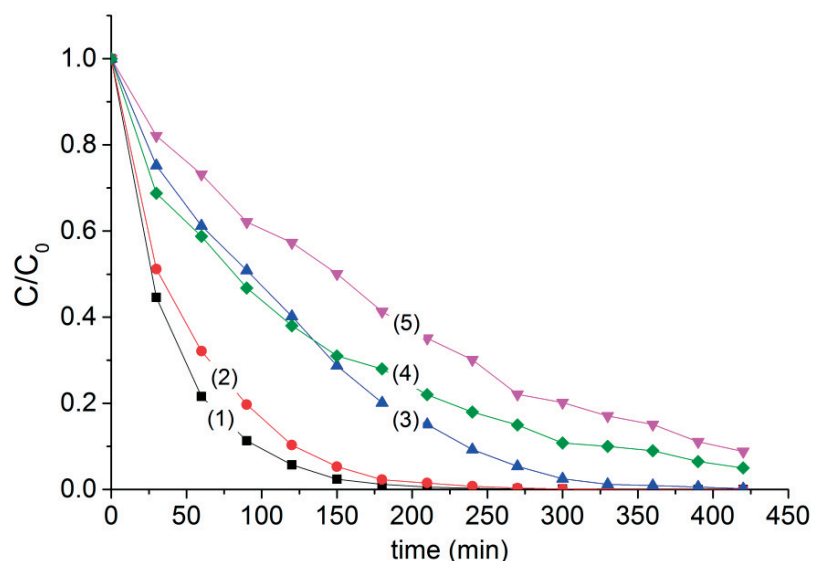


Figure 4.7 Discoloration of MB $4 \times 10^{-5} \text{ mol L}^{-1}$ on RR@TiO₂-Cu-0.004% as a function of the Suntest simulated sunlight intensity: (1) 120 mW cm^{-2} , (2) 90 mW cm^{-2} , (3) 60 mW cm^{-2} , (4) 90 mW cm^{-2} with UV filter at 400 nm and (5) 30 mW/cm^{-2}

Figure 4.8 shows the scavenging of the intermediate radicals generated on the RR@TiO₂-Cu 0.004% surface: a) trace (2) MB-discoloration in the presence of methanol 20 mmol L^{-1} quenching the OH-radicals, b) trace (3) MB-discoloration in the presence of NaN₃ 20 mmol L^{-1} , a scavenger of oxygen singlet ¹O₂ [135, 147], c) trace (4) MB-discoloration in the presence of benzoquinone 20 mmol L^{-1} [60, 87] a quencher of O₂^{•-}/HO₂[•] [136, 137], d) trace (5) MB-discoloration in the presence of 20 mmol L^{-1} ethylenediamine tetra-acetic acid disodium salt (EDTA-2Na), a widely used TiO₂vb(h⁺) scavenger [60-62, 64, 87, 88]. Trace (1) shows MB-discoloration without the addition of scavengers.

Results in Figure 4.8 show that the scavenging follows the series: vb (h⁺) > O₂^{•-}/HO₂[•] > ¹O₂ > [•]OH. The dissolved O₂ (8 mgL^{-1}) is not only a TiO₂ electron scavenger but its presence is necessary to generate the HO₂[•]. At pH > 4.8, more than 50% of the HO₂[•] is present in the form of O₂^{•-}. This form of the HO₂[•] radical predominates, since the initial pH of the MB-solution was ~ 6.0 decreasing during the MB-discoloration to a value of 4.7. The [•]OH-radicals scavenged by methanol in Figure 4.8, trace 2) imply one electron reduction [•]OH/OH⁻ with E₀ 1.90V NHE and show a smaller scavenging effect compared to O₂^{•-}/HO₂[•] with a lower potential of E₀ 0.75V NHE. The lifetime and concentration of the [•]OH-radicals is much lower compared to the less energetic O₂^{•-}/HO₂[•] [138].

Azide NaN₃ has been generally reported as a singlet ¹O₂ scavenger [60, 87]. However, it also reacts with [•]OH-radicals with a similar rate as it does with singlet

$^1\text{O}_2$ [62, 131]. For this reason, the data reported in Figure 4.8 wouldn't indicate in a specific way the effect of the singlet oxygen during MB-discoloration. Another issue to consider is that the $\text{CuO}(\text{cbe}^-)$ could react in two ways: a) directly with O_2 leading to $\text{O}_2^{\cdot-}$ or b) reducing the CuO to Cu^+ , as noted in eqs (4-1) and (4-2) below:



Reaction (4-2) is much faster than the CuO dissolution [140, 141], shown in equation (4-3). The reaction (eq (4-3)) involves $\text{CuO}(\text{Cu}^+)$ and could possibly lead to the reaction of CuO with the holes TiO_2vbh^+ .



EDTA is used generally as a hole scavenger in TiO_2 photocatalysis. But it may not play this role in the case of CuO mediated photocatalysis. We observed that by scavenging TiO_2vbh^+ with EDTA, the MB became colorless. After contacting the MB-solution with fresh air (O_2), the solution became blue again. This suggests that while blocking the TiO_2vbh^+ , MB gets reduced to the leuco form of methylene blue (LMB).

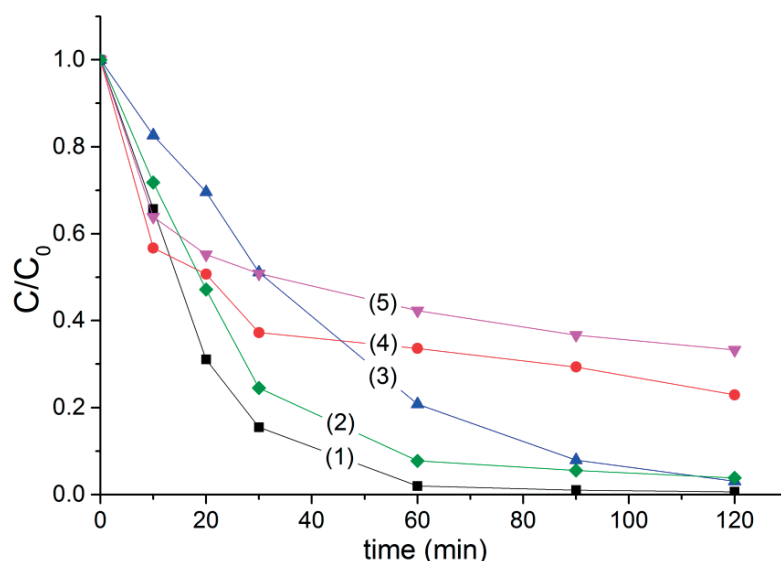
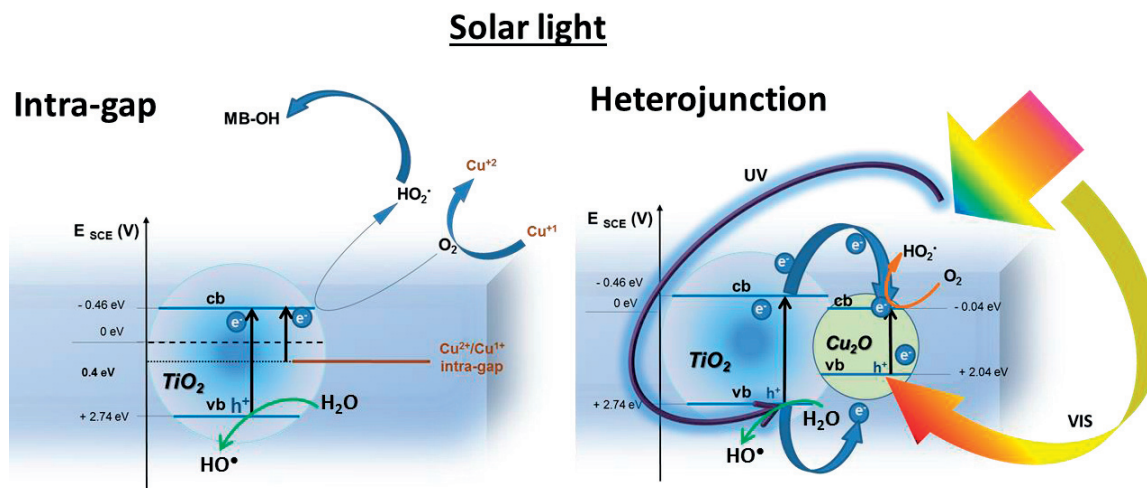


Figure 4.8 Discoloration of a solution MB (4×10^{-5} M) on RR@ TiO_2 -Cu 0.005% showing the intermediates radical-species being identified by appropriate scavengers: (1) run without scavengers, (2) run in the presence of 0.2 mM methanol, (3) run in the presence of 0.2 mM NaN_3 , (4) run in the presence of 0.2 mM p-benzoquinone, (5) run in the presence of 0.2 mM EDTA-2Na

Based on these findings, the design of a reactor with a RR@ TiO_2 -Cu photocatalyst may consider two factors: a) good contact between the photocatalyst and the solution and b) good mixing inside the reactor for oxygen diffusion, which will improve the oxygenated radicals' formation.

4.3.4 Suggested reaction mechanism, involvement of Cu intra-gap states

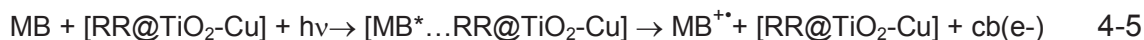
Metals/oxides have been shown to increase the charge separation on semiconductors [60, 64, 140] leading to new interfaces. The discoloration mechanism is suggested to proceed initially by the photogenerated TiO_2 electrons transferred to the TiO_2cb by the Cu intra-gap states in the TiO_2 or by means of heterojunctions as suggested in Scheme 4.1



Scheme 4.1 Suggested scheme for RR@ TiO_2 -Cu intra-gap mediated electron transition under sunlight irradiation leading to MB-discoloration/degradation



The direct photosensitization of MB in the presence of RR@ TiO_2 -Cu under Suntest simulated sunlight shown in Scheme 4.1 may be suggested as:



Under sunlight irradiation, both the MB and TiO_2 are photosensitized, MB injects electrons into the TiO_2cb and in parallel converts MB to the $\text{MB}^{+\bullet}$ cation radical. The electron injected by the MB into the TiO_2 reacts with O_2 and generates highly oxidative radicals leading to the discoloration/degradation of MB as shown in Scheme 4.1 [141]. The low laying Cu intra-gap states promote the indirect transition of the electron from TiO_2 vb (h^+) to the TiO_2cb . This is consistent with the results reported in Figure 4.2 for RR@ TiO_2 -Cu 0.004% photocatalyst. The $\text{Cu}^{1+/2+}$ intra-gap states also interact with the RR@ TiO_2 -Cu 0.004% adsorbed O_2 . In this way, the recombination rate of the TiO_2 e-/h+ pairs is hindered improving the photocatalyst MB-degradation.

The addition of Cu > 0.004% makes the Cu-act as a recombination center because the thickness of the space layers decreases with increasing Cu-content [140]. The Cu^{1+} would also reduce the air (O_2) consuming electrons or re-oxidize to Cu-ions by the photogenerated TiO_2 holes to Cu^{2+} [132, 141, 148].

The $\text{Cu}^{1+/2+}$ and Ti^{3+} intermediate donor levels may be present due to the back charge transfer reaction: $e^- + \text{Ti}^{4+} \rightarrow \text{Ti}^{3+}$ following the reaction shown above in eq.(4-4) [149]. The $\text{vb}(h^+)$ reacts with the TiO_2 O-vacancies formed concomitant to the Ti^{3+} through the channel: $h^+ + \text{O}^{2-} \rightarrow \text{O}^-$ leading subsequently to the re-population of Cu^{1+} in the $\text{Cu}^{1+/2+}$ intra-gap states. Sputtered Cu-polystyrene was reported to present initially Cu^{1+} states followed in later reaction stages by Cu^{2+} [141]. Cu intra-gap states in a TiO_2/Cu sputtered catalyst surface were reported to lead to more $\bullet\text{OH}$ -radicals, due to additional $\text{vb}(h^+)$ [141]. As long as the $\text{RR@TiO}_2\text{-Cu}$ 0.004% in Scheme 4.1 is photoactivated by light, it will continuously produce cbe^- reacting with O_2 leading to the formation of oxidative intermediate radicals.

4.3.5 Surface properties of $\text{RR@TiO}_2\text{-Cu}$

4.3.5.1 Diffuse Reflectance Spectroscopy (DRS)

Figure 4.9 shows the DRS spectra of the samples in Kubelka-Munk units. Cu is seen to move the RR@TiO_2 absorption drastically into the visible region. Similar optical modifications were found by Kapilashrami et al [150] when doping TiO_2 with non-metals. Trace (1) shows the DRS spectrum of TiO_2 Degussa P-25 on glass. The Cu^{2+} ionic-radii are larger than the one of Ti^{4+} , and therefore it would be difficult for the Cu^{2+} to replace Ti^{4+} in the crystal lattice [149, 151]. The Cu-species may decorate the surface of the TiO_2 matrix. If Cu cations would be incorporated in the TiO_2 lattice by substituting Ti^{4+} , the electro-neutrality demand would require the additional formation of O-vacancies. Peaks between 320 and 440 nm in Figure 4.9, traces 2, 3 have been attributed to $(\text{Cu-O-Cu})^{2+}$ clusters in highly dispersed states. The peaks between 400–500 nm (Figure 4.9, traces 4, 5) were assigned to three dimensional Cu^{1+} clusters in CuO [152, 153].

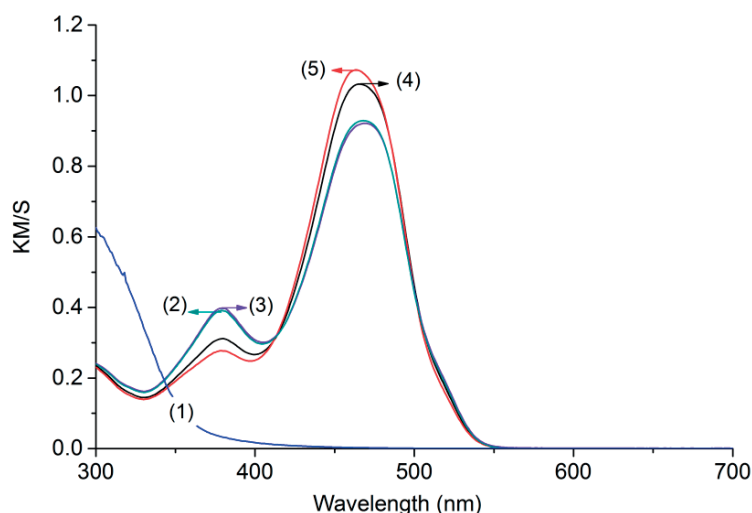


Figure 4.9 DRS spectra for different Cu weight percentages in RR@TiO_2 . (1) RR@TiO_2 , (2) $\text{RR@TiO}_2\text{-Cu}$ 0.004%, (3) $\text{RR@TiO}_2\text{-Cu}$ 0.018%, (4) $\text{RR@TiO}_2\text{-Cu}$ 0.053% and (5) $\text{RR@TiO}_2\text{-Cu}$ 0.081%

4.3.5.2 X-ray Diffraction (XRD)

The XRD-spectrograms in Figure 4.10 are shown for RR@TiO₂-Cu 0.018% in trace (1) and for RR@TiO₂-Cu 0.053% in trace (2). The presence of TiO₂ Degussa P-25 is confirmed by the peaks at 25° and 27.5° for anatase and rutile respectively, as reported by Hanaor et al [154]. The size of the anatase crystals was assessed based on the (101) reflection in the spectra (1) and (2) and the calculations lead to particle size of ~20nm in both cases. The calculations were made by means of the Debye-Scherrer equation, noted in eq. (4-6).

$$D = \frac{\kappa\lambda}{\beta\cos\theta}$$

4-6

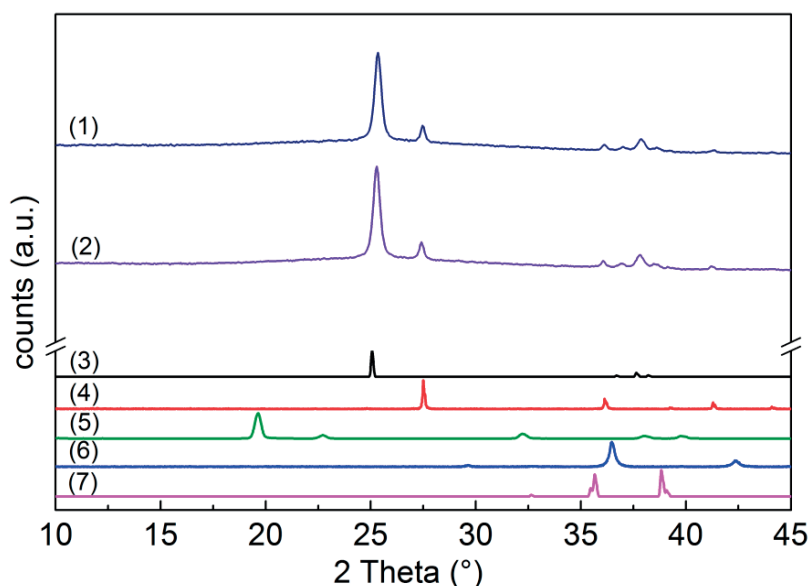


Figure 4.10 XRD for different Cu weight percentages in RR@TiO₂ and references of TiO₂, Cu and Cu oxides. (1) RR@TiO₂ - Cu 0.018%, (2) RR@TiO₂ - Cu 0.053 %. Reference XRD: (3) Anatase (R100013), (4) Rutile (R040049), (5) Copper (R061078), (6) Cu₂O (R050384), (7) CuO (R120076) [155]

For eq. (4-6), D stands for the crystal size in nm, κ = as the shape factor which is usually fixed as 0.89, λ = as the wavelength which is taken as 0.154 nm, β = which is the full width at half maximum for the prominent peak, and θ = as the Bragg's diffraction angle in radians [156, 157]. The characteristic peaks of Cu and Cu oxides between 35° and 40° in Figure 4.10, traces (1) and (2) appear as overlapping peaks of anatase (trace (3)), Cu (trace (5)), Cu₂O (trace (6)) and CuO (trace (7)). Cu-oxides peaks were found by XRD for higher Cu doping percentages (> 5%) by Bensouici et al., [84]. The Cu and Cu-oxide peaks in Figure 4.10 are referenced to the RRUFF database [155]; they appear between 35° and 40° for Cu, Cu₂O and CuO. In the course of this study, we could not sort out the different Cu-oxide species due to the extremely low amounts of Cu deposited on the catalyst surface.

4.3.5.3 Atomic Force Microscopy (AFM) and Roughness (Rg)

Figure 4.11 shows AFM-topography images of RR@TiO₂-Cu 0.018% (a) and RR@TiO₂-Cu 0.081% (b) for two scanning areas of 2x2μM. The topography of RR@TiO₂-Cu 0.004% sample is not presented because the low amount of Cu could not be detected; only TiO₂ aggregates presented adequate signals. Figure 4.11a) shows TiO₂ and Cu-agglomerates of ~200 nm ~20 nm in size respectively. The RR@TiO₂-Cu 0.018% samples presents a roughness (Rg) ≅ 11.8 nm. In this case, the topography of the AFM *contour* in Figure 4.11a) shows peaks relatively closely packed to each other providing the contact points with MB [158]. Figure 4.11b) illustrates the TiO₂-Cu 0.081% sample. TiO₂ and Cu agglomerates of ~200 nm and ~20 nm in size respectively were observed. The RR@TiO₂-Cu 0.081% sample presents roughness (Rg) ≅ 23.9 nm. The topography of the AFM *contour* in Figure 4.11b) shows deeper and wider valleys to accommodate the MB dye providing less surface contact between the photocatalyst and MB.

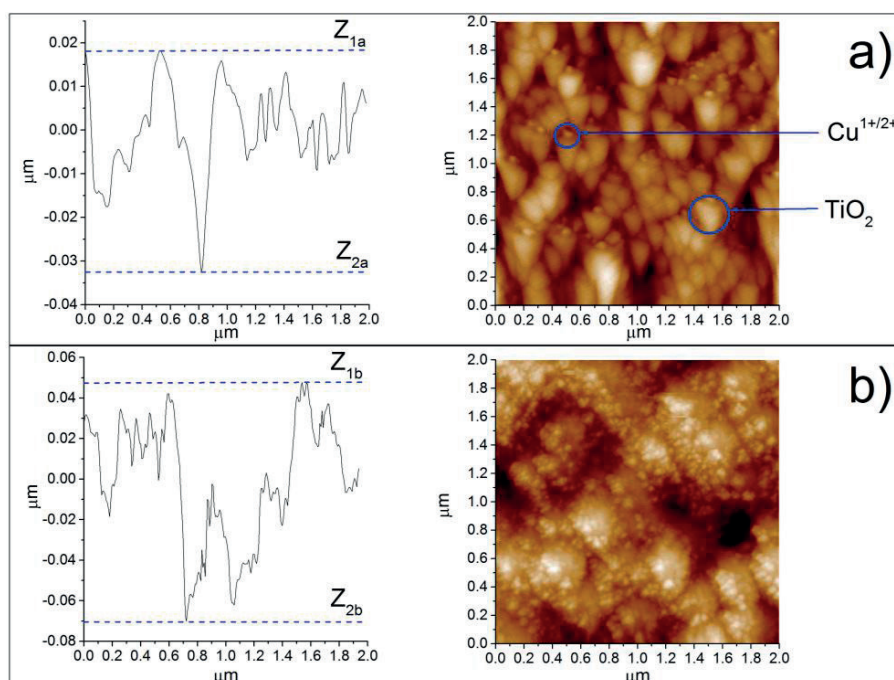


Figure 4.11 (a) AFM- topography of RR@TiO₂-Cu 0.018% taken at a resolution of (2 × 2 μM), (b) AFM-topography of RR@TiO₂-Cu 0.081% taken at a resolution of (2 × 2 μM)

4.3.5.4 X-ray Photoelectron Spectroscopy (XPS)

Figure 4.12 and Table 4.2 show the peak variation and the surface percentage atomic concentration of the elements present in the RR@TiO₂-Cu 0.004% during discoloration/degradation of the MB diluted solution. The XPS signal at time zero was taken after the sample was contacted with the MB solution for 30 min in the dark. Figure 4.12a) shows the Ti2p doublet shift from 456.98 eV to 457.15 eV. This provides the evidence for a redox reaction occurring during the MB-degradation involving Ti³⁺/Ti⁴⁺. The appearance of Ti³⁺ species is associated to the peak initial peak shift of Ti⁴⁺ >0.2 eV [62]. Redox behavior was also observed for Cu2p_{3/2} and O1s since peak

shifts from 930.68 eV to 931.08 eV and from 528.19 to 528.39 were observed for both elements respectively as shown in Figure 4.12b) and Figure 4.12c) [129, 130]. Figure 4.12d) shows the XPS C1s at time zero. It displays the contribution of several carbon bonds like C-C, C=C, COH, C=O, C-H etc., found in the MB such as C-C (sp^2), C-C (sp^3), C-N-R2 [159]. The XPS carbon peaks after 120 minutes irradiation (trace (2) in Figure 4.12d)) were less intense, meaning a decrease in atomic carbon, consistent with the values for C1s reported in Table 4.2, due to changes in the C-C (sp^2) and C-C (sp^3) during the MB degradation.

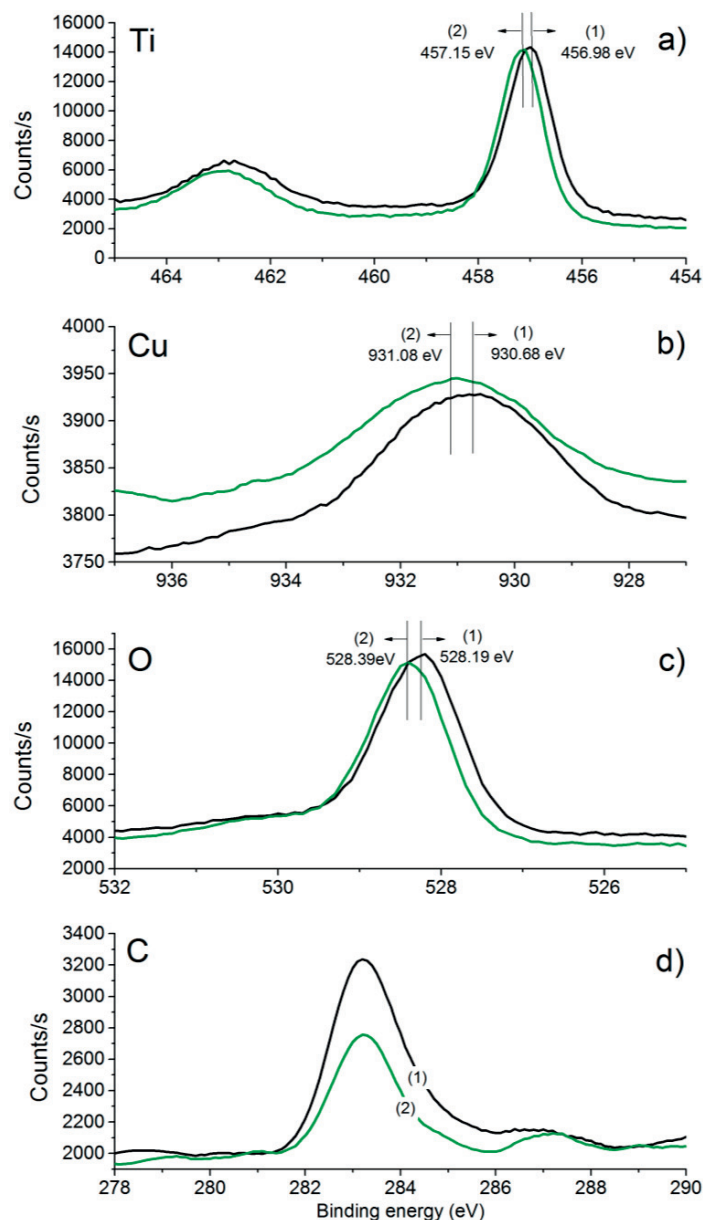


Figure 4.12 XPS signals of Ti a), Cu b), O c) and C d) at time zero (1) and after discoloration of a MB 4×10^{-5} (mol L^{-1}) solution on RR@TiO₂ – Cu 0.004 % (2). Suntest irradiation set at 90 mW cm^{-2}

In Table 4.2 the percentage of C1s is seen to decrease within 120 min due to MB discoloration, but a strong residual C1s is noticed after 120 min. This observation is consistent with the TOC-results reported in Figure 4.5. No N-species adsorbed on the photocatalyst surface were detected by XPS as shown in Table 4.2 by the low atomic percentages found for N. The small amounts of S- remained constant in experimental error during the MB-degradation. A complicated pattern is noticed for the percentage variation of O1s signals as a function of time reported in Table 4.2. This may be due to the complicated nature of the O-containing intermediate radicals generated during the MB-degradation. The percentage of Cu could not be reported in the last column of Table 4.2 due to the low amounts of Cu in the RR@TiO₂-Cu 0.004% sample.

Table 4.2. Atomic percentage concentration of the elements of the sample RR@TiO₂-Cu-0.004%, during the degradation of MB: 4x10⁻⁵ mol L⁻¹

Irradiation time (min)	C1s	N1s	O1s	S2p	Ti2p	Cu2p3
0	18.04	3.54	62.48	0.18	24.06	0
30	16.72	1.40	76.03	0.58	20.23	0
60	13.51	0.44	70.22	0.52	22.30	0
120	13.11	0.40	60.42	0.37	23.72	0

4.4 Conclusions

Cu-decoration seems to induce an intra-gap-electronic state in the TiO₂ facilitating the indirect electron transition in the TiO₂ band-gap and leading to an accelerated MB-degradation kinetics. The results obtained during MB discoloration showed that a Cu- addition of 0.004% on RR@TiO₂ led to the highest photocatalytic activity. The addition of Cu on RR@TiO₂ shifts strongly the photocatalyst absorbance into the visible region. The Cu intra-gap states in RR@TiO₂-Cu could not be characterized due to the low amounts of Cu present in the photocatalyst. Cu-levels above 0.004% on the TiO₂ surface seem to act as recombination centers for the photogenerated charges decreasing the rate of MB-degradation. Regardless the addition of Cu to the TiO₂ (TiO₂vb (h+)) was found to be the most important intermediate species leading to MB-degradation. The XPS-shifts during the photocatalytic degradation of MB provided the evidence for redox events between CuOx/TiO₂ and the MB. The AFM results indicate that low Cu-loadings on the RR@TiO₂ rings display a close packed *contour* compared to the wide-spaced *contour* obtained with higher Cu-loadings. A close packed *contour* in the low Cu-loading provides more contact points with MB leading to faster degradation. Using a support as glass Raschig rings brought solutions to some limitations encountered by the photocatalytic films: a) diffusion limitations were reduced because the bulk of solution was less, b) the contact area between photocatalyst and MB molecules was increased by the use of a higher

specific surface area support, c) the calcination procedure was possible due to the thermal resistance of the support allowing crystallization of the added Cu.

5. Chapter 5: New evidence for disinfection, self-cleaning and pollutant degradation mediated by GF-TiO₂-Cu mats under solar/visible light in mild oxidative conditions

Published work:

Laura Suárez, Stefanos Giannakis, Cesar Pulgarin, Michael Bensimon, John Kiwi. “New evidence for disinfection, self-cleaning and pollutant degradation mediated by GF-TiO₂-Cu mats under solar/visible light in mild oxidative conditions” *Photochemistry and Photobiology A: Chemistry* 346 (2017): 351-363

Web link:

<http://www.sciencedirect.com/science/article/pii/S1010603017306147>

Reproduced with permission of Elsevier, Copyright 2017 (license number 501281572)

Supplementary material:

Annex B

Doctoral Candidate's contribution:

Investigator and co-author

5.1 Introduction

Photocatalysis using solar/visible light for disinfection has been promoted during the last five years [87, 132, 160-164]. Similarly photocatalysts supported on glass or on polymer films for pollutants degradation in solution have been reported to save energy, time, and chemicals in comparison to pollutant degradation via suspensions [62, 165-167]. Adding anions and cations to TiO₂ aims to broaden its light absorption from UV to solar/visible light [168, 169]. Methylene blue (MB) has been used as a model standard to test the degradation of non-biodegradable dyes under light irradiation as well as *E. coli* for assessing bacterial inactivation [51, 61, 63, 64, 131, 170-172]. The effect that TiO₂-Cu has on MB discoloration and bacteria inactivation has been reported [97, 98]. Pham T. T, Carvalho and their collaborators followed MB degradation on TiO₂-Cu films supported on flat glass [85, 173]. In the line of solid-liquid interfaces, Suárez and collaborators reported the degradation of MB in solution by means of RR@TiO₂-Cu which stands for TiO₂-Cu supported on 3D Raschig rings forming a photocatalytic bed simulating a batch packed reactor [174]. Following a solid-air approach, Pham T. D and collaborators reported the improved performance of Cu doped TiO₂/GF and Ag doped TiO₂/GF in bacterial inactivation in air-solid when comparing to TiO₂/GF. The experiments consisted on an *E.coli* bioaerosol passing through an illuminated chamber containing the Cu or Ag doped TiO₂/GF [101, 102]. This work is the continuation of the previous study using Raschig rings as support for Cu-TiO₂. Supplementary materials Ch5-S1 and Ch5-S2 present an estimation of the specific surface area SSA for Raschig rings of ~0.001 m²/g and for GF-mats of ~4.61 m²/g, based on the Denier approach by Vaughn et al [175].

This chapter focuses on the evaluation of GF-TiO₂-Cu-mats effect at the solid-air interface (self-cleaning) and solid-liquid interface (water disinfection/pollutant abatement in solution). Photocatalysts' supports as Glass fiber mats offer higher specific area than flat 2D geometries providing a suitable solution for avoiding its photocatalyst suspension while keeping a good contact with the bacteria or pollutant in solution. Mechanisms for the reactions with the pollutant and bacteria are suggested based on the experimental data and literature. The characterization of the photocatalyst surfaces is reported by surface science methods.

5.2 Experimental section

5.2.1 Photocatalyst preparation and materials

The GF-mats used as support for TiO₂ and Cu were low density Techmat® A 04008, BGF E Glass 1/8" from Porcher Industrial Co, 3802 Robert Porcher Way, Greensboro, NC 27410, USA. These mats are used as low-cost stable thermal insulators. The physical characteristics of this material are reported in Table 5.1. These glass mats consist of SiO₂, CaO, Al₂O₃ and lesser amounts of Na₂O, K₂O, MgO, Fe₂O₃, and P₂O₅. The GF-mats were cleaned from organic impurities to increase the reproducibility during the preparation of TiO₂ and Cu grafted mats. The GF-mats were immersed in HCl 25% solution at 60°C for 30 minutes followed by washing thoroughly with Milli-Q water and drying overnight at 90°C. The loading of

TiO₂ involved the GF mats being dipped in a Degussa P-25 ethanol-suspension (5g/L). Subsequently, the selected Cu-loading was added by the dipping of the GF-TiO₂ mats in a CuNO₃ x 3H₂O solution (Across Organics). The resulting GF-TiO₂-Cu mats were drained and dried again overnight at room temperature followed by calcination at 500°C for 2h.

Table 5.1. Physical properties of the non-woven glass fiber mat (GF) used as support for TiO₂-Cu

Style	Density (lb/ft ³)	Width (in)	Area per roll (ft ²)	Weight (oz/ft ²)	Thickness (in)	Roll length (linear ft)	Roll mass (net lb)	Filament Diameter (μm)
A04008	6	46	1150	1	0.125	300	72	9

The RF-plasma cavity from Harrick and Co, UK (100W, 13.56 MHz) was used for generating O₂ plasma at 1.5 mbar to introduce negative sites on the mats surfaces aiming to improve the binding between the RF-pretreated GF-mat and the slightly positively charged TiO₂.

The methylene blue (3, 7-bis (Dimethylamino) phenazathionium chloride)) which was used as model organic pollutant, was a Sigma-Aldrich reagent (MB). The reactive oxygen species (ROS) scavengers used were Fluka AG and they were: NaN₃ (oxygen singlet scavenger (¹O₂)), 1, 4-benzoquinone (O₂⁻ scavenger), methanol (·OH -scavenger) and ethylene-diamine tetra-acetic acid disodium salt (EDTA-2Na) which is usually employed to scavenge the TiO₂_{vb}holes [60].

5.2.2 Reactors and irradiation source

Reactors for water disinfection and pollutant degradation in solution are shown in Figure 5.1a and Figure 5.1b respectively. During the photocatalysis 2 x 2 cm mats were placed inside a 25 ml glass reactor and held on a stainless steel mesh. The solutions were stirred within the reaction period. Bacteria inactivation and pollutant degradation were monitored after an initial 30 min equilibration period. Reactors for self-cleaning consisted on 2 x 2 cm GF-TiO₂-Cu mats impregnated with 1 ml MB 4x10⁻⁵ M and placed inside small open petri dishes. Images of the mats before and after impregnation are shown in Figure 5.1c and Figure 5.1d respectively.

The Suntest simulator was provided with cut-off filters for the light < 290 nm and above 800 nm allowing for a light dose of 90 mW cm⁻². An additional filter was used to cut-off the visible light < 400nm for runs in the visible region with the consequent light reduction dose to ~70 mW cm⁻². The set-up for water disinfection and pollutant (MB) degradation in solution is shown in Figure 5.2. The Suntest lamp emission spectrum is shown In the Supplementary Figure Ch5-S3.

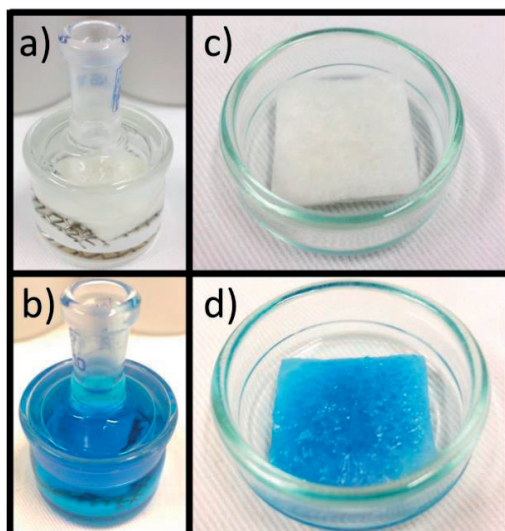


Figure 5.1. a) Reactor used for water disinfection (bacterial inactivation) experiments containing 20 ml of bacterial solution $\sim 10^6$ CFU/ml showing the GF-TiO₂-Cu mats supported on the stainless steel-mesh, b) same reactor as in a) filled with a solution of MB 4×10^{-5} M for pollutant degradation in solution, c) GF-TiO₂-Cu mat placed in a Petri-dish (approach for self-cleaning experiments), d) GF-TiO₂-Cu mat impregnated with 1 ml MB 4×10^{-5} M for self-cleaning runs (time zero: 30 minutes in contact with the MB in the dark)

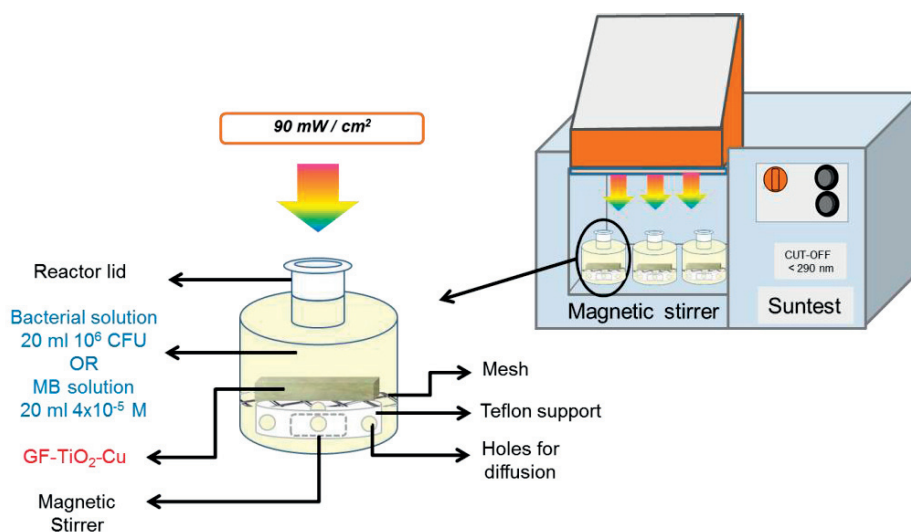


Figure 5.2. Set-up used for water disinfection and pollutant (MB) degradation in solution by means of GF-TiO₂-Cu mats. The suntest provided simulated solar and visible light irradiation

5.2.3 Monitoring water disinfection (*E. coli* inactivation)

The GF-mats were sterilized before use by autoclaving. Details of the bacterial culture have been recently reported by our laboratory [176]. The bacterial solution for water disinfection experiments had a bacterial concentration of $\sim 10^6$ CFU ml⁻¹ and contained NaCl/KCl (8 g/l NaCl and 0.8 g/l KCl). This solution was poured into the sterilized reactor (Figure 5.1a) and left 30 minutes in the dark for equilibration. At

preselected times samples of 100 μ l were transferred into a sterile 2 ml Eppendorf tube containing 900 μ l of autoclaved NaCl/KCl saline solution and homogenized by means of a Vortex for 3 min. Dilutions were made and their aliquots spread on a nutrient agar plate. The plates were placed in an oven at 37°C for 24 h during the colony growth. Subsequently, bacterial counting was carried out by the plate method. Bacterial inactivation experiments were run in duplicate and the mean values are reported.

5.2.4 Monitoring GF-TiO₂-Cu self-cleaning

The self-cleaning performance of the GF-TiO₂-Cu mats was followed during MB stain discoloration. As stated before, the 2 x 2 cm GF-TiO₂-Cu mats were impregnated with 1 ml MB 4x10⁻⁵ M and placed in open small petri dishes, equilibrated in the dark for 30 minutes and then submitted to irradiation. At pre-established times; the mats were removed from irradiation and returned to dark, the MB stain discoloration was evaluated visually. Some on the samples were concomitantly later investigated by X-ray photoelectron spectroscopy (XPS).

5.3 Results and Discussion

5.3.1 Composition of the GF-TiO₂-Cu photocatalysts

The composition of the prepared photocatalysts is presented in Table 5.2 and was evaluated by X-ray Fluorescence method as explained in the materials and methods section.

Table 5.2. Composition of the prepared GF-TiO₂-Cu mats in weight percentage as determined by X-ray fluorescence (XRF). Additionally, assessed cm³ TiO₂-CuOx / cm² GF based on XRF data and material properties.

	GF-TiO ₂	GF-TiO ₂ - Cu 0.05%	GF-TiO ₂ - Cu 0.2%	GF-TiO ₂ - Cu 1%	GF-TiO ₂ - Cu 3%
Na ₂ O	0.4615	0.391	0.3915	0.3615	0.404
MgO	0.5395	0.5195	0.54	0.4155	0.501
Al ₂ O ₃	9.1415	8.514	9.4165	7.39	8.9035
SiO ₂	50.126	50.0675	50.7735	44.4445	48.822
P ₂ O ₅	0.0385	0.031	0.035	0.03	0.034
S	0.027	0.0195	0.0215	0.0545	0.025
K ₂ O	0.127	0.1185	0.1255	0.0935	0.125
CaO	27.441	26.1835	27.8455	20.2765	24.2775
TiO ₂	10.9085	13.103	9.5635	25.8405	15.3605
Fe ₂ O ₃	0.964	0.858	1.022	0.7585	0.93
Cu	< 0.03	0.03	0.038	0.1765	0.4545
(cm ³ TiO ₂ -CuOx / cm ² GF)	3.49E-08	4.19E-08	3.06E-08	8.27E-08	4.97E-08

5.3.2 Water disinfection mediated by GF-TiO₂ and GF-TiO₂-Cu mats under solar simulated light, visible light and in the dark

Figure 5.3a shows the bacterial inactivation of *E. coli* in the reactor shown in Figure 5.1a mediated by the GF-TiO₂-Cu mats irradiated under the full solar emission of the Suntest simulator. Trace 1 shows that GF-TiO₂ mats under sunlight led to a bacterial inactivation of $\sim 3\log_{10}$ within 120 min. Irradiation of supported TiO₂ leads to the generation of several pathways leading to bacterial inactivation. In principle, the generation of ROS which leads to lipid and protein oxidation of the bacterial membrane [177]. Furthermore, excitation of electrons by light and the presence of oxygen as electron acceptor leads to the generation of superoxide radical anions (in the working pH, the HO₂[•] radical is stable and at pH < 4.8 it is present in the form of O₂^{•-}). A mechanism is suggested in equations (5-1 - 5-6).

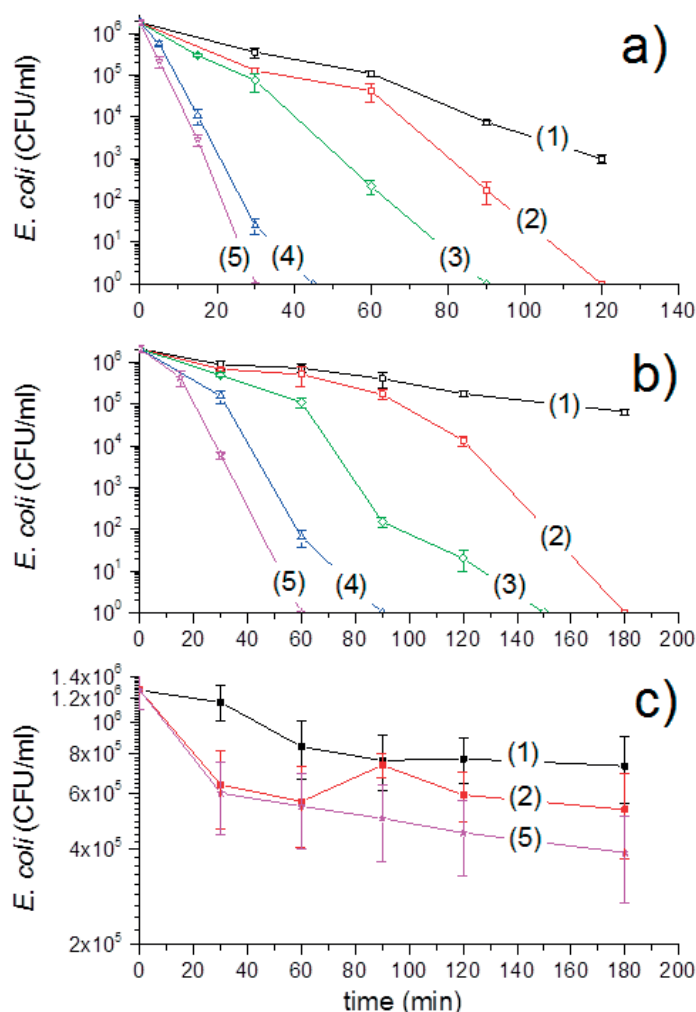


Figure 5.3. *E. coli* inactivation (water disinfection) for an initial bacterial solution ($\sim 10^6$ CFU/ml) by means of GF-TiO₂-Cu mats under: (a) solar light irradiation (90 mW cm^{-2}), (b) visible light irradiation (filter cut-off at 400 nm / 70 mW cm^{-2}) and (c) in the dark. (1) GF-TiO₂, (2) GF-TiO₂-Cu 0.05%, (3) GF-TiO₂-Cu 0.2%, (4) GF-TiO₂-Cu 1%, (5) GF-TiO₂-Cu 3%.

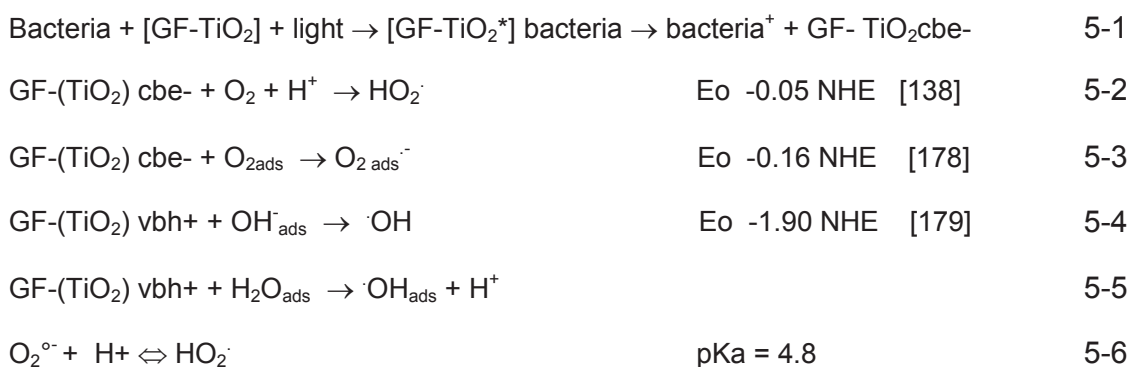


Table 5.3. Ti and Cu ions concentration detected by ICP-MS in the bulk of the reactor after water disinfection under Suntest irradiation (90 mW/cm²), visible light irradiation (cut-off at 400nm / 70 mW/cm²) and in the dark

	Different TiO ₂ -Cu supported on GF	Ti (ppb)	Cu (ppb)
Irradiation with Suntest light (90 mW/cm ²)	GF-TiO ₂	13.63	
	GF-TiO ₂ -Cu 0.05%	15.93	9.9
	GF-TiO ₂ -Cu 0.2%	16.49	36.2
	GF-TiO ₂ -Cu 1%	14.08	29.5
	GF-TiO ₂ -Cu 3%	15.82	74.7
Irradiation with visible light (Suntest light with cut-off at 400nm / 70 mW/cm ²)	GF-TiO ₂	20.97	
	GF-TiO ₂ -Cu 0.05%	21.72	12.9
	GF-TiO ₂ -Cu 0.2%	19.22	37.7
	GF-TiO ₂ -Cu 1%	16.23	32.3
	GF-TiO ₂ -Cu 3%	14.56	59.4
Experiments in the dark	GF-TiO ₂	0.62	
	GF-TiO ₂ -Cu 0.05%	1.15	1.92
	GF-TiO ₂ -Cu 3%	1.25	45.9

In Figure 5.3a, traces 2 - 5 describe the photocatalytic inactivation of bacteria in presence of Cu in the GF- TiO₂-mats. More specifically, GF-TiO₂-Cu 3% mats lead to a fast bacterial inactivation within ~30 min. The bacterial inactivation becomes slower as the Cu-percentage on the GF-mats decrease. This can be observed in Figure 5.3a, trace 2 in which GF-TiO₂-Cu 0.05% leads to a bacterial inactivation within 120 min. The slow bacterial inactivation time reported in Figure 5.3a, trace 1, when no Cu was added to the GF-mats, validates the important role of Cu in the mats.

Amounts of Cu of 9.9 ppb and 74.7 ppb were eluted during the bacterial inactivation period by the GF-TiO₂-Cu 0.05% mats and the GF-TiO₂-Cu 3% mats respectively as determined by ICP-MS (see Table 5.3). Thus, the role of copper in bacterial inactivation is dual, as the detected copper is found both in the bulk and on the GF-TiO₂-Cu mat surface. Inactivation of bacteria by contact with the mats may proceed through an oligodynamic effect due to the very low ppb amounts of Cu involved. [144, 146]. This includes: a) Cu-binding of S, N and COO⁻ and other electron donor groups of the bacteria cell wall and b) Cu in ppb amounts permeating the cell membrane reaching the cytoplasm and leading to bacterial inactivation [104]. Also, copper has been reported to undergo photo-reduction in the UV/vis region, when bound with organic ligands [180]. This process may enhance bacterial inactivation due to a ligand-to-metal charge transfer event, with the bacterial surface acting as a sacrificial electron donor, eventually leading to extensive cell damages.

Additionally, release of copper in the bulk in presence of oxygen has been related to the generation of superoxide radical anion, the formation of H₂O₂ and consecutively the participation of Fenton-like reactions driven by copper [181, 182]. At near-neutral pH, the presence of the hexa-aquo complex, with predominant Cu-species has been linked with the Fenton-like process, resulting in the formation of •OH-radical [183]. A mechanism for the inactivation of bacteria with the participation of copper is suggested below in equations (5-7 - 5-12):



In equation (5-12) L stands for the ligand binding copper on the bacterial cell wall.

Figure 5.3b describes the bacterial inactivation when a UV filter was used, screening light < 400 nm. First and foremost, the bacterial inactivation by TiO₂ alone is dramatically reduced. As the main indirect transition of TiO₂ takes place at 366 nm, filtering wavelengths < 400 nm makes the system rely on the visible light activity of

the supported TiO₂ of the mats, blocking the main electronic transition. However, the addition of Cu in the GF-TiO₂-Cu mats displaces the TiO₂ light absorption into the visible. For instance, the bacterial inactivation reported in Figure 5.3b, trace 5 induced by visible light > 400nm by means of GF-TiO₂-Cu 3% mats occurs within 60 min. This effect is partially due to the lower light dose reaching the mat surface (70 mW cm⁻²) compared to the Suntest full light emission (90 mW cm⁻²), and to the absence of more energetic UVA-photons. Nevertheless, the direct cytotoxic events of copper, and the Fenton-like processes that take place in the sample maintain its antibacterial properties.

Furthermore, the Cu eluted from the mats amounted to 59.4 ppb for the GF-TiO₂-Cu 3% when irradiated with visible light. This amount of Cu is lower compared to the amount of Cu eluted by the runs under solar light (74.7 ppb). A possible reason could be the lower interfacial charge transfer events between TiO₂ and Cu [119]. GF-TiO₂-Cu 3% mats led to a modest bacterial inactivation even in the dark as shown in Figure 5.3c, trace (5) of ~0.5log₁₀, the correspondent Cu released is also shown in Table 5.3. This suggests that with longer treatment times by means of GF-TiO₂-Cu 3% mats, no energy would be necessary to induce antibacterial processes in the dark.

The disinfection by Cu/TiO₂ in the dark was reported previously to proceed with slow kinetics by Hashimoto et al. [184] and this agrees with the findings from this chapter. The Cu concentrations reported on Table 5.3 are well below the Cu-compatible levels for *mammalian* cells. These values have been reported with a median L(E)C50 of 5-8 parts per million (ppm) Cu [185-187].

5.3.3 Self-cleaning of MB stains on GF-TiO₂ and GF-TiO₂-Cu mats under solar irradiation

For the self-cleaning tests on GF-TiO₂-Cu mats, these were placed in a Petri dish and the set-up is shown in Figure 5.4. The MB-stain discoloration under solar light irradiation (90 mW cm⁻²) is shown in Figure 5.5 up to 240 min. When mats with a low Cu-loading of ~0.05% were used, the Cu acted as a trap for the generated TiO₂cb(e-) electrons consequently leading to a decrease in the TiO₂ electron/hole recombination rate [60, 61] favoring the self-cleaning reaction kinetics. Nevertheless, the GF-TiO₂-Cu 3% mats showed slow MB discoloration. This is due to the higher amounts of Cu acting as recombination sites for the electrons/holes generated under TiO₂ band-gap irradiation not allowing the charges to diffuse to the semiconductor surface and participate in the photocatalytic reactions. Also, Cu has a screening effect on the TiO₂ surface, when higher amounts of Cu are added this limits the light reaching the TiO₂ and consequently the production of photo-generated charges.

The microstructure of the GF-mats seems to play an important role in self-cleaning process since the 3D-structured non-woven mat contains the MB-dye in its void spaces. The discoloration of the stain reported in Figure 5.5 involves hydrophilic

groups on the GF-TiO₂-Cu-mats regulating its surface electrostatic potential as the MB dye gets in contact with it. Degradation redox reactions are more likely to happen if the pollutant molecule and the photocatalyst surface are brought closer together (electrostatic interaction). Monitoring of the surface redox events reflecting the change in the binding energies of C, O, Ti and Cu within the 10 nm topmost layers of the GF-TiO₂ and GF-TiO₂-Cu mats was possible and the XPS data will be presented in section 5.3.7.

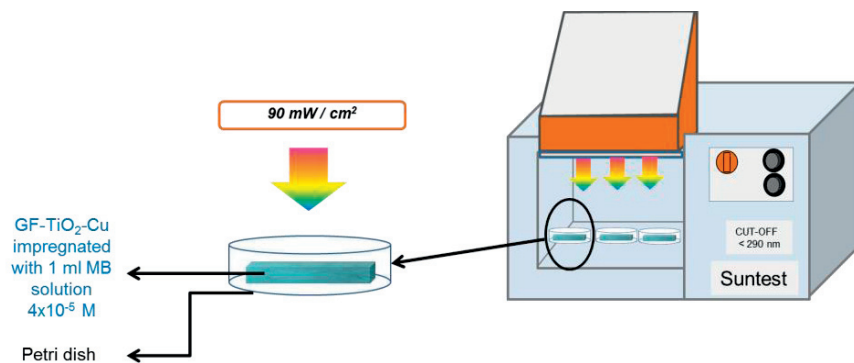


Figure 5.4. Set-up used for the evaluating MB self-cleaning of GF-TiO₂ and GF-TiO₂-Cu-mats

	0 min	15 min	30 min	45 min	60 min	240 min
GF-TiO ₂						
GF-TiO ₂ -Cu 0.05%						
GF-TiO ₂ -Cu 3%						

Figure 5.5. MB self-cleaning on GF-TiO₂ and GF-TiO₂-Cu mats irradiated up to 240 min under solar light (90 mW cm⁻²). Samples: GF-TiO₂, GF-TiO₂-Cu 0.05% and GF-TiO₂-Cu 3% mats

5.3.4 MB solution degradation by means of GF-TiO₂-Cu mats

Figure 5.6 shows the decrease of MB-solution concentration under solar light mediated by GF-TiO₂-Cu mats with their respective control experiments (carried out in the set-up shown in Figure 5.2). By comparing traces (1) and (3) in Figure 5.6, for Cu- loadings of 0.05% and 3% respectively, it is seen that an increase in the Cu-content in the GF-TiO₂ mats affects adversely the MB degradation kinetics. The reasons for this decrease have been previously discussed in section 6.3.2. Traces (4) – (7) in Figure 5.6 represent the control experiments in the dark and under solar simulated light; these results validate the data reported in traces (1) – (3).

The beneficial effect of the low Cu-addition on accelerating the pseudo-first order rate constant k for MB degradation is reported in Figure 5.7. For low Cu-loadings (0.05%) an increase of 40% in the rate constant was observed when compared to GF-TiO₂ mats. This is due to the charge separation induced by a low percentage of added Cu. A higher Cu-content on GF-TiO₂ mats leads to bigger Cu-agglomerates. This increases the inward diffusion of the photo-generated charges to the bulk of the photocatalyst [188]. Degradation runs of MB under visible light (> 400nm) were also carried out and in this case no effect of the higher Cu loadings of the GF-TiO₂-Cu mats on the kinetics was observed. These results can be consulted in Supplementary material Ch5-S4. The Cu amounts added to the TiO₂ are too low to induce a significant difference in the MB degradation kinetics under visible light. Experiments were carried out in triplicate and the error was below 10%.

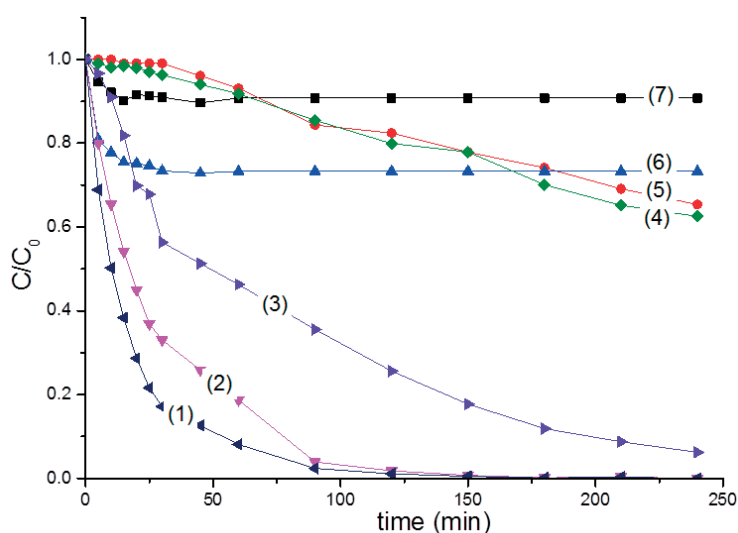


Figure 5.6. Decrease of concentration for a MB 4×10^{-5} M solution (model organic pollutant) under Suntest irradiation (90 mW cm^{-2}) or dark mediated by GF, GF-TiO₂, or GF-TiO₂-Cu mats. Traces: (1) Degradation mediated by GF-TiO₂-Cu 0.05% under suntest irradiation; (2) Degradation mediated by GF-TiO₂ under suntest irradiation; (3) Degradation mediated by GF-TiO₂-Cu 3% under suntest irradiation; (4) MB discoloration under Suntest irradiation (5) MB discoloration in the presence of GF-mat under Suntest irradiation, (6) MB intake of GF-TiO₂-Cu 0.05% in the dark, (7) MB intake of GF-mat in the dark. Initial solution pH=5.7

RF-plasma modification of the GF- TiO₂ mats was carried out to see whether: 1) an increase in the MB-adsorption on the GF surface taking place or 2) new/additional mostly negative binding sites could be induced enhancing the TiO₂ attachment to the GF mats, thus preserving the degradation performance over several cycles [38, 189]. An increase of ~16 % of the MB-adsorption on the GF mats was achieved upon RF treatment and in the case of GF-TiO₂ mats, RF-plasma pre-treatment lead to a ~30 % increase of MB adsorption. These tests were performed in the dark. Results can be found in the supplementary material Ch5-S5. Next, the TOC after 12 h irradiation in the presence of regular GF-TiO₂ and RF-plasma pre-treated GF-TiO₂ mats (RF-

GF-TiO₂) were assessed. The results indicated no significant changes when comparing the regular and the RF-Plasma pre-treated mats. Furthermore, the mineralization performance was seen to be similar during the recycling of the regular and RF-plasma pre-treated mats up to the 3rd cycle; (See Supplementary material Ch5-S6). The RF-plasma pretreatment approach was not continued since it did not lead to a meaningful increase in the MB-degradation.

Figure 5.8 presents the total organic carbon (TOC) decrease for and MB-solution by the action of GF-TiO₂-Cu mats during 12 h irradiation periods. It shows a) practically no effect of the Cu-loading on the GF-TiO₂-Cu mats and b) no complete mineralization of MB being reached within a period 10 times longer than MB-degradation reported in Figure 5.6, trace (1). However, taking into account the absorption/adsorption period in the dark (first 30 minutes), the GF-TiO₂-Cu 0.2% leads to the greatest mineralization. This is still in line with hypothesis of low Cu concentrations inducing better degradation.

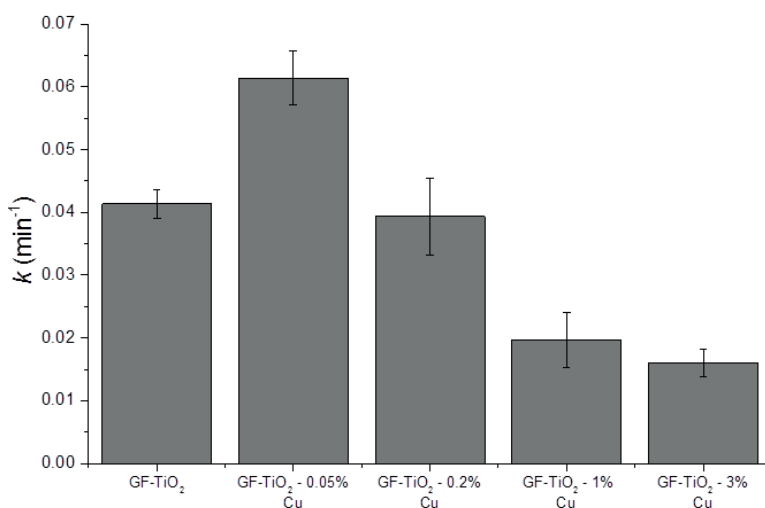


Figure 5.7. Pseudo-first order rate constant (k) for the degradation of MB (4×10^{-5} M) in solution as a function of the Cu-content on GF-TiO₂-Cu mats. Reactions taking place under Suntest irradiation (90 mW cm^{-2}). Initial MB solution pH=5.7.

The degradation of a MB-solution by means of the GF-TiO₂-Cu mats under Suntest light irradiation was also followed by high performance liquid chromatography (HPLC) and results are shown in Figure 5.9. The decrease in the MB's characteristic peaks shown in the insert (6) of Figure 5.9 was followed at wavelengths: 245, 292, 615 and 668 nm. A similar approach was reported for MB degradation monitored by HPLC by Rauf and collaborators [190]. The presence of aromatic rings fragments in solution (peaks detected at 245nm) [142] is noticed for all of the catalysts after 240 min irradiation. No complete reduction of the TOC was found for the same GF-TiO₂-Cu mats (Figure 5.8) and the HPLC results in Figure 5.9 confirm this result. The HPLC peaks detected between at 615 nm and 668 nm are attributed to conjugated π -system containing MB monomers/dimers and N de-methylation intermediates [191]. According to this, the conjugated π -systems, the MB dimers and the N de-

methylation moieties disappear around 120 minutes reaction for GF-TiO₂ and GF-TiO₂-Cu 0.05% (Figure 5.9, inserts (1) and (2) respectively). Additionally, Houas et. al. have reported MB-degradation in solution by TiO₂ suspensions under UV-light and found long-lived aromatic intermediates in solution during the photocatalytic degradation [133], which is in line with our findings.

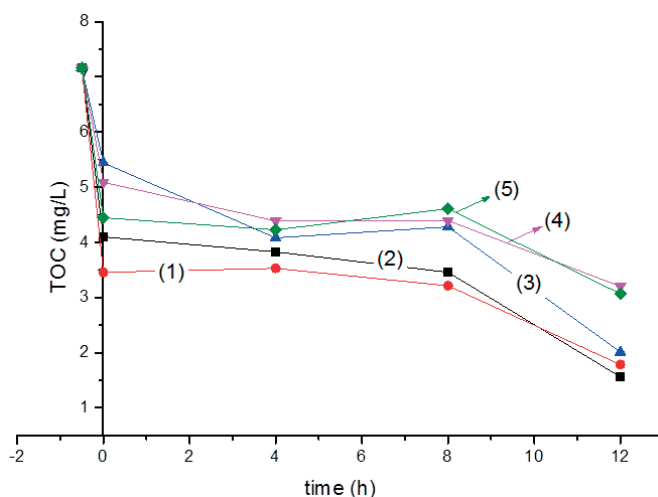


Figure 5.8. Total organic carbon (TOC) decrease for MB 4×10^{-5} M by the action of GF-TiO₂-Cu mats under Suntest light (90 mW cm^{-2}). Equilibration period in the dark: 30 minutes. Traces: (1) GF-TiO₂-Cu 0.05%, (2) GF-TiO₂, (3) GF-TiO₂-Cu 0.2%, (4) GF-TiO₂-Cu 1%, (5) GF-TiO₂-Cu 3%

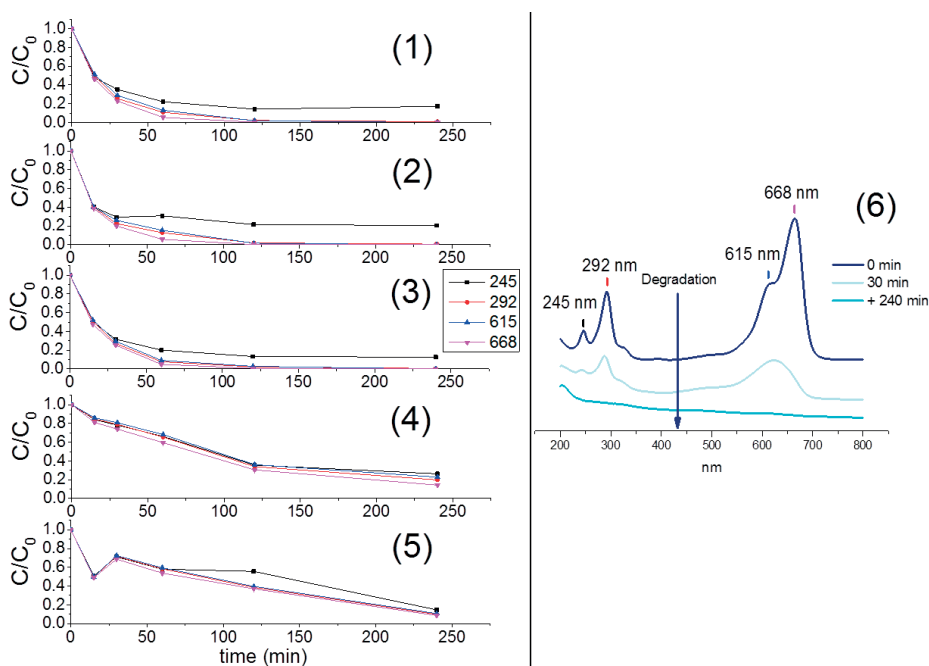


Figure 5.9. Degradation of a MB 4×10^{-5} M solution by means of GF-TiO₂-Cu mats under Suntest light irradiation (90 mW cm^{-2}) followed by high performance liquid chromatography (HPLC). The characteristic peaks of MB at 245, 292, 615 and 668 nm were monitored as a function of reaction time for: (1) GF-TiO₂, (2) GF-TiO₂-Cu 0.05%, (3) GF-TiO₂-Cu 0.2%, (4) GF-TiO₂-Cu 1%, (5) GF-TiO₂-Cu 3% mats

5.3.5 Identification of photo-generated radical-species in solution

Reactive oxygen species (ROS) generated during TiO₂ photocatalysis are shown in equations (5-2 - 5-6) in section 5.3.2. Figure 5.10a/b shows the runs aiming at the identification of the radicals leading to MB degradation. NaN₃ was used as a scavenger of oxygen singlet ¹O₂, benzoquinone as quencher of O₂^{-•}/HO₂[•], methanol as a quencher of [•]OH-radicals and ethylene-diamine tetra-acetic acid disodium salt (EDTA-2Na) used to scavenge TiO₂vb(h⁺) [63, 192, 193]. Figure 5.10a shows that the degradation in the presence of benzoquinone (BQ) (which scavenges HO₂[•] radical-intermediate at pH > 4.5 (see equation 5-6)) proceeds in a slower way than in presence of the rest of the scavengers. In this way, HO₂[•] was identified as the most important radical leading to MB degradation by means of GF-TiO₂. MB and HO₂[•] radical would react as shown in eq (5-13)

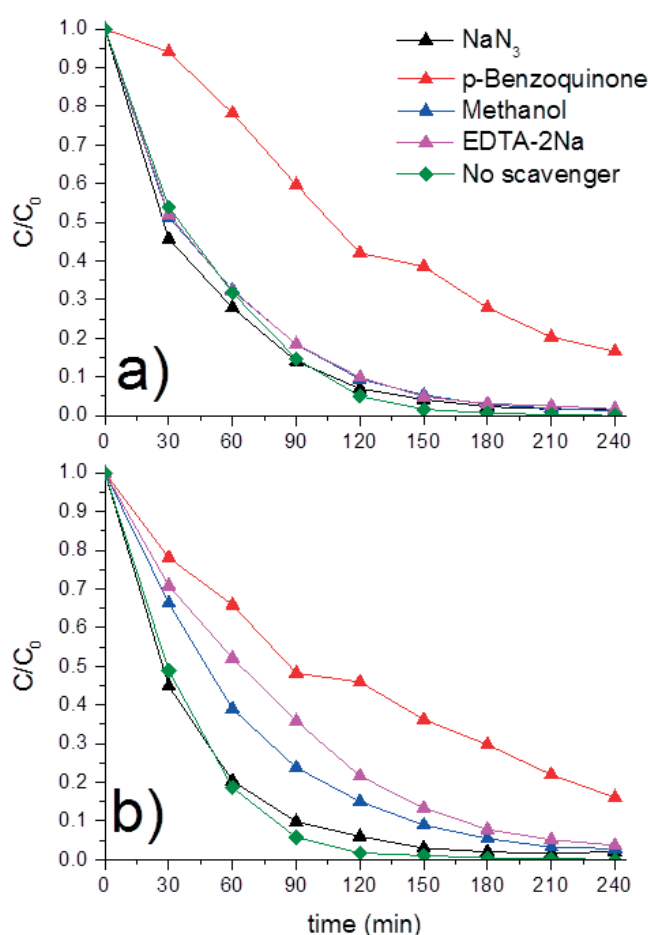
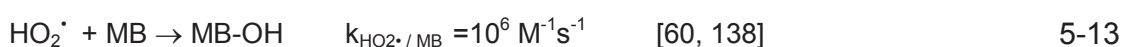


Figure 5.10. Degradation of MB 4×10^{-5} M solution under Suntest irradiation (90 mW cm^{-2}) in the absence of a radical scavenger and in the presence of radical scavengers (0.2mM): NaN₃, p-benzoquinone, methanol and EDTA-2Na. Mats used: a) GF-TiO₂, b) GF-TiO₂-Cu 0.05%

Figure 5.10b shows that during the degradation of MB by GF-TiO₂-Cu 0.05%, the most active radical species was again HO₂[•], followed by TiO₂vb(h⁺), and by the [•]OH-radicals. The azide NaN₃ has been widely used as an oxygen singlet (¹O₂) scavenger. However, NaN₃ also reacts with [•]OH with a rate close to the rate of the singlet oxygen [63, 131, 138]. Taking into consideration this information, the data reported for ¹O₂ in Figure 5.10a/b would not specifically/accurately reflect the quenching of ¹O₂. EDTA-2Na is used generally as a TiO₂vb(h⁺) scavenger, but may not necessarily work in the same way for GF-TiO₂-Cu 0.05% reported in Figure 5.10b.

Table 5.4. Ti and Cu ions concentration detected by ICP-MS in the bulk of the reactor after MB 4x10⁻⁵ M degradation by means of GF-TiO₂-Cu under Suntest irradiation (90 mW/cm²) after several use cycles

	Different TiO ₂ -Cu supported on GF	Ti (ppb)	Cu (ppb)
1 st use cycle	GF-TiO ₂	9.56	
	GF-TiO ₂ -Cu 0.05%	18.29	22.5
5 th use cycle	GF-TiO ₂	11.81	
	GF-TiO ₂ -Cu 0.05%	22.26	30.3
10 th use cycle	GF-TiO ₂	12.69	
	GF-TiO ₂ -Cu 0.05%	16.73	13.1

Inspection of Figure 5.10b suggests that besides HO₂[•] other intermediate oxidative radical species are present in solution in comparison with the solution treated with GF-TiO₂ mats (Figure 5.10a). As HO₂[•] radical was found to be the most active ROS produced by both photocatalysts, its mean free path away from the mats was estimated by means of the Smoluschowski approximation. A mean free path of 3.5 microns was estimated (see supplementary information Ch5-S7). In conclusion, the presence of Cu in the GF-TiO₂-Cu 0.05% mats led to a variety of the ROS generated. Figure 5.11 shows the stable repetitive MB degradation on mats proceeding up to 10 cycles. This shows the potential for the practical application of these mats in environmental cleaning. Moreover, Table 5.4 shows the Ti- and Cu-ions leached during the mats

recycling reported in Figure 5.11. The Ti and Cu leaching was well below the limits set by environmental regulations [192-194].

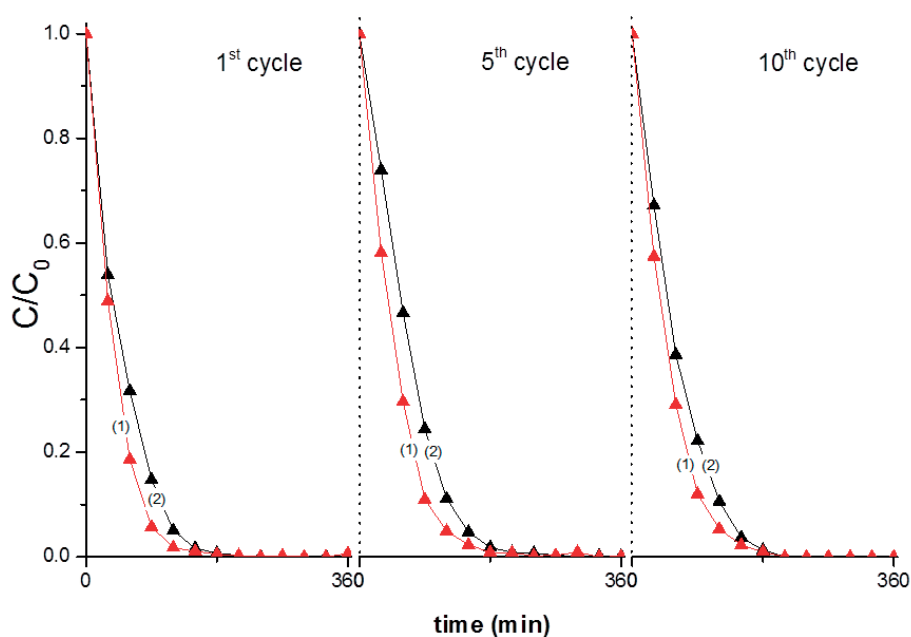


Figure 5.11. Degradation cycles of MB solution (4×10^{-5} M) under Suntest irradiation (90 mW cm^{-2}). (1) GF-TiO₂ mats, (2) GF-TiO₂-Cu mats

5.3.6 In situ monitoring of the surface potential and pH and suggested mechanism of degradation

Figure 5.12 presents the pH-shift and the surface potential change of three types of mats during MB degradation under Suntest irradiation up to 330 min (20000 s). The addition of Cu on the TiO₂ modifies surface properties as BET surface area, porosity, and the availability of TiO₂ sites. Figure 5.12b) and Figure 5.12c) show a different surface potential at time zero for GF-TiO₂-Cu 0.05% and GF-TiO₂-Cu 3% respectively, providing evidence for a surface modification by the amount of Cu added. A higher Cu content on the GF-TiO₂-Cu 3% mats led to a decrease in the degradation of MB.

Figure 5.12, a/b) notes a pH decreases of ~ 1 unit occurring during MB solution degradation. This is equivalent to a ~ 10 times increase in the concentrations of [H⁺] and is due to the generation of intermediate degradation short-chain carboxylic acids in solution (branched or not) with a pK_a ~ 3 . For longer reaction times (not shown in Figure 5.6) the pH would increase due to the mineralization of the carboxylic acids generating CO₂ in a photo-Kolbe type of reaction. This stage is not seen in Figure 5.12 since it was beyond 20 000s [195]. Such a process would occur after 8 hours (>30 000s) in agreement with the TOC results reported in Figure 5.8. The shift to more acid pH-values in Figure 5.12 cannot be explained by: a) equation (5-5) since the $\cdot\text{OH}$ -radicals do not play an important role during MB solution degradation (Figure 5.10a/b)) nor b) the formation of MB⁺-cations as noted in equation (5-14) since MB⁺.

is a short-lived acidic cationic species [60, 63, 87]. The first reaction of MB on GF-TiO₂-Cu-mats under sunlight is suggested in equation (5-14):

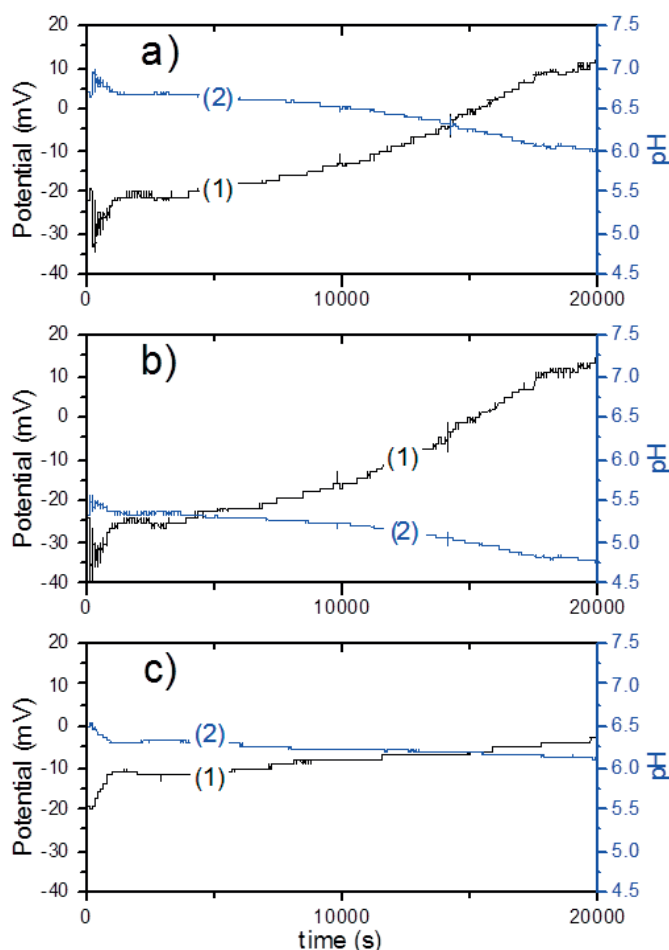
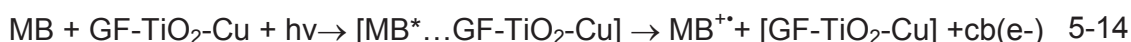


Figure 5.12. Evolution of surface potential (trace (1)) and solution's pH (trace (2)) in the solid-liquid interface during the degradation of MB 4×10^{-5} M solution by means of GF-TiO₂-Cu mats under Suntest irradiation (90 mW cm^{-2}): a) GF-TiO₂, b) GF-TiO₂-Cu 0.05%, c) GF-TiO₂-Cu 3%

During the initial period of MB degradation both the MB and TiO₂ are photosensitized, MB injects electrons into the TiO₂cb and in parallel converts MB to the MB^{+·} short-lived cation radical. The electron injected by the MB into the TiO₂ reacts with O₂ and generates highly oxidative radicals leading to the degradation of MB as suggested in section 6.3.3. Acceleration of the MB degradation was observed when low Cu was added to the GF-TiO₂ mats due to Cu intra-gap states promoting the indirect electronic transition from the TiO₂vb to the TiO₂cb. Cu^{1+/2+} intra-gap states have been reported before for TiO₂ films [118] and for metal-doped TiO₂ powders [196].

5.3.7 Surface characteristics of GF-TiO₂-Cu mats detected by SEM, EDX and XPS analyses

SEM images are shown Figure 5.13. Figure 5.13a/b confirm a size of ~9 μm diameter for the A04008 glass fibers in the mats. Samples of GF-TiO₂-Cu 0.05% are shown in Figure 5.13c and Figure 5.13d with a magnification of 1.500 times and 50.000 times respectively. Figure 5.13d) presents TiO₂ aggregates with a particle size of ~20 nm. Figure 5.13e and Figure 5.13f show the images for the GF-TiO₂-Cu 3% with a magnification of 1.500 and 50.000 times respectively. The energy dispersive X-ray (EDX) analysis for this sample is shown in supplementary material Ch5-S8. The elements found on the GF-TiO₂-Cu 3% mat surface were: C, O, Al, Si, Ca, Ti, Ni and Cu. EDX weight percentages were: 0.57% for Cu and 17.49% for Ti. These values were very close to the XRF values reported in Table 5.2 for the GF-TiO₂-Cu 3% mat.

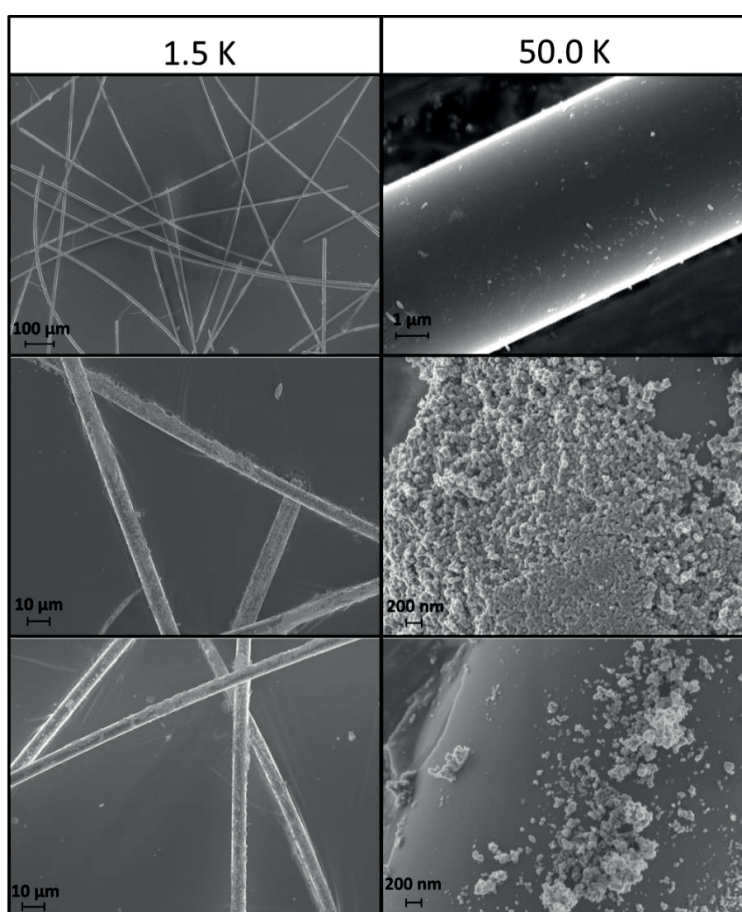


Figure 5.13. Scanning electron microscopy (SEM) of mats' fibers. a) Fibers from GF, 1.5K magnification; b) Fibers from GF, 50.00K magnification; c) Fibers from GF-TiO₂-Cu 0.05%, 1.5K magnification; d) Fibers from GF-TiO₂-Cu 0.05%, 50.00K magnification; e) Fibers from GF-TiO₂-Cu 3%, 1.5K magnification; d) Fibers from GF-TiO₂-Cu 3%, 50.00K magnification

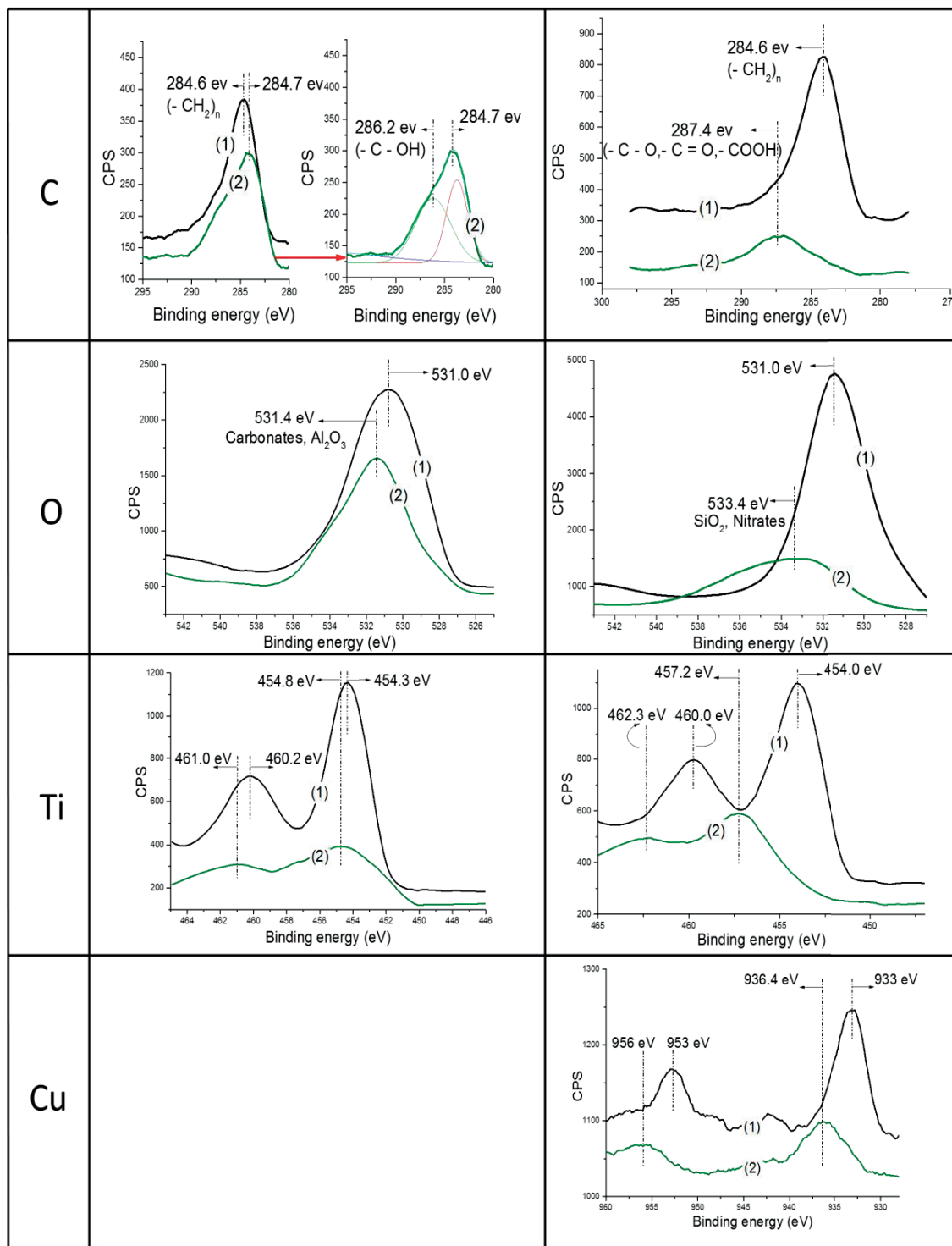


Figure 5.14. XPS signals for GF-TiO₂-Cu 0.05% samples (left hand side column) and for GF-TiO₂-Cu 3.0% samples (right hand side column). Time zero (30 minutes MB in contact with the GF-TiO₂-Cu mat) corresponds to Trace (1) and Trace (2) corresponds to 60 minutes reaction under irradiation by sunlight of a 2x2 cm sample stained with 1ml MB 4×10^{-5} M

X-ray photoelectron spectroscopy (XPS) results are shown in Figure 5.14 for self-cleaning samples at different times under light irradiation (Section 6.3.2). The binding energy (BE) shifts observed for C, O and Ti are more significant for the GF-TiO₂-Cu 3% samples compared to GF-TiO₂-Cu 0.05% samples. Practically no C1s BE shifts were observed for the -(CH₂)_n- bonds in the GF-TiO₂-Cu 0.05% mats after 60 min irradiation. However, if the peak for C1s after 60 min of irradiation is de-convoluted, an important contribution of a peak at 286.2 eV was detected for the -C-OH groups, this suggests the occurrence of a mild oxidation reaction. A shift of 1.8 eV towards a higher C1s oxidation state in the BE of -CH₂- bonds was observed for the GF-TiO₂-Cu 3% mat after 60min reaction. The O1s BE shifts for the GF-TiO₂-Cu 0.05% samples were different to the shifts registered for the GF-TiO₂-Cu 3%. This applies for the O1s signals found in carbonates, Al₂O₃, SiO₂ and nitrates. The BE shifts > 0.2 eV reflect a change in the oxidation state of the C1s and O1s [128-130]. These BE shifts suggest *redox* reactions taking place during the MB self-cleaning. The Ti2p_{3/2} doublet shifts in Figure 5.14 were stronger for the GF-TiO₂-Cu 3% compared to the GF-TiO₂-Cu 0.05% sample due to Ti³⁺/Ti⁴⁺ *redox* processes on the mat surface. On GF-TiO₂-Cu 0.05% surface, the highest peak of the Ti2p_{3/2} signal changes from 454.3 eV to 454.8 eV within the 60 min. In contrast, BE-shifts of almost 3 units were detected for the Ti doublet on the GF-TiO₂-Cu 3% surface due to the higher Cu-loading. The last row in the left hand side of Figure 5.14 shows no data for the BE-shifts of Cu in the GF-TiO₂-Cu 0.05% sample due to their very low Cu-content. This was not the case of GF-TiO₂-Cu 3% mats as there was enough Cu-present to register the XPS BE signals. The shift toward higher BE provides the evidence for the oxidation to higher CuOx oxidation states.

5.4 Conclusions

This chapter reports the preparation, of low cost, stable, light, flexible, thermal and mechanically resistant Techmat® A 04008 E Glass mats grafted with TiO₂ and Cu. These mats offer a higher specific surface area than Rashig rings and that is why their performance was assessed not only for MB degradation in solution but also for water disinfection and self-cleaning. GF-TiO₂-Cu 3% mats induced a slow kinetics bacterial inactivation in the dark but led to complete water disinfection within 3h indoor light irradiation (visible light). Self-cleaning and pollutant (MB) degradation in solution by means of GF-TiO₂-Cu 0.05% were accelerated when compared to GF-TiO₂. The MB degradation process was observed to remain independent of Cu-content when irradiated with visible light (> 400 nm). GF-TiO₂-Cu 0.05% photocatalyst showed to produce a wider variety of oxidative radical species by means of solar irradiation due to the Cu-presence compared to radicals generated by the GF-TiO₂ mats. Evidence is presented for the stable photocatalytic recycling of the mats under sunlight irradiation. Results suggest the practical potential of these mats for environmental applications: in the field of organic pollutants abatement in water and water potabilization. Moreover, natural fibers offering a similar specific surface area as the one of the glass fiber mats could be used as support for photoactive material, simplifying the preparation procedure.

6. Chapter 6: Sputtered Cu-Polyethylene films inducing bacteria inactivation in the dark and under low intensity sunlight

Published work:

Laura Suárez, Oualid Baghriche, Sami Rtimi, Cesar Pulgarin, John Kiwi. “Sputtered Cu-polyethylene films inducing bacterial inactivation in the dark and under low intensity sunlight”. *Journal of Photochemistry and Photobiology A: Chemistry* 330 (2016) 163 – 168.

Web link:

<http://www.sciencedirect.com/science/article/pii/S1010603016302283>

Reproduced with permission of Elsevier, Copyright 2017 (license number 4077120555286)

Doctoral Candidate’s contribution:

Investigator and co-author

6.1 Introduction

Nanoparticulate films preparation able to avoid the formation of infecting biofilms spreading pathogenic bacteria is a topic of increasing attention and has led recently to an intensive research on Cu antibacterial films on textiles, polymer and glass [103-105]. Bacterial inactivation on textiles by Ag has been reviewed [112] and textiles sputtered by Cu have been recently gaining attention. Studies on Cu-polyester [113-116] and Cu/CuO-TiO₂ mediated bacterial inactivation [117-119] have been reported during the last few years. Investigation of Cu/CuOx-antibacterial films started become popular due to the increase in the hospital acquired infections (HAIs) with the concomitant higher treatment cost [106-109]. These nosocomial infections caused by antibiotic resistant bacteria have been reported recently to become more widespread [5]. At the present time there is a need to prepare effective, uniform and adhesive films to decrease the health risk associated with HAI's infections.

Recently Hashimoto et al. reported the preparation of the Cu/CuO and TiO₂/Cu films by sol-gel methods inducing significant bacterial inactivation under UV-Visible light [97, 98]. Nevertheless, sol-gel deposited films were not mechanically stable, not reproducible and presented low uniformity. Generally sol-gel films are used as catalysts or photocatalysts on supports showing high thermal resistance. With polyethylene (PE) being thermally stable up to 90 °C it does not allow the annealing at a few hundred degrees of Cu/CuOx films for inducing adequate adhesion/stability/reproducibility. This is why sputtering techniques at relatively low temperatures for short times allow the deposition of antibacterial films on non-thermal resistant polymer sheets.

This chapter addresses the deposition of CuOx-films by sputtering and the bacterial inactivation kinetics in the dark and under light usually found in hospitals and other health care facilities. This chapter also reports on the CuOx film redox behavior, repetitive antibacterial film performance, semiconductor character, film composition and PE-CuOx spectral features [112-119]. Recent reviews presenting the action of innovative photocatalysts supported or not, made-up by semiconductors, doped-semiconductors, meta/oxides active disinfection processes under solar light have been recently reported [87, 161]. Cu was selected as the active agent to preclude biofilm formation and bacterial growth [60, 110, 160]. During the last decade several research groups have reported antibacterial Ag, Cu and TiO₂ coatings on glass and polymer films by chemical vapor deposition (CVD) and by other sputtering related techniques [111]. Direct current (DC) magnetron sputtering as used in this work allows the deposition of metal/metal oxides at relatively low temperatures not exceeding 120-140°C [37].

6.2 Experimental section

6.2.1 Photocatalyst preparation

The low-density polyethylene (LDPE) used in this study consists of a highly branched low crystalline film with formula H(CH₂-CH₂)_nH. The (LDPE) 0.1 mm thick and was obtained from Goodfellow, UK (ET311201). The LDPE film presented mechanical stability, had a density of 0.92 g/cm³ and was thermally stable up to 90°C.

Polyethylene (PE) is a low cost and widely available material. It is chemically inert, mechanically stable and flexible, UV-resistant and does not oxidize in air under sunlight. For this reasons PE has been selected as a substrate for Cu. The PE-CuOx films presented low scattering due to the uniform and adhesive Cu-layers on PE.

Thin Cu-films were sputtered on PE in the direct current magnetron sputtering (DCMS) using a Cu Lesker, Hastings, UK target 2 inches diameter applying three different currents between 50mA and 200mA. The substrate-to-target distance was 10 cm. The sputtering was carried out in a reactive atmosphere in the DCMS chamber made up of 95% Ar and 5% O₂. The geometry of the sample chamber has been previously reported [113]. Taking the composition of each layer as made up by 10¹⁵ atoms/cm² and an average of 0.2 nm for the Cu layer thickness, Figure 6.1 shows that after 50s a Cu-layer with a thickness of 12.5 nm/62 layers was deposited on the PE-polymer. This is equivalent to an atomic rate deposition of 1.25x10¹⁵ Cu atoms cm⁻² s⁻¹. The nominal thickness calibration of the PE-CuOx film thickness was carried out on Si-wafers with a profilometer (Alphastep500, TENCOR) with an error of ±10%.

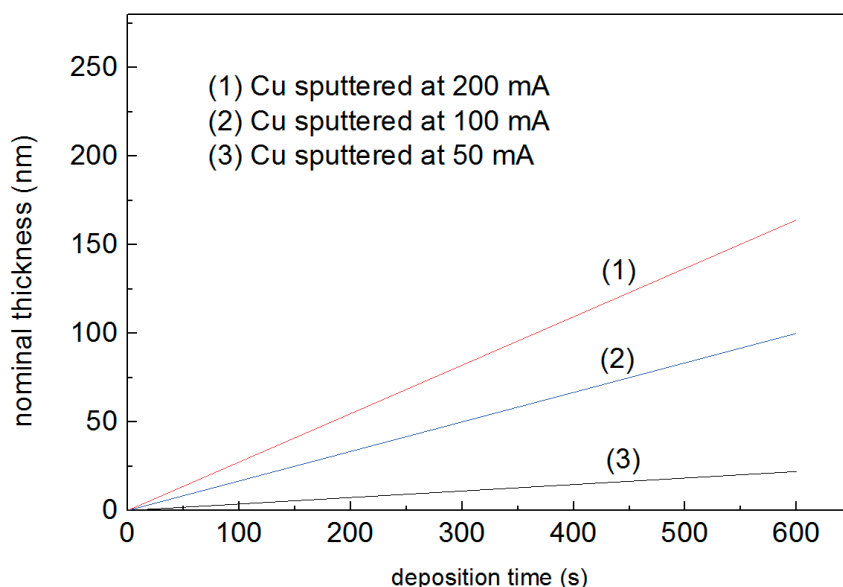


Figure 6.1 Nominal thickness of Cu-layers detected by profilometry on Si-wafers sputtered at: (1) 200 mA, (2) 100 mA and (3) 50 mA

6.2.2 Irradiation source and reactors

The PE-CuOx samples were irradiated with the Xe-400W light in the Suntest solar simulator CPS (Atlas GmbH, Hanau, Germany). The light intensity, in the range of 310 to 800 nm, was tuned at 5 mW cm⁻², 10 mW cm⁻² and 20 mW cm⁻² (~0.3x10¹⁶ photons cm⁻² s⁻¹). A cut-off filter was positioned in the Suntest cavity to filter the light < 310 nm.

The PE-CuOx samples were placed in petri dishes to carry out the bacterial inactivation runs, following a set-up similar to that shown in Chapter 5, in Figure 5.4;

nonetheless for this approach the petri dishes were provided with lids to prevent evaporation, as the volume of bacterial solution in contact with the film was very low (50 μ l).

6.2.3 Monitoring bacterial inactivation

The PE-films were sterilized keeping them at 70°C overnight. Aliquots of 50 μ L bacterial culture suspended in a NaCl/KCl (8 g/l NaCl and 0.8 g/l KCl) solution with a concentration of $\sim 10^6$ CFU ml^{-1} were placed on either PE-CuOx samples or un-sputtered PE control sample. The samples were placed on Petri dishes provided with a lid to prevent evaporation. At preselected times, the samples were transferred into a sterile 2 ml Eppendorf tube containing 950- μ l autoclaved NaCl/KCl saline solution. These solutions were subsequently mixed thoroughly using a Vortex for 3 min. Serial dilutions were made in NaCl/KCl solution taking 100- μ l aliquots. These 100- μ l aliquots were pipetted onto a nutrient agar plate, for the bacterial counting by the standard plate method. These agar plates were incubated, lid down, at 37°C for 24 h before the colonies were counted. Triplicate runs were carried for the bacterial CFU ml^{-1} determination reported in this study. To verify that no re-growth of *E. coli* occurs after the first bacterial inactivation, the nanoparticle film was incubated again on an agar Petri dish at 37°C for 24h. No bacterial re-growth was observed. The agar was purchased from Merck GmbH, Microbiology division KGaA under the catalogue N° 1.05463.0500.

The statistical analysis of the results was performed for the CFU values calculating the standard deviation values. The average values were compared by one-way analysis of variance and with the value of statistical significance. The one-way analysis of variance (one-way ANOVA) was used to compare the mean of the samples using the Fisher distribution. The response variable was approximated for the sample data obtained from the photocatalytic inactivation of test samples presenting the same distribution within the same sputtering time ($P < 0.05$).

6.2.4 Monitoring Cu-leaching by Inductively Coupled Plasma Mass Spectrometry (ICP-MS)

The PE-CuOx samples were placed into Eppendorfs centrifugating plastic tubes containing 1 ml NaCl/KCl 0.08% solution after the bacterial inactivation cycle. The solutions resulting from this rinsing were subsequently diluted 10 times to meet the minimal volume needed for the ICP-MS analyses.

6.2.5 Composition of the PE-CuOx photocatalysts

The chemical composition of the prepared photocatalysts is presented in Table 6.1 prior the discussion of the photocatalysts performance. The composition was evaluated by X-ray Fluorescence method as explained in the materials and methods section.

Table 6.1 X-ray Fluorescence (XRF) determination of the Cu weight % / weight PE-film. Additionally, assessed $\text{cm}^3 \text{Cu}_2\text{O} / \text{cm}^2 \text{PE}$ based on XRF data and material properties.

Current	PE-CuOx, (sputtering time)	Wt%Cu/wt PE	Error %	($\text{cm}^3 \text{Cu}_2\text{O} / \text{cm}^2 \text{PE}$)
100 mA	40 s	0.06	0.008	9.20E-07
200 mA	5 s	0.03	0.008	4.60E-07
	10 s	0.07	0.008	1.07E-06
	20 s	0.12	0.01	1.84E-06
	40 s (Sample I)	0.16	0.01	2.45E-06
	60 s	0.29	0.02	4.45E-06

6.3 Results and discussion

6.3.1 Optical properties of PE-CuOx films

The absorbance of PE-CuOx films detected by diffuse reflectance spectroscopy (DRS) is shown for the most active samples in Figure 6.2. The rough UV-Vis reflectance data cannot be used directly to assess the optical absorption of the samples because of the scattering contribution of the PE-films to the DRS spectra. Normally a weak dependence is assumed for the scattering coefficient S on the wavelength. The DRS spectra in Figure 6.2 are plotted in Kubelka-Munk (KM) units. The relationship between the Kubelka-Munk (K-M) and the transport scattering coefficient is obtained through a semi-empirical approach for an incident diffuse light beam. In such systems, the Kubelka-Munk equation can be stated:

$$\frac{K}{S} = \frac{(1 - R)^2}{2R_\infty} \quad (6-1)$$

where: R_∞ reflectance of reflectance of the sputtered layer, S the specific scattering and K the absorption coefficient.

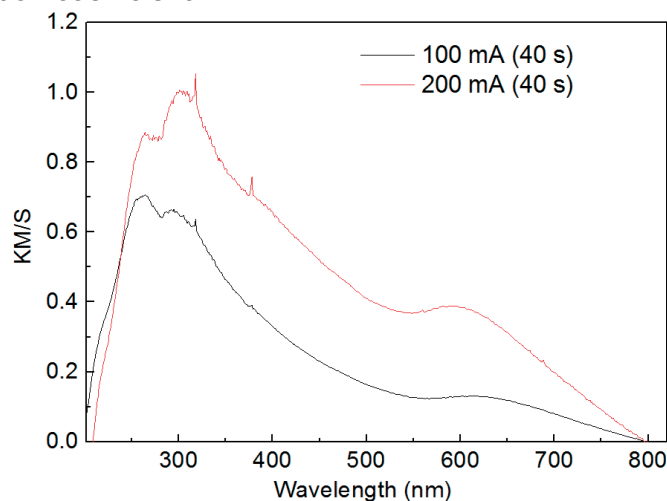


Figure 6.2 Absorption of PE-CuOx films in Kubelka-Munk units detected by Diffuse reflectance spectroscopy (DRS). Cu-layers sputtered during 40s at: (1) 100 mA and (2) 200 mA

The two spectra shown in Figure 6.2 were sputtered with two different DCMS currents. A very wide spectral range is seen for CuOx extending up to 800 nm corresponding to a band-gap of ~1.7 eV as reported previously by Bard [197]. The absorption between 600-800 nm is due to the intrinsic d-d transition of the Cu(II)-species [198] and the 500-600 nm absorption is due to the inter-band transition of Cu(I)-species [199].

6.3.2 Bacterial inactivation kinetics, Cu-release during repetitive recycling and effect of the applied light intensity

Figure 6.3 shows the bacterial inactivation under dark conditions and under sunlight intensity of 20 mW/cm² for samples sputtered for different times with different energies. Figure 6.3, trace 7) shows that in the dark the complete bacterial reduction is attained within 90 min. Figure 6.3, trace 8 shows that PE by itself under light does not lead to bacterial loss of viability. Figure 6.3, trace 1 shows that samples sputtered with 200mA/300V for 40s lead to the fastest bacterial inactivation (15 min). As this was the best performing PE-CuOx when inactivating bacteria, it was chosen for the subsequent experiments and it will be referred to as "Sample (I)" in this chapter from now on. Figure 6.3 traces 2 and 3 show a slower bacterial inactivation kinetics but for different reasons. The lower kinetics reported in Figure 6.3, trace 2) is attributed to a bulk inward diffusion of the charge carriers, given the thicker sputtered film some of the charges do not reach the PE-CuOx surface but diffuse inwards [118]. Such bulk inward diffusion would lead to a decrease in the amount of highly oxidative radicals, which prompt the photo-induced bacterial inactivation.

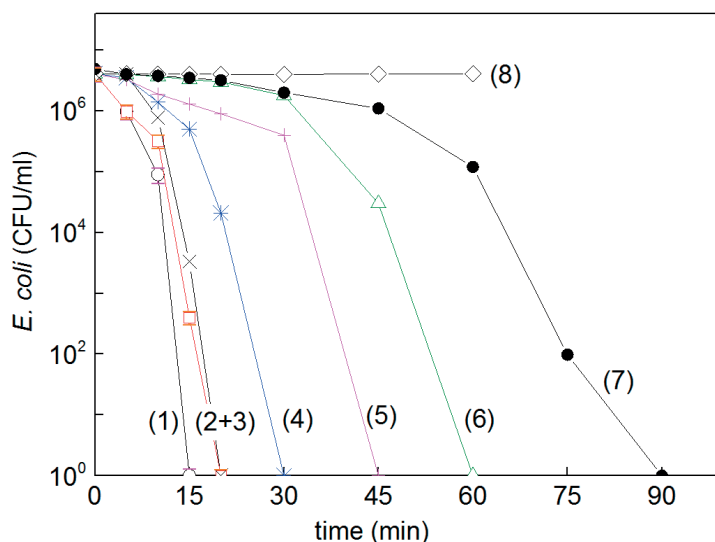


Figure 6.3 *E. coli* inactivation on PE-CuOx sputtered at different energies: (1) Cu sputtered for 40 s on PE at 200 mA (Sample (I)), (2) Cu sputtered for 60 s on PE at 200 mA, (3) Cu sputtered for 20 s on PE at 200 mA, (4) Cu sputtered for 40 s on PE at 100 mA, (5) Cu sputtered for 10 s on PE at 200 mA, (6) Cu sputtered for 5 s on PE at 200 mA, (7) Cu sputtered for 40 s on PE at 200 mA in the dark, (8) the irradiation of the PE sample was carried out in the cavity of a Suntest simulator (20 mW/cm²). Error bars: standard deviation (P<0.05)

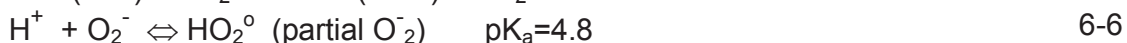
Visible light photons reaching PE-CuOx lead to the reaction (1) [113-115]. CuO is a p-type semiconductor with a band-gap of 1.7 eV (cb -0.3eV and vb 1.4 eV SCE) [116]. The mechanism suggested for the generation of highly oxidative intermediates involving the photo-generated charges on CuOx surface, leads subsequently to bacterial reduction



In eq. (6-2) e^-_{cb} refers to conduction band electron and h^+_{vb} refers to valence band hole. The excited electron reacts with O_2 producing O_2^- eq. (6-3) or reducing the Cu^{2+} in the CuOx lattice to Cu^+ as noted in eq. (6-4):



Additional O_2^- is produced as shown in eq(6-5) [117-119]. The O_2^- generated would lead to HO_2^\cdot radical production, as shown in eq(6-6) as well as to the production of H_2O_2 , as shown in eq. (6-7)



The leaching of Cu was almost negligible as presented in Table 6.2. This is consistent with the fact that eq (6-4) is much faster than the CuOx dissolution described in reaction (6-7).

Longer sputtering times also lead to Cu-agglomerates. Figure 6.3, traces 3, 5 and 6, shows that with less sputtering time a smaller amount of CuOx is grafted on PE slowing down bacterial inactivation. Figure 6.3, trace 4) indicates that less Cu-species are generated at 100mA (Cu^0 , Cu^+ , Cu^{2+}) compared to DCMS-sputtering with 200mA [200]. This in turn leads to a lower amount of Cu-grafted on the PE-film as noted in Table 6.1 and consequently to longer bacterial inactivation times. Bacterial inactivation kinetics of *E. coli* has been reported on DCMS sputtered Cu-cotton within 30 min and on on PDCMS (P=Pulsed) sputtered Cu-cotton within 10 min [113]. When applying highly ionized pulsed plasma magnetron sputtering (HIPIMS) on PE the bacterial inactivation proceeded within 60 minutes [118]. DCMS was carried out at a lower energy compared to pulsed direct current magnetron sputtering (PDCMS), being one of the reasons to account for the longer bacterial inactivation times [112-119]. In the case of HIPIMS, the longer bacterial reduction time of 60 min can be attributed to the highly compact adhesive coating of CuOx releasing less Cu-ions

during the bacterial inactivation time. A preliminary account for this observation has been recently reported [201].

Figure 6.4 shows the recycling of the PE-CuOx film under low intensity sunlight irradiation up to the fifth recycling. Although the kinetics is in principle conserved, after the second recycling the complete bacterial inactivation seem not attain completion. Table 6.2 shows the Cu released after the 1st, 3rd and 5th film recycling. The second column shows the data for the PE-CuOx films contacted with bacteria for 3s before each disinfection cycle. The first column shows the Cu-released as a function of the film recycling releasing higher amounts of Cu. This suggests electrostatic adhesion between the positively charged PE-CuOx film (+) and the negatively charged adhering bacteria envelope (-).

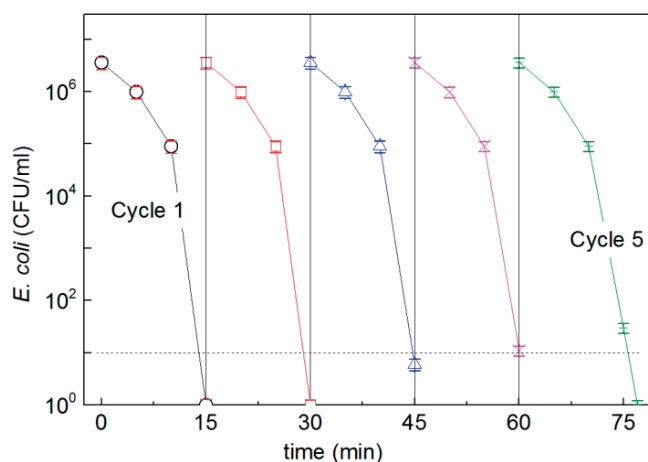


Figure 6.4 Recycling of *E. coli* inactivation on PE-CuOx (Sample (I)) up to five cycles under sunlight irradiation (20 mW/cm^2). Error bars: standard deviation ($P < 0.05$)

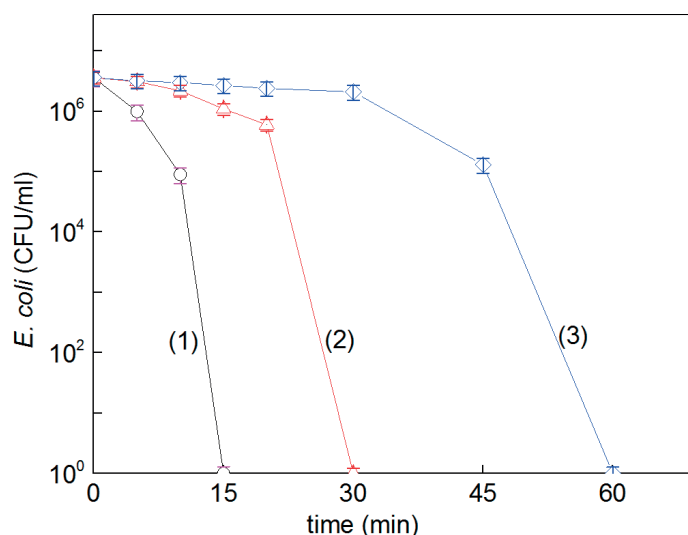


Figure 6.5 *E. coli* inactivation on PE-CuOx films sputtered for 40 s at 200 mA as a function of the applied solar simulated light intensity: (1) 20 mW/cm^2 , (2) 10 mW/cm^2 and (3) 5 mW/cm^2 . Error bars: standard deviation ($P < 0.05$)

Table 6.2 Cu-release in ppb from CuOx-PE films as found by ICP-MS after different washing cycles for Cu-PE films contacted and not contacted with bacteria.

	Cu-released for PE-CuOx non-contacted with bacteria (ppb)	Cu-released for PE-CuOx contacted with bacteria (ppb)
Cycle 1	29.3	22.4
Cycle 3	17.1	12.6
Cycle 5	11.9	9.9

Figure 6.5 shows the effect of the applied light intensity generated in the Suntest solar simulated cavity on the bacterial inactivation kinetics. A higher light intensity photo-generates a higher amount of intermediate highly oxidative radical species leading to bacterial inactivation. Cu and Ag-nanoparticulate films have been reported leading to highly oxidative intermediates not being significantly dependent on the applied light intensity [37, 60, 87].

6.3.3 X-ray photoelectron spectroscopy (XPS) species found during bacterial inactivation

Figure 6.6 presents the XPS-spectrograms for the Cu2p deconvoluted peaks before and after the 15 min bacterial inactivation period. The peaks in Figure 6.6a/b have been assigned according to the information found in references [128, 129]. Figure 6.6a shows the Cu₂O XPS-peak component before the bacterial inactivation process at 932.0 eV and the CuO peak at 931.2 eV and the Cu2p doublet satellite peaks. The shift of the XPS-peaks are considered as being beyond experimental error providing a proof for a new species, when the XPS-shift is >0.2 eV [130]. Figure 6.6b shows XPS shifts taken for samples after bacterial inactivation for the Cu₂O and two CuO-species. A decrease in the Cu₂O (932.3 eV) intensity is detected in Figure 6.6b with respect to the Cu₂O peak in Figure 6a. A concomitant increase in the CuO areas after bacterial inactivation is consistent with the decrease of the Cu₂O-peaks shown in Figure 6.6b.

Table 6.3 shows the variation of the surface atomic concentration percentage before and after the bacterial inactivation. The first row shows the PE-CuOx sample (I) composition in contact with a 50 µl aliquot of NaCl/KCl solution at time zero. The second row shows the PE-CuOx sample (I) in contact with 50 µl of bacterial culture suspended in NaCl/KCl solution at time zero. The third row shows the atomic composition on the surface of PE-CuOx sample (I) after bacterial inactivation.

The percentage of Cu on the PE-CuOx topmost layers immediately after the catalyst sputtering is seen to decrease by about 40% due to the bacteria coverage of the film. The amount of Cu on the CuOx-PE surface is seen to increase after bacterial inactivation (36.44%) compared to the value of (29.67%) found at time zero since the bacterial inactivation involves destruction of the bacterial residues on the topmost film layers. In the case of oxygen (O) in Table 6.3, the initial oxygen content is mainly due to the CuO of the fresh CuOx films. At time zero, when the film is contacted with

bacteria the (O) percentage decreases and due to bacterial degradation the (O) signal increases again after bacterial inactivation. The percentage of C- on the *PE-CuOx* fresh films is due to the C- of the PE and CO₂ adsorbed from the air. The content of C- increased upon bacterial contact and decreased after 15 min bacterial disinfection. The amounts detected by XPS of N and S before and after bacterial inactivation shown in Table 6.3 are similar. This points out to the effective catalytic performance of the *PE-CuOx* leading to bacterial photo-killing since the N, S-bacterial percentages did not increase during the disinfection process. The presence of N1s and S2p might come from ambient contamination and not necessarily due to the bacteria's wall degradation. The non-accumulation of N, S-bacterial components reflects the rapid catalytic destruction of bacterial residues precluding the further accumulation of the residual fragments on the *PE-CuOx* film during the photocatalysis.

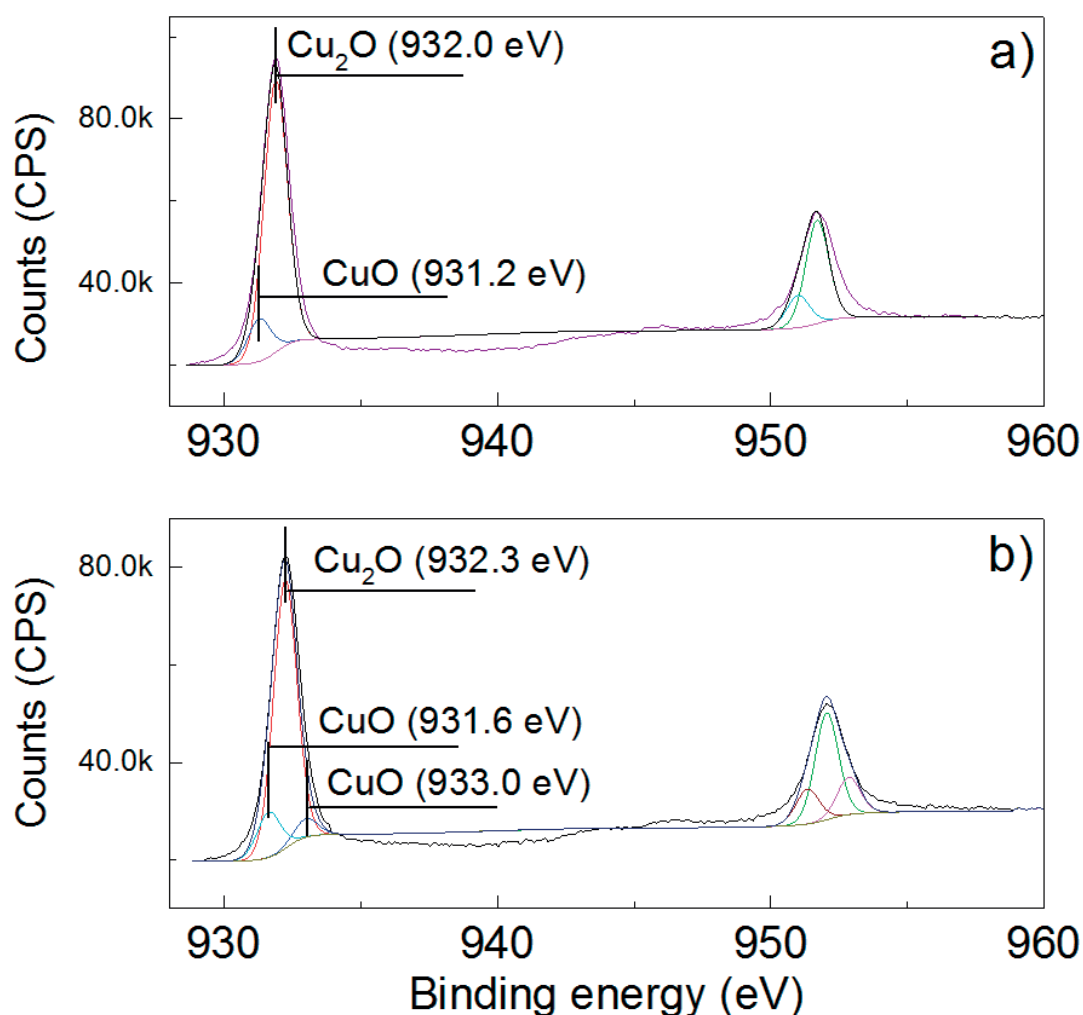


Figure 6.6 XPS peak signal deconvolution of the Cu₂p peaks for a *PE-CuOx* film sputtered for 40 s at 200 mA a) before and b) after bacterial inactivation. For other details see text

Table 6.3. Surface atomic concentration percentages found by XPS on the PE-CuOx (Sample (I)) before and after bacterial inactivation

	Cu	O	C	N	S
PE-CuOx (Sample (I)) (non-used)	59.11	33.07	7.81	--	--
PE-CuOx (Sample (I)) contacted with bacteria (3 s)	29.67	20.91	43.10	5.21	2.31
PE-CuOx (Sample (I)) after bacterial inactivation under light (20 mW/cm²)	36.44	26.72	29.99	4.46	2.50

6.4 Conclusions

The experimental conditions of the sputtering employed to graft the Cu/CuOx on PE were optimized to attain rapid bacterial inactivation kinetics. A detailed study on the PE-CuOx films photo-induced inactivation of bacteria is presented. Very low levels of sunlight were necessary to induce an acceptable bacterial inactivation. Acceptable inactivation times in the minute range were obtained on uniform adhesive flexible films in the dark as well, which confirms the hypothesis of the cytotoxic properties of Cu/CuOx. This property of the Cu-films is more important in practical applications compared to the photo-induced bacterial inactivation processes since the bacterial inactivation in this case proceeds not needing an external energy source. The antibacterial property of the PE-CuOx films is due predominantly to the Cu-oxides behaving as semiconductor as shown by the effect of the applied light intensity on the bacterial inactivation kinetics. Given all these promising results the possibility of depositing CuOx on different supports as fabrics or other kind of polymers could be studied in a deeper way aiming to create antibacterial films that stop the bacterial infections due to skin contact.

7. Chapter 7: Innovative Photo-Fenton catalysis by PE-FeOx films leading to methylene blue (MB) degradation: kinetics, surface properties and mechanism

Published work:

Laura Suárez, Huiyu Dong, Cesar Pulgarin, Rosendo Sanjines, Zhimin Qiang, John Kiwi. "Innovative photo-Fenton catalysis by PE-FeOx films leading to methylene blue (MB) degradation: Kinetics, surface properties and mechanism". Applied Catalysis A: General 519 (2016) 68-77.

Web link:

<http://www.sciencedirect.com/science/article/pii/S0926860X16301521>

Reproduced with permission of Elsevier, Copyright 2017 (license number 4077021491505)

Supplementary material:

Annex C

Doctoral Candidate's contribution:

Investigator and co-author

7.1 Introduction

This chapter addresses the preparation, evaluation and surface characterization of a polyethylene Fe-oxide (PE-FeOx) polymer absorbing visible light up to ~520-530 nm [202]. Polymer thin films have shown to be flexible catalysts supports leading to catalysis/photocatalysis with acceptable kinetics and some reviews have reported the degradation of organic compounds/dyes under UV/sunlight on polymers coated with TiO₂ and Au [127, 203]. However a good adhesion of the photocatalyst semiconductor particles on the polymer surface starting with a colloidal suspension remains a problem since polymers do not present thermal resistance. Therefore, calcination of oxides/composites on polymers is not possible [160].

Methylene blue (MB) has been taken as the model pollutant to test discoloration/degradation on PE-FeOx films. The band-gap of Fe₂O₃ has been reported as 2.2 eV with the positions of the conduction band at 0.4 eV and of the valence band at 2.6 eV respectively [140].

This part of the Thesis provides findings about about: a) an innovative and simple preparation of a stable PE-FeOx photocatalyst film, b) the unambiguous identification of the highly oxidative radicals leading to MB-degradation done by appropriate use of scavengers of the species: •OH-radical, ¹O₂-singlet, HO₂•-radical and vbh⁺, c) the estimation of both lifetime and diffusion length of the •OH-radical away of the PE-FeOx surface d) the determination of the Fe-ions released from the PE-FeOx surface during MB-degradation, e) the evidence for the stable repetitive MB photodegradation on PE-FeOx adhesive films, f) the evaluation of the Fe-Cl species left on the PE-catalyst surface during the photocatalyst preparation and the equilibrium of these species during the discoloration reaction, and finally g) the shift of the Fe, O and C peaks obtained by XPS during MB degradation. The Fe³⁺/Fe²⁺ and O1s reduction and the oxidation of the C1s in the topmost film layers will be evaluated quantitatively within the photocatalysis time.

7.2 Experimental section

7.2.1 Photocatalyst preparation

Low-density PE-films were washed with Milli-Q water followed by acetone and dried at room temperature to eliminate surface contaminants. The PE film was then attached on a cylindrical Teflon support and immersed in a FeCl₃.7H₂O solution stirring for one hour at 80°C. The films were left to dry at room temperature then washed with distilled water and dried at 80 °C for 15 min.

The low-density polyethylene (LDPE) used in this study is a highly branched low crystalline film with formula H(CH₂-CH₂)_nH. The (LDPE) 0.1 mm thick was obtained from Goodfellow, UK (ET311201). The film presented mechanical stability, had a density of 0.92 g cm⁻³ and was thermally stable up to 96°C.

7.2.2 Irradiation source and reactors

Photolysis experiments were performed in a solar simulated Hanau Suntest Lamp with a tunable light intensity attachment equipped with an IR filter to remove IR

radiation > 800 nm. The UV-radiation < 305 nm was removed by the Pyrex wall of the reaction vessels. The PE-FeOx films were positioned at the bottom of the reactor (See supplementary material Ch7-S1 in Annex C). The photochemical reactor was made out of glass and presented cylindrical shape with a diameter of 8 cm and contained an MB volume of 60 ml. The MB-solution in the reactor was stirred during the photolysis. The height of the solution in the reactor was ~2 cm and the MB-solutions were pre-equilibrated for half an hour before each run in the dark.

7.3 Results and discussion

7.3.1 MB discoloration kinetics as a function of solution parameters, MB and H₂O₂ concentration and identification of the radical intermediates leading to MB-degradation

Figure 7.1 presents the MB discoloration results under different experimental conditions. Figure 7.1, trace 1 presents the discoloration of a solution of MB (4×10^{-5} M) by itself under low intensity solar simulated radiation (50 mW/cm^2). Figure 7.1, trace 2 shows the data for MB degradation by a PE-FeOx (Fe 0.30%) solution containing H₂O₂ (10 mM) in the dark. In both cases practically no MB-discoloration was observed. A MB-discoloration of about 30% under solar simulated irradiation was attained within 7h (Figure 7.1, trace 3) for a solution made up by MB and H₂O₂. MB-discoloration within 7h reaching 50% was observed upon addition of 1 mg/L Fe-ions and H₂O₂ (10 mM). In this case, the MB-degradation proceeds through a photo-Fenton process due to suspended iron in the MB solution as shown in Figure 7.1, trace 4. Figure 7.1, trace 5 shows a run under Suntest irradiation in the presence of a 400 nm cut-off filter. The visible light drives the MB-discoloration almost to completion within 7 hours. Finally, Figure 7.1, trace 6 presents the complete MB-discoloration by a PE-FeOx (Fe 0.30%) film in a solution containing H₂O₂ (10 mM). The insert in Figure 7.1, shows the MB total organic carbon (TOC) of ~66% reduction for the solution reported in Figure 7.1, trace 6. Different Fe-loadings on the PE-FeOx films did not significantly modify the MB-discoloration kinetics reported in Figure 7.1, trace 6. The lowest Fe-loading of 0.17% (see Table 7.1) lead to a 70% MB-discoloration within 7h compared to the complete discoloration induced by the PE-FeOx (Fe 0.30%) (See supplementary material Ch7-S2).

Figure 7.2a presents the MB-discoloration on PE-FeOx (Fe 0.30%) under simulated sunlight for MB-solutions presenting different concentrations. Similar end-points for the complete MB-discoloration suggest a mass transfer controlled type of reaction. Figure 7.2b shows the MB discoloration kinetics being accelerated by increasing H₂O₂ concentrations. The effect of an increasing concentration of H₂O₂ can be understood by the reaction (7-1) showing that higher concentrations of peroxide lead to a higher concentration of •OH. The scavenging of the •OH-radicals on the MB-degradation is reported next in Figure 7.3.

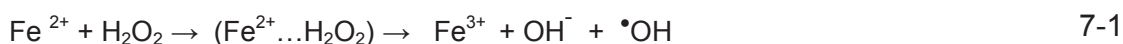


Figure 7.3 shows the scavenging of the holes and radical intermediates generated in MB solutions under Suntest light irradiation. It is readily seen that a 0.2 mM methanol in solution quenches 55% of the MB-degradation and 0.2 mM NaN_3 in solution reduces the MB-degradation by 60%. NaN_3 quenches both $\bullet\text{OH}$ -radical and $^1\text{O}_2$ this is why Figure 7.3 trace (2) shows a lower effect as the NaN_3 is reacting with two different ROS. Results indicate that the $\bullet\text{OH}$ -radical is the most active intermediate leading to MB-degradation. The $\text{HO}_2\bullet/\text{O}_2^-$ quencher p-benzoquinone and the EDTA-2Na hole quencher $\text{vb}(\text{h}^+)$ did practically not preclude the MB-degradation under light irradiation. The limited semiconductor effect by the PE-FeOx film on MB degradation becomes evident since the valence band holes $\text{vb}(\text{h}^+)$ were practically not scavenged by EDTA-2Na. Another evidence for the predominant effect for the photo-Fenton effect leading to the MB-degradation comes from the observation that sunlight light doses between 30 mW/cm^2 and up to 90 mW/cm^2 affected only marginally the rate of MB-degradation (see Supplementary material Ch7-S3).

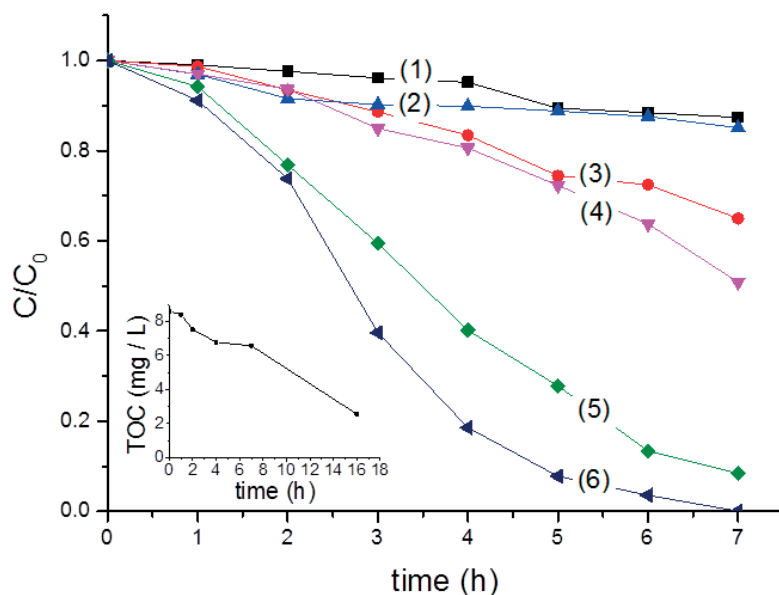


Figure 7.1. Discoloration of MB ($4 \times 10^{-5} \text{ M}$) under different conditions at an initial pH 6 in solution: (1) MB alone under solar simulated irradiation (50 mW/cm^2), (2) PE-FeOx (Fe 0.30%) in the presence of H_2O_2 (10mM) in the dark, (3) H_2O_2 (10mM) under solar simulated irradiation (50 mW/cm^2), (4) Fe-ions in solution added to the MB-solution containing H_2O_2 (10mM) under solar simulated irradiation (50 mW/cm^2), (5) MB discoloration on PE-FeOx (Fe 0.30%) in the presence of H_2O_2 (10mM) under solar simulated irradiation (50 mW/cm^2) in the presence of a cut-off filter at 400 nm, (6) MB discoloration on PE-FeOx (Fe 0.30%) in the presence of H_2O_2 (10mM) under solar simulated irradiation (50 mW/cm^2). Insert: TOC decrease of MB ($4 \times 10^{-5} \text{ M}$) in the presence of PE-FeOx (Fe 0.30%) film and H_2O_2 (10mM). Suntest light intensity: 50 mW/cm^2

With this information we suggest the nature of the radicals leading to MB-degradation [14-17].

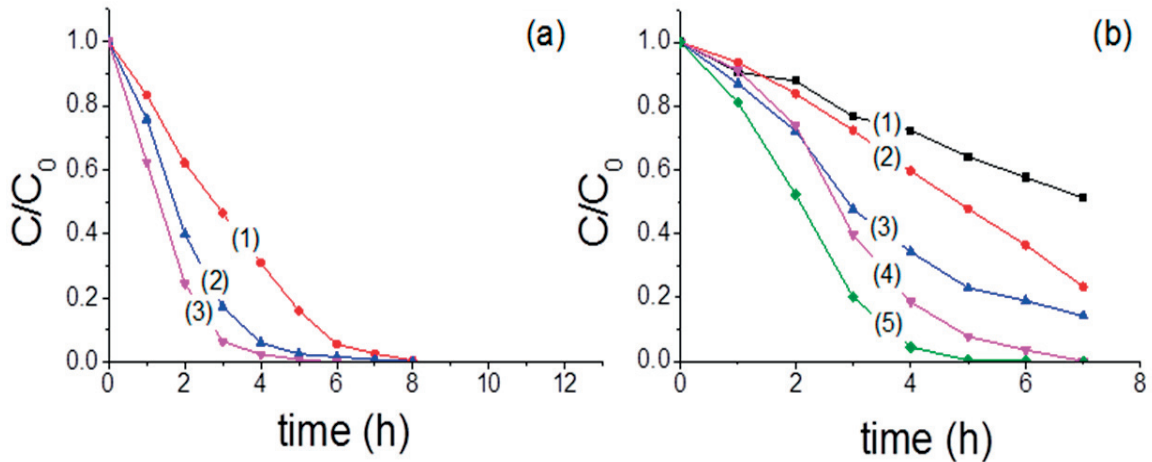
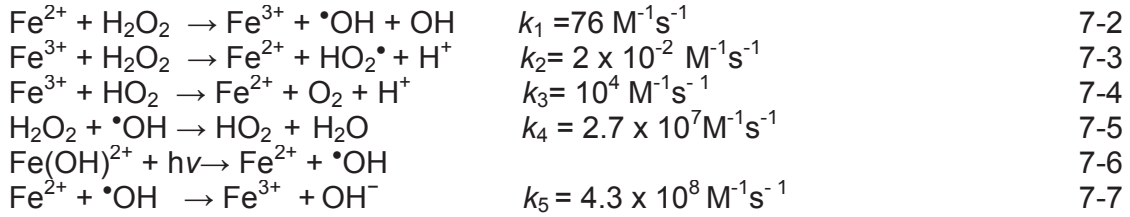


Figure 7.2. (a) Discoloration of MB by on a PE-FeOx (Fe 0.30%) film irradiated under solar simulated irradiation ($50 \text{ mW}/\text{cm}^2$) as a function of the initial MB concentration initial in a solution H_2O_2 (10mM). MB: (1) 4×10^{-5} M, (2) 2×10^{-5} M, (3) 1×10^{-5} M. (b) Discoloration of MB by on a PE-FeOx (Fe 0.30%) film irradiated under solar simulated irradiation ($50 \text{ mW}/\text{cm}^2$) as a function of the initial H_2O_2 concentration, MB 4×10^{-5} M, and the H_2O_2 concentration in traces: (1) 1 mM, (2) 2 mM, (3) 5 mM, (4) 10 mM, (5) 20 mM.

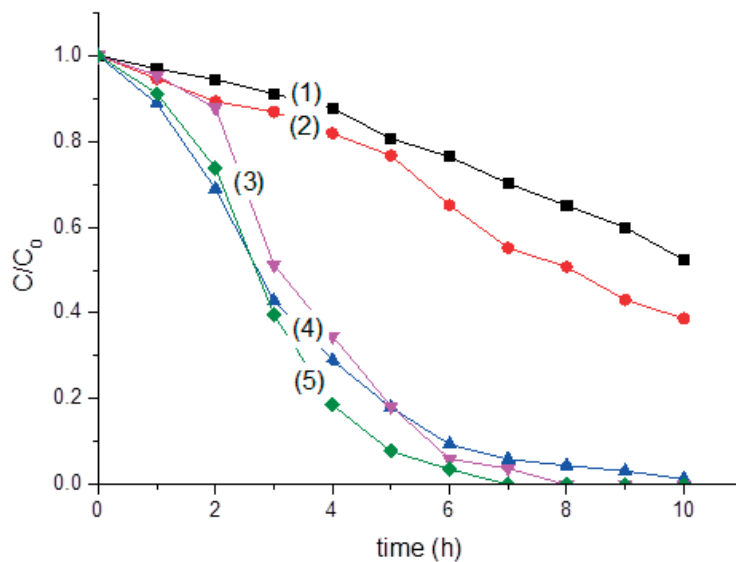


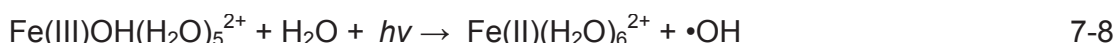
Figure 7.3. Discoloration of MB (4×10^{-5} M) by means of PE-FeOx (Fe 0.30%) film, H_2O_2 (10mM) and ROS scavengers under sunlight irradiation: (1) 0.2 mM methanol, (2) 0.2 mM NaN_3 , (3) 0.2 mM p-benzoquinone, (4) 0.2 mM EDTA-2Na, (5) run without scavengers

The degradation of MB due to the Suntest sunlight simulated alone is negligible as shown in Figure 7.1, trace 1. The H₂O₂ decomposition leading to •OH-radicals under the experimental conditions used: H₂O₂ + hv → 2 •OH-radicals is not important as shown in Figure 7.2, trace 3 due to the low absorption coefficient of H₂O₂ > 305 nm, which is close to 0.7 M⁻¹cm⁻¹ [204]. Reactions 7-1 and 7-2 present the classical Fenton mechanism playing a role in MB-degradation. Reaction (7-3) seems not to be important since the amount of HO₂• radicals produced is negligible during the MB-degradation as shown in Figure 7.3, trace 3. During the MB-degradation the near natural pH of the MB- solution of 6.0 was seen to decrease by 2 - 2.5 units as noted by the H⁺-species in eqs.7-3 and 7-4 (see Supplementary Material Ch7-S4).

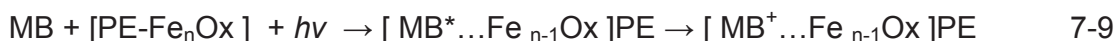
Figure 7.2b shows that increasing the concentration of H₂O₂ (10mM) to H₂O₂ (20mM) led to a faster MB-degradation kinetics. Therefore, there was no scavenging of the •OH-radicals by the H₂O₂. Eq.(7-6) shows the effect of light in the reduction of Fe³⁺ (or regeneration of Fe²⁺) consistent with the data reported in Figure 7.1, trace 2 [205].

No MB-degradation in the absence of light seems to take place due to the extremely slow rate of reaction for the conversion Fe³⁺/Fe²⁺ noted in eq (7-3). Eq (7-7) does not seem to proceed, since the pH within the degradation time moves to more acidic values and this excludes the formation of OH⁻.

The MB-degradation kinetics was found to be faster at more acidic pH-values. An initial pH of 8.5 lead to a 50% MB-degradation within 7 hours while a 100% degradation was attained at pH-values 6.8 and 5.0. At pH 4 the complete MB-degradation was completed within 5 hours (see Supplementary Material Ch7-S5). At pH >4.5 the Fe(II/III)-aqua complexes on the PE-FeOx liberate •OH-radicals under light as shown in reaction (7-8) [21]. This reaction becomes faster as the pH becomes more acidic producing a higher amount of the Fe-hydroxy species Fe(III/II)(H₂O)₆^{3+/2+}.



The FeOx film probably undergoes a *redox* reaction between MB and the Fe³⁺ on the PE-film leading to Fe²⁺ and the formation of the unstable MB⁺-cation



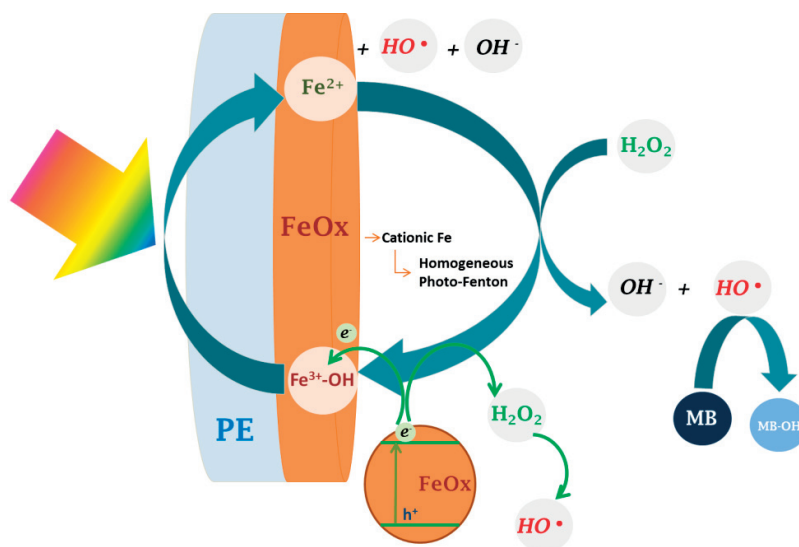
The MB* excited singlet in eq.(7-9) has been reported to have a lifetime of 358ps [206]. This excited singlet intercrosses subsequently to the triplet state with a lifetime of 4.6ms. From this state an unstable MB⁺-cation is formed responsible for the MB degradation/discoloration [80]. The *redox* reaction between MB and Fe^{2+/3+} is shown to be accelerated by increasing amounts of H₂O₂ as shown above in Figure 7.2b and is in agreement with earlier results reported by our laboratory [207]. Figure 7.1 reports the total organic carbon decrease occurring during MB-discoloration, an

indirect indication of CO₂ formation. The MB generates short-lived organic acids branched or not preceding the final CO₂ mineralization step [195]. The last mineralization step of organic compounds proceeds due to the photo-Kolbe reaction. This reaction is outlined below in eq.(7-10), where R is a short notation for the intermediate short carboxylic-acid in solution preceding the CO₂ evolution



From the information presented in Figure 7.1 and from information presented in Supplementary material (Ch7-S2 to Ch7-S5) a simplified MB-degradation mechanism under sunlight/visible irradiation is suggested in the Scheme 7.1.

The PE-FeOx film was prepared using FeCl₃·7H₂O as the iron and chloride source. The Cl⁻-anions on the film surface may as well play a role during the degradation of organic compounds as documented previously [208] leading to highly oxidative Cl₂⁻ radicals:



Scheme 7.1 Outline the MB-degradation mechanism on PE-FeOx films under sunlight/visible irradiation

7.3.2 Lifetime and diffusion distance of the OH-radical away from the PE-FeOx intervening in MB-degradation

Figure 7.3 shows that the [•]OH-radical is the most important oxidative radical leading to MB-degradation. Estimation of the [•]OH-radical lifetime takes into account: a) its production rate constant as noted in eq (7-2) $\text{Fe}^{2+} + \text{H}_2\text{O}_2 \rightarrow \text{Fe}^{3+} + \text{OH}^- + \text{OH}^\cdot$, ($k_1 = 76 \text{ M}^{-1}\text{s}^{-1}$) and b) its reaction with an aromatic organic molecule ($\text{OH}^\cdot + \text{MB (RH)} \rightarrow$

products ($k_6 \sim 10^{10} \text{ M}^{-1}\text{s}^{-1}$). By knowing the solution parameters $\text{MB} = 4 \times 10^{-5} \text{ M}$, $\text{H}_2\text{O}_2 = 10^{-2} \text{ M}$, $\text{Fe}^{3+} = 2 \times 10^{-5} \text{ M}$ (equivalent to 1 mg Fe/L leached in the solution during MB-degradation) and knowing that in the quasi-stationary state the $\bullet\text{OH}$ -radical production as function of time is close to zero; the estimation of $3.8 \times 10^{-11} \text{ M}$ for the $\bullet\text{OH}$ -radical concentration is possible.

To estimate the $\bullet\text{OH}$ -radical mean-free path (x) away from the PE-FeOx surface, the Smoluchowski simplified approximation is used ($x^2 \sim D\tau$). Taking again into consideration the reaction constant of hydroxyl radical ($\bullet\text{OH}$) and MB ($k_6 \sim 10^{10} \text{ M}^{-1}\text{s}^{-1}$), and the known MB concentration, τ can be calculated as $\tau = 1/(k_6 \times [\text{MB}])$. Taking D as the known value for diffusion of molecules with a low molecular weight like MB, and introducing it in the relation $x^2 \sim D\tau$, the mean-free path found x is $\sim 35 \text{ nm}$ (see Supplementary material Ch7-S6 and Ch7-S7).

7.3.3 Fe-leached out during MB-degradation and repetitive dye degradation

Figure 7.4 shows the Fe-ions leached into the solution during the degradation of the MB-solution. The total Fe-ions leached out after 7 hours was $\sim 0.9 \text{ mg/L}$. This amount of Fe is close to the Fe-ions concentration added in the run reported in Figure 7.1 trace 4 (1 mg/L Fe-ions), leading to a 50% MB-degradation within 7 hours. Therefore, as the reaction time progresses, the PE-FeOx film would catalyze the MB-degradation through a progressively heterogeneous / homogeneous reaction. The Fe^{3+} -ions make up about 90% of the Fe-ions detected in the solution after 7 hours, while the Fe^{2+} -ions make up the residual Fe-ions. This is expected due to two reasons: a) the solution contains H_2O_2 during the entire degradation process and b) the conversion in the dark of Fe^{2+} to Fe^{3+} -ions proceeds with a rate $k_1 = 76 \text{ M}^{-1}\text{s}^{-1}$ while the back reaction to the Fe^{2+} proceeds with a slow rate of $k_2 = 2 \times 10^{-2} \text{ M}^{-1}\text{s}^{-1}$ as noted by equations (7-2) and (7-3) above in section 7.3.1.

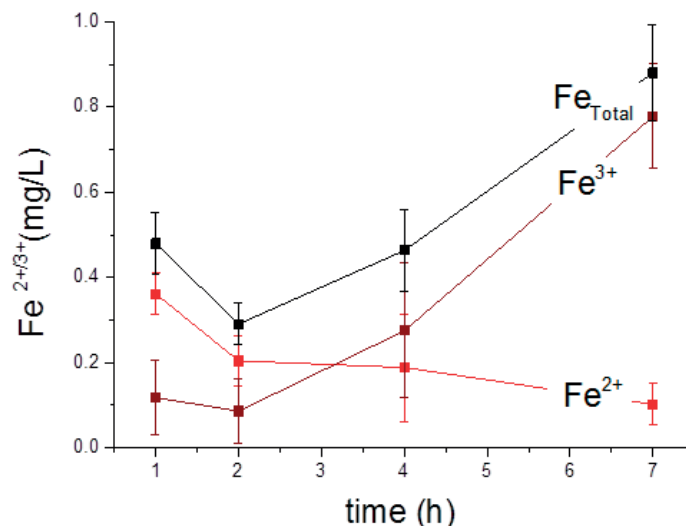


Figure 7.4 Fe-ions released by the PE-FeOx (0.30%) film into the MB ($4 \times 10^{-5} \text{ M}$) solution containing H_2O_2 (10mM), Suntest light intensity 50 mW/cm^2

Figure 7.5 shows repetitive MB-degradation cycles. The $\text{Fe}^{3+}/\text{Fe}^{2+}$ -ions leached into the solution during the MB-degradation revert back to the PE-FeOx film surface containing the Fe-agglomerates after degrading the dye. This is the way nature is cleaned either by a dark or photo-activated Fenton reagent in water bodies containing micro-molar peroxide/oxidative radical concentrations and Fe-ions [209, 210].

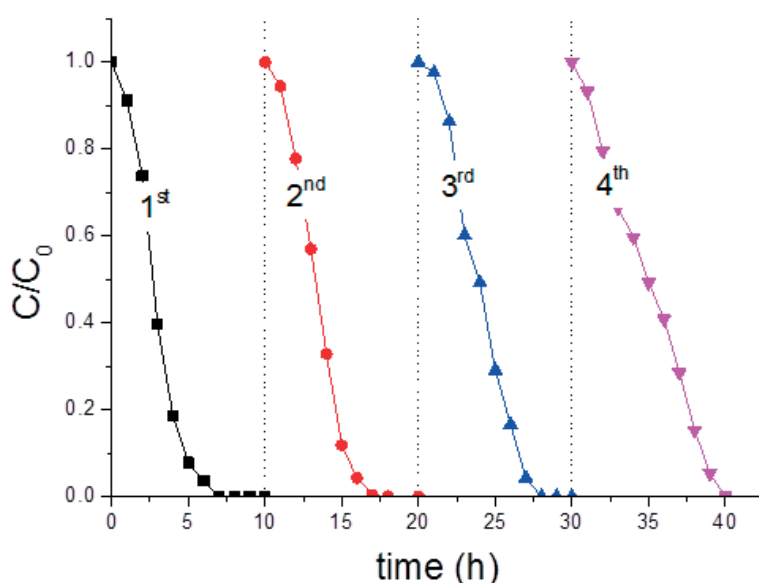


Figure 7.5 Repetitive MB (4×10^{-5} M) discoloration on PE-FeOx (Fe 0.30%), H_2O_2 (10mM), Suntest light intensity 50 mW/cm^2

7.3.4 Properties of PE-FeOx films: optical absorption, X-ray diffraction (XRD) particle size, film roughness and X-ray photoelectron spectroscopy (XPS)

Figure 7.6 presents optical absorption of PE-FeOx films prepared with a different loading of Fe as shown in Table 7.1. As the Fe loading increases on the PE-film, the optical Fe d-d transition also increased. The onset of the Fe_2O_3 absorption at 550-600nm (2.1-2.2 eV) is in good agreement with the values reported by Bard [202]. The $\text{Fe}_2\text{O}_3/\text{cb}$ with a cb at 0.4-0.5 eV pH 0 vs SCE does not allow the reduction of O_2 (air) requiring potentials of ~ 0.16 eV [60, 87] which would subsequently attack MB. This provides a further evidence for the MB-degradation occurring due to photo-Fenton catalysis and not through to a light induced PE-FeOx semiconductor effect. The MB-degradation was due to the PE-FeOx film comprising a mixture of iron species. This will be shown by XRD next in Figure 7.7.

Figure 7.7 shows FeOCl , $\text{FeCl}_2 \cdot 2\text{H}_2\text{O}$, $\text{FeCl}_2 \cdot 4\text{H}_2\text{O}$ and FeCl_3 species in the XRD spectrogram of PE-FeOX films for: a) sample with a Fe 0.37%/0.39 Cl% content and b) a sample with a Fe 0.30%/0.31 Cl% content. The possible participation of Fe-ions and Cl^- species has been described in eqs.(7-11 - 7-14) and the role of the highly oxidative

radicals $\text{Cl}_2^{\cdot-}$ and ClOH^{\cdot} may also be important during the MB-degradation due to the high reduction potential of the $\text{Cl}/\text{Cl}_2^{\cdot-}$ pair [208].

Figure 7.8a shows AFM images of PE-FeOx (Fe 0.37%) film scanning an area ($20 \times 20 \mu\text{m}$). The surface morphology shows micro-agglomerates of $\sim 6 \mu\text{m}$ size and present a roughness of $\text{RMS} = 148 \text{ nm}$ (see Table 7.2). The values for the RMS reported in Table 7.2 are the median in the Z plane of $Z_{1a} - Z_{2a}$ shown in the right hand-side of Figure 7.8 a-d. The distance between the peaks and the valleys is taken for many particles in the agglomerates and the final values summation are averaged for resolutions of $4 \times 4 \mu\text{m}$ or $20 \times 20 \mu\text{m}$.

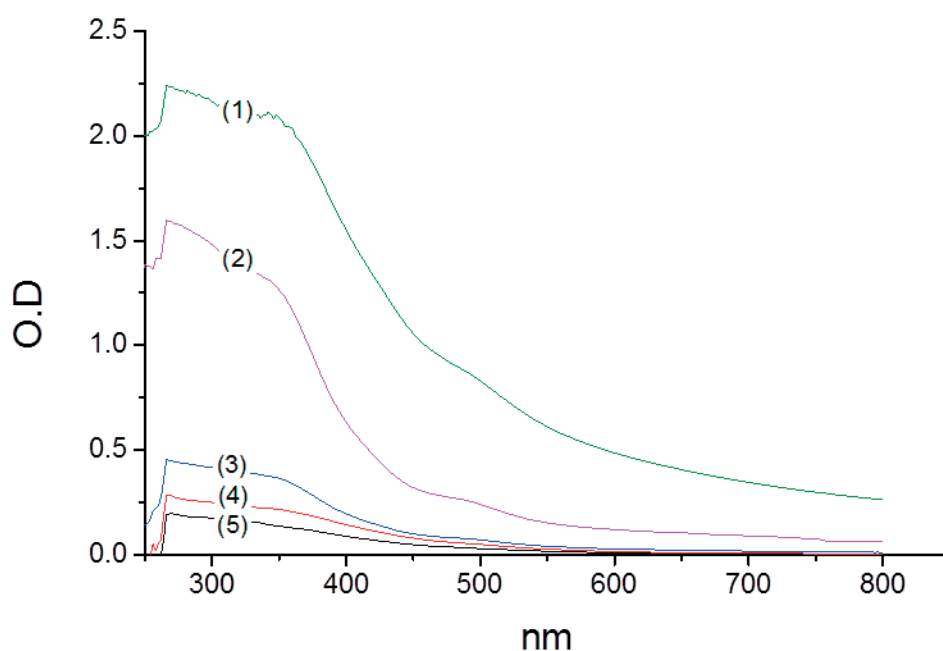


Figure 7.6 Optical density (O.D) of PE-FeOx films: (1) 0.37 Fe wt % / wt PE, (2) 0.30 Fe wt % / wt PE, (3) 0.18 Fe wt % / wt PE, (4) 0.17 Fe wt % / wt PE, (5) 0.10 Fe wt % / wt PE

Figure 7.8b shows the agglomerates formed in a $4 \times 4 \mu\text{m}$ scanning area as noted in Table 7.2. The Figure 7.8c shows AFM images for PE-FeOx (Fe 0.17%) film scanning an area of $20 \times 20 \mu\text{m}$. The surface morphology shows the micro-agglomerates of $\sim 10 \mu\text{m}$ with a roughness of $\text{RMS} = 60 \text{ nm}$. Figure 7.8d show sizes $\sim 100 \text{ nm}$ for the nano-particles PE-FeOx films (Fe 0.17%). Scanning an area of $20 \times 20 \mu\text{m}$ area renders an $\text{RMS} = 60 \text{ nm}$ (Table 7.2) while scanning an area of $4 \times 4 \mu\text{m}$ shows the presence of triangular shaped nano-particle of sizes $\sim 100 \text{ nm}$ and roughness $\text{RMS} = 20.5 \text{ nm}$. Figure 7.8 shows that decreasing in the Fe-content in the films lead to: a) lower surface roughness and b) an increase in the average particle size.

Table 7.1 Fe and Cl wt % /wt PE determined by X-ray fluorescence as a function of the FeCl₃ content during the preparation of PE-FeOx. Additionally, assessed cm³ FeCl₃ / cm² PE based on XRF data and material properties.

FeCl ₃ ·7H ₂ O suspension concentration (g/L)	Fe wt % /wt PE	Cl wt % /wt PE	(cm ³ FeCl ₃ / cm ² PE)
0	0.1	<0.20	3.17E-06
0.5	0.17	<0.20	5.39E-06
1	0.18	<0.20	5.71E-06
10	0.3	0.31	9.52E-06
20	0.37	0.39	1.17E-05

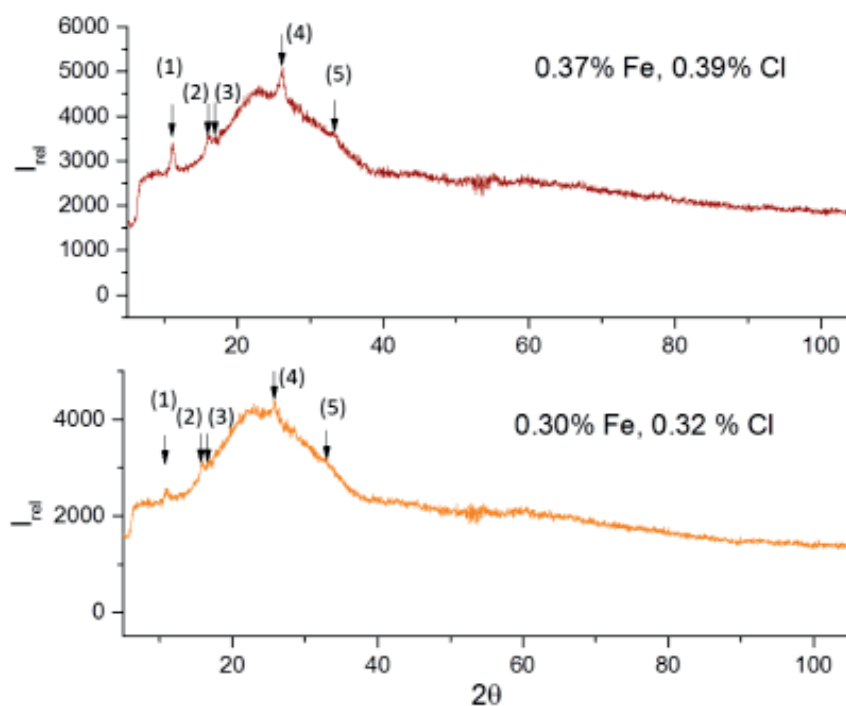


Figure 7.7 XRD results for FeOx deposited on glass under the similar conditions as used to load Fe on PE. Peak in Figure 7b for the two Fe and Cl-loading % used: (1) ClFeO, (2) FeCl₂·2H₂O, (3) FeCl₂·4H₂O, (4) FeCl₃, (5) FeCl₃

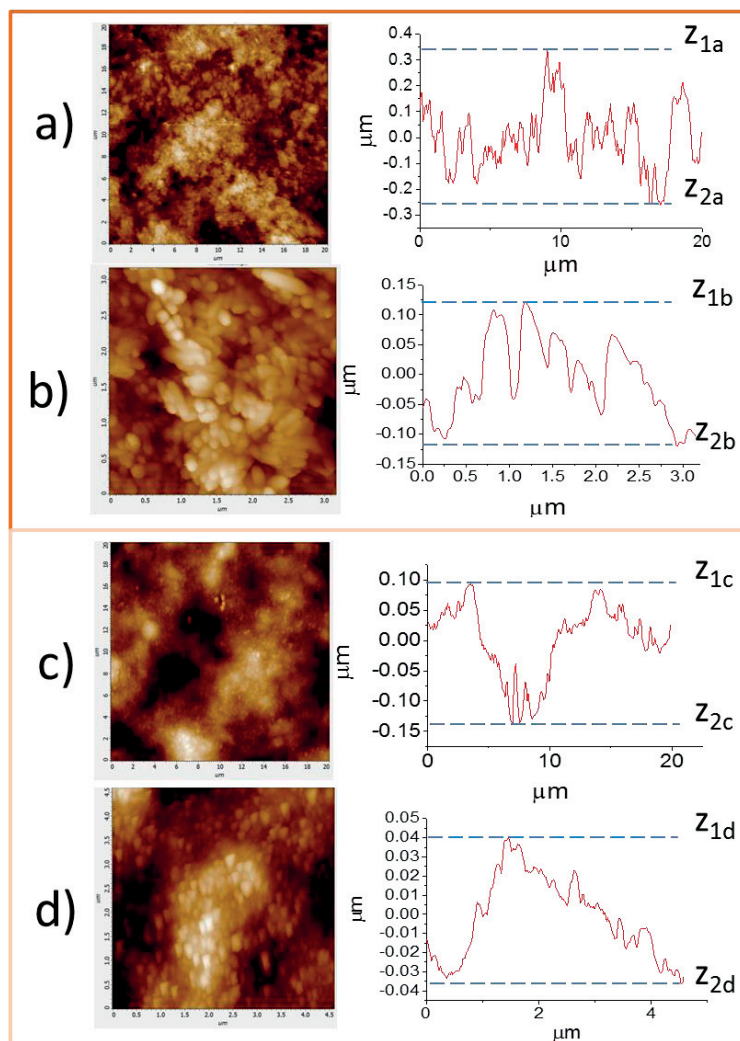


Figure 7.8 (a) Roughness of PE-FeOx (Fe 0.37%) film taken at a roughness resolution of 20x20 μm , (b) Roughness of PE-FeOx (Fe 0.37%) film taken at a roughness resolution of 4x4 μm , (c) Roughness of PE-FeOx (Fe 0.17%) film taken at a roughness resolution of 20x20 μm , (d) Roughness of PE-FeOx (Fe 0.17%) film taken at a roughness resolution of 4x4 μm .

Table 7.2 PE-roughness as a function of Fe loadings in the PE-FeOx film

	Roughness Low resolution (20x20 μm)		Roughness High resolution (4x4 μm)	
	RMS (nm)	Average (nm)	RMS (nm)	Average (nm)
PE-FeOx, Fe 0.37%	148	120	78.4	63.3
PE-FeOx, Fe 0.17%	60.08	47.3	20.5	16.5

Figure 7.9 presents the results of the XPS runs within the MB-degradation time. The Fe2p peak shifts in the binding energies (BE) from 709.72eV to 709.96 eV show the

oxidation of Fe2p states [128, 129]. The shift towards higher BE-values for the Fe2p-states means that the Fe is being oxidized within a period of 10 hours. A new oxidation state appears since the BE displacement was > 0.2 eV corrected for electrostatic charging effects [130]. Therefore, the MB-degradation involves concomitant *redox* Fe-reactions on the film surface. The O1s spectral shift in Figure 7.9 from 530.18 eV to 530.48 eV involves a modest reduction to O1s reduced species. This shows again *redox* processes during the MB-degradation time. The O1s are seen to be broad with multiple overlapping components. This makes difficult to accurately quantify the oxygen chemical states [128, 129]. O-species have been reported in metal oxides with different binding energies and their interpretation is not straight forward since the O1s binding energy of many metal-oxides fall within a narrow range. This is also complicated by the presence organic C-O compounds and carbonates. The *redox* reactions involving C1s-species during the MB-degradation are also shown in Figure 7.9. A shift in the C-peak from 283.46eV to 283.66 eV means an oxidation of the C1s-species -whatever their identity- on the topmost PE-layers during MB-degradation. This is to be expected due of the nature of the Fenton reagent $\text{Fe}^{2+}/\text{H}_2\text{O}_2$ that transforms instantaneously the Fe^{2+} -ions into Fe^{3+} -ions by contact with H_2O_2 .

Table 7.3 shows the surface percentage atomic concentration of the elements making-up the PE-FeOx as determined by XPS. Previous to the XPS measurements, the PE-FeOx samples were put in contact with MB in the dark (for 30 min) to deposit a fine layer of MB on the of PE-FeOx film surface. During 30 min the MB undergoes adsorption on the PE-FeOx film in the absence of H_2O_2 in the dark. At time zero, Table 7.3 shows the C-content is 82.03% and the C-content decreases afterwards due to the loss of C during the MB-degradation (see insert Figure 7.1). The N- content found in the MB formulation is shown to decrease within the time of photocatalysis. The O-increases with time due to the generation of carboxylic acid intermediates in the solution. This is in agreement with results reported by Houas et. al. [133]. Table 7.3 also shows that the S-content decreases by more than 70% within the MB-degradation time. The Fe-content on the PE-FeOx surface is shown to increase since the topmost PE-FeOx surface is cleaned progressively from the dye during MB-degradation.

Table 7.3. Surface percentage atomic concentration of PE-FeOx during MB discoloration determined by XPS. The PE-FeOx samples used were put in contact with MB for a short period in the dark (30s)

Reaction time (h)	C	N	O	S	Fe
PE	93.13		4.66		
0	82.03	2.33	13.02	1.03	1.17
2	74.43	3.20	18.91	1.37	1.52
10	76.81	0.20	18.12	0.36	2.28

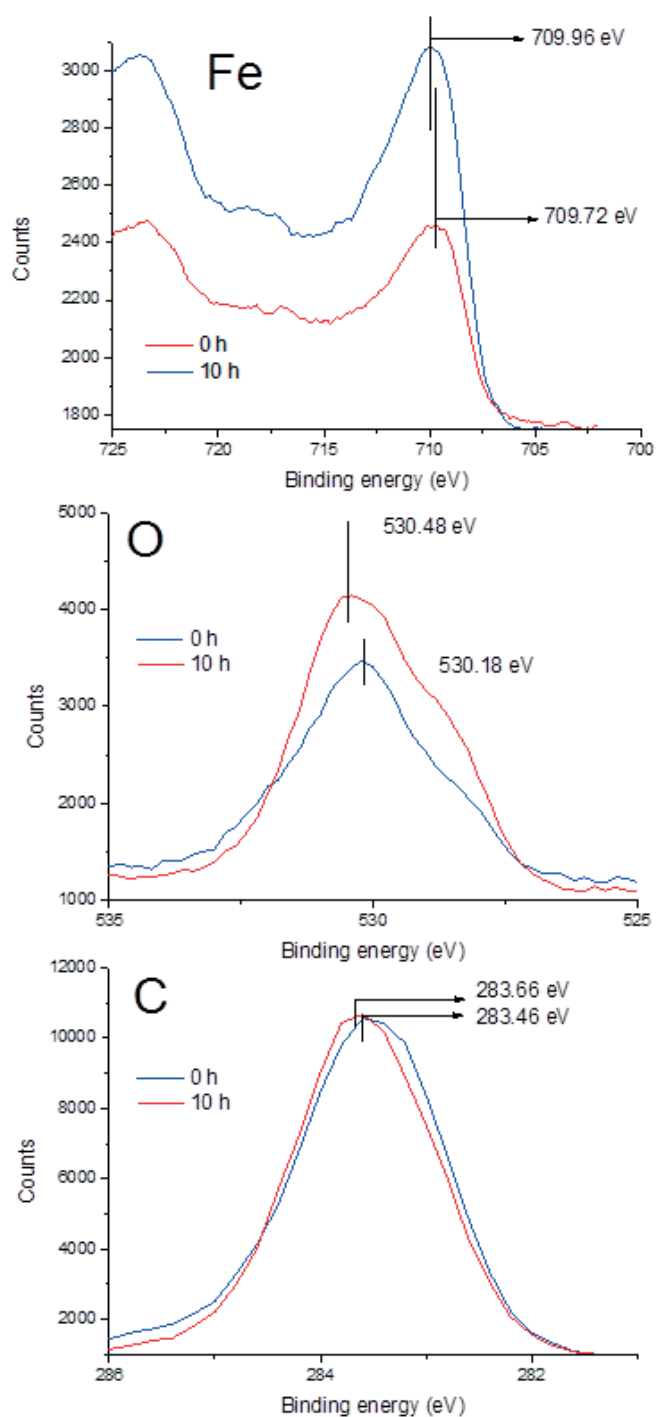


Figure 7.9 XPS signals of Fe, O and C at time zero and after discoloration of a MB 4×10^{-5} (mol L^{-1} solution), under Suntest irradiation 50 mW/cm^2 on PE-FeOx films (0.30 Fe wt % / wt PE)

Figure 7.5 shows stable repetitive cycling of the PE-FeOx film leading to MB-degradation and provides the proof that the surface of the PE-FeOx does not accumulate intermediate residual species hindering the repetitive catalyst use. This

observation is consistent with the XPS data described in the preceding paragraph suggesting that the catalytic destruction of the intermediates during MB-degradation is a fast process.

7.4 Conclusions

This chapter describes MB-degradation by PE-FeOx films inducing photo-Fenton reactions under low intensity sunlight/visible irradiation. The PE-FeOx resulted as a simple photocatalyst, prepared with economic highly accessible materials. The use of iron oxides allowed the absorption of not only UV-light but also visible-light, increasing the light use to a wider range of the solar spectra. The MB-degradation kinetics follows the kinetics typical of mass transfer controlled reactions on the PE-FeOx film. Evidence is presented for the specific nature of the oxidative radical intermediates intervening in the MB- degradation. The limited vb hole (h^+) effects and the quasi-absence of light intensity effects suggest that the FeOx intervening as a semiconductor plays a modest role during MB-degradation. A mechanism leading to MB-degradation is suggested based on the experimental work carried out during this study. The PE-FeOx films induce Fenton/photo-Fenton catalysis leading to MB-degradation by a progressive co-participation of homogeneous and heterogeneous catalysis in solution. The PE-FeOx film surface composition was characterized by several overlapping surface techniques. Although activity under solar light was achieved, still there are diffusion limitations due to the bulk of solution, so considerations as stirring, reactor design and reduction of bulk have to be accounted. Due to the coexistence of homogeneous and heterogeneous photocatalysis observed during experimental work of testing the PE- FeOx, this photocatalyst could also be used as a source that gradually releases iron oxides making them available to be consumed during a determined amount of operation cycles. More importantly, the results obtained for this photocatalyst can be extrapolated to solid-air interface for its use as self-disinfecting or self-cleaning material because the diffusion limitations would be eliminated. FeOx constitutes an ecofriendly semiconductor as it occurs naturally, its use instead of CuOx would avoid the controversy of heavy metals leaching.

8. Chapter 8: Conclusions and perspectives

This Thesis comprises the preparation of supported photocatalysts active in the degradation of a model pollutant in solution and bacterial inactivation, both in solution and at the solid-air interface. The main photoactive materials used were TiO_2 , iron oxides, Cu-decorated TiO_2 and copper oxides. The supports used were either polymeric films or inorganic materials as glass Rashig rings or glass fiber mats. The explored deposition techniques followed mostly wet impregnation except for the antibacterial films which involved sputtering due to uniformity, stability and other more exigent requirements. Polymeric sheets are good support for antibacterial films and self-cleaning applications; they represent materials commonly used in daily life and especially in hospitals. For applications as degradation of pollutants in solution, the study of polymeric films as supports still faces the challenge of overcoming diffusion limitations and photocatalyst fixation. Inorganic supports made up of glass (rashig rings of glass fiber mats) could offer higher surface contact between targets and photocatalyst reducing in some extent the diffusion limitations while allowing solar light penetration, nevertheless the mechanical resistance or preparation procedure can pose a limitation. From the work carried out during this Thesis, the following conclusions and perspectives can be highlighted:

- PE- TiO_2 and PE-FeOx films leading to the degradation of MB were investigated. Both supported photocatalysts were prepared under mild conditions, at low temperatures and did not require expensive instrumentation. Both of the films showed potential for practical applications in water treatment for degrading methylene blue in solution due to their stable repetitive photocatalytic performance. The prepared and tested PE- TiO_2 films used a UV light intensity equivalent to 1% of the of the light intensity used for PE-FeOx films, knowing that the UV portion of solar light is 5%, the performance of the PE- TiO_2 under solar light is expected to improve proportionally.

As mentioned before, the results obtained for these two photocatalysts give a good indication of their potential application in air-solid interfaces for self-cleaning and self-disinfecting materials; in absence of diffusion limitations posed by the bulk of solution, the films are expected to perform much better in the degradation of molecules or bacterial inactivation. Continuing in the line of water decontamination, the use of photocatalytic films disposed in reactors in a way that increases contact between targets and photoactive material could be explored. Moreover, the study of degradation of molecules that do not absorb visible light which concentration can be assessed by means of simple techniques can be explored as a more suitable approximation for understanding and generalization of the photocatalytic degradation mechanism. The application of films for water decontamination faces the challenge of optimization of reactors design. Further work on more advanced photocatalytic films together with the exploration of their geometrical

disposition in reactors for pollutants degradation in solution remains a task of the future.

- RR@TiO₂-Cu and GF-TiO₂-Cu: these approaches were followed for two main reasons: a) increase the contact between target and photocatalyst and b) shift the TiO₂ activity to the visible range by the addition of small amounts of Cu. Cu-decoration seemed to induce an intra-gap-electronic state in the TiO₂ facilitating the indirect electron transition in the TiO₂ band-gap and leading to an accelerated MB-degradation kinetics. As Cu-decorated TiO₂ supported on Raschig rings performed well for low Cu percentages in MB degradation, glass fiber mats were used as supports for a new catalyst active not only in MB solution degradation but also in its degradation at the solid-air interface (self-cleaning) as well as in water disinfection. The use of Cu showed to have an important effect in water disinfection as not only the electronic Cu intra-gap was made available for increasing TiO₂ activity in the visible, also the Cu cytotoxic property was exploited, which additionally can be related to the induction of Fenton-like reactions. The Raschig rings and the glass fiber mats are more suitable materials to be used as support for photocatalyst in the industry; the design of reactors using these photocatalysts together with the exploration of other semiconductors or iron sources for inducing photo-Fenton reactions is a field of further studies.
- The PE-CuOx films showed to be active in photo-induced inactivation of bacteria. Low levels of sunlight were necessary to induce bacterial inactivation but these films showed also antibacterial activity in the dark. This property of the Cu-films is key for practical applications compared to the photo-induced bacterial inactivation processes since the bacterial inactivation would proceed in places not reached by light such as drawers and wardrobes. The antibacterial property of the PE-CuOx films induced by light is due to the Cu-oxides behaving as semiconductor; the higher the light intensity is the faster the bacterial inactivation kinetics will be. PE-CuOx films seem to be a good approach for avoiding bacteria spreading due to hands contact. The use of Cu-sputtered materials for situations that involve contact with bloodstream or mucous membranes would be yet a field of optimization and thoughtful research as the effect of Cu-ions in human health would have to be carefully assessed.

Perspectives:

In general for supported photocatalysts active in degradation of a model pollutant in solution and in water disinfection, the future work is wide. For instance in Medellín-Colombia there is a major challenge to be faced by the industrial contamination of the Medellín River. The river turns red or blue do to the dyes contained in residual water from textile industry. The use of supported

photocatalysts could address this problem and find a partial solution to the current situation. Furthermore, supported photocatalysts using natural fibers that have a similar morphology as the glass fiber mats (high specific surface area) could also be used in water disinfection for human consumption. Natural fibers and iron oxides could be readily available in some locations where high level of solar irradiation is also abundant. Another interesting approach could be the use of plastic Raschig rings as supports for photoactive material as TiO_2 showed to strongly attach to polyethylene. Raschig rings of polymeric materials having negatively charged groups in their structure could offer an interesting option as this characteristic would imply better attachment of positively charged TiO_2 .

Self-cleaning fabrics or self-disinfecting fabrics could also be of big impact in locations where the water is scarce and there are risks of diseases. The catalyst/photocatalysts developed during this work could serve as a basis for further and improved materials. Also, techniques for polymers modification could offer great improvement in both photocatalyst fixation and photocatalytic performance, due to improved wettability or interaction between target and photocatalyst.

The development of films with antiviral and fungicide properties needs to be explored in further investigations. It is known that some fungi are responsible for skin conditions and some viruses are hard or impossible to cure, for instance, the inactivation of a virus on a surface before it finds a host could reduce its propagation among human population.

References

- [1] P.H. Gleick, *Water in crisis: a guide to the worlds fresh water resources*, (1993).
- [2] W.H. Organization, UNICEF, *Progress on sanitation and drinking water–2015 update and MDG assessment*, World Health Organization 2015.
- [3] C.L. Moe, R.D. Rheingans, *Global challenges in water, sanitation and health*, *Journal of Water and Health* 4 (2006) 41-57.
- [4] A. Kramer, I. Schwebke, G. Kampf, *How long do nosocomial pathogens persist on inanimate surfaces? A systematic review*, *Bmc Infect Dis* 6 (2006).
- [5] S.J. Dancer, *The role of environmental cleaning in the control of hospital-acquired infection*, *J Hosp Infect* 73 (2009) 378-385.
- [6] R. Plowman, N. Graves, M.A.S. Griffin, J.A. Roberts, A.V. Swan, B. Cookson, L. Taylor, *The rate and cost of hospital-acquired infections occurring in patients admitted to selected specialties of a district general hospital in England and the national burden imposed*, *J Hosp Infect* 47 (2001) 198-209.
- [7] M.R. Hoffmann, S.T. Martin, W.Y. Choi, D.W. Bahnemann, *Environmental Applications of Semiconductor Photocatalysis*, *Chem Rev* 95 (1995) 69-96.
- [8] C. Walling, *Fentons Reagent Revisited*, *Accounts Chem Res* 8 (1975) 125-131.
- [9] I.K. Konstantinou, T.A. Albanis, *TiO₂-assisted photocatalytic degradation of azo dyes in aqueous solution: kinetic and mechanistic investigations - A review*, *Appl Catal B-Environ* 49 (2004) 1-14.
- [10] J.M. Herrmann, *Heterogeneous photocatalysis: fundamentals and applications to the removal of various types of aqueous pollutants*, *Catal Today* 53 (1999) 115-129.
- [11] O. Legrini, E. Oliveros, A.M. Braun, *Photochemical processes for water treatment*, *Chem Rev* 93 (1993) 671-698.
- [12] J.R. Bolton, S.R. Cater, *Homogeneous Photodegradation of Pollutants in Contaminated Water - an Introduction*, *Aquatic and Surface Photochemistry* (1994) 467-490.
- [13] P.K.J. Robertson, *Semiconductor photocatalysis: an environmentally acceptable alternative production technique and effluent treatment process*, *Journal of Cleaner Production* 4 (1996) 203-212.
- [14] A. Fujishima, K. Honda, *Electrochemical photolysis of water at a semiconductor electrode*, *Nature* 238 (1972) 37-38.
- [15] D.F.a.A.E. Ollis, H., *Photocatalytic purification and treatment of water and air*, Amsterdam, 1993.
- [16] D. Blake, *Bibliography of work on the heterogeneous photocatalytic removal of hazardous compounds from water and air*, National Technical Information Service (NTIS), U.S. Department of commerce, Springfield, VA 22161, USA, 2001.
- [17] A. Fujishima, K. Hashimoto, T. Watanabe, *TiO₂ Photocatalysis: Fundamentals and Applications*, BKC1999.
- [18] E.J. Wolfrum, D.F. Ollis, *Hydrogen-Peroxide in Heterogeneous Photocatalysis*, *Aquatic and Surface Photochemistry* (1994) 451-465.
- [19] P. Pichat, C. Guillard, L. Amalric, A.C. Renard, O. Plaidy, *Assessment of the Importance of the Role of H₂O₂ and O₂(O⁻) in the Photocatalytic Degradation of 1,2-Dimethoxybenzene*, *Sol Energy Mat Sol C* 38 (1995) 391-399.
- [20] S. Malato, P. Fernández-Ibáñez, M.I. Maldonado, J. Blanco, W. Gernjak, *Decontamination and disinfection of water by solar photocatalysis: Recent overview and trends*, *Catal Today* 147 (2009) 1-59.
- [21] B.J. Safarzadeh-Amiri A, Cater S, *The use of iron in advanced oxidation processes*, *J. Adv. Oxid. Technol* 1 (1996) 18-26.
- [22] Y.F. Sun, J.J. Pignatello, *Activation of Hydrogen-Peroxide by Iron(III) Chelates for Abiotic Degradation of Herbicides and Insecticides in Water*, *J Agr Food Chem* 41 (1993) 308-312.

- [23] J. Bandara, C. Morrison, J. Kiwi, C. Pulgarin, P. Peringer, Degradation/decoloration of concentrated solutions of Orange II. Kinetics and quantum yield for sunlight induced reactions via Fenton type reagents, *J Photoch Photobio A* 99 (1996) 57-66.
- [24] R.G. Zepp, B.C. Faust, J. Hoigne, Hydroxyl Radical Formation in Aqueous Reactions (Ph 3-8) of Iron(II) with Hydrogen-Peroxide - the Photo-Fenton Reaction, *Environ Sci Technol* 26 (1992) 313-319.
- [25] A.G. Rincon, C. Pulgarin, N. Adler, P. Peringer, Interaction between E-coli inactivation and DBP-precursors - dihydroxybenzene isomers - in the photocatalytic process of drinking-water disinfection with TiO₂, *J Photoch Photobio A* 139 (2001) 233-241.
- [26] R. Bauer, G. Waldner, H. Fallmann, S. Hager, M. Klare, T. Krutzler, S. Malato, P. Maletzky, The photo-fenton reaction and the TiO₂/UV process for waste water treatment - novel developments, *Catal Today* 53 (1999) 131-144.
- [27] M.R. Dhananjeyan, E. Mielczarski, K.R. Thampi, P. Buffat, M. Bensimon, A. Kulik, J. Mielczarski, J. Kiwi, Photodynamics and Surface Characterization of TiO₂ and Fe₂O₃ Photocatalysts Immobilized on Modified Polyethylene Films, *The Journal of Physical Chemistry B* 105 (2001) 12046-12055.
- [28] J. Fernandez, J. Bandara, A. Lopez, P. Buffat, J. Kiwi, Photoassisted Fenton degradation of nonbiodegradable azo dye (Orange II) in Fe-free solutions mediated by cation transfer membranes, *Langmuir* 15 (1999) 185-192.
- [29] X. Lv, Y. Xu, K. Lv, G. Zhang, Photo-assisted degradation of anionic and cationic dyes over iron(III)-loaded resin in the presence of hydrogen peroxide, *Journal of Photochemistry and Photobiology A: Chemistry* 173 (2005) 121-127.
- [30] A. Noorjahan, V.D. Kumari, A. Subrahmanyam, L. Panda, Immobilized Fe(III)-HY: an efficient and stable photo-Fenton catalyst, *Appl Catal B-Environ* 57 (2005) 291-298.
- [31] J.H. Ramirez, C.A. Costa, L.M. Madeira, G. Mata, M.A. Vicente, M.L. Rojas-Cervantes, A.J. López-Peinado, R.M. Martín-Aranda, Fenton-like oxidation of Orange II solutions using heterogeneous catalysts based on saponite clay, *Applied Catalysis B: Environmental* 71 (2007) 44-56.
- [32] W.J. Song, M.M. Cheng, J.H. Ma, W.H. Ma, C.C. Chen, J.C. Zhao, Decomposition of hydrogen peroxide driven by photochemical cycling of iron species in clay, *Environ Sci Technol* 40 (2006) 4782-4787.
- [33] J. Kiwi, C. Pulgarin, P. Peringer, Effect of Fenton and Photo-Fenton Reactions on the Degradation and Biodegradability of 2-Nitrophenols and 4-Nitrophenols in Water-Treatment, *Appl Catal B-Environ* 3 (1994) 335-350.
- [34] M. Rodriguez, V. Timokhin, F. Michl, S. Contreras, J. Gimenez, S. Esplugas, The influence of different irradiation sources on the treatment of nitrobenzene, *Catal Today* 76 (2002) 291-300.
- [35] H. Fallmann, T. Krutzler, R. Bauer, S. Malato, J. Blanco, Applicability of the Photo-Fenton method for treating water containing pesticides, *Catal Today* 54 (1999) 309-319.
- [36] F. Herrera, C. Pulgarin, V. Nadtochenko, J. Kiwi, Accelerated photo-oxidation of concentrated p-coumaric acid in homogeneous solution. Mechanistic studies, intermediates and precursors formed in the dark, *Applied Catalysis B: Environmental* 17 (1998) 141-156.
- [37] C.M. Chan, T.M. Ko, H. Hiraoka, Polymer surface modification by plasmas and photons, *Surface Science Reports* 24 (1996) 1-54.
- [38] A. Bozzi, T. Yuranova, J. Kiwi, Self-cleaning of wool-polyamide and polyester textiles by TiO₂-rutile modification under daylight irradiation at ambient temperature, *J Photoch Photobio A* 172 (2005) 27-34.
- [39] T. Yuranova, D. Laub, J. Kiwi, Synthesis, activity and characterization of textiles showing self-cleaning activity under daylight irradiation, *Catal Today* 122 (2007) 109-117.
- [40] A. Bozzi, T. Yuranova, I. Guasaquillo, D. Laub, J. Kiwi, Self-cleaning of modified cotton textiles by TiO₂ at low temperatures under daylight irradiation, *J Photoch Photobio A* 174 (2005) 156-164.
- [41] K.T. Meilert, D. Laub, J. Kiwi, Photocatalytic self-cleaning of modified cotton textiles by TiO₂ clusters attached by chemical spacers, *J Mol Catal a-Chem* 237 (2005) 101-108.

- [42] K. Qi, J.H. Xin, W.A. Daoud, C.L. Mak, Functionalizing Polyester Fiber with a Self-Cleaning Property Using Anatase TiO₂ and Low-Temperature Plasma Treatment, *International Journal of Applied Ceramic Technology* 4 (2007) 554-563.
- [43] H.K. Yasuda, Y.S. Yeh, S. Fusselman, A Growth-Mechanism for the Vacuum Deposition of Polymeric Materials, *Pure Appl Chem* 62 (1990) 1689-1698.
- [44] R. d'Agostino, F. Cramarossa, F. Fracassi, F. Illuzzi, 2 - Plasma Polymerization of Fluorocarbons, in: R. d'Agostino (Ed.) *Plasma Deposition, Treatment, and Etching of Polymers*, Academic Press, San Diego, 1990, pp. 95-162.
- [45] J.C. J. Pitts, *Photochemistry*, John Wiley & Sons, New York, 1964.
- [46] W. Kern, Photochemical modification of polymer surfaces, *Trends in Photochemistry & Photobiology* 7 (2001) 11 - 30.
- [47] X.L. Yan, T. Ohno, K. Nishijima, R. Abe, B. Ohtani, Is methylene blue an appropriate substrate for a photocatalytic activity test? A study with visible-light responsive titania, *Chem Phys Lett* 429 (2006) 606-610.
- [48] I.T.F. ceramics, ISO 10678:2010. Fine ceramics (advanced ceramics, advanced technical ceramics) -- Determination of photocatalytic activity of surfaces in an aqueous medium by degradation of methylene blue, 2010, pp. 12.
- [49] A. Mills, An overview of the methylene blue ISO test for assessing the activities of photocatalytic films, *Appl Catal B-Environ* 128 (2012) 144-149.
- [50] F. Green, *Sigma-Aldrich Handbook of Stains, Dyes and Indicators: Sigma-aldrich*, (1990).
- [51] A. Mills, S. Le Hunte, An overview of semiconductor photocatalysis, *Journal of Photochemistry and Photobiology A: Chemistry* 108 (1997) 1-35.
- [52] S.C. Edberg, E.W. Rice, R.J. Karlin, M.J. Allen, Escherichia coli: the best biological drinking water indicator for public health protection, *J Appl Microbiol* 88 (2000) 106s-116s.
- [53] J. Lin, A. Ganesh, Water quality indicators: bacteria, coliphages, enteric viruses, *Int J Environ Heal R* 23 (2013) 484-506.
- [54] H.S. University, A prokaryote Cell: size and composition, in: *ProKar_Cell* (Ed.) JPEG <http://users.humboldt.edu/rpaselk/C431.F08/C431Notes/C431nLec02.htm>, 2008, pp. Typical prokaryote cell. E. coli cell.
- [55] A.A. Gomes, L.M.B.O. Asad, I. Felzenszwalb, A.C. Leitao, A.B. Silva, H.C.R. Guillobel, N.R. Asad, Does UVB radiation induce SoxS gene expression in Escherichia coli cells?, *Radiat Environ Bioph* 43 (2004) 219-222.
- [56] R.L. Knowles, A. Eisenstark, Near-Ultraviolet Mutagenesis in Superoxide Dismutase-Deficient Strains of Escherichia-Coli, *Environ Health Persp* 102 (1994) 88-94.
- [57] R.M. Tyrrell, M. Pidoux, Singlet oxygen involvement in the inactivation of cultured human fibroblasts by UVA (334 nm, 365 nm) and near-visible (405 nm) radiations, *Photochem Photobiol* 49 (1989) 407-412.
- [58] S. Basu-Modak, R.M. Tyrrell, Singlet oxygen: a primary effector in the ultraviolet A/near-visible light induction of the human heme oxygenase gene, *Cancer research* 53 (1993) 4505-4510.
- [59] A.L. Linsebigler, G.Q. Lu, J.T. Yates, Photocatalysis on TiO₂ Surfaces - Principles, Mechanisms, and Selected Results, *Chem Rev* 95 (1995) 735-758.
- [60] A. Fujishima, X. Zhang, D.A. Tryk, TiO₂ photocatalysis and related surface phenomena, *Surface Science Reports* 63 (2008) 515-582.
- [61] J. Schneider, M. Matsuoka, M. Takeuchi, J.L. Zhang, Y. Horiuchi, M. Anpo, D.W. Bahnemann, Understanding TiO₂ Photocatalysis: Mechanisms and Materials, *Chem Rev* 114 (2014) 9919-9986.
- [62] S. Banerjee, S.C. Pillai, P. Falaras, K.E. O'Shea, J.A. Byrne, D.D. Dionysiou, New Insights into the Mechanism of Visible Light Photocatalysis, *J Phys Chem Lett* 5 (2014) 2543-2554.
- [63] A. Mills, S.K. Lee, A web-based overview of semiconductor photochemistry-based current commercial applications, *J Photoch Photobio A* 152 (2002) 233-247.
- [64] C. Pulgarin, J. Kiwi, Overview on photocatalytic and electrocatalytic pretreatment of industrial non-biodegradable pollutants and pesticides, *Chimia* 50 (1996) 50-55.

- [65] S. Ponce, E. Carpio, J. Venero, W. Estrada, J. Rodríguez, C. Reche, J. Candal Roberto, Titanium Dioxide onto Polyethylene for Water Decontamination, *Journal of Advanced Oxidation Technologies*, 2009, pp. 81.
- [66] S. Naskar, S.A. Pillay, M. Chanda, Photocatalytic degradation of organic dyes in aqueous solution with TiO₂ nanoparticles immobilized on foamed polyethylene sheet, *J Photoch Photobio A* 113 (1998) 257-264.
- [67] X. Zhao, Z. Li, Y. Chen, L. Shi, Y. Zhu, Enhancement of photocatalytic degradation of polyethylene plastic with CuPc modified TiO₂ photocatalyst under solar light irradiation, *Applied Surface Science* 254 (2008) 1825-1829.
- [68] A.M. Braun, M.T. Maurette, E. Oliveros, *Technologie photochimique*, Presses Polytechniques Romandes 1986.
- [69] A. Dutschke, C. Diegelmann, P. Lobmann, Preparation of TiO₂ thin films on polystyrene by liquid phase deposition, *J Mater Chem* 13 (2003) 1058-1063.
- [70] M.N. Tchoul, S.P. Fillery, H. Koerner, L.F. Drummy, F.T. Oyerokun, P.A. Mirau, M.F. Durstock, R.A. Vaia, Assemblies of Titanium Dioxide-Polystyrene Hybrid Nanoparticles for Dielectric Applications, *Chemistry of Materials* 22 (2010) 1749-1759.
- [71] C.X. Ye, H.Q. Li, A.A. Cai, Q.Z. Gao, X.R. Zeng, Preparation and Characterization of Organic Nano-Titanium Dioxide/Acrylate Composite Emulsions by in-situ Emulsion Polymerization, *J Macromol Sci A* 48 (2011) 309-314.
- [72] A. Mesnage, M.A. Magied, P. Simon, N. Herlin-Boime, P. Jegou, G. Deniau, S. Palacin, Grafting polymers to titania nanoparticles by radical polymerization initiated by diazonium salt, *J Mater Sci* 46 (2011) 6332-6338.
- [73] S. Lu, S.-S. Sun, J. Niu, L. Zeng, H. Liu, X. Zhao, Poly (thienylene methine) grafted nanocrystalline TiO₂ based hybrid solar cells, *Journal of Materials Science: Materials in Electronics* 23 (2012) 251-256.
- [74] A.A. Essawy, A.E.-H. Ali, M.S.A. Abdel-Mottaleb, Application of novel copolymer-TiO₂ membranes for some textile dyes adsorptive removal from aqueous solution and photocatalytic decolorization, *J Hazard Mater* 157 (2008) 547-552.
- [75] Y. Zhiyong, E. Mielczarski, J. Mielczarski, D. Laub, P. Buffat, U. Klehm, P. Albers, K. Lee, A. Kulik, L. Kiwi-Minsker, A. Renken, J. Kiwi, Preparation, stabilization and characterization of TiO₂ on thin polyethylene films (LDPE). Photocatalytic applications, *Water research* 41 (2007) 862-874.
- [76] Y. Zhiyong, E. Mielczarski, J.A. Mielczarski, D. Laub, L. Kiwi-Minsker, A. Renken, J. Kiwi, Stabilization mechanism of TiO₂ on flexible fluorocarbon films as a functional photocatalyst, *Journal of Molecular Catalysis A: Chemical* 260 (2006) 227-234.
- [77] Y. Zhiyong, D. Laub, M. Bensimon, J. Kiwi, Flexible polymer TiO₂ modified film photocatalysts active in the photodegradation of azo-dyes in solution, *Inorganica Chimica Acta* 361 (2008) 589-594.
- [78] S. Rtimi, C. Pulgarin, R. Sanjines, V. Nadtochenko, J.C. Lavanchy, J. Kiwi, Preparation and Mechanism of Cu-Decorated TiO₂-ZrO₂ Films Showing Accelerated Bacterial Inactivation, *Acs Applied Materials & Interfaces* 7 (2015) 12832-12839.
- [79] S. Rtimi, J. Nestic, C. Pulgarin, R. Sanjines, M. Bensimon, J. Kiwi, Effect of surface pretreatment of TiO₂ films on interfacial processes leading to bacterial inactivation in the dark and under light irradiation, *Interface Focus* 5 (2015).
- [80] S. Rtimi, C. Pulgarin, R. Sanjines, J. Kiwi, Kinetics and mechanism for transparent polyethylene-TiO₂ films mediated self-cleaning leading to MB dye discoloration under sunlight irradiation, *Applied Catalysis B: Environmental* 162 (2015) 236-244.
- [81] S. Rtimi, R. Sanjines, M. Andrzejczuk, C. Pulgarin, A. Kulik, J. Kiwi, Innovative transparent non-scattering TiO₂ bactericide thin films inducing increased E. coli cell wall fluidity, *Surf Coat Tech* 254 (2014) 333-343.
- [82] D. Ni, H. Shen, H. Li, Y. Ma, T. Zhai, Synthesis of high efficient Cu/TiO₂ photocatalysts by grinding and their size-dependent photocatalytic hydrogen production, *Applied Surface Science*.
- [83] T. Čižmar, U.L. Štangar, I. Arčon, Correlations between photocatalytic activity and chemical structure of Cu-modified TiO₂-SiO₂ nanoparticle composites, *Catal Today*.

- [84] F. Bensouici, M. Bououdina, A.A. Dakhel, R. Tala-Ighil, M. Tounane, A. Iratni, T. Souier, S. Liu, W. Cai, Optical, structural and photocatalysis properties of Cu-doped TiO₂ thin films, *Applied Surface Science*.
- [85] T.-T. Pham, C. Nguyen-Huy, H.-J. Lee, T.-D. Nguyen-Phan, T.H. Son, C.-K. Kim, E.W. Shin, Cu-doped TiO₂/reduced graphene oxide thin-film photocatalysts: Effect of Cu content upon methylene blue removal in water, *Ceramics International* 41 (2015) 11184-11193.
- [86] C. Garlisi, G. Scandura, J. Szlachetko, S. Ahmadi, J. Sa, G. Palmisano, E-beam evaporated TiO₂ and Cu-TiO₂ on glass: Performance in the discoloration of methylene blue and 2-propanol oxidation, *Applied Catalysis A: General* 526 (2016) 191-199.
- [87] M. Pelaez, N.T. Nolan, S.C. Pillai, M.K. Seery, P. Falaras, A.G. Kontos, P.S.M. Dunlop, J.W.J. Hamilton, J.A. Byrne, K. O'Shea, M.H. Entezari, D.D. Dionysiou, A review on the visible light active titanium dioxide photocatalysts for environmental applications, *Applied Catalysis B: Environmental* 125 (2012) 331-349.
- [88] V. Etacheri, C. Di Valentin, J. Schneider, D. Bahnemann, S.C. Pillai, Visible-light activation of TiO₂ photocatalysts: Advances in theory and experiments, *J Photoch Photobio C* 25 (2015) 1-29.
- [89] M.J. Sampaio, C.G. Silva, A.M.T. Silva, V.J.P. Vilar, R.A.R. Boaventura, J.L. Faria, Photocatalytic activity of TiO₂-coated glass raschig rings on the degradation of phenolic derivatives under simulated solar light irradiation, *Chemical Engineering Journal* 224 (2013) 32-38.
- [90] S. Sabar, M.A. Nawi, W.S.W. Ngah, Photocatalytic removal of Reactive Red 4 dye by immobilised layer-by-layer TiO₂/cross-linked chitosan derivatives system, *Desalin Water Treat* 57 (2016) 5851-5857.
- [91] J. Saien, M. Asgari, A.R. Soleymani, N. Taghavinia, Photocatalytic decomposition of direct red 16 and kinetics analysis in a conic body packed bed reactor with nanostructure titania coated Raschig rings, *Chemical Engineering Journal* 151 (2009) 295-301.
- [92] P. Raja, V. Nadtochenko, U. Klehm, J. Kiwi, Structure and performance of a novel TiO₂-phosphonate composite photocatalyst, *Appl Catal B-Environ* 81 (2008) 258-266.
- [93] P. Raja, M. Bensimon, A. Kulik, R. Foschia, D. Laub, P. Albers, R. Renganathan, J. Kiwi, Dynamics and characterization of an innovative Raschig rings-TiO₂ composite photocatalyst, *J Mol Catal a-Chem* 237 (2005) 215-223.
- [94] P. Raja, J. Bandara, P. Giordano, J. Kiwi, Innovative supported composite photocatalyst for the oxidation of phenolic waters in reactor processes, *Ind Eng Chem Res* 44 (2005) 8959-8967.
- [95] D. Robert, A. Piscopo, O. Heintz, J.V. Weber, Photocatalytic detoxification with TiO₂ supported on glass-fibre by using artificial and natural light, *Catal Today* 54 (1999) 291-296.
- [96] P. Sun, R. Xue, W. Zhang, I. Zada, Q. Liu, J. Gu, H. Su, Z. Zhang, J. Zhang, D. Zhang, Photocatalyst of organic pollutants decomposition: TiO₂/glass fiber cloth composites, *Catal Today* 274 (2016) 2-7.
- [97] K. Sunada, T. Watanabe, K. Hashimoto, Bactericidal Activity of Copper-Deposited TiO₂ Thin Film under Weak UV Light Illumination, *Environ Sci Technol* 37 (2003) 4785-4789.
- [98] H. Ishiguro, Y. Yao, R. Nakano, M. Hara, K. Sunada, K. Hashimoto, J. Kajioka, A. Fujishima, Y. Kubota, Photocatalytic activity of Cu²⁺/TiO₂-coated cordierite foam inactivates bacteriophages and *Legionella pneumophila*, *Applied Catalysis B: Environmental* 129 (2013) 56-61.
- [99] S. Lin, X. Zhang, Q. Sun, T. Zhou, J. Lu, Fabrication of solar light induced Fe-TiO₂ immobilized on glass-fiber and application for phenol photocatalytic degradation, *Materials Research Bulletin* 48 (2013) 4570-4575.
- [100] C.J. Bodson, B. Heinrichs, L. Tasseroul, C. Bied, J.G. Mahy, M. Wong Chi Man, S.D. Lambert, Efficient P- and Ag-doped titania for the photocatalytic degradation of waste water organic pollutants, *Journal of Alloys and Compounds* 682 (2016) 144-153.
- [101] T.-D. Pham, B.-K. Lee, Cu doped TiO₂/GF for photocatalytic disinfection of *Escherichia coli* in bioaerosols under visible light irradiation: Application and mechanism, *Applied Surface Science* 296 (2014) 15-23.

- [102] T.-D. Pham, B.-K. Lee, Photocatalytic comparison of Cu- and Ag-doped TiO₂/GF for bioaerosol disinfection under visible light, *Journal of Solid State Chemistry* 232 (2015) 256-263.
- [103] G. Borkow, J. Gabbay, Copper, An Ancient Remedy Returning to Fight Microbial, Fungal and Viral Infections, *Current Chemical Biology* 3 (2009) 272-278.
- [104] C. Espirito Santo, E.W. Lam, C.G. Elowsky, D. Quaranta, D.W. Domaille, C.J. Chang, G. Grass, Bacterial killing by dry metallic copper surfaces, *Appl Environ Microbiol* 77 (2011) 794-802.
- [105] G. Grass, C. Rensing, M. Solioz, Metallic Copper as an Antimicrobial Surface, *Appl Environ Microb* 77 (2011) 1541-1547.
- [106] A.L. Casey, D. Adams, T.J. Karpanen, P.A. Lambert, B.D. Cookson, P. Nightingale, L. Miruszenko, R. Shillam, P. Christian, T.S.J. Elliott, Role of copper in reducing hospital environment contamination, *J Hosp Infect* 74 (2010) 72-77.
- [107] J.O. Noyce, H. Michels, C.W. Keevil, Use of copper cast alloys to control *Escherichia coli* O157 cross-contamination during food processing, *Appl Environ Microb* 72 (2006) 4239-4244.
- [108] S.W.J. Gould, M.D. Fielder, A.F. Kelly, M. Morgan, J. Kenny, D.P. Naughton, The antimicrobial properties of copper surfaces against a range of important nosocomial pathogens, *Ann Microbiol* 59 (2009) 151-156.
- [109] S.R. John Kiwi, Cesar Pulgarin, Cu, Cu/TiO₂ thin films sputtered by up to date methods on non-thermal thin resistant substrates leading to bacterial inactivation, in: A. Mendez-Vilas (Ed.) *Microbial pathogens and strategies for combating them: science, technology and education*, Formatex Research Center ISBN2013, pp. 74-82.
- [110] J.A. Byrne, P.S.M. Dunlop, J.W.J. Hamilton, P. Fernandez-Ibanez, I. Polo-Lopez, P.K. Sharma, A.S.M. Vennard, A Review of Heterogeneous Photocatalysis for Water and Surface Disinfection, *Molecules* 20 (2015) 5574-5615.
- [111] P.S.M. Dunlop, C.P. Sheeran, J.A. Byrne, M.A.S. McMahon, M.A. Boyle, K.G. McGuigan, Inactivation of clinically relevant pathogens by photocatalytic coatings, *J Photoch Photobio A* 216 (2010) 303-310.
- [112] M. Radetic, Functionalization of textile materials with TiO₂ nanoparticles, *J Photoch Photobio C* 16 (2013) 62-76.
- [113] P. Osorio-Vargas, R. Sanjines, C. Ruales, C. Castro, C. Pulgarin, A.J. Rengifo-Herrera, J.C. Lavanchy, J. Kiwi, Antimicrobial Cu-functionalized surfaces prepared by bipolar asymmetric DC-pulsed magnetron sputtering (DCP), *J Photoch Photobio A* 220 (2011) 70-76.
- [114] L. Rio, E. Kusiak-Nejman, J. Kiwi, B. Betrisey, C. Pulgarin, A. Trampuz, A. Bizzini, Comparison of Methods for Evaluation of the Bactericidal Activity of Copper-Sputtered Surfaces against Methicillin-Resistant *Staphylococcus aureus*, *Appl Environ Microb* 78 (2012) 8176-8182.
- [115] S. Rtimi, M.K.S. Ballo, D. Laub, C. Pulgarin, J.M. Entenza, A. Bizzini, R. Sanjines, J. Kiwi, Duality in the *Escherichia coli* and methicillin resistant *Staphylococcus aureus* reduction mechanism under actinic light on innovative co-sputtered surfaces, *Appl Catal a-Gen* 498 (2015) 185-191.
- [116] E. Kusiak-Nejman, A.W. Morawski, A.P. Ehiasarian, C. Pulgarin, O. Baghriche, E. Mielczarski, J. Mielczarski, A. Kulik, J. Kiwi, *E. coli* Inactivation by High-Power Impulse Magnetron Sputtered (HIPIMS) Cu Surfaces, *J Phys Chem C* 115 (2011) 21113-21119.
- [117] S. Rtimi, O. Baghriche, C. Pulgarin, A. Ehiasarian, R. Bandorf, J. Kiwi, Comparison of HIPIMS sputtered Ag- and Cu-surfaces leading to accelerated bacterial inactivation in the dark, *Surf Coat Tech* 250 (2014) 14-20.
- [118] S. Rtimi, O. Baghriche, C. Pulgarin, J.C. Lavanchy, J. Kiwi, Growth of TiO₂/Cu films by HiPIMS for accelerated bacterial loss of viability, *Surf Coat Tech* 232 (2013) 804-813.
- [119] S. Rtimi, S. Giannakis, R. Sanjines, C. Pulgarin, M. Bensimon, J. Kiwi, Insight on the photocatalytic bacterial inactivation by co-sputtered TiO₂-Cu in aerobic and anaerobic conditions, *Applied Catalysis B: Environmental* 182 (2016) 277-285.

- [120] M.R. Dhananjeyan, J. Kiwi, K.R. Thampi, Photocatalytic performance of TiO₂ and Fe₂O₃ immobilized on derivatized polymer films for mineralisation of pollutants, *Chem Commun* (2000) 1443-1444.
- [121] A.T.M.O.P.Y. Tesfa Oluma Fufa, Synthesis, Characterization and Photocatalytic Activity of MnO₂/Al₂O₃/Fe₂O₃ Nanocomposite For Phenol Degradation *Chemistry and Materials Research* 6 (2014) 73-86.
- [122] O. Deutschmann, H. Knözinger, K. Kochloefl, T. Turek, Heterogeneous Catalysis and Solid Catalysts, *Ullmann's Encyclopedia of Industrial Chemistry*, Wiley-VCH Verlag GmbH & Co. KGaA2000.
- [123] L.F. González-Bahamón, F. Mazille, L.N. Benítez, C. Pulgarín, Photo-Fenton degradation of resorcinol mediated by catalysts based on iron species supported on polymers, *Journal of Photochemistry and Photobiology A: Chemistry* 217 (2011) 201-206.
- [124] F. Mazille, T. Schoettl, N. Klammerth, S. Malato, C. Pulgarin, Field solar degradation of pesticides and emerging water contaminants mediated by polymer films containing titanium and iron oxide with synergistic heterogeneous photocatalytic activity at neutral pH, *Water research* 44 (2010) 3029-3038.
- [125] F. Mazille, A. Moncayo-Lasso, D. Spuhler, A. Serra, J. Peral, N.L. Benítez, C. Pulgarin, Comparative evaluation of polymer surface functionalization techniques before iron oxide deposition. Activity of the iron oxide-coated polymer films in the photo-assisted degradation of organic pollutants and inactivation of bacteria, *Chemical Engineering Journal* 160 (2010) 176-184.
- [126] K.-i. Ishibashi, A. Fujishima, T. Watanabe, K. Hashimoto, Detection of active oxidative species in TiO₂ photocatalysis using the fluorescence technique, *Electrochemistry Communications* 2 (2000) 207-210.
- [127] S. Singh, H. Mahalingam, P.K. Singh, Polymer-supported titanium dioxide photocatalysts for environmental remediation: A review, *Applied Catalysis A: General* 462–463 (2013) 178-195.
- [128] C.D. Wanger, Riggs W. M., Davis L. E., Moulder J. F. and Muilenberg G. E., *Handbook of X-ray Photoelectron Spectroscopy* Perkin-Elmer Corp., Physical Electronics Division, Eden Prairie, Minnesota, USA, 1979., Heyden & Son Ltd.1979.
- [129] J. Nogier, M. Delamar, P. Ruiz, B. Delmon, J.P. Bonnelle, M. Guelton, L. Gengembre, J.C. Vedrine, M. Brun, P. Albers, K. Seibold, M. Baerns, H. Papp, J. Stoch, L.T. Andersson, J. Kiwi, R. Thampi, M. Gratzel, G.C. Bond, N. Verma, J.C. Vickerman, R.H. West, X-Ray Photoelectron-Spectroscopy of TiO₂/V₂O₅ Catalysts, *Catal Today* 20 (1994) 109-123.
- [130] D.A. Shirley, High-Resolution X-Ray Photoemission Spectrum of the Valence Bands of Gold, *Physical Review B* 5 (1972) 4709-4714.
- [131] A. Mills, J.S. Wang, Photobleaching of methylene blue sensitised by TiO₂: an ambiguous system?, *J Photoch Photobio A* 127 (1999) 123-134.
- [132] X.Q. Qiu, M. Miyauchi, K. Sunada, M. Minoshima, M. Liu, Y. Lu, D. Li, Y. Shimodaira, Y. Hosogi, Y. Kuroda, K. Hashimoto, Hybrid Cu_xO/TiO₂ Nanocomposites As Risk-Reduction Materials in Indoor Environments, *Acs Nano* 6 (2012) 1609-1618.
- [133] A. Houas, H. Lachheb, M. Ksibi, E. Elaloui, C. Guillard, J.M. Herrmann, Photocatalytic degradation pathway of methylene blue in water, *Appl Catal B-Environ* 31 (2001) 145-157.
- [134] T.A. Egerton, C.J. King, Influence of Light-Intensity on Photoactivity in TiO₂ Pigmented Systems, *J Oil Colour Chem As* 62 (1979) 386-391.
- [135] K. Vinodgopal, P.V. Kamat, Photochemistry of Textile Azo Dyes - Spectral Characterization of Excited-State, Reduced and Oxidized Forms of Acid Orange-7, *J Photoch Photobio A* 83 (1994) 141-146.
- [136] P. Piccinini, C. Minero, M. Vincenti, E. Pelizzetti, Photocatalytic interconversion of nitrogen-containing benzene derivatives, *J Chem Soc Faraday T* 93 (1997) 1993-2000.
- [137] K.B. Patel, R.L. Willson, Semiquinone free radicals and oxygen. Pulse radiolysis study of one electron transfer equilibria, *Journal of the Chemical Society, Faraday Transactions 1: Physical Chemistry in Condensed Phases* 69 (1973) 814-825.

- [138] P. Wardman, Reduction Potentials of One-Electron Couples Involving Free-Radicals in Aqueous-Solution, *J Phys Chem Ref Data* 18 (1989) 1637-1755.
- [139] S. Rtimi, C. Pulgarin, R. Sanjines, J. Kiwi, Innovative semi-transparent nanocomposite films presenting photo-switchable behavior and leading to a reduction of the risk of infection under sunlight, *Rsc Adv* 3 (2013) 16345-16348.
- [140] A.J. Nozik, Photoelectrochemistry - Applications to Solar-Energy Conversion, *Annu Rev Phys Chem* 29 (1978) 189-222.
- [141] S. Rtimi, C. Pulgarin, R. Sanjines, J. Kiwi, Accelerated self-cleaning by Cu promoted semiconductor binary-oxides under low intensity sunlight irradiation, *Applied Catalysis B: Environmental* 180 (2016) 648-655.
- [142] J. Tang, Z. Zou, J. Yin, J. Ye, Photocatalytic degradation of methylene blue on CaIn_2O_4 under visible light irradiation, *Chem Phys Lett* 382 (2003) 175-179.
- [143] B. Roig, C. Gonzalez, O. Thomas, Monitoring of phenol photodegradation by ultraviolet spectroscopy, *Spectrochim Acta A* 59 (2003) 303-307.
- [144] E. Rentz Do Comm Cnmo, Viral Pathogens and Severe Acute Respiratory Syndrome: Oligodynamic Ag^+ for Direct Immune Intervention, *Journal of Nutritional & Environmental Medicine* 13 (2003) 109-118.
- [145] H.A. Jeng, J. Swanson, Toxicity of metal oxide nanoparticles in mammalian cells, *J Environ Sci Heal A* 41 (2006) 2699-2711.
- [146] W.K. Nägeli., *Neue Denkschr. Allgeein. Schweiz. Gesellsch. English archive: Nägeli, Denkschr. Allgemein. Naturfors Ges, Ges. Naturweiss* 33 (1893) 174-182.
- [147] L. Suárez, C. Pulgarin, C. Roussel, J. Kiwi, Preparation, kinetics, mechanism and properties of semi-transparent photocatalytic stable films active in dye degradation, *Applied Catalysis A: General* 516 (2016) 70-80.
- [148] L.G. Devi, R. Kavitha, A review on non metal ion doped titania for the photocatalytic degradation of organic pollutants under UV/solar light: Role of photogenerated charge carrier dynamics in enhancing the activity, *Appl Catal B-Environ* 140 (2013) 559-587.
- [149] R.D. Shannon, Revised Effective Ionic-Radii and Systematic Studies of Interatomic Distances in Halides and Chalcogenides, *Acta Crystallogr A* 32 (1976) 751-767.
- [150] M. Kapilashrami, Y. Zhang, Y.-S. Liu, A. Hagfeldt, J. Guo, Probing the Optical Property and Electronic Structure of TiO_2 Nanomaterials for Renewable Energy Applications, *Chem Rev* 114 (2014) 9662-9707.
- [151] L. Yu, S. Yuan, L.Y. Shi, Y. Zhao, J.H. Fang, Synthesis of Cu^{2+} doped mesoporous titania and investigation of its photocatalytic ability under visible light, *Micropor Mesopor Mat* 134 (2010) 108-114.
- [152] G. Colón, M. Maicu, M.C. Hidalgo, J.A. Navío, Cu-doped TiO_2 systems with improved photocatalytic activity, *Applied Catalysis B: Environmental* 67 (2006) 41-51.
- [153] H. Praliaud, S. Mikhailenko, Z. Chajar, M. Primet, Surface and bulk properties of Cu-ZSM-5 and $\text{Cu}/\text{Al}_2\text{O}_3$ solids during redox treatments. Correlation with the selective reduction of nitric oxide by hydrocarbons, *Appl Catal B-Environ* 16 (1998) 359-374.
- [154] D.A.H. Hanaor, C.C. Sorrell, Review of the anatase to rutile phase transformation, *J Mater Sci* 46 (2011) 855-874.
- [155] U.o.A. Department of Geosciences, RRUFF Project, 2016.
- [156] B.D. Cullity, *Elements of X-ray diffraction*, Addison-Wesley Pub. Co., Reading, Mass., 1956.
- [157] H.P. Klug, *X-ray diffraction procedures for polycrystalline and amorphous materials / Harold P. Klug, Leroy E. Alexander*, Wiley, New York, 1974.
- [158] O. Seddiki, C. Harnagea, L. Levesque, D. Mantovani, F. Rosei, Evidence of antibacterial activity on titanium surfaces through nanotextures, *Applied Surface Science* 308 (2014) 275-284.
- [159] I. Uvarova, *Nanostructured materials in medicine. State of the art in Ukraine*, *Nato Sci Ser li Math* 102 (2003) 1-13.
- [160] L. Zhang, R. Dillert, D. Bahnemann, M. Vormoor, Photo-induced hydrophilicity and self-cleaning: models and reality, *Energy & Environmental Science* 5 (2012) 7491-7507.

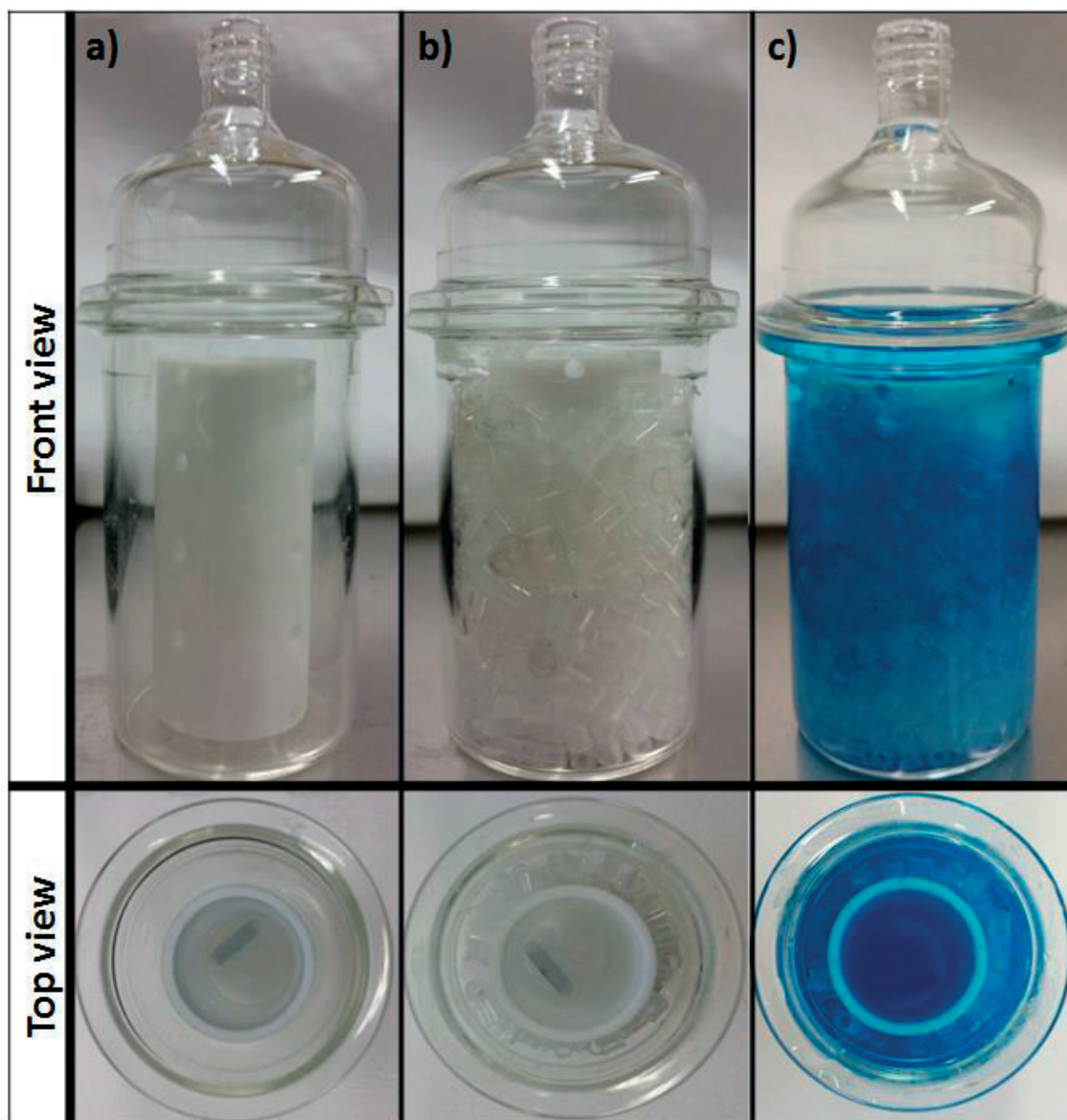
- [161] R. Fagan, D.E. McCormack, D.D. Dionysiou, S.C. Pillai, A review of solar and visible light active TiO₂ photocatalysis for treating bacteria, cyanotoxins and contaminants of emerging concern, *Materials Science in Semiconductor Processing* 42, Part 1 (2016) 2-14.
- [162] M. Miyauchi, H. Irie, M. Liu, X. Qiu, H. Yu, K. Sunada, K. Hashimoto, Visible-Light-Sensitive Photocatalysts: Nanocluster-Grafted Titanium Dioxide for Indoor Environmental Remediation, *The Journal of Physical Chemistry Letters* 7 (2016) 75-84.
- [163] P. Fernández, J. Blanco, C. Sichel, S. Malato, Water disinfection by solar photocatalysis using compound parabolic collectors, *Catal Today* 101 (2005) 345-352.
- [164] S. Barreca, J.J. Velez Colmenares, A. Pace, S. Orecchio, C. Pulgarin, Escherichia coli inactivation by neutral solar heterogeneous photo-Fenton (HPF) over hybrid iron/montmorillonite/alginate beads, *Journal of Environmental Chemical Engineering* 3 (2015) 317-324.
- [165] F. Mazille, T. Schoettl, C. Pulgarin, Synergistic effect of TiO₂ and iron oxide supported on fluorocarbon films. Part 1: Effect of preparation parameters on photocatalytic degradation of organic pollutant at neutral pH, *Applied Catalysis B: Environmental* 89 (2009) 635-644.
- [166] F. Mazille, A. Lopez, C. Pulgarin, Synergistic effect of TiO₂ and iron oxide supported on fluorocarbon films: Part 2: Long-term stability and influence of reaction parameters on photoactivated degradation of pollutants, *Applied Catalysis B: Environmental* 90 (2009) 321-329.
- [167] L. Suárez, H. Dong, C. Pulgarin, R. Sanjines, Z. Qiang, J. Kiwi, Innovative photo-Fenton catalysis by PE-FeOx films leading to methylene blue (MB) degradation: Kinetics, surface properties and mechanism, *Applied Catalysis A: General* 519 (2016) 68-77.
- [168] N.T. Nolan, D.W. Synnott, M.K. Seery, S.J. Hinder, A. Van Wassenhoven, S.C. Pillai, Effect of N-doping on the photocatalytic activity of sol-gel TiO₂, *J Hazard Mater* 211-212 (2012) 88-94.
- [169] R. Fagan, D.E. McCormack, S. Hinder, S.C. Pillai, Improved high temperature stability of anatase TiO₂ photocatalysts by N, F, P co-doping, *Materials & Design* 96 (2016) 44-53.
- [170] S. Rtimi, C. Pulgarin, J. Kiwi, 10 - Uniform, adhesive, and low cytotoxic films accelerating bacterial reduction in the dark and under visible light A2 - Griesser, Hans J, *Thin Film Coatings for Biomaterials and Biomedical Applications*, Woodhead Publishing 2016, pp. 225-260.
- [171] D.W. Synnott, M.K. Seery, S.J. Hinder, G. Michlits, S.C. Pillai, Anti-bacterial activity of indoor-light activated photocatalysts, *Applied Catalysis B: Environmental* 130-131 (2013) 106-111.
- [172] J. Lalley, D.D. Dionysiou, R.S. Varma, S. Shankara, D.J. Yang, M.N. Nadagouda, Silver-based antibacterial surfaces for drinking water disinfection — an overview, *Current Opinion in Chemical Engineering* 3 (2014) 25-29.
- [173] H.W.P. Carvalho, A.P.L. Batista, P. Hammer, T.C. Ramalho, Photocatalytic degradation of methylene blue by TiO₂-Cu thin films: Theoretical and experimental study, *J Hazard Mater* 184 (2010) 273-280.
- [174] L. Suárez, Z. Wei, H. Teixidó, R. Sanjinés, M. Bensimon, C. Pulgarín, J. Kiwi, Cu-decorated Raschig-TiO₂ rings inducing MB repetitive discoloration without release of Cu-ions under solar light, *Journal of Environmental Chemical Engineering* 5 (2017) 310-318.
- [175] E. Vaughn, G. Ramachandran, Fiberglass vs. synthetic air filtration media, *INJ Fall* 11 (2002) 41-53.
- [176] S. Giannakis, A.I. Merino Gamo, E. Darakas, A. Escalas-Cañellas, C. Pulgarin, Impact of different light intermittence regimes on bacteria during simulated solar treatment of secondary effluent: Implications of the inserted dark periods, *Solar Energy* 98, Part C (2013) 572-581.
- [177] G. Carre, E. Hamon, S. Ennahar, M. Estner, M.C. Lett, P. Horvatovich, J.P. Gies, V. Keller, N. Keller, P. Andre, TiO₂ photocatalysis damages lipids and proteins in Escherichia coli, *Appl Environ Microbiol* 80 (2014) 2573-2581.
- [178] L.M. Dorfman, U.S.N.B.o. Standards, G.E. Adams, Reactivity of the Hydroxyl Radical in Aqueous Solutions, U.S. Department of Commerce, National Bureau of Standards 1973.

- [179] B. Sulzberger, S. Canonica, T. Egli, W. Giger, J. Klausen, U. von Gunten, Oxidative transformations of contaminants in natural and in technical systems, *Chimia* 51 (1997) 900-907.
- [180] G. Ferraudi, S. Muralidharan, Photochemical properties of copper complexes, *Coordination Chemistry Reviews* 36 (1981) 45-88.
- [181] J.I. Nieto-Juarez, K. Pierzchla, A. Sienkiewicz, T. Kohn, Inactivation of MS2 coliphage in Fenton and Fenton-like systems: role of transition metals, hydrogen peroxide and sunlight, *Environmental Science and Technology* 44 (2010) 3351-3356.
- [182] A.N. Pham, G. Xing, C.J. Miller, T.D. Waite, Fenton-like copper redox chemistry revisited: Hydrogen peroxide and superoxide mediation of copper-catalyzed oxidant production, *Journal of Catalysis* 301 (2013) 54-64.
- [183] J.K. Kim, I.S. Metcalfe, Investigation of the generation of hydroxyl radicals and their oxidative role in the presence of heterogeneous copper catalysts, *Chemosphere* 69 (2007) 689-696.
- [184] K. Hashimoto, H. Irie, A. Fujishima, TiO₂ photocatalysis: A historical overview and future prospects, *Japanese Journal of Applied Physics* 44 (2005) 8269-8285.
- [185] O. Bondarenko, K. Juganson, A. Ivask, K. Kasemets, M. Mortimer, A. Kahru, Toxicity of Ag, CuO and ZnO nanoparticles to selected environmentally relevant test organisms and mammalian cells in vitro: a critical review, *Archives of Toxicology* 87 (2013) 1181-1200.
- [186] C. Gunawan, W.Y. Teoh, C.P. Marquis, R. Amal, Cytotoxic Origin of Copper(II) Oxide Nanoparticles: Comparative Studies with Micron-Sized Particles, Leachate, and Metal Salts, *ACS Nano* 5 (2011) 7214-7225.
- [187] C.A. Grillo, M.A. Reigosa, M.A. Fernández Lorenzo de Mele, Does over-exposure to copper ions released from metallic copper induce cytotoxic and genotoxic effects on mammalian cells?, *Contraception* 81 (2010) 343-349.
- [188] Y. Jeyachandran, S.K. Narayandass, The effect of thickness of titanium nitride coatings on bacterial adhesion, *Trends in Biomaterials and Artificial Organs* 24 (2010) 90-93.
- [189] M.I. Mejía, J.M. Marín, G. Restrepo, C. Pulgarín, E. Mielczarski, J. Mielczarski, Y. Arroyo, J.C. Lavanchy, J. Kiwi, Self-cleaning modified TiO₂-cotton pretreated by UVC-light (185 nm) and RF-plasma in vacuum and also under atmospheric pressure, *Applied Catalysis B: Environmental* 91 (2009) 481-488.
- [190] M.A. Rauf, M.A. Meetani, A. Khaleel, A. Ahmed, Photocatalytic degradation of Methylene Blue using a mixed catalyst and product analysis by LC/MS, *Chemical Engineering Journal* 157 (2010) 373-378.
- [191] N.C. Castillo, A. Heel, T. Graule, C. Pulgarin, Flame-assisted synthesis of nanoscale, amorphous and crystalline, spherical BiVO₄ with visible-light photocatalytic activity, *Applied Catalysis B: Environmental* 95 (2010) 335-347.
- [192] H. Roques, *Chemical Water Treatment: Principles and Practice*, Wiley 1996.
- [193] T. Oppenländer, *Photochemical Purification of Water and Air: Advanced Oxidation Processes (AOPs) - Principles, Reaction Mechanisms, Reactor Concepts*, Wiley 2007.
- [194] T.R. Compton, *Toxicants in the Aqueous Ecosystem*, Wiley 1997.
- [195] B. Kraeutler, C.D. Jaeger, A.J. Bard, Direct observation of radical intermediates in the photo-Kolbe reaction - heterogeneous photocatalytic radical formation by electron spin resonance, *Journal of the American Chemical Society* 100 (1978) 4903-4905.
- [196] J. Kiwi, C. Morrison, Heterogeneous Photocatalysis - Dynamics of Charge-Transfer in Lithium-Doped Anatase-Based Catalyst Powders with Enhanced Water Photocleavage under Ultraviolet-Irradiation, *Journal of Physical Chemistry* 88 (1984) 6146-6152.
- [197] K.L. Hardee, A.J. Bard, Semiconductor Electrodes .10. Photoelectrochemical Behavior of Several Polycrystalline Metal-Oxide Electrodes in Aqueous-Solutions, *Journal of Electrochemical Society* 124 (1977) 215-224.
- [198] N.L. Dias, Adsorption of Cu(II) and Co(II) complexes on a silica gel surface chemically modified with 2-mercaptoimidazole, *Mikrochimica Acta* 130 (1999) 233-240.
- [199] S. Banerjee, D. Chakravorty, Optical absorption by nanoparticles of Cu₂O, *Europhys Letters* 52 (2000) 468-473.

- [200] I. Petrov, A. Myers, J.E. Greene, J.R. Abelson, Mass and Energy-Resolved Detection of Ions and Neutral Sputtered Species Incident at the Substrate during Reactive Magnetron Sputtering of Ti in Mixed Ar+N₂ Mixtures, *J Vac Sci Technol A* 12 (1994) 2846-2854.
- [201] S. Rtimi, S. Giannakis, M. Bensimon, C. Pulgarin, R. Sanjines, J. Kiwi, Supported TiO₂ films deposited at different energies: Implications of the surface compactness on the catalytic kinetics, *Applied Catalysis B: Environmental* 191 (2016) 42-52.
- [202] K.L. Hardee, A.J. Bard, Semiconductor Electrodes .5. Application of Chemically Vapor-Deposited Iron-Oxide Films to Photosensitized Electrolysis, *J Electrochem Soc* 123 (1976) 1024-1026.
- [203] B. Ohtani, S. Adzuma, H. Miyadzu, S. Nishimoto, T. Kagiya, Photocatalytic Degradation of Polypropylene Film by Dispersed Titanium-Dioxide Particles, *Polym Degrad Stabil* 23 (1989) 271-278.
- [204] J.R. Bolton, C.A.C. Cotton, *The Ultraviolet Disinfection Handbook*, American Water Works Association 2011.
- [205] G. Ruppert, R. Bauer, G. Heisler, The photo-Fenton reaction — an effective photochemical wastewater treatment process, *Journal of Photochemistry and Photobiology A: Chemistry* 73 (1993) 75-78.
- [206] P.V. Kamat, Photochemistry on nonreactive and reactive (semiconductor) surfaces, *Chem Rev* 93 (1993) 267-300.
- [207] V.Y. Gak, V.A. Nadtochenko, J. Kiwi, Triplet-excited dye molecules (eosine and methylene blue) quenching by H₂O₂ in aqueous solutions, *J Photoch Photobio A* 116 (1998) 57-62.
- [208] V.A. Nadtochenko, J. Kiwi, Photolysis of FeOH₂⁺ and FeCl₂⁺ in Aqueous Solution. Photodissociation Kinetics and Quantum Yields, *Inorganic Chemistry* 37 (1998) 5233-5238.
- [209] J.J. Morgan, W. Stumm, *Aquatic chemistry*, Wiley, New York, 1970.
- [210] G.R. Helz, R.G. Zepp, D.G. Crosby, *Aquatic and surface photochemistry*, Lewis Publishers, Boca Raton, FL 552, 1994.

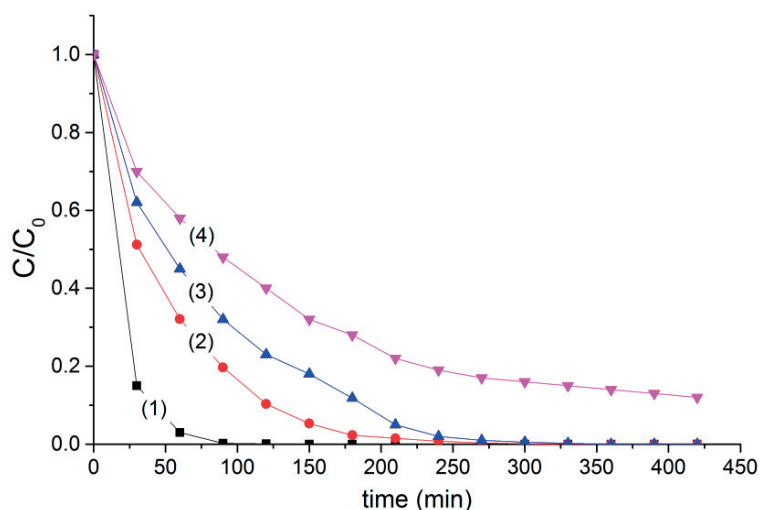
Annex A: Supplementary material for Chapter 4

Supplementary material 1



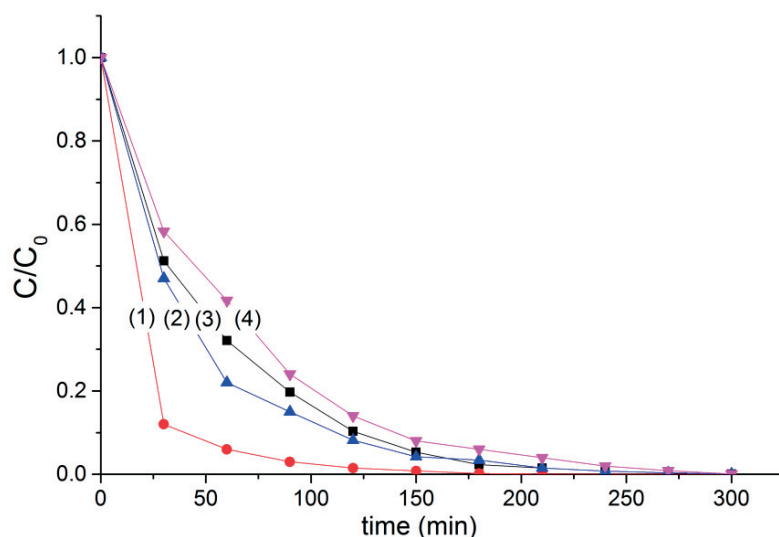
Ch4-S1. Reactor's front view and top view without the reactor lid. a) reactor, Teflon support placed concentrically inside the reactor and magnetic stirrer at the bottom of reactor. b) reactor, photocatalyst (RR-TiO₂-Cu 0.004%), Teflon support holding the rings and magnetic stirrer at the bottom of the reactor. c) reactor filled with MB solution, photocatalyst (RR-TiO₂-Cu 0.004%), Teflon support holding the rings and magnetic stirrer at the bottom of the reactor

Supplementary material 2



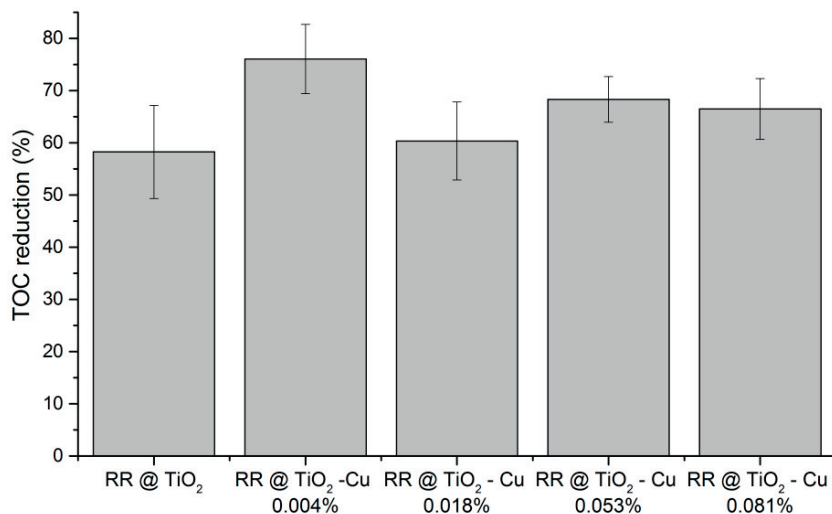
Ch4-S2. MB-discoloration kinetics on RR@TiO₂-Cu-0.004% as a function of MB concentration. (1) MB 2×10^{-5} mol L⁻¹, (2) MB 4×10^{-5} mol L⁻¹, (3) MB 6×10^{-5} mol L⁻¹, (4) MB 8×10^{-5} mol L⁻¹. Suntest light set at 90 mW cm⁻². For initial concentrations (2×10^{-5} mol L⁻¹, 4×10^{-5} mol L⁻¹, 6×10^{-5} mol L⁻¹ and 8×10^{-5} mol L⁻¹), the initial discoloration rates (r_0) were estimated as: 1.3×10^{-6} mol L⁻¹ min⁻¹, 7.1×10^{-7} mol L⁻¹ min⁻¹, 7.5×10^{-7} mol L⁻¹ min⁻¹ and 6×10^{-7} mol L⁻¹ min⁻¹ respectively

Supplementary material 3



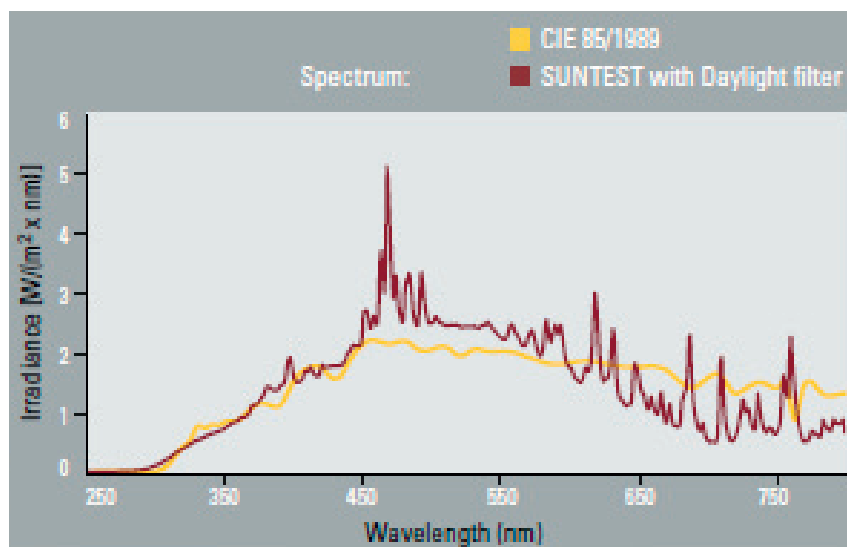
Ch4-S3. Discoloration of MB on RR@TiO₂-Cu 0.004% as a function of initial pH: (1) pH = 10, (2) pH = 7, (3) pH = 5.7, (4) pH = 4. MB concentration: 4×10^{-5} mol L⁻¹, Suntest light set at 90 mW cm⁻².

Supplementary material 4



Ch4-S4. TOC reduction percentage as a function of the Cu-added to RR@TiO₂, MB initial concentration: 4×10^{-5} mol L⁻¹. Suntest light intensity set at 90 mW cm^{-2} .

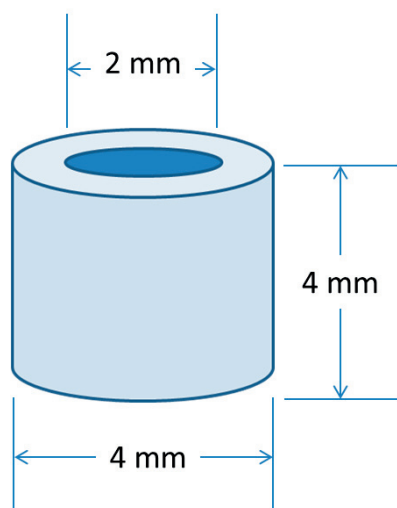
Supplementary material 5



Ch4-S5. Suntest solar simulator light wavelength emission spectrum. Suntest Xenon lamp (Heraeus, Hannau, Germany) with tunable light intensity.

Annex B: Supplementary material for Chapter 5

Supplementary material 1



1 ring ~ 0.089 g (AVG)

Surface area of 1 Raschig ring:

- Outside surface (A):

$$2\pi * \frac{4mm}{2} * 4mm = 50.266mm^2$$

- Inner surface (B):

$$2\pi * \frac{2mm}{2} * 4mm = 25.132mm^2$$

- 2 x Annulus surface (C):

$$2x\pi \left(\left(\frac{4mm}{2} \right)^2 - \left(\frac{2mm}{2} \right)^2 \right) = 18.849mm^2$$

- Total Surface Area per Raschig ring:

$$\mathbf{A + B + C = 94.247 \text{ mm}^2/\text{Raschig ring} \rightarrow 1058.955 \text{ mm}^2/\text{g}}$$

$$\rightarrow \mathbf{1.0589 \times 10^{-3} \text{ m}^2/\text{g}}$$

$$\text{Reactor's Rasching ring bed: } \sim \mathbf{35g} \rightarrow \mathbf{3.371 \times 10^{-2} \text{ m}^2}$$

Ch5-S1. Calculations for the Specific Surface Area (SSA) of Glass Raschig Rings

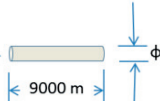
Supplementary material 2

Parameters of the GF mat:

- **Basis Weight** of the GF mat: 10z/ft² → **93.010 g/m²**
- **Density** of the GF mat: 6lb/ft³ → **0.096 g/m³**
- **Diameter** of the GF filaments conforming the mat: **9 μm**

Definition:

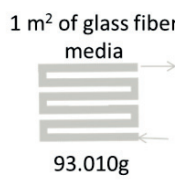
- **Denier** is a unit of weight for expressing the fineness of fibers, it is used in the following equation

$$\phi(\mu\text{m}) = 11.87 \sqrt{\frac{\text{Denier}}{\text{Density}}}$$


In this equation, it is assumed that the calculations are made for a 9000 m long fiber.

Thus, the analysed glass fiber has a **0.055 g Denier**, meaning this would be **the weight of a 9000 m** length filament.

A second assumption is that the fiber media is continuous and laid side by side forming a 1m² square:



Thus, the glass media basis weight of 93.010 g is equivalent to a total length of fiber of:

$$\frac{(93.010\text{g}) \times (9000\text{ m})}{0.055\text{g}} = 15,219,818.180\text{m}$$

Now, 1m² of glass fiber media with a weight of 93.010 g has a surface area of

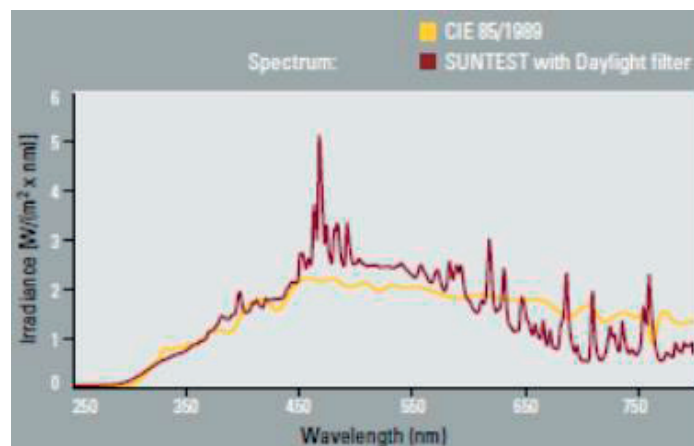
$$\pi * \phi * \text{length} = \pi * 9\mu\text{m} * \frac{1\text{m}}{1000000\mu\text{m}} * 15,219,818.180\text{m} = 430.330\text{m}^2$$

Defining the Specific Surface Area as Surface/Weight of media:

$$\frac{430.330\text{ m}^2}{93.010\text{ g}} = 4.611\text{ m}^2/\text{g}$$

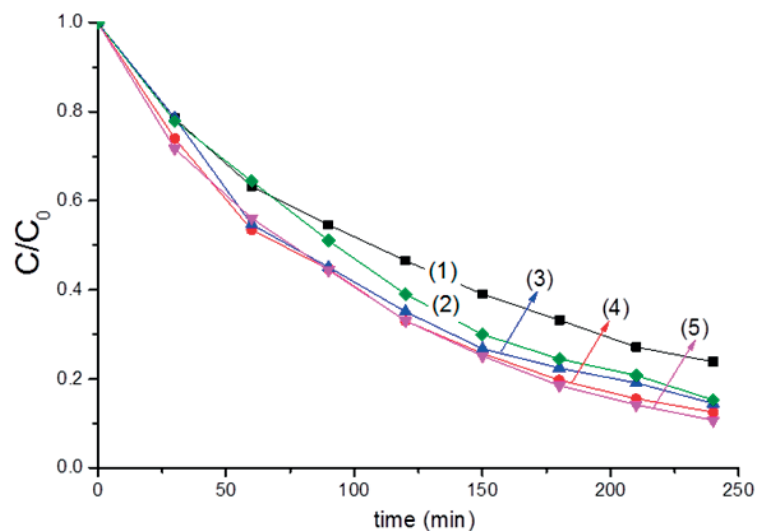
Ch5-S2. Calculations for the Specific Surface Area (SSA) of Glass fiber mats (A04008).

Supplementary material 3



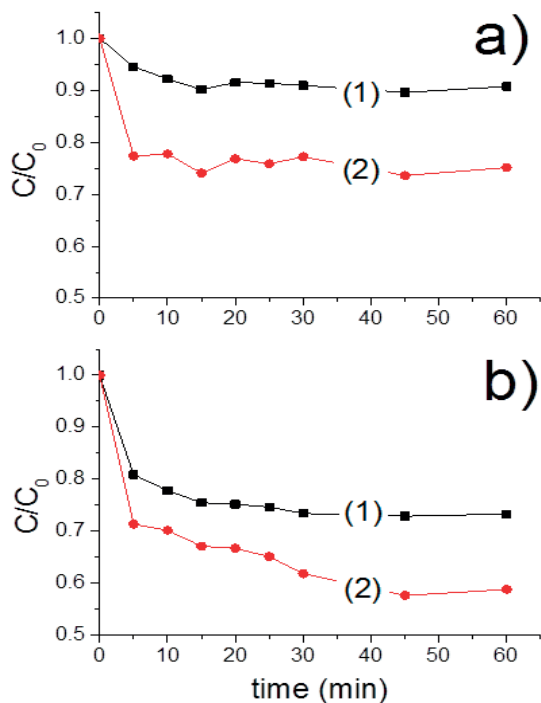
Ch5-S3. Light wavelength emission spectrum of the used Suntest solar simulator (Heraeus, Hannau, DE).

Supplementary material 4



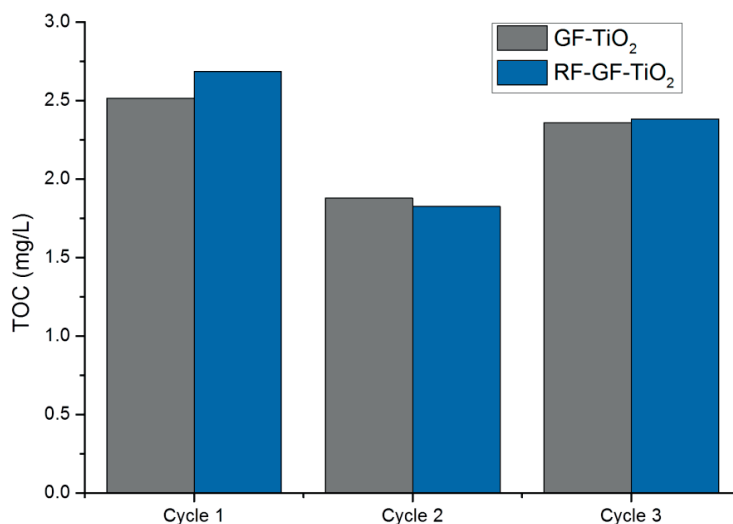
Ch5-S4. Degradation of a solution MB 4×10^{-5} M by means GF-TiO₂-Cu mats under visible light (70 mW cm^{-2} , light $> 400 \text{ nm}$). Trace (1) GF-TiO₂, trace (2) GF-TiO₂-Cu 3%, trace (3) GF-TiO₂-Cu 0.2%, trace (4) GF-TiO₂-Cu 0.05%, trace (5) GF-TiO₂-Cu 1%

Supplementary material 5



Ch5-S5. Adsorption of MB 4×10^{-5} M onto: a) glass fiber mats (GF) and b) glass fiber mats with TiO₂ (GF-TiO₂) in the dark, (1) Non-pre-treated samples, (2) RF-Plasma pre-treated samples.

Supplementary material 6



Ch5-S6. Residual TOC of MB solution after 12 h irradiation in contact with RF-plasma pre-treated mats (RF-GF-TiO₂) and non-pre-treated (GF-TiO₂) mats. Suntest irradiation (90 mW cm⁻²), initial TOC of MB (4 x 10⁻⁵ M): 7.23 ± 0.03 mg/L

Supplementary material 7 (Ch5-S7)

Smoluchowski approximation

Mean free path for the OH₂[•] radical



$$[MB]: 4 \times 10^{-5} M$$

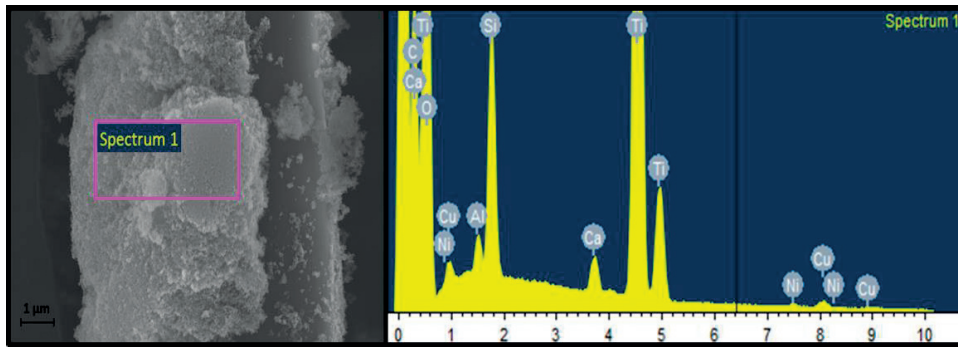
$$\frac{1}{\tau} = k_2[MB] = 10^6 \times 4 \times 10^{-5} = 40 s^{-1}$$

$$\tau = \frac{1}{40 s^{-1}} = 0.025 s$$

Diffusion of small molecule MB $\approx 5 \times 10^{-6} \text{ cm}^2 \text{ s}^{-1}$

$$X^2 = D\tau = 5 \times 10^{-6} \text{ cm}^2 \text{ s}^{-1} \times 0.025 s \approx 3.5 \mu m$$

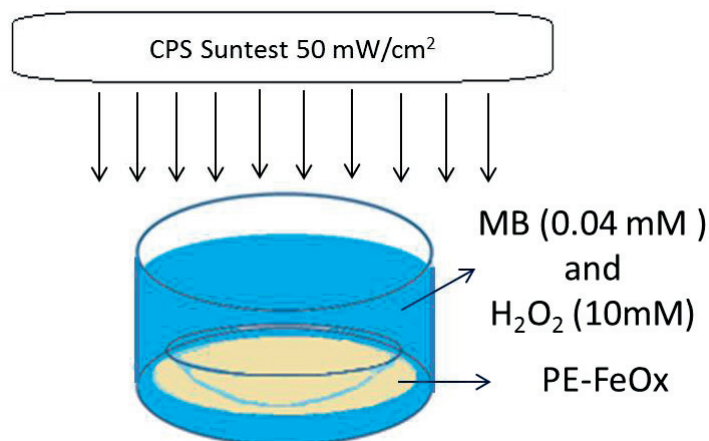
Supplementary material 8



Ch5-S8. Energy dispersive X-ray (EDX) spectra for the specified region of the GF-TiO₂-Cu 3% mat

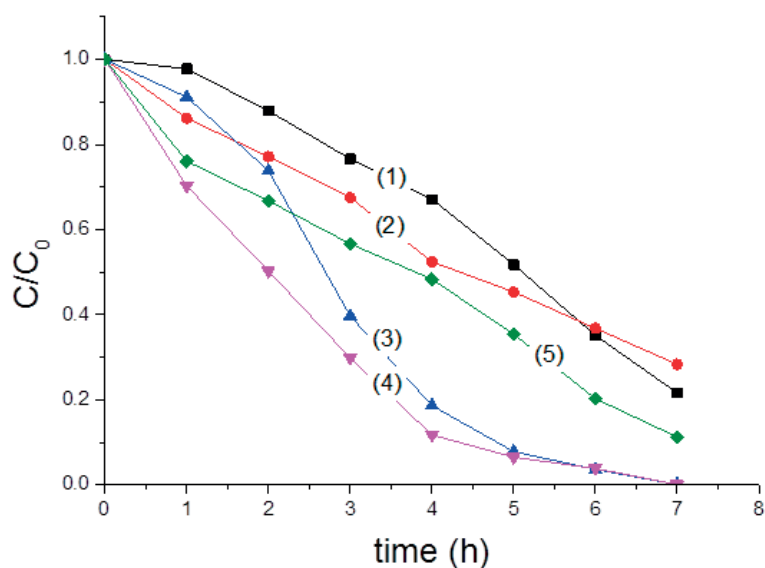
Annex C: Supplementary material for Chapter 7

Supplementary Material 1



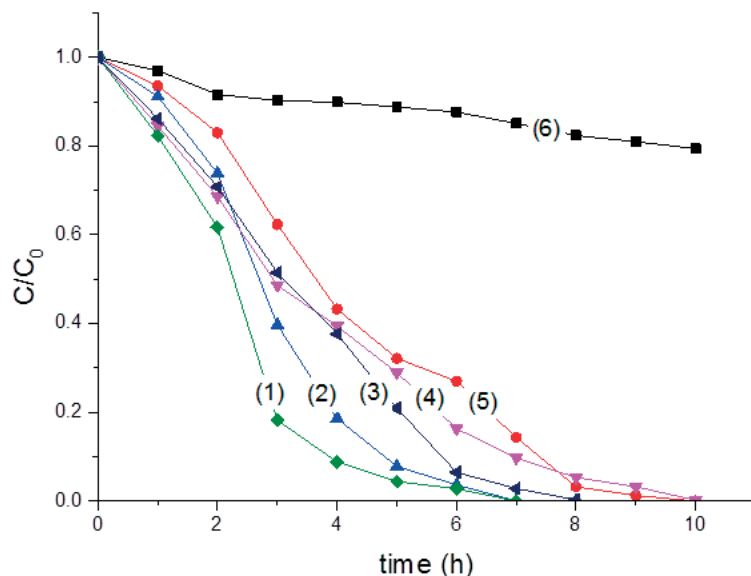
Ch7-S1. Scheme of reactor and illumination source

Supplementary Material 2



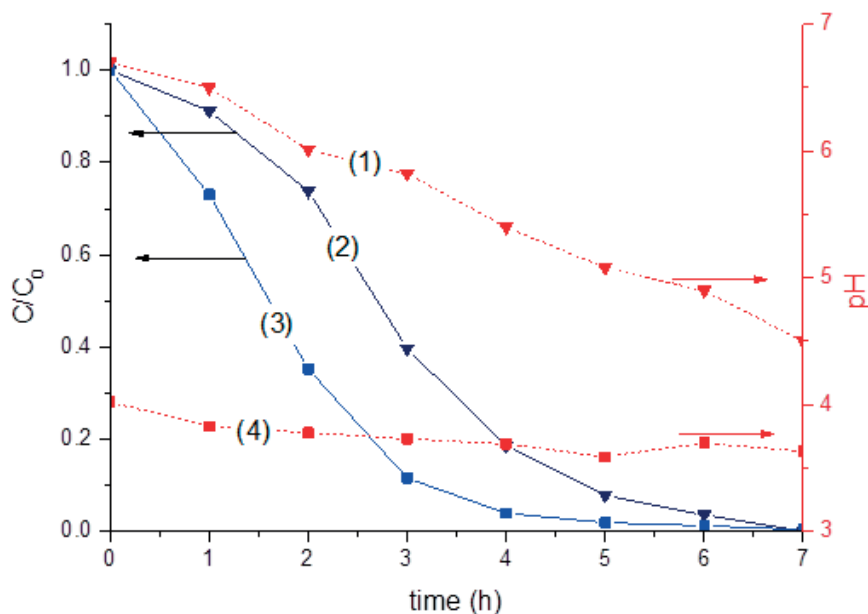
Ch7-S2. Discoloration of MB (4×10^{-5} M) by PE-FeOx under solar simulated irradiation (50 mW/cm^2) in the presence of H_2O_2 (10mM) as a function of FeOx loading: (1) 0.10% Fe, <0.2%Cl (2) 0.17%Fe <0.2%Cl (3) 0.18%Fe <0.2%Cl (4) 0.30%Fe 0.31%Cl (5) 0.37%Fe 0.39%Cl.

Supplementary Material 3



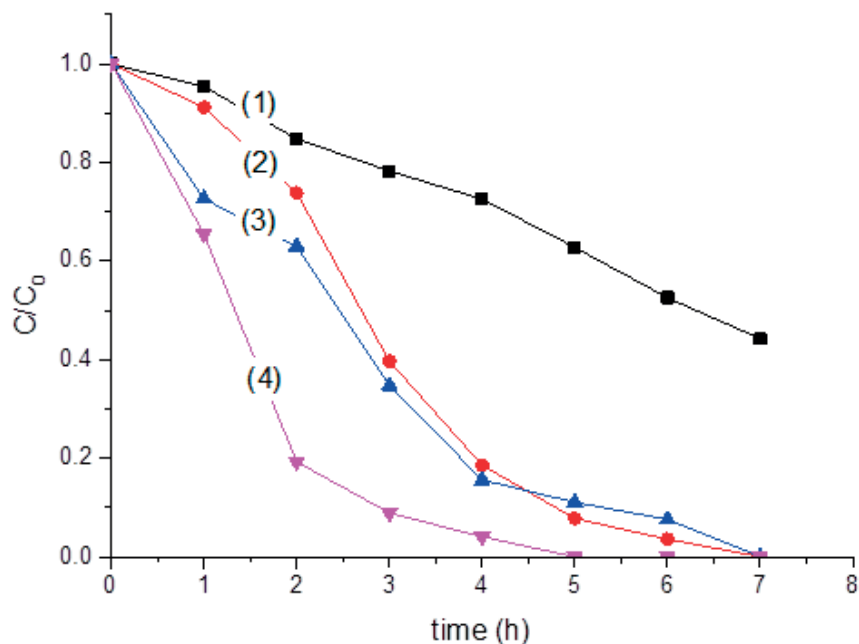
Ch7-S3. Discoloration of MB (4×10^{-5} M) by PE-FeOx under solar simulated irradiation (50 mW/cm^2) in the presence of H_2O_2 (10mM) as a function of light intensity: (1) 90 mW/cm^2 , (2) 50 mW/cm^2 , (3) 90 mW/cm^2 (with cut off at 400 nm), (4) 50 mW/cm^2 (with cut off at 400 nm), (5) 30 mW/cm^2 and (6) dark.

Supplementary Material 4



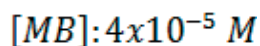
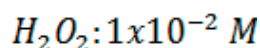
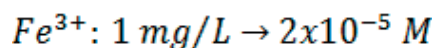
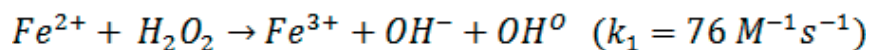
Ch7-S4. MB (4×10^{-5} M) discoloration and variation of pH mediated by PE-FeOx films at initial pH 6.7 and pH 4: (1) pH variation MB initial pH 6.7, (2) MB-discoloration at initial pH 6.7 (3) MB-discoloration initial pH=4. (4) pH variation MB initial pH 4. Other parameters Suntest light intensity: 50 mW/cm^2 and H_2O_2 (10mM).

Supplementary Material 5



Ch7-S5. Discoloration of MB (4×10^{-5} M) mediated by PE-FeOx under solar simulated irradiation (50 mW/cm^2) in the presence of H_2O_2 (10mM) as a function of initial pH: (1) 8.5, (2) 6.8, (3) 5.0 (4) 4.0

Supplementary Material 6 (Ch7-S6)



$$\frac{d[\text{OH}^\bullet]}{dt} = k_1 [\text{Fe}^{2+}] [\text{H}_2\text{O}_2] - k_2 [\text{OH}^\bullet] [\text{MB}] \sim 0$$

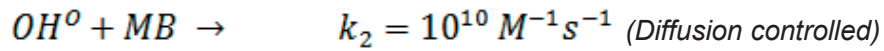
Quasi stationary state given the low concentration of $\bullet\text{OH}$

$$[\text{OH}^\bullet] = \frac{76 \times 1 \times 10^{-2} \times 2 \times 10^{-5}}{10^{10} \times 4 \times 10^{-5}} = 0.38 \times 10^{-12} [\text{M}]$$

Supplementary Material 7 (Ch7-S7)

Smoluchowski approximation

Mean free path for $\cdot\text{OH}$ radical



$$[\text{MB}]: 4 \times 10^{-5} \text{ M}$$

$$\frac{1}{\tau} = k_2[\text{MB}] = 10^{10} \times 4 \times 10^{-5} = 4 \times 10^5 \text{ s}^{-1}$$

$$\tau = \frac{1}{4 \times 10^5 \text{ s}^{-1}} = 2.5 \times 10^{-6} \text{ s} \text{ Time of encounter for pair } [\cdot\text{OH}] [\text{MB}]$$

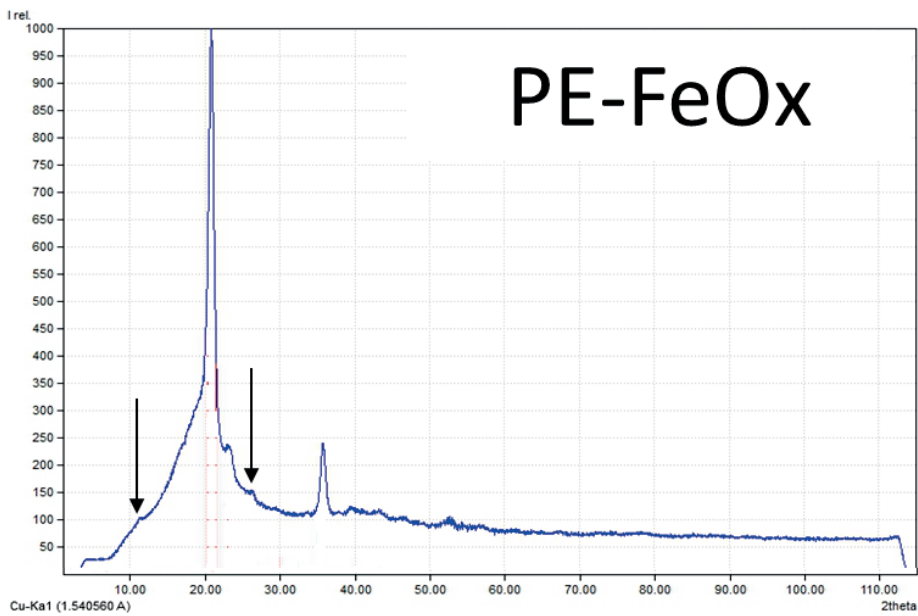
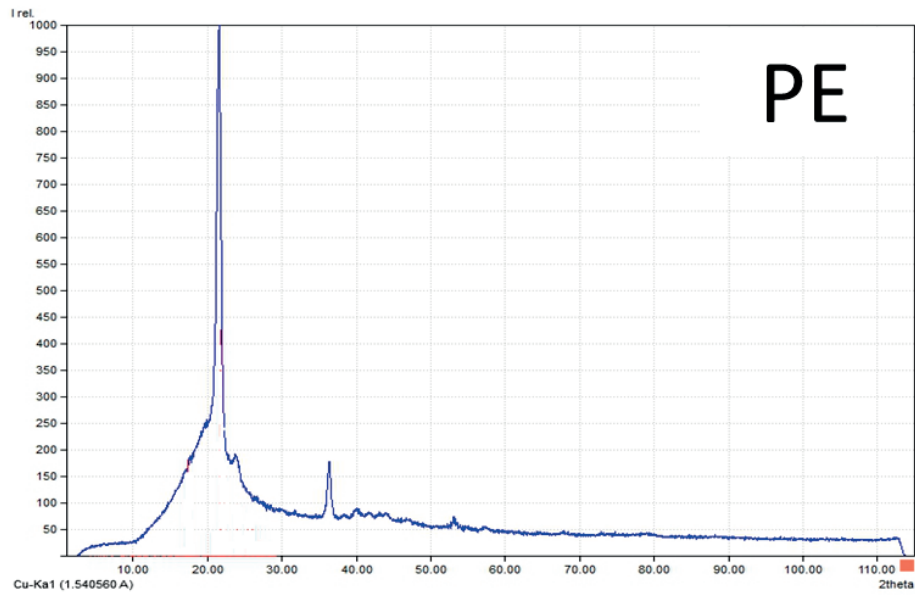
If diffusion constant for a small molecule MB $\approx 5 \times 10^{-6} \text{ cm}^2 \text{ s}^{-1}$, then the diffusion distance x can be calculated

$$x^2 = D\tau = 5 \times 10^{-6} \times 2.5 \times 10^{-6}$$

$$x = \sqrt{5 \times 10^{-6} (\text{cm}^2 \text{ s}^{-1}) \times 2.5 \times 10^{-6} (\text{s}^1)} = \sqrt{1.25 \times 10^{-11} \text{ cm}^2}$$

$$x \sim 35 \text{ nm}$$

Supplementary Material 8



Ch7-S8. XRD results for PE matrix and PE-FeOx (Fe 0.3%)

Curriculum Vitae of the candidate

Laura Victoria Suárez Murillo

Av. de la Gare, 29
1003, Lausanne, Switzerland
+41 78 964 3601
suarezmurillo.lauravictoria@gmail.com

Skype: lauroncha1

LinkedIn:

<https://www.linkedin.com/in/lavisumu/>

ResearchGate:

https://www.researchgate.net/profile/Laura_Suarez11



Strengths

- Pollutants degradation and bacterial inactivation by means of photocatalytic films
- Life Cycle Assessment / Water footprint Assessment along production line
- Trilingual Researcher: Spanish, English, Italian

Education

École Polytechnique Fédéral de Lausanne (EPFL) Advanced Oxydation Processes Group (GPAO) (http://gpao.epfl.ch/) Focus on supported photocatalysts for model pollutant degradation and bacterial inactivation. Doctor in Science	2013 – Present Expected (08/2017)
Polytechnic University of Turin, First Engineering Faculty, Turin, Italy M.Sc. Chemical Engineering (Under Double Degree Agreement) Grade: 99/110	2008 - 2011
University of Antioquia, Medellin, Colombia Chemical Engineer Diploma (B.Sc + 2 Years) Grade: 4/5	2002 - 2008

Special mentions

- Swiss Government PhD Scholarship holder: “Bourse d’excellence de la confederation” 15.09.2013 – 31.08.2017

Experience

École Polytechnique Fédéral de Lausanne (EPFL), Advanced Oxydation Processes Group (GPAO), Supervisor: César Pulgarín Coordination of work packages contribution from GPAO-EPFL for European Project FP7: LIMPID	2013 – 2015
Swiss Embassy in Colombia, SDC, Swiss Agency for Development and Cooperation – Colombia, Supervisor: Diana Rojas. Water Footprint Assessment for SuizAgua – Colombia Project	2012 – 2013
Swiss Federal Laboratories for Material Science and Technology (EMPA), Hydrogen and Energy Department, Dübendorf, Switzerland. Supervisor: Ulrich Vogt Master Thesis research: “ Study of electrochemical behaviour of membranes for alkaline electrolysis ”	2011
Environmental Catalysis Research Group. Supervisors: Consuelo Montes de Correa (Deceased) and Carlos Andrés González Research assistant at Universidad de Antioquia: Evaluation of Pd/TiO₂ wash coated cordierite monoliths for dicloromethane hydrodechlorination.	2006 – 2007

Additional Experience (Teaching / Tutoring)

École Polytechnique Fédéral de Lausanne (EPFL), Advanced Oxydation Processes Group (GPAO) 2016
Students project: TiO₂ on Glass fiber mats for pollutants degradation

École Polytechnique Fédéral de Lausanne (EPFL) 2013-2016

Chemical Engineering and lab project

Laboratory Assistant. Professors: Liubov Kiwi, Kevin Sivula

École Polytechnique Fédéral de Lausanne (EPFL) 2013-2016

Introduction to chemical Engineering laboratory works

Laboratory Assistant. Professor: Kevin Sivula

University of Antioquia 2006-2007

General Chemistry lab practice

Laboratory Assistant. Professor: Miriam Ramírez

Technical Skills

Supported photocatalysts preparation and characterization	Wet deposition, dip coating, sol-gel, Atomic Force Microscopy (AFM), Diffuse Reflectance Spectroscopy (DRS), X-ray Photoelectron Spectroscopy (XPS)
Analytical Chemistry	UV-Vis Spectrophotometry, High-performance Liquid Chromatography (HPLC), Total Organic Carbon analysis (TOC), Chemical Oxygen Demand analysis (COD)
Informatics	Matlab, Origin, EndNote, Multipak for XPS data treatment

Main Publications

- L. Suárez, C. Pulgarin, S. Giannakis, M. Bensimon, J. Kiwi, New evidence for disinfection, self-cleaning and pollutant degradation mediated by GF-TiO₂-Cu mats under solar/visible light in mild oxidative conditions, *Journal of Photochemistry and Photobiology A: Chemistry*, 346 (2017) 351-363.
- L. Suárez, Z. Wei, H. Teixidó, R. Sanjinés, M. Bensimon, C. Pulgarin, J. Kiwi, Cu-decorated Raschig-TiO₂ rings inducing MB repetitive discoloration without release of Cu-ions under solar light, *Journal of Environmental Chemical Engineering* 5 (2017) 310-318.
- L. Suárez, O. Baghriche, S. Rtimi, C. Pulgarin, J. Kiwi, Sputtered Cu-polyethylene films inducing bacteria inactivation in the dark and under low intensity sunlight, *Journal of Photochemistry and Photobiology A: Chemistry* 330 (2016) 163-168.
- L. Suárez, H. Dong, C. Pulgarin, R. Sanjines, Z. Qiang, J. Kiwi, Innovative photo-Fenton catalysis by PE-FeOx films leading to methylene blue (MB) degradation: Kinetics, surface properties and mechanism, *Applied Catalysis A: General* 519 (2016) 68-77.
- L. Suárez, C. Pulgarin, C. Roussel, J. Kiwi, Preparation, kinetics, mechanism and properties of semi-transparent photocatalytic stable films active in dye degradation, *Applied Catalysis A: General*, 516 (2016) 70-80.
- Link to all publications: <https://scholar.google.ch/citations?hl=en&user=-4EQPw0AAAAJ>

Languages

- English Fluent spoken (C2) and written (C2), IELTS certificate from 2011.
- Italian Upper intermediate level spoken and written (B2) (Studies in Turin – Italy, 3 years)
- French Low intermediate level spoken and written (A2) (Studies in Lausanne – Switzerland, 4 years)
- Spanish Native Language

Association membership

Member of ACIS “Asociación Colombiana de Investigadores en Suiza” (Colombian Association of Researches in Switzerland) since 2013

Personal interests

Farming, Sustainable Gardening, Sustainable Tourism, Concerts, Tropical Dances, Snorkeling, Swimming

Personal information

31, single, Colombian citizenship, Swiss B-permit (since 2013)

